ELECTROCHEMICAL SYNTHESIS AND FUNCTIONALIZATION OF CARBON BASED NANOMATERIALS

A THESIS

SUBMITTED TO THE

UNIVERSITY OF PUNE

FOR THE DEGREE OF

DOCTOR OF PHILOSOPHY

IN

CHEMISTRY

BY

DHANRAJ B. SHINDE

UNDER THE GUIDENCE OF

Dr. K. VIJAYAMOHANAN

PHYSICAL AND MATERIALS CHEMISTRY DIVISION

NATIONAL CHEMICAL LABORATORY

PUNE – 411 008

INDIA

July 2013

DECLARATION

I hereby declare that all the experiments embodied in this thesis entitled, **"ELECTROCHEMICAL SYNTHESIS AND FUNCTIONALIZATION OF CARBON BASED NANOMATERIALS"**, submitted for the degree of Doctor of Philosophy in Chemistry, to the University of Pune have been carried out by me at the Physical and Materials Chemistry Division, National Chemical Laboratory, Pune, 411 008, India, under the supervision of Dr. K. Vijayamohanan. The work is original and has not been submitted in part or full by me, for any degree or diploma to this or to any other University.

Date: 19 July, 13

Dhanraj B. Shinde

Physical and Materials Chemistry Division
National Chemical Laboratory
Pune – 411 008

Dr. K. Vijayamohanan
Scientist

Physical and Materials
Chemistry Division
National Chemical Laboratory
Pune – 411 008
INDIA

Tel: 91-020-2590 2588
Res: 91-020-2587 0307
Fax: 91-020-2590 2636
Email: vk.pillai@ncl.res.in

CERTIFICATE

This is to certify that the work incorporated in the thesis entitled, "**ELECTROCHEMICAL SYNTHESIS AND FUNCTIONALIZATION OF CARBON BASED NANOMATERIALS**" submitted by **Mr. DHANRAJ B. SHINDE ,** has been carried out by him under my supervision at the Physical and Materials Chemistry Division, National Chemical Laboratory, Pune, 411 008, India. All the materials from other sources have been duly acknowledged in the thesis.

Research Guide
(K. Vijayamohanan)

Date : 19 July 2013
Place : Pune

Dedicated to My Parents …

Acknowledgements

There are so many people, whose support, encouragement & inspiration are very much essential to accomplish major achievements in life, especially, if it involves the elements of fulfilling one's cherished dreams. For me, this thesis is such an important destiny & I am indeed, indebted to lot of people for their well wishes & blessings, for completing this journey.

I would like to take this opportunity first, to pay my sincere admiration to Dr. K. Vijayamohanan, whose motivation, inspiration, encouragement & persistent guidance have lead me to bring my dream to reality. His knowledge is like an ever-expanding encyclopedia, which has all possible solutions to help me out of any problem. I must also mention that he is also a very good teacher & a wonderful research guide, which is often quite rare. His constant effort to imbue us with several, most essential habits, like weekly seminars & group meetings, monthly reports & daily planning, makes me confident to start an independent scientific carrier.

I would also like to offer my sincere appreciation to Dr. Manjusha Shelke and Dr. K. Sreekumar for all help, support, suggestion & advice during the course of this study.

I also extend my sincere appreciation to Mrs. Manju (Madam) for her motherly care, blessing & constant support.

I wish to thank Dr. S. Pal, the Director, NCL for providing me all infrastructural facilities. I am also grateful to Dr. Anilkumar, head of Physical & Materials Chemistry Division for allowing me to use all the available facilities in the division & for his constant encouragement. I also would like to extend my sincere thanks to my teachers, A special thanks to our collaborators, Profs. M. G. Kulkarni, Aslam, T. Pradeep, Satish Ogale, Rahul Banerjee, Neetu Singh, Datta Late & Rahul Diggikar for their precious help & valuable discussions.

My sincere gratitude to Drs. P. A. Joy, B.L.V. Prasad, P. Poddar, Rahul Banerjee, Kreeshamurthy, &S. Asha for their advice & help. I am highly indebted to Dr. K.R. Patil, Mr. Gholap & Mr. A.B. Gaikwad also Mr. Ketan, Anuj, pankaj, Naren & shravani for helping me a lot in characterising my samples. Timely help from Mr. Dipak & Mr. Punekar & the entire library staff for excellent facilities is gratefully acknowledged. Further, CSIR is gratefully acknowledged for the financial support.

I can never forget the help from my seniors, Drs. Bhlachandra, Mahima, Bhaskar, Kannan, Meera, for their mentoring & care during my initial research days. I would like to thank Dr. Nagesh khupse for his constant encouragement & always being with me in all sorts of situations. A special thanks to all my labmates Joyashish, Beena, Vishal, Kuttan, vinayak, Ashvini, Palani, Vinisha, Sandeep, Bipin, Bihag, Pandiraj, Siddu, Neeta, Vrashali, Harshita, sachin, Rami, chaitnya, Raja, Vedi & Indrapal, who have helped me in all possible ways & have

been my extended family during the tenure of my work at NCL. I wish to extend my thanks to my senior Mahima chichi, Hari & project student Sonu for love, constant efforts & enthusiasm.

I would also like to express my sincere thanks to all my divisional colleagues Vijay Anna, Mangesh, Pankaj, Shraedha, Gitanjali, Sarita, Arpan, Shashi, Sachin, Raja, Ravi, Tamas, Arijeet,I also extend my thanks to several other friends in NCL, Prakash, Pradeep, Sachin, Sandeep, Malvi, Lenin, Manoj, Venu, Vivek, Amol, Narayan. A special mention of thanks to my hostel friends Abhijeet, Ganesh, Aba, Prakash, Dipak, Ankush,Prasad, Pankaj, Majid, Atul, Bhausaheb, Asif, Malvi, joby, Edwin. I have to express all my gratitude to my dearest friends Pradip, Kiran, Chinmay, Digamber for their constant encouragement. I also extend my special thanks to my collaborators Satish, Ajay, Hemen, Robin, Anil, Bishnu, & Vishal for their valuable help & support.

As always, it is impossible to mention everybody who had an impact on this work although there are those whose spiritual support is even more important. I find no words to express my feelings for my parents, whose moral support, love & constant encouragement have helped me to complete this journey. This thesis is also a dream for my elder brother 'Anna', whose support has always played a key role in my career. I wish to express my gratitude to my beloved sister Shailaja, who have always inspired me at every stage of life & my studies as well. I wish to extend my sincere gratitude to my grandmother & all other relatives for their blessings & love. Finally, a very special gratitude to my wife Manju not only for her constant encouragement but also for her patience & understanding throughout.

Dhanraj B. Shinde

List of Abbreviations

Abbreviation	Expansion
1-D	One-Dimensional
2-D	Two-Dimensional
3-D	Three-Dimensional
ac	Alternating Current
AFM	Atomic Force Microscope
BE	Binding Energy
bcc	Body Centered Cubic
CB	Conduction Band
CNTs	Carbon Nanotubes
CV	Cyclic Voltammetry
CVD	Chemical Vapor Deposition
dc	Direct Current
DCM	Dichloromethane
DFT	Density Functional Theory
DRIFT	Diffused Reflectance Infrared Fourier Transform
DMS	Dimethyl sulphide
DMSO	Dimethyl sulfoxide
DOS	Density of States
DDA	Dodecyl amine
DPV	Differential Pulse Voltammetry
DSC	Differential Scanning Calorimetry
DT	Differential Thermogravimetry
DWCNT	Double Wall Carbon Nanotube
EDX or EDS	Energy Dispersive X-Ray Spectroscopy
ESCA	Electron Scanning for Chemical analysis
ET	Electron Transfer
fcc	Faced Centered Cubic

FESEM	Field Emission Scanning Electron Microscopy
FET	Field-Effect Transistors
FFT	Fast Fourier Transform
FRA	Frequency Response Analyzer
FTIR	Fourier Transform Infrared
GNRs	Graphene nanoribbons
GQDs	Graphene Quantum dots
HiPCO	High pressure Carbon Monoxide Process
HOMO	Highest Occupied Molecular Orbital
HRTEM	High-Resolution Transmission Electron Microscopy
LCD	Liquid Crystal Display
LSV	Linear Sweep Voltammetry
LUMO	Lowest Unoccupied Molecular Orbital
MEMS/NEMS	Micro/Nano-Electromechanical Systems
MPCs	Monolayer Protected Nanoclusters
MWCNTs	Multi-Walled Carbon Nanotubes
NMR	Nuclear Magnetic Resonance
ODA	Octadecylamine
PL	Photoluminescence
PPy	Polypyrrole
PANI	Polyaniline
PTFE	Polytetrafluroethane
PET	Polyethylene terypthalate
PZC	Potential at Zero Charge
QDL	Quantized Double Layer Charging
Q-dots	Quantum Dots
QHE	Quantum Hall Effect
RBM	Radial Breathing Mode
SAED	Selected Area Electron Diffraction
SAM	Self-Assembled Monolayer
SCCM	Standard cubic centimeters per minute
SDS	Sodium dodecylsulphonate

SECM	Scanning Electrochemical Microscopy
SET	Single-Electron Transfer
SPR	Surface Plasmon Resonance
STM	Scanning Tunnelling Microscope
STS	Scanning Tunnelling Spectroscopy
SWCNTs	Single Walled Carbon Nanotubes
TBAP	Tetrabutyl ammonium perchlorate
TDA	Tridecylamine
TEM	Transmission Electron Microscopy
TG	Thermogravimetry
THF	Tetrahydrofuran
UV	Ultra-Violet
Uv-vis	Ultra-Violet-Visible
Uv-vis-NIR	Ultra-Violet-Visible- Near infrared
VB	Valence Band
VLS	Vapor-Liquid-Solid
XPS	X-ray Photoelectron Spectroscopy
XRD	X-ray Diffraction

Table of Contents

Chapter 1

Chapter-2

Chapter 3

Chapter – 5

Hydrothermal Synthesis of GNRs: Transparent Conducting thin films and Electrocatalysis

Chapter 6

Electrochemical Synthesis and Functionalization of Carbon Based Nanomaterials

This chapter presents a critical review of literature on the synthesis, characterization, and functionalization of graphene nanoribbons (GNRs) and graphene quantum dots (GQDs). The scope of these structures in nanotechnology along with several fundamental and applied aspects of GQDs and GNRs are discussed. Particular emphasis is placed on contemporary issues related to the development of electrochemical methods for the synthesis of high quality GNRs and GQDs followed by their precise characterization to understand these properties. Finally, the objectives of the present thesis are discussed with this perspective along with the abstract and limitations of the overall investigations at the end.

1.1 Introduction to carbon based nanomaterials:

Carbon is one of the most interesting elements in the periodic table and plays a unique role in nature. The formation of carbon [Fig.1.1] in stars as a result of the merging of three particles, known as triple alpha process is crucial which leads to the existence of all the relatively heavy elements in the universe.[1]

$$2He^4 + 2He^4 \rightarrow 4Be^8$$

$$4Be^8 + 2He^4 \rightarrow 6C^{12} + \gamma + 7.367\ MeV$$

Carbon has the ability to form very long chains interconnecting C–C bonds, known as catenation. This ability allows carbon to form an almost infinite number of compounds; in fact, there are more known carbon-containing compounds than all the compounds of the other chemical elements. The capability of carbon atoms to form complicated network[2] is fundamental to organic chemistry and is the basis for the existence of life, at least in its known forms. Even elemental carbon demonstrates unusually complicated behavior, forming a number of very different structures. For example, it forms many allotropes such as diamond and graphite including the recently discovered fullerenes[3] and nanotubes.[4]

Among those, diamond and graphite are much popular and well-known, since ancient time. However, recently discovered fullerenes and nanotubes are currently a focus of attention by many physicists and chemists. Thus, only three-dimensional (diamond, graphite), one-dimensional (nanotubes), and zero-dimensional (fullerenes) allotropes of carbon were known. The two-dimensional analogue was evidently missing, resisting any attempt at experimental observation – until recently.

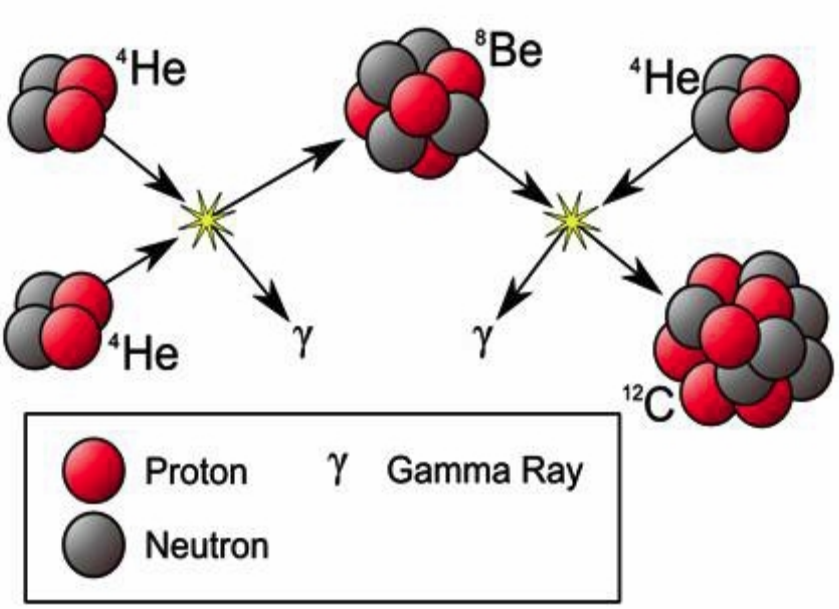

Figure 1.1 Over view of triple –alpha process responsible for the stellar formation of carbon from various elements. (Adopted from [1]).

1.2 Structure of carbon nanotubes (CNTs) and graphene:

Graphite is thermodynamically more stable than diamond under ambient conditions while the reverse is true at higher pressures/temperatures (the standard free energy difference is -2.90 kJ/mol at 298 K).[5] However, this is not the case when there is only a finite number of carbon atoms, since, a high density of dangling bonds dominates, the size of the graphite crystallites becomes very small (i.e. nano size). At smaller sizes, the structures get stabilized energetically by closing onto themselves to eliminate all the dangling bonds. For instance, preliminary experiments in the mid 1980s,[6] for developing the precursors to the fullerene,[7] suggested that when the number of carbon atoms is smaller than a few hundred, curved structures preferentially form a planar fragment of graphite through the introduction of a positive curvature by creating pentagons in the hexagonal lattice. Thus, a greatly elongated fullerene could be produced with exactly 12 pentagons (irrespective of however big the closed structure is!) and millions of hexagons.[2a] This would correspond to a carbon nanotubes,[8] as the geometry of the structure in figure 1.2 (a) reveals: a long cylinder of the hexagonal honeycomb lattice of carbon, bound by two pieces of fullerenes at both the ends.

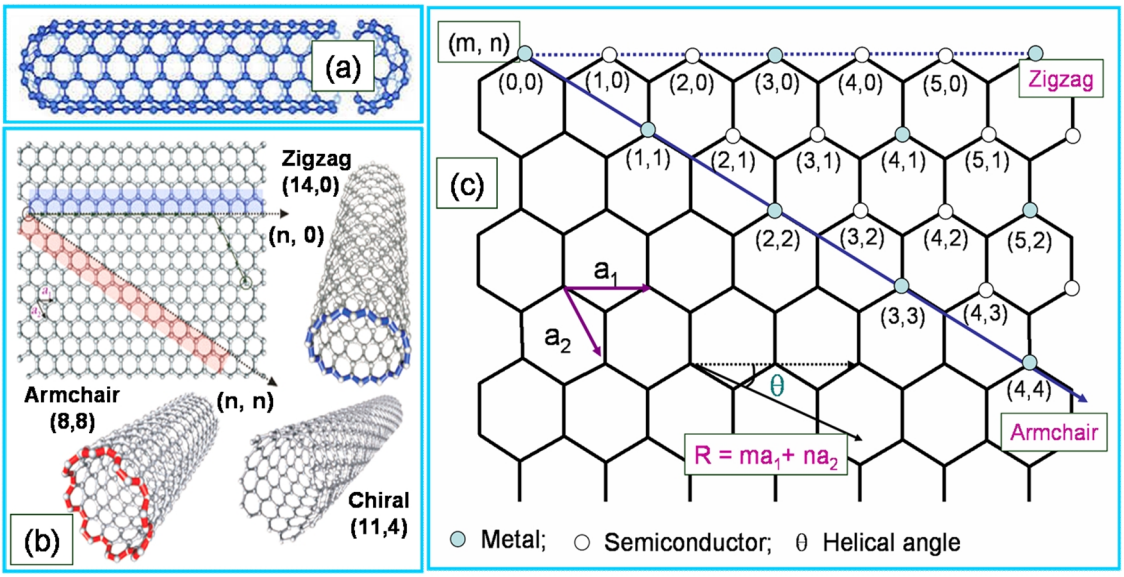

Figure 1.2 (a) Honeycomb hexagonal lattice structure of a typical CNT with fullerene caps **(b)** roll-up of a graphene sheet leading to the three different types of nanotubes **(c)** possible vectors specified by the integers (m, n) for general nanotubes, including zigzag, armchair and chiral nanotubes; the green colored dots denote metallic nanotubes while white dots are semiconducting nanotubes; a_1 and a_2 are unit vectors with a chiral angle of θ resulting into a new vector as R, called Hamada vector. (Adopted from [9]).

Single walled CNT can be considered as a single sheet of graphite, that has been rolled up into a tube, having a length to diameter ratio of about 1000 (also known as aspect ratio), so that, they can be considered as nearly one-dimensional (quasi 1-D) structures. As a result, one can only roll the sheet in a discrete set of directions in order to form a closed cylinder. [Fig. 1.2 (b)]. Two atoms in the graphene sheet (two dimensional graphitic networks having a honeycomb lattice) are chosen; one of which serves the role as origin and the sheet is rolled until the two atoms coincide. The vector pointing from the first atom towards the other is called the chiral vector and its length is equal to the circumference of the nanotubes and hence, the direction of the nanotube axis is perpendicular to the chiral vector.[9] The rolling action could be carried out in several ways, still satisfying the essential criterion that the dangling bonds present at both edges are matched. Any translational shift along the edges before fitting the dangling bonds will lead to a different orientation of the lattice with respect to an arbitrary tube axis. Thus, in a general nanotube structure, on the curved surface of the tube, the hexagonal arrays of carbon atoms can be pictured to wind around in a helical fashion, introducing '*helicity*' to the structure. This important variation in the graphene stacking sequence as a result of the change in bond lengths

and helical angle (θ) (due to rolling of graphene) is called '*helicity*' and introduces chirality and different types of CNTs.[9]

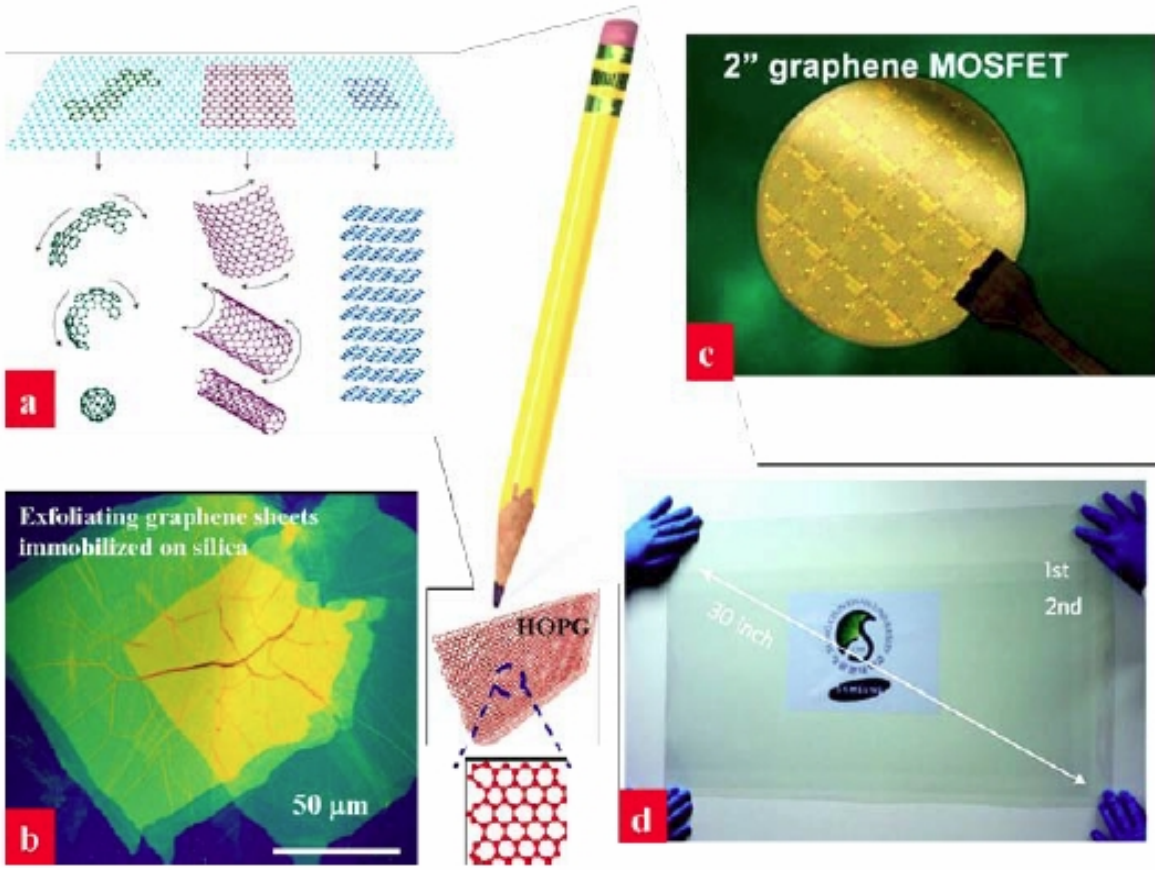

Figure 1.3 (a) Mother of all graphitic forms. Graphene is a 2D building material for carbon with all other dimensionalities. It can be wrapped up into 0-D bucky balls, rolled into 1-D nanotube or stacked into 3-D graphite. **(b)** AFM image of exfoliated graphene sheets immobilized on silica. **(c)** Application of graphene in MOSFET and **(d)** Large area graphene synthesis on Cu substrate using CVD method. (Adopted from [10]).

Graphene is one atom thick planar sheet of sp^2 bonded carbon atoms, densely packed in a honeycomb lattice, whereas, carbon nanotube is a one dimensional (1D) material. The dimensionality, determines most of the physical properties of the material. In graphene, carbon atoms create a honeycomb structure with hexagons on a plane. In carbon nanotubes, these hexagons are not planar, but they are rolled to create a cylinder. In fullerenes, however, the structure is just a sphere, which makes them zero dimensional (0-D) with discrete energy states. However graphite is made out of stacks of graphene layers which are weakly bound by van der Waals forces. Therefore, graphite can be expected to have closer physical properties to graphene.

Suddenly in 2004, this two-dimensional form, which was considered earlier as an '*academic*' material turned into reality, when free-standing graphene was obtained by a group of physicists from Manchester University. The group led by Andre Geim and Kostya Novoselov used a very different, even naive approach to obtain graphene and lead a revolution in the field. They started with three-dimensional graphite and extracted a single sheet (a monolayer of atoms) using a technique called micromechanical cleavage[10] [Fig. 1.3 (b)]. Graphite is a layered material and can be viewed as a number of two-dimensional graphene crystals weakly coupled together – exactly the property used by the Manchester team. By using this top-down approach and starting with large, three-dimensional crystals, these researchers avoided all the issues with the stability of small crystallites. Since its discovery, many groups have rapidly developed a variety of methods to produce single-layer graphene on various substrates – both conducting, and to a less extent, insulating.

1.1.1 Graphene nanoribbons (GNRs):

Graphene nano-ribbons (GNRs) are considered as elongated strips with a rectangular shape, carved out from a graphene sheet. Since, they have finite width and length, in nano scale, they are considered to be again quasi-1D structures. They can have different physical properties depending on their width, length and chirality, if we consider the length to be infinite, and width tending to zero they become an 1-D structure.[11] Consequently, the extension of graphene in one direction yields GNRs which can be considered as elongated strips. GNRs are originally introduced as a theoretical model by Fujita et *al* to examine the edge and size effects in graphene.[12] However, a major paradigm shift occurred since 2004 when it was realized that the massless Dirac-fermions predicted from the band structure were observable in table-top experiments at room temperature.[10c] The lateral confinement of the 2-D lattice into nearly 1-D ribbon more interestingly effected band gap opening, facilitating many possibilities to exploit the electronic properties of graphene in semiconductor device applications. In addition to 1-D patterning, this band gap opening is also possible by other means like applying a vertical electric field to break the symmetry in bi-layer graphene.[13] Consequently, various types of graphene based field effect transistors have been demonstrated showing respectable modulation, high current drive, and high mobility.[14]

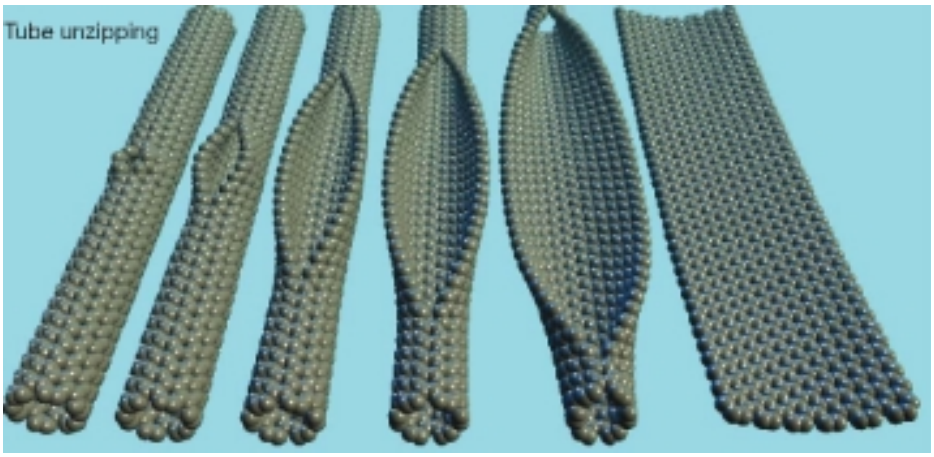

Figure 1.4 Representation of sequential unzipping of CNTs to graphene nanoribbons. (Adopted from [15]).

1.2.2 Graphene Quantum Dots (GQDs):

The term quantum dot (QD) stands for the confinement of electrons in all three spatial dimensions, which leads to quantization of the energy spectrum. This is in analogy to atoms, where the positive charge of the nucleus traps the electrons. The GQDs (0D) are the new type of quantum dots, which attract tremendous attention due to the possibility of creating finite gap states on an otherwise zero-band gap material like graphene by surface confinement and edge effects. The strong and tunable luminescence of GQDs is especially attractive, because of its promising applications in light emitting diodes, electroluminescence, organic photovoltaic devices, biological labeling and medicine.[16] Typically, GQDs contain carboxylic acid moieties at the edge, which is similar to those groups at the edges of graphene, thus imparting them with excellent water solubility and suitability for subsequent functionalization with various organic, polymeric, inorganic or biological species.[17]

In addition, GQDs have some excellent physico-chemical characteristics, such as high surface area, tunable diameter, and better surface grafting possibility using the π-π conjugated network or surface groups and other special physical properties due to the intrinsic structure. As a consequence, GQDs now occupy the center of significant research efforts to develop low-toxicity, eco-friendly synthesis and applications that can demonstrate many superior performance characteristics with respect to device applications.

1.3 Synthetic methods for graphene nanoribbons

In order to achieve a large-scale production of high-quality GNRs with narrow widths, numerous fabrication strategies, including both top-down and bottom-up approaches, have been proposed and subsequently demonstrated. This include techniques such as lithographic patterning followed by plasma etching of graphene.[18] Bottom-up approach for the synthesis of edge controlled graphene nanoribbons[19] metal-catalyzed[20] or oxidation cutting of graphene,[15, 21] direct chemical vapor deposition synthesis (CVD),[22] chemical synthesis,[15] and unzipping of carbon nanotubes[15, 18, 20-21, 23] with a wide variety of quality parameters as summarized in Table 1.1.

1.3.1 Longitudinal Unzipping of MWCNTs

One of the more successful approaches to date, to convert CNTs to graphene nanosheets is the longitudinal unzipping, using a mixture of potassium permanganate and concentrated sulphuric acid, facilitating a large scale preparation of GNRs. The opening of MWCNTs occurs along longitudinal direction resulting in to straight edges and this process largely depends on the chirality of the CNTs.[15]

The mechanism of opening is based on the oxidation of alkenes by permanganate in acid media. The rate determining step in the process is ester formation and further oxidation is possible to afford the dione in the dehydrating medium. Hence, once an opening has been initiated, its further progress is ensured relative to an unopened tube or to an uninitiated site on the same tube. This method can produce large amount of GNRs with 100 % yield. However, this method has several problems primarily involving the selection of strong oxidizing agents.

Table 1.1: Various approaches for the preparation of GNRs. (Adopted from[24]):

Method	T	Environment	Yield	Width (nm)	Edge quality	Band gap	Ref.
Plasma etching of CNTs	N/A	CNTs partially embedded in polymer film	medium (20%)	10-20	High	small	[18]
Chemical attack on CNTs	330K	H_2SO_4 /$KMnO_4$ Solution	nearly 100%	100-500	low	metallic	[15, 25]
Intercalation and exfoliation of CNTs	300-500 K	solution	high (60%)	100–250	low	N/A	[26]
Metal-catalyzed cutting of CNTs	1100 K	Si substrate	low (5%)	15–40	high	N/A	[27]
Sonochemical unzipping of CNTs	N/A	solution	low (2%) high	10–30	high	10–15 meV	[28]
Laser irradiation of CNTs	Laser energy (~200-350 mJ)	substrate	high (60%)	60-160	N/A	N/A	[29]
Hydrogen treatment and annealing of CNTs	~670-820 K	substrate with Fe catalyst	N/A	N/A	N/A	N/A	[30]
Unzipping functionalized CNTs by STM tips	N/A	substrate	N/A	N/A	N/A	N/A	[31]
Electrical unwrapping of CNTs by TEM	3000 K	substrate	N/A	~45	low	N/A	[32]
Patterning and etching of Graphene	N/A	Si/SiO2 substrates	high	6–100	low	0.1–0.5 eV	[33]
Metal-catalyzed cutting of Graphene	1200-1300 K	Si/SiO2 substrates	very low	10–15	high	N/A	[34]
Oxidation cutting of graphene	300-350 K	solution	0				[35]
CVD	1000-1700 K	templated substrate	high	20-300	low	0 V	[36]
Chemical synthesis	500-700 K	solution or Au substrate	N/A	0.18-0.25 nm	high	1.6 eV	[37]

Various approaches for the synthesis of GNRs using CVD, pyrolysis of THF and ferrocene, chemical and hydrothermal method and corresponding TEM, SEM, AFM and STM images as summarized in figure 1.5.

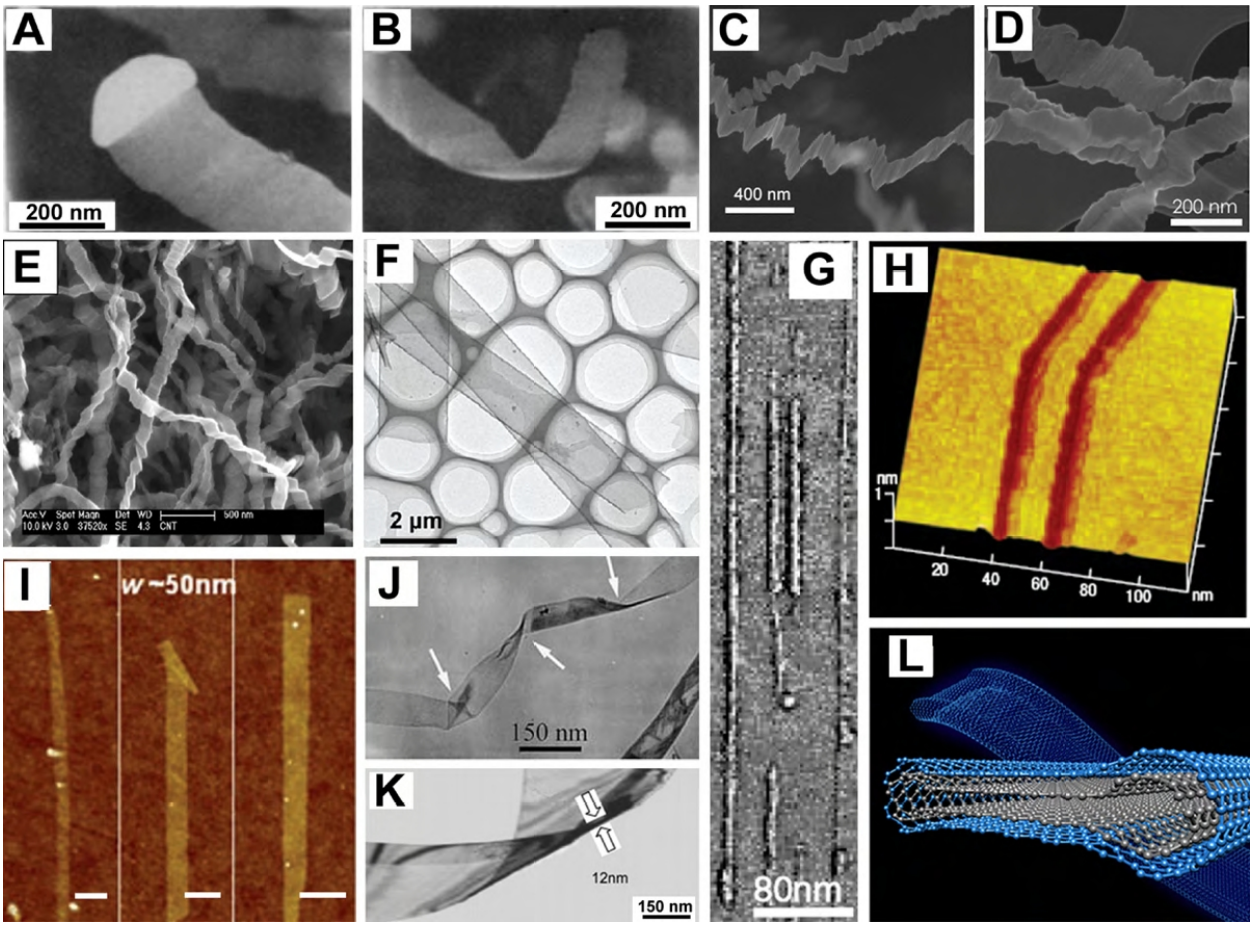

Figure 1.5 CVD and other production methods of graphitic nanoribbons. **(a and b)** Scanning electron micrographs of filamentous graphite, showing Fe particles at the ends of the structures;[38] **(c and d)** SEM images of the graphitic nanoribbons from the pyrolysis of ethanol—ferrocene—thiophene solutions;[39] **(e)** SEM image of the nanoribbons from the pyrolysis of THF and ferrocene solutions;[40] **(f)** Low magnification TEM image of the nanoribbons produced by the ZnS template method;[41] **(g)** AFM image of the nanoribbons obtained through high temperature treatments of diamond nanoparticles;[42] **(h)** 3-D STM image of an 8-nm-wide graphene nanoribbon patterned by STM lithography;[43] **(i)** AFM image of chemically derived nanoribbons from graphite (scale bars = 100 nm);[44] **(j and k)** TEM images of an amorphous carbon nanoribbon and graphitic nanobelt, respectively, produced by hydrothermal processes; [44b, 45] (l) Scheme illustrating the structure of a collapsed nanotubes.[46]

1.4 Synthetic methods for graphene quantum dots:

All efforts so far expended for the development of synthetic methods of GQDs can be classified into two main types: top-down and bottom-up methods. The top-down methods include electron beam lithography, acidic exfoliation, electrochemical oxidation, microwave-assisted hydrothermal synthesis, and so on [46-55], In these methods, GQDs are derived from the breaking of carbonaceous materials. In contrast, bottom-up routes, focus on building up of molecular species often in solution or gas phase using different chemistries like cyclo-dehydrogenation of polyphenylene precursors, carbonization or fragmentation of special organic precursors,(for example, the C_{60}) and some typical strategies are enlisted in Table 1.2.

Conversely, the bottom-up methods offer exciting opportunities to precisely control many important parameters of GQDs like size, shape, and edge states which in turn control their properties.[8] Nevertheless, these method always involve complex synthetic procedures, and sometimes the special organic precursors may be too difficult to be obtained in high purity form. More importantly, the poor solubility and strong tendency of aggregation of the GQDs limit their practical applications. Besides, the sizes of these GQDs obtained via the solution chemistry are lower than 5 nm, which poses additional processability deterrants for the state-of-the-art lithography (10 nm).

Table 1.2: A brief summary of the typical synthetic strategies for GQDs. (Adopted from [16h]).

Methods	Sub classification	Starting materials	Size (nm)	Height (nm)	color	Yield (%)	Ref.
Top-down	Acidic oxidation	GO	5-19		Blue		[47]
		GO	5-25		Blue		[48]
		Carbon black	15	0.5	Green	44.5	[49]
			18	1-3	Yellow	9.0	[49]
	Hydrothermal	GO	5-13	1-2	Blue Green	5	[17a]
		GO	1.5-5	1.5-1.9	Blue		
		RGO	2-5		Blue		[50]
	Amino-hydrothermal	GO	2.5	1.13	Blue-yellow		[51]
	Solvothermal	GO	5.3	1.2	Blue-Green		[17e]
	Microwave	GO	3-5	0.9	Blue	1.6	[52]
	Microwave-hydrothermal	GO	2-3	0.5-2	Green, Blue	1.6	[53]
		GO	3	< 0.7	Blue	8	[54]

	Electrochemical	Graphene Graphene rod	3-5 5-10	1-2	Green Yellow		[55] [56]
	Photo-Fenton Reaction	GO	40	1.2	Blue	45	[57]
	Oxygen plasma etching	Graphene	11±4.3	4.5			[58]
	K intercalation	MWCNTs Graphite flakes	20 ~20	<1 0.9	Blue Blue	22.96 9.9	[59] [59]
Bottom-up	Stepwise solution chemistry Precursor pyrolysis	Organic precursors Glucose Citric acid	~2.5-5 1.6-21 15	3.2 0.5-2	Red DUV,		[17b, 60] [61]
	Catalyzed cage-opening pyrolysis and exfoliation	C60			blue		[62] [63]
		Un-substituted HBC	60	2-3	blue	15-30	[64]

- GO- graphene oxide, HBC-Hexabenzyl carbonate.

1.5 Theoretical Models for unzipping of CNTs

A few theoretical studies on the cutting mechanism and design of new methods using ab initio level are available where graphene oxide having epoxy groups preferentially get aligned during the oxidation of CNTs.[65] Li and Yang *et al.* further revealed how oxygen-atom attack can transform a pair of epoxy groups due to the high symmetry of the honeycomb lattice of graphene, where the cutting directions of graphene sheet are random during oxidation.[66] Thus, producing graphene nanoribbons with smooth edges by means of oxygen attack is likely to be not possible. Interestingly by employing density functional theory (DFT) calculations, Ding *et al.* proposed recently an effective way of cutting strained graphene into GNRs along a specific direction.[67] The presence of uniaxial external strain not only guided the alignment of oxygen atoms along Z-direction that is closely perpendicular to the strain, but also significantly lowered the reaction barrier and enthalpy of graphene cutting along that direction.[68] Moreover, the applied strain simultaneously increased the reaction barrier of cutting along other directions. Hence, orientation-selective cutting of graphene into GNRs upon oxidation could be achieved.[67] A potential experimental route to cut graphene into GNRs by applying external strain in terms of stretching embedded graphene on a polymer was also possible.[69] Also, Bottom-up approach for the synthesis of edge controlled graphene nanoribbons has been reported by Cai *et al.* as shown

in figure 1.6. Where intermolecular colligation through radical addition is thermally activated by annealing at 200 °C, at which temperature, the de-halogenated intermediates have enough thermal energy to diffuse along the surface and form single covalent C–C bonds between each monomer to give polymer chains. Scanning tunneling microscopy (STM) images of the colligated monomers show protrusions that appear alternately on both sides of the chain axis.[19]

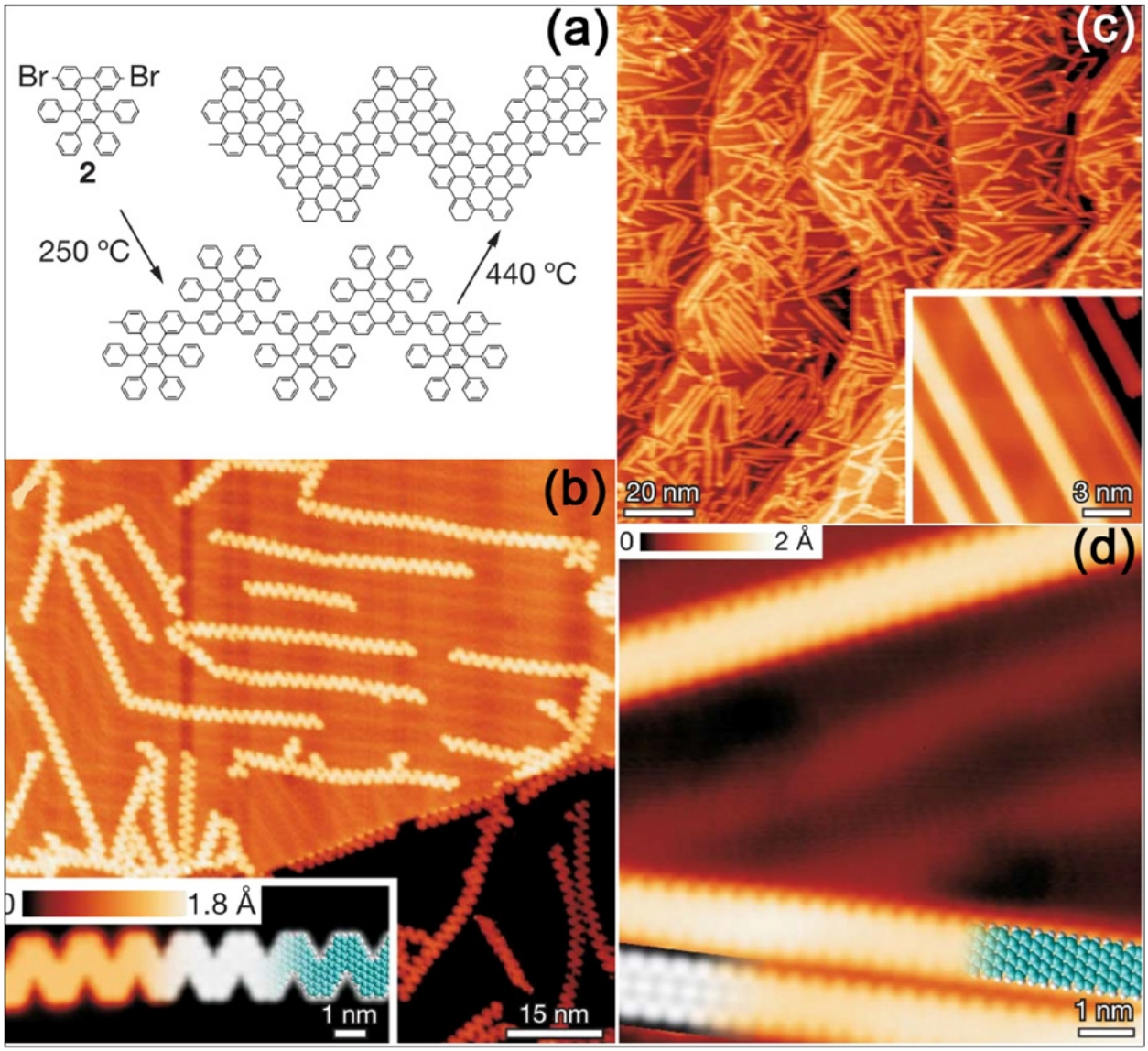

Figure 1.6 Bottom-up approach for the synthesis of edge controlled graphene nanoribbons. **(a)** Reaction scheme of chevron-type GNRs from tetraphenyl-triphenylene monomers. **(b)** STM image of chevron-type GNRs fabricated on a Au (1 1 1) surface (T = 35 K, U = −2V, I = 0.02 nA). The inset shows a high-resolution STM image (T = 77 K, U = −2V, I = 0.5 nA). **(c)** STM image of straight GNRs from bianthryl monomers after cyclodehydrogenation at 400 ◦C. The inset shows a higher resolution STM image. ***(d)*** High-resolution STM image with partly overlaid molecular model (blue) of the ribbon. (Adopted from [19]).

1.7 Properties of GNRs and GQDs:

1.7.1 Electronic structure of graphene:

Graphene has two atoms per unit cell, which results in two 'conical' points per Brillouin zone, where band crossing occurs, K and K'. Near these crossing points, the electron energy is linearly dependent on the wave vector. Actually, this behavior follows from symmetry considerations[70] and thus, is robust with respect to long-range hopping processes [Fig 1.7]. The interesting point is that, the charge carriers in graphene behave as massless relativistic particles.[71] The Dirac equation describes relativistic quantum particles with spin ½, such as electrons. The essential feature of the Dirac spectrum, following from the basic principles of quantum mechanics and relativity theory, is the existence of antiparticles. Vector k, $E = c\hbar k$. For massless Dirac fermions, the gap is zero and this linear dispersion law holds at any energy. In this case, there is an intimate relationship between the spin and motion of the particle: spin can only be directed along the propagation direction (say, for particles) or only opposite to it (for antiparticles). In contrast, massive spin -½ particles can have two values of spin projected onto any axis. In a sense, we have a unique situation here: charged massless particles. Although, this is a popular textbook example, no such particle has been observed earlier. The fact that charge carriers in graphene are described by a Dirac-like spectrum, rather than the usual Schrödinger equation for non-relativistic quantum particles, can be seen as a consequence of the crystal structure. This consists of two equivalent carbon sub-lattices A and B [Fig 1.7]. Quantum-mechanical hopping between the sub-lattices leads to the formation of two energy bands, and their intersection near the edges of the Brillouin zone yields the conical energy spectrum. As a result, quasi-particles in graphene exhibit a linear dispersion relation $E = \hbar k \upsilon_F$, as if they were massless relativistic particles (for example, photons), but the role of the speed of light is played here by the Fermi velocity $\upsilon_F \approx c/300$. Because of the linear spectrum, one can expect that quasi-particles in graphene behave differently from those in conventional metals and semiconductors, where the energy spectrum can be approximated by a parabolic (free electron- like) dispersion relation.[14a]

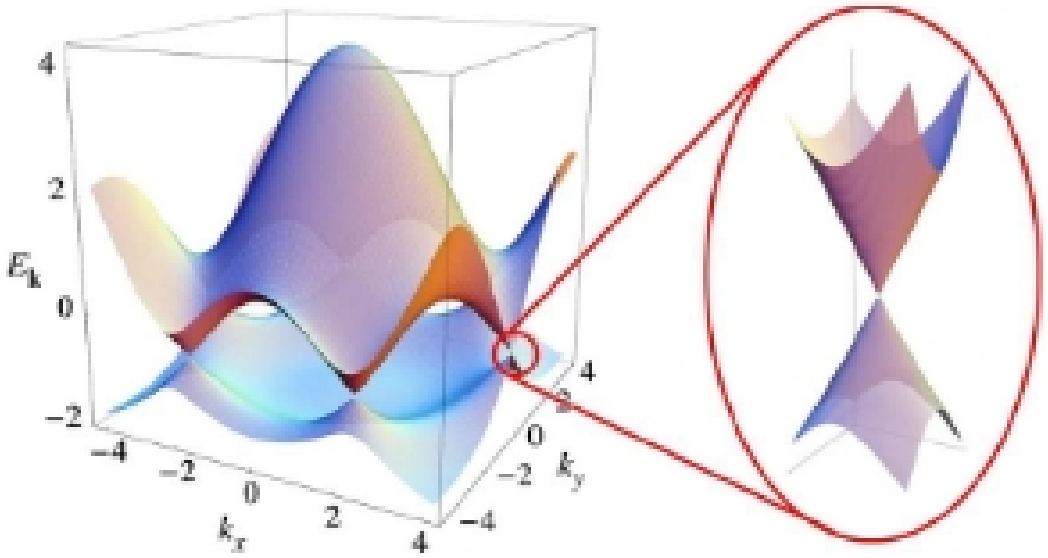

Figure 1.7 Energy bands of graphene. (left) Energy spectrum in units of γ_0 = 2.8 eV (nearest neighbor hopping energy) as a function of momentum *kx*. (right) Zoomed portion of the linear energy band near the Dirac point14a.

1.7.2 Defects in graphene nanoribbons:

Defects play a crucial role in the properties of crystals and nanostructures, including graphitic systems. Graphene-like systems are so versatile that they can accommodate different kinds of defects that change completely their structure and also their physicochemical properties. In particular, defects which change the structure could also change the topology or the curvature. However, it is difficult to identify accurately and quantitatively the type of defects in graphene-like materials, and researchers have not been able to distinguish them systematically. Depending on the nature of the defective surface, the chemical activity of graphene may be quite different. For instance, the inclusion of twelve pentagons in a graphitic cluster can form a fullerene and in general, the type of defects is categorized into five different groups [Fig. 1.8]:

(1) *Structural defects*, related to imperfections that significantly distort the curvature of the hexagonal carbon lattice. These defects are usually caused by the presence of non-hexagonal rings (e.g. pentagons, heptagons, or octagons) surrounded by hexagonal rings. For example, if a single or a few pentagons are embedded into the graphene lattice, nano-cones with different apex angles are obtained [Fig. 1.8 (a)]. A 30° angle in SWCNTs could also be explained by the presence of pentagon on one side of the tube and a heptagon on the opposite side. The reactivity

of pentagons, heptagons or octagons with specific acceptor or donor molecules has still to be determined from the theoretical and experimental stand points.

(2) *Bond rotations or grain boundaries*, which occur on graphene surfaces, and do not result in large curvature distortions of the sheet [Fig. 1.8 (b)]. In particular, these defects could be 5-7-7-5 pairs embedded in the hexagonal network or Stone—Thrower—Wales (STW type) defects [72] that could be created by rotating a carbon–carbon bond 90° within four neighboring hexagons, thus resulting in the transformation of two pentagons and two heptagons.[73] 2-D planar graphene-like systems containing pentagons, hexagons and heptagons, called Haeckelites, have been proposed to be metallic in theoretical studies.[74] Nanoribbons constructed from Haeckelites could be considered as new hypothetical nano-architectures with fascinating properties that could be applied in electronics. Isolated pentagon-heptagon pairs could also be introduced to form a grain boundary in graphene[75] or in graphitic nanoribbons, thus changing their edge termination and electronic properties.

3) *Doping-induced defects*, arising from substitutional non-carbon atoms embedded in the graphitic lattice [Fig. 1.8 (c)]. In this case, it has been demonstrated that nitrogen and boron atoms can be introduced into the hexagonal sp^2 hybridized carbon lattice. With both dopants, the chemical reactivity of the graphene surface increases, in one case due to the fact that N has one electron more than that in C, in the other because B has one electron less than that in C. Therefore, these type of defects could be used to tune the type of conduction in graphene-like materials, ranging from n-type transport (substitutional nitrogen doping) to p-type conduction (substitutional boron atoms in the lattice).[76]

4*) Non-sp^2 carbon defects,* caused by the presence of highly reactive carbon such as dangling bonds, carbon chains, interstitials (free atoms trapped between SWCNTs or between graphene sheets), edges (open nanotubes), ad-atoms and vacancies [Fig. 1.8 (d)]. These defects are usually observed in HRTEM, when the adsorbed atoms on these reactive sites are removed by the electron beam energy. It has been demonstrated that the creation of such defects could promote the formation of covalent nanotube junctions[77] and trigger the coalescence of nanotubes.[78] However, for nanoribbons, the dynamics of these defects has not been investigated and further research is required in this direction.

(5) *High-strain folding of graphene sheets* (loop formation), which can be induced by annealing two adjacent graphene layers [Fig. 1.8 (e)]. These types of ‘‘loops’’ have often been observed in thermal annealing above 1500 °C[79] but their chemical reactivity and electronic properties have not been investigated in detail.

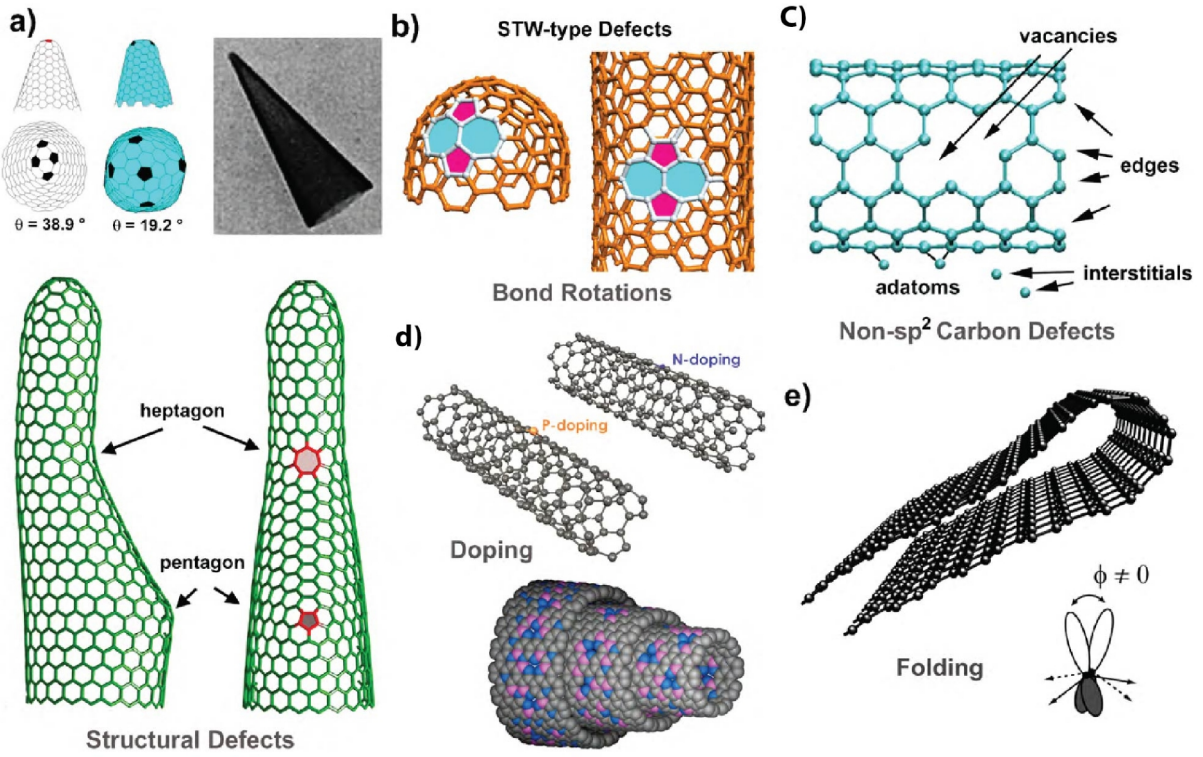

Figure 1.8 Schematic models representing different types of defects in graphene-like materials. **(a)** *Structural defects* induce significant structural changes caused by the presence of pentagons or heptagons within the hexagonal sp^2 hybridized carbon lattice (Image of cones courtesy of M. Endo and T.W. Ebbesen); **(b)** *Topological defects*, also termed Stone-Thrower-Wales defects, do not result in big structural changes. Shown here is the formation of 5-7-7-5 pairs created by rotating an individual carbon-carbon bond 90°; **(c)** *Non-sp^2 hybridized carbon defects*, including vacancies, edges, ad-atoms, interstitials, carbon chains, etc.; **(d)** *Doping* consists of replacing a carbon atom with another element within the hexagonal lattice (here, N and P) or a CNT randomly doped with B and N; **(e)** *Folding-induced defects*, which result from significant deformation of the graphene sheet, thus altering the orbitals. The direction of the orbital is then called the orbital axis vector (POAV). The angle between the POAV and a direction (i.e., a bond) indicates the degree of ‘pyramidalization’ and the hybridization. For 90° (planar system), the orbitals are in a sp^2 hybridization and the orbital is a pure *pz* orbital. For a folded graphene sheet, has an intermediate value which decreases as the inverse of the radius of the curvature of the folding, and reaches 90° at the limit $R \rightarrow \infty$. (Adopted from [80]).

1.7.3 Quantum Hall effect (QHE) at room-temperature:

The quantum Hall effect is a quantum-mechanical version of the Hall effect, observed in two-dimensional electron systems subjected to low temperatures and strong magnetic fields, in which the Hall conductivity σ takes on the quantized values:

$$\sigma = \frac{I_{\text{channel}}}{V_{\text{Hall}}} = \nu \frac{e^2}{h},$$

Where, $I_{channel}$ is the channel current, V_{Hall} is the Hall voltage, *e* is the elementary charge and *h* is Planck's constant. The pre-factor ν is known as the "filling factor", and can take on either integer (ν = 1, 2, 3,...) or fractional (ν = 1/3, 2/5, 3/7, 2/3, 3/5, 1/5, 2/9, 3/13, 5/2, 12/5) values. The quantum Hall effect is referred to as the integer or fractional quantum Hall effect depending on whether ν is an integer or fraction respectively. The integer quantum Hall effect is very well understood, and can be simply explained in terms of single-particle orbitals of an electron in a magnetic field (Landau quantization). In contrast, the fractional quantum Hall effect is more complicated, as its existence relies fundamentally on electron–electron interactions.

As with many other quantum phenomena, the experimental observation of the QHE usually requires low temperatures, typically below the boiling point of liquid helium.[81] Efforts to extend the QHE temperature range by, for example, using semiconductors with small effective masses of charge carriers have so far failed to reach temperatures above 30 K.[82] These efforts have been carried out to observe apparently fragile quantum phenomena under ambient conditions.

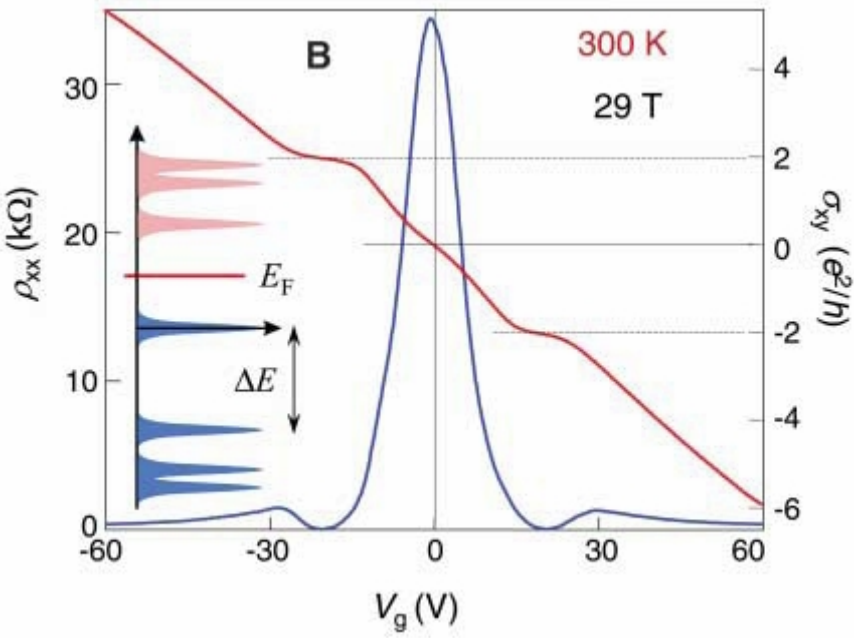

Figure 1.9 Room temperature quantum hall effect - σxy (red) and ρxx (blue) as a function of gate voltages *V*g in a magnetic field of 29 T. Positive (negative) gate voltages *V*g induce electrons (holes) in concentrations $n = (7.2 \times 10^{10}\ \text{cm}^{-2}/\text{V})/V\text{g}$. The inset illustrates the Landau level quantization for Dirac fermions.[14a, 83]

The QHE can be observed in graphene even at room temperature [Fig. 1.9] due to the highly unusual nature of charge carriers in graphene, which behave as massless relativistic particles (Dirac fermions) and move with little scattering under ambient conditions.[84] These results have been observed experimentally by Geim *et al.* as shown in Figure 1.9.

1.7.4 Optical properties of GQDs:

GQDs usually show well-established absorption bands in the UV region, with an absorption peak around 230 nm due to the π–π* transition of aromatic sp^2 domains[10c, 17a, 61] and a long tail extending into the visible range. Many GQDs also have another absorption (shoulder) peak centered at a wavelength between 270 to 390 nm, which has been associated with the n / π * transition of C=O.[17e] This peak position depends more on the preparation method than the size of the dots. For example, GQDs (9.6 nm) by the hydrothermal route show an absorption band at 320 nm,[17a] the same position as those of GQDs (5.3 nm) from a solvothermal synthesis[17e] and by GQDs (3–5 nm) from an electro chemical method, while a further decrease in GQD size down to 1.5–5 nm by a hydrothermal approach makes the shoulder red- shifted to ca. 360 nm,[85]

although this absorption peak is similar to those of GQDs prepared (diameter of 5–10 nm) by the electrolysis route from graphite.[56]

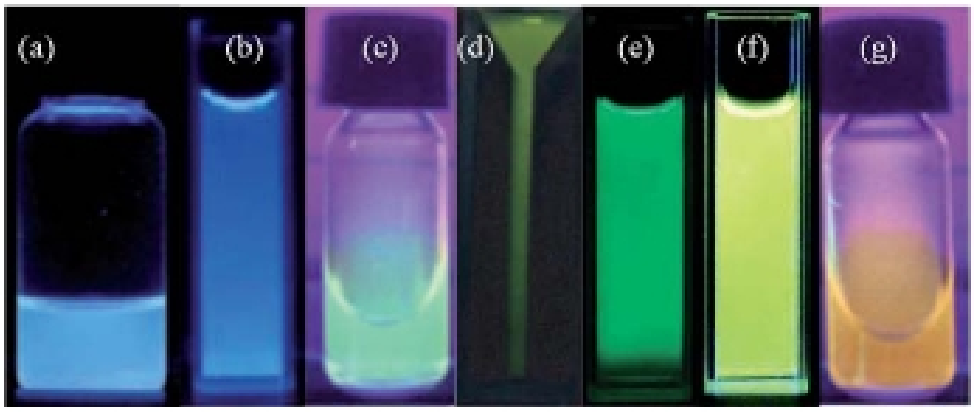

Figure 1.10 Photographs taken for solutions of different GQD under 365 nm UV light irradiation (except for (e) where 375 nm was used) (a-g). (Adopted from [47, 49, 53, 86]).

However, one of the common phenomena often observed in GQDs is the excitation-dependent PL emission. When the excitation wavelength is changed from 320 to 420 nm, the PL peak of hydrothermally cut GQDs shift to longer wavelengths and the PL intensity decreases remarkably,[17a] as observed also in GQDs synthesized from other methods.[17e, 47, 49, 53, 56, 61, 64, 85, 87] This is generally interpreted to be related to the presence of emissive traps, [88] electronic conjugate structures,[87b] and free zigzag sites having a carbene-like triplet ground state,[17a] with some researchers claiming that the surface states also have an important role.[61] It is possible that a combination of these parameters might be relevant, as both the edge structures and the defects/surface states can significantly change the electronic properties of GQDs.[89] Exceptionally, a handful of GQDs have been reported to emit PL independent of the excitation wavelength.[90]

The PL of some of the GQDs reveals interesting pH-dependent and solvent-dependent behavior facilitating the tuning of their optical properties. For example, GQDs prepared by the hydrothermal exfoliation method, show strong PL under alkaline conditions, whereas under acidic conditions, this type of PL evinces nearly a complete quenching. If pH is switched repeatedly between 13 and 1, the PL intensity varies reversibly[17a, 85] and this is explained in terms of the protonation and deprotonation of free zigzag sites under acidic and alkaline conditions. The incoherence in pH-dependent PL behaviors and the distinctive solvent-

dependence clearly indicate dissimilar PL mechanisms in different GQDs, a puzzle which needs to be solved with more experimental and theoretical results in the near future.

1.7.5 Electrochemical properties:

The tunable size of nanoparticles has been found to reveal several interesting electrochemical properties like quantized charging behavior depending upon the core size and the nature of the surface passivating molecules. At present, there are neither theoretical nor experimental evidence to show that the open circuit potential of GQDs is size dependant although the pH dependence and pseudocpacitance could be explained due to the presence of surface functional groups. A major emphasis has been placed on the investigation of the double-layer charging properties of smaller nanoparticles (< 3 nm) to understand their electron transfer features.[91] The freely diffusing or surface attached nanoparticles on electrode surface show discrete double layer charging features with respect to one electron, where the capacitance (auto farads; aF) is associated with ionic space charge formed around each GQDs in the electrolyte solution, known as quantized double layer (QDL) charging.[92] The QDL phenomenon has been reported for various nanoparticles especially for Au and several effects, like core size, chain length, nature of monolayer, temperature and magnetic field, have been studied, although this property is not known for GQDs.

1.8 Applications of GNRs:

As explained earlier, Graphene is a unique material because it displays an outstanding combination of electron and phonon transport at room temperature, in which electrons behave as massless particles without experiencing scattering. Therefore, the imminent applications of this layered material are in electronics such as in the fabrication of ultrafast transistors[18] able to operate in the terahertz frequency range. Its low capacitance is also important for the fabrication of biosensors or chemical sensors due to the resulting low values of the signal to noise ratios. However, due to the large number of reactive edges in graphene nanoribbons, it is expected that the sensing abilities of ribbons are superior to those shown in graphene. In addition, by doping or by applying different edge spin orientations; the band gap of nanoribbons may be controllable, thus having important implications in the fabrication of novel and ultrafast electronic devices with outstanding sensing abilities. Research in this direction needs to be focused both

experimentally and theoretically to improve our understanding since there are several promising results. For example, Lin *et al.* have shown that wafer-scale production of graphene (grown epitaxially over SiC) FETs is possible especially for circuits function at 100 GHz switching frequencies. In addition to transistors, GNRs could find applications in nano-electromechanical systems (NEMS). An example of this was reported by Wei *et al.*[93] who produced a few-layer graphene ribbon (NEM) switch with good reversibility, which was used in an OR gate. Graphene nanoribbons could be used as fillers in the fabrication of robust polymer composites, highly conducting transparent films, high thermal conducting polymers, and other composites with different metals and ceramics. Due to the presence of defects and dopants, it may also be possible to use these locations as catalytic spots for anchoring specific bio-molecules, drugs, heavy metals, and other species. Another application for graphene is as the thinnest possible support film for HRTEM, and this has been shown to allow, for example, observation of individual adatoms over graphene[84] and atomic resolution imaging of soft hard interfaces. These graphene film grids can easily be made in the laboratory by transferring graphene flakes over TEM grids, and are starting to be commercially available. Few-layer graphene films have also been shown to offer advantages in TEM.

1.9 Applications of GQDs:

1.9.1 Bio-imaging Applications:

Traditional semiconductor quantum dots such as CdSe or CdS and their core–shell nanoparticles have been used in various *in vitro* or *in vivo* optical imaging[94]. However, these QDs dots have elicited serious health and environ mental concerns due to high toxicity of the heavy metal elements.[94b] GQDs are attractive alternatives for bioimaging applications as a consequence of their tunable and strong PL properties established with low toxicity and eco-friendly nature. In the above example, green GQDs were selected to incubate with T47D human breast cancer cells and the nucleus stained by,[95] 6-diamidino-2- phenylindole (DAPI, blue color). As shown in figure 1.11 (a), the fluorescent image clearly shows the phase contrast of labeled T47D cells, with the nucleus stained in blue by DAPI and green GQDs agglomerated around each nucleus.[49, 86b] In another experiment, Dong et *al.* found that the GQDs-stained MCF-7 cells exhibited a

bright green color when imaged with excitation at 488 nm on the confocal laser scanning microscope and the section analysis of one MCF-7 cell indicated that GQDs could label the cell membrane, the cytoplasm and the nucleus simultaneously, using luminescent carbon nanomaterials to label the cell nucleus [Fig. 1.11 (b)].[49]

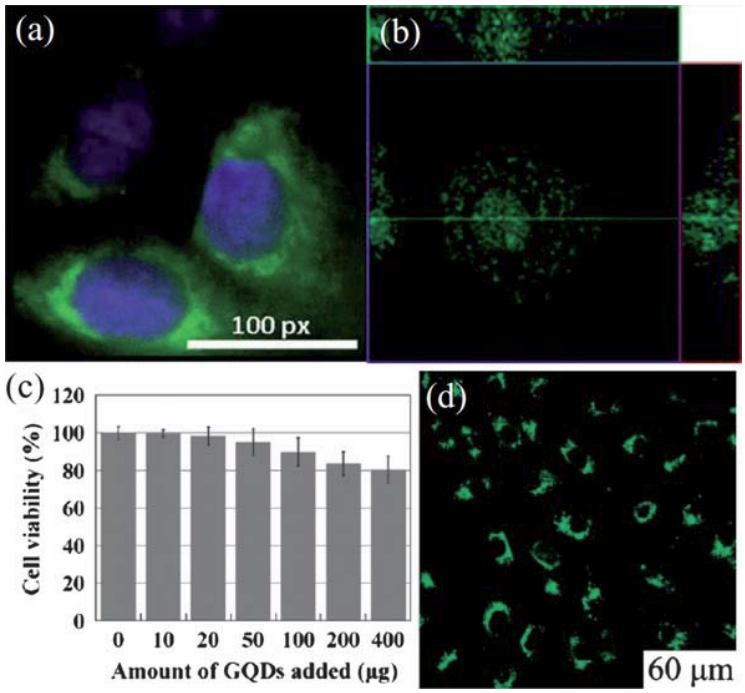

Figure 1.11 (a) A comparison of high contrast images of a nucleolus stained with blue DAPI and GQDs (green). **(b)** Section analysis of human breast cancer MCF-7 cells labeled with GQDs derived from carbon black**. (c)** Effect of solvothermally produced GQDs on MG-63 cells viability. **(d)** Cellular imaging of GQDs less than 405 nm. (Adopted from [17e, 49, 86b]).

Additionally, Zhu *et al.* showed a case of two-color imaging with GQDs. After the uptake of hydrothermally prepared GQDs, bright green areas inside the MG-63 cells were observed when excited at 405 nm [Fig. 1.11 (d)] and cellular imaging changed to a green-yellow color when the excitation shifted to 488 nm, both indicating translocation of GQDs through the cell membrane.[17e] However, agglomeration of GQDs in organic or inorganic solvents mainly quenches the fluorescence and subsequently hampers their application in optoelectronic devices in the solid state. Furthermore, GQDs have non-stoichiometric nature and hence, achieving a control on the optical properties becomes extremely challenging without using any external capping agents like PEG polyethelene glycol and/or dodecyl amine. Hence, it is important to

stabilize GQDs by functionalization or confining within a solid matrix to utilize their excellent fluorescence properties in devices.

1.9.2 Single electron transistor:

Quantum confinement and edge effect cause peculiar electronic properties in the GQDs like band gap opening, coulomb blockade phenomenon and high mobility.[14a] These mechanisms can be generally grouped into various categories such as surface scattering including grain boundary scattering, quantized conduction including ballistic transport, Coulomb charging and tunneling, widening of band gap along with reorganization of energy levels [96]. In addition, increased structural perfection during growth kinetics such as reduced impurity level, control of structural defects and dislocations by annealing and similar post-synthetic treatments would also affect electrical conductivity.[97]

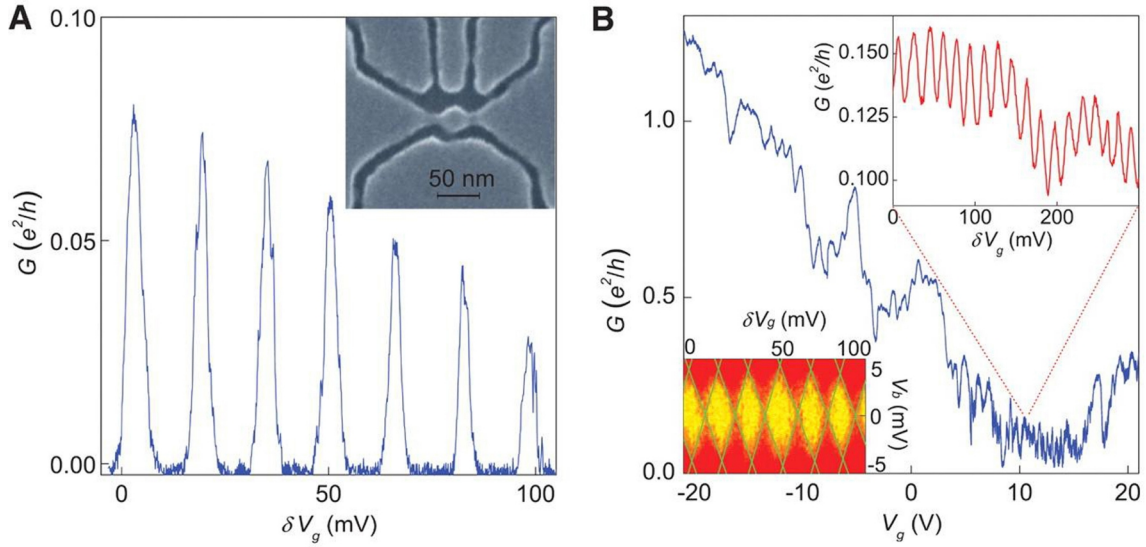

Figure 1.12 Graphene-based single-electron transistors. a, Conductance G of a device with the central island of 250 nm in diameter and distant side gates as a function of Vg in the vicinity of +15V; T =0.3K. The inset shows one of our smaller devices to illustrate the high resolution of our electron-beam lithography that allows features down to 10 nm. Dark areas in the scanning electron micrograph are gaps in the PMMA mask so that graphene is removed from these areas by plasma etching. In this case, a 30-nm QD is connected to contact regions through narrow constrictions and there are 4 side gates. b, Conductance of the same device as in Fig. 1.12a over a wide range of Vg (T =4K). Upper inset: Zooming into the low-G region reveals hundreds of CB oscillations. The lower inset shows Coulomb diamonds: differential conductance G_{diff} =dI/dV as a function of Vg (around +10V) and bias Vb (yellow-to-red scale corresponds to G_{diff} varying from zero to $0.3e^2/h$; note that our color diagrams often appear smudged if printed in gray).[97]

Accordingly, electronic properties of GQDs would be promising for constructing electrical devices based on single electron transfer (SET), superior to presently available Si based integrated circuits and information storage devices. Although their typical resistivity value suggests semiconducting behavior, especially if the size is < ~2 nm, the I-V curves show Coulomb blockade behavior that manifests single electron tunneling at room temperature as shown in figure 1.12. Further, organized/superlattice assemblies of these nanoparticles have unique electronic properties due to their collective tunable interactions although the I-V behavior is strongly affected by the nature of capping molecule, including its length and functional groups.

1.10 Conclusions and perspectives:

Some of the most recent developments in the interesting aspects of GNRs and GQDs have been presented in this chapter with particular emphasis on their preparation, properties and various applications. Both theory and experiments clearly show extraordinary structure and size-dependent properties of GNRs and GQDs. The opening of band gap in both GNRs and GQDs enable a broad range of promising applications in nano-electronics. Also, having vast tunability with respect to their structure and property, these applications are expected to lead the prospect of this field for continuing decades perhaps, with immense benefits in many areas like energy, healthcare, and environmental monitoring. More specifically, these nanostructures act as indispensable building blocks for creating designer materials, devices and especially catalysis, transparent touch screens,[14a] carbon fiber spinning,[10a] formation of conductive polymer as well as low-loss-high permittivity composites.[98] Although there are many methods to synthesize and understand the properties, several daunting challenges of these materials such as control of edge states and quality of both GQDs and GNRs , issue of scale-up and cost effectiveness, require breakthrough results to utilize these technological benefits.

1.11 Motivation, scope and organization of the thesis:

The genesis of the present thesis is inspired by many of these interesting issues unfolded during the preparation of above critical review related to both fundamental and applied aspects of GQDs

and GNRs. This includes the development of electrochemical methods for the synthesis of high quality GNRs and GQDs followed by their precise characterization to understand these properties. If such nanostructures are made to organize in a controllable fashion along with their related hybrid structures, they can open up several unprecedented application possibilities. Consequently, it is imperative to study different properties such as electrochemical, coulomb blockade, electrical, optical, catalytic etc. of these materials for the pursuit of various applications.

1.12 Objective of present investigation:

The foregoing critical review of GNRs and GQDs shows several recent innovative methods for their synthesis, functionalization, and applications. Despite these impressive developments, several lacunae still exist which prevent their wide utilization for various applications. For instance, most of the nanostructures synthesized by chemical methods contain oxidized GNRs, which dramatically hamper the electronic conductivity. Consequently, the use of electrochemical approach is rather crucial to design these nanostructures in a desired manner. Since the nanostructures like GNRs and GQDs are very important as a backbone for the fabrication of field effect transistors, electrochemical devices and flat panel displays, it is of immense importance to understand the effect of cations and anions during their preparation in an electrochemical method. Furthermore, the use of GNRs as a field effect transistor and transparent conductive thin films has tremendous utility due to their favorable characteristics such as finite band gap, high surface area, mechanical strength, inert carbon network and chemically tunable topography. Hence, it will be interesting to explore the preparation methods, which gives high quality carbon nanostructures. The specific objectives of the work embodied in this thesis are set out in this perspective as follows:

(a) To synthesize GNRs from CNTs using electrochemical unzipping approaches.

(b) To explore the effect of cations, anions and temperature on the quality of GNRs during chemical as well as electrochemical unzipping of CNTs.

(c) To Synthesize GQDs from various CNTs in suitable solvents and counter ions using both chemical and electrochemical approaches.

(d) To elucidate the effect of different sizes of GQDs and nitrogen doped GQDs (N-GQDs) on the electrocatalytic properties of oxygen reduction reaction (ORR).

(e) To functionalize and characterize monodispersed GQDs revealing some of their unique behavior like single electron transfer and luminescence.

(f) To synthesize highly conductive GNRs using hydrothermal method and revealing unique applications like FET, Thin films and electrocatalysis.

The present thesis discusses several electrochemical approaches to the synthesis of graphene nanoribbons and GQDs, their characterization details followed by potential applications in five separate chapters. Chapter **I** represents a critical review of synthesis, characterization, properties and various applications of the graphene nanoribbons and GQDs. A tentative mechanism has been proposed to explain the transformation of CNTs to GNRs and GQDs along with their associated topological changes and thermodynamics considerations. The electron transfer features of these nanosized particles have been elaborately discussed to explain their potential impact for diverse applications such as nanoelectronics, catalysis, bio-imaging and magnetic devices, medical diagnostics and therapeutics, environmental and pollution control. The chapter concludes by setting up the specific objectives for the present study, future prospects and finally mentioning some of the existing limitations of these carbon based nanomaterials.

Chapter **II** illustrates the electrochemical unzipping of both single walled and MWCNTs for facile synthesis of high quality graphene nanoribbons (GNRs) and also the effect of annealing on their quality. GNRs have been characterized using scanning electron microscopy (SEM), Transmission electron microscopy (TEM), Atomic Force Microscopy (AFM), X-ray photoelectron spectroscopy (XPS) measurements. The role of electric field, pH, counter ions, and duration in attaining good yield of unzipped CNTs is also discussed in this chapter. The importance of in-situ Raman experiments for unraveling the mechanism of unzipping of CNTs is discussed along with different parameters in controlling yield and functionality as electrochemical method with a potentiostatic control using selective oxidation followed by reduction would be beneficial to obtain GNRs by precise control of the size and shape. Also the present method is unique, since an accurate control of potential enables a means of monitoring the width of GNRs, despite small yield.

Chapter **III** describes the size controlled electrochemical synthesis of luminescent GQDs and N-doped GQDs from CNTs and N-MWCNTs respectively. These experiments were conducted in non-aqueous media like propylene carbonate and acetonitrile in order to obtain GQDs unlike that of GNRs in aqueous media. More specifically, sustained oxidation (15 h) of MWCNTs in propylene carbonate with $LiClO_4$ at 1 V followed by reduction yielded discrete spherical particles of GQDs presumably due to lateral unzipping. Also the role of electric field, dependence on cation, anion, solvent and temperature were systematically investigated to unravel their size dependent optical and electrochemical properties. These GQDs were characterized by Transmission and Scanning electron microscopy, Atomic force microscopy (AFM), Raman Spectroscopy and X-ray Diffraction (XRD) and their remarkable size-dependant light-emitting behavior are described in this chapter to enable promising applications.

The chapter **IV** starts with the discussion of the effect of particle size and temperature on charging energy of GQDs for Coulomb blockade phenomenon using a simple theoretical model. In later sections, the electron transfer features of *ca.* 3, 2.6, 2.2 and 5 nm sized dodecyl amine protected GQDs have been discussed using electrochemical techniques. Further, various parameters such as capacitance calculation and adsorption phenomena of these GQDs have also been discussed to understand stability issues relevant to specific applications.

The chapter **V** gives elaborate discussion about the synthesis of high quality GNRS using hydrothermal experiments and the effect of cations, anions and temperature on the quality of GNRs. Also applications of GNRs by decorating Pt nanoparticles as support material for electrocatalysis and field effect transistor have been discussed.

A summary of all the major conclusions of the present study with respect to preparation, characterization, properties and potential applications of these carbon based nanomaterials are given in Chapter **VI**, indicating the possible advantages of Graphene and GQDs in the fabrication of Single electron transistors and molecular switches. One of the unique observations is the control of the orientation of CNTs in presence of electric field helping for longitudinal unzipping and also for intercalation of supporting electrolytes ions in nonaqueous media presumably facilitating the lateral unzipping (or possible breakdown of structure) to form GQDs. This chapter also outlines some of the limitations of this electrochemical synthesis along with ample scope of further work in this area and its bright future prospects.

1.13 References:

[1] W. A. Fowler, *Rev. Mod. Phys* **1984**, *56*, 149.

[2] a)T. W. Ebbesen, *Carbon Nanotubes : Preparation and Properties CRC Press Boca Raton* **1997**; b)L. Pauling, *The Nature of the Chemical Bond, Cornell University Press, Ithaca, NY,* **1960**.

[3] a)R. F. Curl, *Rev. Mod. Phys* **1997**, *69*, 691; b)H. Kroto, *Rev. Mod. Phys.* **1997**, *69*, 703; c)R. E. Smalley, *Rev. Mod. Phys.,* **1997**, *69*, 723.

[4] S. Iijima, *Nature* **1991**, *354*, 56.

[5] Carbon Materials for Advanced Technologies, *Edited by Burchell, T. D. (Pergamon, An Imprint of Elsevier Science, UK).* **1999**.

[6] E. A. Rohlfing, D. M. Cox, A. J. Kaldor, *Chem. Phys. Carbon* **1984**, *81*, 3322.

[7] H. W. Kroto, J. R. Heath, S. C. O'Brien, S. C. Curl, R. E. Smalley, *Nature* **1985**, *318*, 162.

[8] a)M. S. Dresselhaus, G. Dresselhaus, P. C. Eklund, *Science of Fullerenes and Carbon Nanotubes; Academic Press: New York,* **1996**; b)C. H. Kiang, W. A. Goddard, R. Beyers, D. S. Bethune, *Carbon* **1995**, *33*, 903; c)P. M. Ajayan, T. W. Ebbesen, *Rep. Prog. Phys.* **1997**, *60*, 1025; d)B. I. Yakabson, R. E. Smalley, *Am. Sci. July-August* **1997**, *324*; e)R. D. Saito, M. S.; Dresselhaus, G. , *Physical Properties of Carbon Nanotubes; World Scientific: New York* **1998**.

[9] a)J. W. Mintmire, B. I. Dunlap, C. T. Carter, *Phys. Rev. Lett.* **1992**, *68*, 631; b)N. S. Hamada, S.; Oshiyama, A. , *Phys. Rev. Lett.* **1992**, *68*, 1579; c)M. S. D. Dressselhaus, G.; Saito,, *R. Phys. Rev. B* **1992**, *45*, 6234; d)K. B. Balasubramanian, M. , *Small* **2005**, *1*, 180.

[10] a)A. K. Geim, K. S. Novoselov, *Nature Materials* **2007**, *6*, 183; b)K. S. Novoselov, et al., *Proc. Natl. Acad. Sci. USA,* **2005**, *102*, 10451; c)K. S. Novoselov, et al., *Science* **2004**, *306*, 666.

[11] D. Sudipta, K. P. Swapan, *Journal of Materials Chemistry* **2010**, *20*, 8207.

[12] K.Nakada, M.Fujita, G.Dresselhaus, M.S.Dresselhaus, *Physical Review B* **1996**, *54*, 17954.

[13] S. Virendra, J. Daeha, Z. Lei, D. Soumen, I. K. Saiful, S. Sudipta, *Progress in Materials Science* **2011**, *56*, 1181.

[14] a)A. H. C. Neto, N. M. R. Peres, K. S. Novoselov, A. K. Geim, *Reviews of Modern Physics* **2009**, *81*; b)L. Vicarelli, M. Vitiello, D. Coquillat, A. Lombardo, A. Ferrari, W. Knap, M. Polini, V. Pellegrini, A. Tredicucci, *Nature materials* **2012**, *11*, 865.

[15] D. Kosynkin, A. Higginbotham, A. Sinitskii, J. Lomeda, A. Dimiev, B. Price, J. Tour, *Nature* **2009**, *458*, 872.

[16] a)S. Baker, G. Baker, *Angewandte Chemie* **2010**, *49*, 6726; b)L. Cao, M. Meziani, S. Sahu, Y.-P. Sun, *Accounts of chemical research* **2013**, *46*, 171; c)Y. Fang, S. Guo, D. Li, C. Zhu, W. Ren, S. Dong, E. Wang, *ACS Nano* **2012**, *6*, 400; d)V. Gupta, N. Chaudhary, R. Srivastava, G. Sharma, R. Bhardwaj, S. Chand, *J. Am. Chem. Soc.* **2011**, *133*, 9960; e)L. Haitao, K. Zhenhui, L. Yang, L. Shuit-Tong, *Journal of Materials Chemistry* **2012**, *22*; f)S. Jin, D. H. Kim, G. Jun, S. Hong, S. Jeon, *ACS Nano* **2013**, *7*, 1239; g)H. Li, X. He, Z. Kang, H. Huang, Y. Liu, J. Liu, S. Lian, C. Tsang, X. Yang, S.-T. Lee, *Angewandte Chemie* **2010**, *49*, 4430; h)L. Li, G. Wu, G. Yang, J. Peng, J. Zhao, J. Zhu, *Nanoscale* **2013**; i)J. Lu, J.-x. Yang, J. Wang, A. Lim, S. Wang, K. Loh, *ACS Nano* **2009**, *3*, 2367; j)J. Shen, Y. Zhu, C. Chen, X. Yang, C. Li, *Chemical communications (Cambridge, England)* **2011**, *47*, 2580.

[17] a)D. Pan, J. Zhang, Z. Li, M. Wu, *Advanced materials* **2010**, *22*, 734; b)X. Yan, X. Cui, L.-S. Li, *J. Am. Chem. Soc.* **2010**, *132*, 5944; c)L. Yu Teng, K. V. Baiju, L. Olga, A. G. Kimberly, C. H. Mark, *The Journal of Physical Chemistry Letters* **2012**, *3*; d)Z. Zhipan, Z. Jing, C. Nan, Q. Liangti, *Energy & Environmental Science* **2012**, *5*, 8869; e)S. Zhu, J. Zhang, C. Qiao, S. Tang, Y. Li, W. Yuan, B. Li, L. Tian, F. Liu, R. Hu, H. Gao, H. Wei, H. Zhang, H. Sun, B. Yang, *Chemical communications* **2011**, *47*, 6858; f)S. Zhuo, M. Shao, S. T. Lee, *ACS Nano* **2012**, *6*, 1059.

[18] L. Jiao, L. Zhang, X. Wang, G. Diankov, H. Dai, *Nature* **2009**, *458*, 877.

[19] J. Cai, P. Ruffieux, R. Jaafar, M. Bieri, T. Braun, S. Blankenburg, M. Muoth, A. Seitsonen, M. Saleh, X. Feng, K. Müllen, R. Fasel, *Nature* **2010**, *466*, 470.

[20] a)W. Jinlan, M. Liang, Y. Qinghong, Z. Liyan, D. Feng, *Angewandte Chemie* **2011**, *50*; b)M. Paiva, W. Xu, M. Proença, R. Novais, E. Laegsgaard, F. Besenbacher, *Nano Letters* **2010**, *10*, 1764; c)C. Seungchan, K. Keiko, K. Akira, *Carbon*, *49*.

[21] H. Santos, L. Chico, L. Brey, *Physical review letters* **2009**, *103*, 086801.

[22] a)K. Kim, Y. Zhao, H. Jang, S. Lee, J. Kim, K. Kim, J.-H. Ahn, P. Kim, J.-Y. Choi, B. Hong, *Nature* **2009**, *457*, 706; b)A. Reina, X. Jia, J. Ho, D. Nezich, H. Son, V. Bulovic, M. Dresselhaus, J. Kong, *Nano Letters* **2009**, *9*, 30.

[23] a)J. Carretero-Gonzalez, E. Castillo-Martinez, M. Dias-Lima, M. Acik, D. M. Rogers, J. Sovich, C. S. Haines, X. Lepro, M. Kozlov, A. Zhakidov, Y. Chabal, R. H. Baughman, *Advanced Materials* **2012**, *24*, 5695; b)C. Chen, L. Miao, K. Xu, J. Yao, C. Li, J. Jiang, *Physical chemistry chemical physics : PCCP* **2013**, *15*, 6431; c)R. Cruz-Silva, A. Morelos-Gómez, S. Vega-Díaz, F. Tristán-López, A. Elias, N. Perea-López, H. Muramatsu, T. Hayashi, K. Fujisawa, Y. Kim, M. Endo, M. Terrones, *ACS Nano* **2013**, *7*, 2192; d)L. Feng, K. Erjun, L. RuiFeng, X. Chuanyun, D. Kaiming, S. Haibin, *Nanoscale*, *4*; e)A. Hirsch, *Angewandte Chemie (International ed. in English)* **2009**, *48*, 6594; f)P. Kumar, L. Panchakarla, C. Rao, *Nanoscale* **2011**; g)G. L. Luque, M. I. Rojas, E. P. M. Leiva, *Journal of Solid State Electrochemistry* **2013**, *17*, 1189; h)S. Mohammadi, Z. Kolahdouz, S. Mohajerzadeh, *Journal of Materials Chemistry C* **2013**, *1*, 1309; i)A. Morelos-Gómez, S. Vega-Díaz, V. González, F. Tristán-López, R. Cruz-Silva, K. Fujisawa, H. Muramatsu, T. Hayashi, X. Mi, Y. Shi, H. Sakamoto, F. Khoerunnisa, K. Kaneko, B. Sumpter, Y. Kim, V. Meunier, M. Endo, E. Muñoz-Sandoval, M. Terrones, *ACS Nano* **2012**, *6*, 2261; j)C.-S. Rodolfo, M.-G. Aaron, V.-D. Sofia, T.-L. Ferdinando, L. E. Ana, P.-L. Nestor, M. Hiroyuki, H. Takuya, F. Kazunori, K. Yoong Ahm, E. Morinobu, T. Mauricio, *ACS Nano* **2013**, *7*; k)C. Seungchan, K. Keiko, K. Akira, *Carbon* **2011**, *49*; l)N. Wan, L. T. Sun, S. N. Ding, T. Xu, X. H. Hu, J. Sun, H. C. Bi, *Carbon* **2013**, *53*, 260; m)H. Wang, Y. Wang, Z. Hu, X. Wang, *ACS applied materials & interfaces* **2012**, *4*, 6827; n)Y. Wang, Z. Shi, J. Yin, *The Journal of Physical Chemistry C* **2010**.

[24] L. Ma, J. Wang, F. Ding, *Chemphyschem : a European journal of chemical physics and physical chemistry* **2013**, *14*, 47.

[25] F. Cataldo, G. Compagnini, G. Patane, O. Ursini, G. Angelini, P. R. Ribic, G.Margaritondo, A. Cricenti, G. Palleschi, F. Valentini, *carbon* **2010**, *48*, 2596.

[26] a)A. G. Cano-Morquez, F. J. Rodriguez-Macias, J. Campos-Delgado, C. G. Espinosa-Gonzalez, F. Tristan-Lopez, D. Ramirez-Gonzalez, D. A. Cullen, D. J. Smith, M. Terrones, Y. I. Vega-Cantu, *Nano Lett.* **2009**, *9*, 1527; b)D. V. Kosynkin, W. Lu, A. Sinitskii, G. Pera, Z. Sun, J. M. Tour, *ACS Nano* **2011**, *5*, 968.

[27] a)A. L. Eloas, A. R. Botello-Mendez, D. Meneses-Rodriguez, D. V. J. Gonzalez, Ramirez-Gonzalez, E. M.-S. L. Ci, P. M. Ajayan, M. H. Terrones, Terrones, *Nano Lett.* **2010**, *10*, 366; b)U. K. Parashar, S. Bhandari, R. K. Srivastava, D. Jariwala, A. Srivastava, *Nanoscale* **2011**, *3*, 3876.

[28] a)L. Jiao, X. Wang, G. Diankov, H. Wang, H. Dai, *Nat. Nanotechnol.* **2010**, *5*, 321; b)L. Xie, H. Wang, C. Jin, X. Wang, L. Jiao, K. Suenaga, H. Dai, , *J. Am. Chem.Soc.* **2011,**, *133,*, 10394.

[29] P. Kumar, L. S. Panchakarla, C. N. R. Rao, *Nanoscale* **2011**, *3*, 2127.

[30] A. V. Talyzin, S. Luzan, I. V. Anoshkin, A. G. Nasibulin, H. Jiang, E. I. Kauppinen, V. M. Mikoushkin, V. V. Shnitov, D. E. Marchenko, D. Noreus, *ACS Nano* **2011**, *5*, 5132.

[31] M. C. Paiva, W. Xu, M. F. Proenca, R. M. Novais, E. Laegsgaard, F. Besenbacher, *Nano Lett.* **2010**, *10*, 1764.

[32] K. Kim, A. Sussman, A. Zettl, *ACS Nano* **2010**, *4*, 1362.

[33] a)Z. Chen, Y.-M. Lin, M. J. Rooks, P. Avouris, , *Phys. E* **2007**, *40*, 228; b)J. Bai, X. Duan, Y. Huang, *Nano Lett.* **2009**, *9*, 2083; c)L. Tapaszto, G. Dobrik, P. Lambin, L. P. Biro, *Nat. Nanotechnol.* **2008**, *3*, 397; d)M. Y. Han, B. Ozyilmaz, Y. Zhang, P. Kim, , *Phys. Rev. Lett.* **2007**, *98*, 206805.

[34] a)S. S. Datta, D. R. Strachan, S. M. Khamis, A. T. C. Johnson, *Nano Lett.* **2008**, *8*, 1912; b)L. Ci, Z. Xu, L. Wang, W. Gao, F. Ding, K. F. Kelly, B. I. Yakobson, P. M.Ajayan, *Nano Res.* **2008**, *1*, 116; c)N. Severin, S. Kirstein, I. M. Sokolov, J. P. Rabe, *Nano Lett.* **2009**, *9*, 457; d)L. Ci, L. Song, D. Jariwala, A. L. Elias, W. Gao, M. Terrones, P. M. Ajayan, *Adv. Mater.* **2009,**, *21*, 4487.

[35] a)S. Fujii, T. Enoki, *J. Am. Chem. Soc.* **2010**, *132*, 10034; b)M. J. McAllister, J.-L. Li, D. H. Adamson, H. C. Schniepp, A. A. Abdala, J.Liu, M. Herrera-Alonso, D. L. Milius, R. Car, R. K. Prud'homme, I. A. Aksay, *Chem. Mater.* **2007**, *19*, 4396.

[36] a)J. Campos-Delgado, J. M. Romo-Herrera, D. A. C. X. Jia, H. Muramatsu, Y. A. Kim, T. Hayashi, Z. Ren, D. J. Smith, Y. Okuno, T. Ohba, H. Kanoh, K. Kaneko, M. Endo, H. Terrones, M. S. Dresselhaus, M. Terrones, *Nano Lett.* **2008**, *8*, 2773; b)D. Wei, Y. Liu, H. Zhang, L. Huang, B. Wu, J. Chen, G. Yu, *J. Am. Chem. Soc.* **2009**, *131*, 11147; c)M. Sprinkle, M. Ruan, Y.

Hu, J. Hankinson, M. Rubio-Roy, B. Zhang, X. Wu, C. Berger, W. A. de Heer, , *Nat. Nanotechnol.* **2010**, *5*, 727.

[37] a)X. Yang, X. Dou, A. Rouhanipour, L. Zhi, H. J. Rader, K. Mullen, *J. Am. Chem. Soc.* **2008**, *130*, 4216; b)J. Cai, P. Ruffieux, R. Jaafar, M. Bieri, T. Braun, S. Blankenburg, M. Muoth, A. P. Seitsonen, M. Saleh, X. Feng, K. Mullen, R. Fasel, , *Nature* **2010**, 466.

[38] H. Murayama, T. Maeda, , *Nature* **1990**, *345*, 791.

[39] Y. Okuno, T. Ohba, H. Kanoh, K. Kaneko, M. Endo, H. Terrones, M.S. Dresselhaus, M. Terrones, J. Campos-Delgado, J.M. Romo-Herrera, X. Jia, D.A. Cullen, H. Muramatsu, Y.A.Kim, T. Hayashi, Z. Ren, D.J. Smith, , *Nano Lett.* **2008**, *8*, 27738.

[40] P. Mahanandia, K. Nanda, V. Prasad, S. Subramanyam, *Mater.Res. Bull.* **2008**, *43*, 32522.

[41] D. Wei, Y. Liu, H. Zhang, L. Huang, B. Wu, J. Chen, G. Yu, *J. Am. Chem. Soc.* **2009**, *131*, 1114754.

[42] A.M. Affoune, B.L.V. Prasad, H. Sato, T. Enoki, Y. Kaburagi, Y.Hishiyama, *Chem. Phys. Lett.* **2001**, *348*, 17.

[43] L.G. Canc¸ado, M.A. Pimenta, B.R.A. Neves, G. Medeiros-Ribeiro, T. Enoki, Y. Kobayashi, K. Takai, K. Fukui, M.S. Dresselhaus, R. Saito, A. Jorio, *Phys. Rev. Lett.* **2004**, *93*, 047403.

[44] a)X. Li, X. Wang, L. Zhang, S. Lee, H. Dai, *Science* **2008**, *319*, 12292; b)Y. Xiong, Y. Xie, X. Li, Z. Li, *Carbon* **2004**, *42*, 14473.

[45] Z. Kang, E. Wang, B. Mao, Z. Su, L. Gao, S. Lian, L. Xu, *J. Am. Chem. Soc.* **2005**, *127*, 65345.

[46] a)N.G. Chopra, L.X. Benedict, V.H. Crespi, M.L. Cohen, S.G. Louie, A. Zettl, *Nature* **1995**, *377*, 135; b)H.R. Gutiérrez, U.J. Kim, J.P. Kim, P.C. Eklund, *Nano Lett.* **2005**, *5*, 21951; c)C. Lin, T. Chen, T. Chin, C. Lee, H. Chiu, *Carbon* **2008**, *46*, 741; d)M. Motta, A. Moisala, I. Kinloch, A. Windle, *Adv. Mater.* **2007**, *19*, 37216.

[47] J. Shen, Y. Zhu, C. Chen, X. Yang, C. Li, *Chem. Commun.* **2011**, *47*, 2580.

[48] J. Shen, Y. Zhu, X. Yang, J. Zong, J. Zhang, C. Li, *New J. Chem.* **2012**, *36*, 97.

[49] Y. Dong, C. Chen, X. Zheng, L. Gao, Z. Cui, H. Yang, C. Guo, Y.Chi, C. M. Li, *J. Mater. Chem.* **2012**, *22*, 8764.

[50] F. Yang, M. Zhao, B. Zheng, D. Xiao, L. Wu, Y. Guo, , *J. Mater.Chem.* **2012**, *22*, 25471.

[51] H. Tetsuka, R. Asahi, A. Nagoya, K. Okamoto, I. Tajima, R. Ohta, A. Okamoto, *Advanced materials* **2012**, *24*, 5333.

[52] S. Zhu, J. Zhang, X. Liu, B. Li, X. Wang, S. Tang, Q. Meng, Y. Li, C. Shi, R. Hu, B. Yang, *RSC Adv.* **2012**, *2*, 2717.

[53] L. L. Li, J. Ji, R. Fei, C. Z. Wang, Q. Lu, J. R. Zhang, L. P. Jiang, J. J. Zhu, *Adv. Funct. Mater.* **2012**, *22*, 2971.

[54] S. Chen, J.-W. Liu, M. L. Chen, X. W. Chen, J. H. Wang, *Chem Commun.* **2012**, *48*, 7637.

[55] Y. Li, Y. Hu, Y. Zhao, G. Shi, L. Deng, Y. Hou, L. Qu, *Advanced materials* **2011**, *23*, 776.

[56] M. Zhang, L. Bai, W. Shang, W. Xie, H. Ma, Y. Fu, D. Fang, H. Sun, L. Fan, M. Han, C. Liu, S. Yang, *J. Mater. Chem.* **2012**, *22*, 7461.

[57] X. Zhou, Y. Zhang, C. Wang, X. Wu, Y. Yang, B. Zheng, H. Wu, S.Guo, J. Zhang, *ACS Nano* **2012**, *6*, 6592.

[58] T. Gokus, R. R. Nair, A. Bonetti, M. Bŏhmler, A. Lombardo, K. S.Novoselov, A. K. Geim, A. C. Ferrari, A. Hartschuh, *ACS Nano* **2009**, *3*, 3963.

[59] L. Lin, S. Zhang, *Chem. Commun.* **2012**, *48*, 10177.

[60] a)X. Yan, X. Cui, B. Li, L.S. Li, *Nano Lett.* **2010**, *10*, 1869; b)M. L. Mueller, X. Yan, J. A. McGuire, L.S. Li, *Nano Lett.* **2010**, *10*, 2679.

[61] L. Tang, R. Ji, X. Cao, J. Lin, H. Jiang, X. Li, K. S. Teng, C. M. Luk, S. Zeng, J. Hao, S. P. Lau, *ACS Nano* **2012**, *6*, 5102.

[62] Y. Dong, J. Shao, C. Chen, H. Li, R. Wang, Y. Chi, X. Lin, G.Chen, *Carbon* **2012**, *50*, 4738.

[63] J. Lu, P. S. E. Yeo, C. K. Gan, P. Wu, K. P. Loh, *Nature nanotechnology* **2011**, *45*, 247.

[64] R. Liu, D. Wu, X. Feng, K. Müllen, *J. Am. Chem. Soc.* **2011**, *133*, 15221.

[65] Z. Li, W. Zhang, Y. Luo, J. Yang, J. G. Hou, *Journal of the American Chemical Society* **2009**, *131*, 6320.

[66] J. L. Li, K. N. Kudin, M. J. McAllister, R. K. Prud'Homme, I. A. Aksay, R. Car, *Phys. Rev. Lett.* **2006**, *96*, 176101.

[67] J. P. Perdew, K. Burke, M. Ernzerhof, *Phys. Rev. Lett.* **1996**, *77*, 3865.

[68] Y.-R. Kang, Y.-L. Li, M.-Y. Deng, *Journal of Materials Chemistry* **2012**, *22*, 16283.

[69] E. Sanville, S. D. Kenny, R. Smith, G. Henkelman, *J. Comput. Chem.* **2007**, *28*, 899.

[70] J. C. Slonczewski, P. R. Weiss, *Phys. Rev.* **1958**, *109*, 272.

[71] G. W. Semenoff, *Phys. Rev. Lett.* **1984**, *53*, 2449.

[72] a)A. Stone, D. Wales, , *Chem. Phys. Lett.* **1986**, *128*, 501; b)P.A. Thrower, , *Chem. Phys. Carbon* **1969**, *5*, 217.

[73] a)M. Terrones, G. Terrones, H. Terrones, , *Struct. Chem.* **2002**, *13*, 373; b)M. Terrones, H. Terrones, *Fuel Energy Abstr.* **1996**, *37*, 269.

[74] H. Terrones, M. Terrones, E. Hernández, N. Grobert, J.C.Charlier, P.M. Ajayan, , *Phys. Rev. Lett.* **2000**, *84*, 1716.

[75] P.A. Thrower, *Chem. Phys. Carbon* **1969**, *5*, 217.

[76] M.S. Dresselhaus, M. Terrones, A. Jorio, M. Endo, A. Rao, Y. Kim, T. Hayashi, H. Terrones, J. Charlier, G. Dresselhaus, *Mater. Today* **2004**, *7*, 30.

[77] M. Terrones, F. Banhart, N. Grobert, J.C. Charlier, H. Terrones, P.M. Ajayan, *Phys. Rev. Lett.* **2002**, *89*, 075505.

[78] M. Terrones, H. Terrones, F. Banhart, J.C. Charlier, *Science* **2000**, *288*, 12269.

[79] a)Z. Liu, K. Suenaga, P.J.F. Harris, S. Iijima, , *Phys. Rev. Lett.* **2009**, *102*, 015501; b)H. Murayama, T. Maeda, *Nature* **1990**, *345*, 791; c)J. Campos-Delgado, T. H. Y. Kim, A. Morelos-

Gómez, M. Hofmann, H. Muramatsu, M. Endo, H. Terrones, R. Shull, M.S. Dresselhaus, M. Terrones, *Chem. Phys. Lett.* **2009**, *469*, 177.

[80] T. Mauricio, R. B.-M. Andrés, C.-D. Jessica, L.-U. Florentino, I. V.-C. Yadira, J. R.-M. Fernando, E. Ana Laura, M.-S. Emilio, G. C.-M. Abraham, C. Jean-Christophe, *Nano Today* **2010**, *5*.

[81] S. Das Sarma, A. Pinczuk, , *Perspectives in Quantum Hall Effects ,Wiley, New York,* **1997**.

[82] a)S. Q. Murphy, *Physica E (Amsterdam)* **2000**, *6*, 293; b)G. Landwehr, *Physica E (Amsterdam)* **2000**, *6*, 713.

[83] a)Firsov, A. K. Geim, *Phys. Rev. B* **2005**, *72*, 201401; b)A. F. Morpurgo, F. Guinea, , *Phys. Rev. Lett.* **2006**, *97*, 196804.

[84] K. S. Novoselov, *Nature* **2005**, *197*, 438.

[85] D. Pan, L.Guo, J. Zhang, C. Xi, Q. Xue, H. Huang, J. Li, Z. Zhang, W.Yu, Z.Chen, Z.LiandM.Wu, *J. Mater.Chem.* **2012**, *22*, 3314.

[86] a)J. Y. Luo, L. J. Cote, V. C. Tung, A. T. L. Tan, P. E. Goins, J. S. Wu, J. X. Huang, *J. Am. Chem. Soc.* **2010**, *132*, 17667; b)J. Peng, W. Gao, B. Gupta, Z. Liu, R. Romero-Aburto, L. Ge, L. Song, L. Alemany, X. Zhan, G. Gao, S. Vithayathil, B. Kaipparettu, A. Marti, T. Hayashi, J.-J. Zhu, P. Ajayan, *Nano Letters* **2012**, *12*, 844; c)N. Mohanty, D. Moore, Z. Xu, T. S. Sreeprasad, A. Nagaraja, A. A. Rodriguez, V. Berry, *Nat. Commun.* **2012**, *3*, 844.

[87] a)Y. Li, Y. Hu, Y. Zhao, G. Q. Shi, L. E. Deng, Y. B. Hou, L. T. Qu, *Adv. Mater.* **2011**, *23*, 776; b)Y. Li, Y. Zhao, H. H. Cheng, Y. Hu, G. Q. Shi, L. M. Dai, L. T. Qu, *J. Am. Chem. Soc.* **2012**, *134*, 15.

[88] Y. P. Sun, X. Wang, F. Lu, L. Cao, M. J. Meziani, P. G. Luo, L. R. Gu, L. M. Veca, *J. Phys. Chem. C,* **2008**, *112*, 18295.

[89] K. A. Ritter, J. W. Lyding, *Nat. Mater.,* **2009**, *8*, 235.

[90] O. Micic, H. Cheong, H. Fu, A. Zunger, J. Sprague, A.Mascarenhas, A. Nozik, *J. Phys. Chem. B* **1997**, *101*, 4904.

[91] F. F. Fan, *Science* **1997**, *277*.

[92] C. Nirmalya Kumar, K. Bhalchandra, P. V. Kunjukrishna, *Electrochemistry Communications* **2004**, *6*, 661.

[93] Xu D., Ivan S., Anthony B., Eva Y. A., *Nature Nanotechnology* **2008**, *3*, 491.

[94] a)P. Recher, J. Nilsson, G. Burkard, B. Trauzettel, *Phys. Rev. B. Condens. Matter Mater. Phys.,* **2009**, *79*, 085407; b)A. P. Alivisatos, *Science* **1996**, *271*, 933.

[95] L. Yuan, J. Dai, X. Fan, T. Song, Y. T. Tao, K. Wang, Z. Xu, J. Zhang, X. Bai, P. Lu, J. Chen, J. Zhou, Z. L. Wang, *ACS Nano* **2011**, *5*, 4007.

[96] F. Sols, F. Guinea, A. Neto, *Physical review letters* **2007**, *99*, 166803.

[97] L. Ponomarenko, F. Schedin, M. Katsnelson, R. Yang, E. Hill, K. Novoselov, A. Geim, *Science* **2008**, *320*, 356.

[98] L. Gomez De Arco, Y. Zhang, C. Schlenker, K. Ryu, M. Thompson, C. Zhou, *ACS Nano* **2010**, *4*, 2865.

Electrochemical Unzipping of Carbon Nanotubes

This chapter describes the transformation of carbon nanotubes (CNTs) to graphene nanoribbons composed of a few layers of graphene by a two-step electrochemical approach. This consists of the oxidation of CNTs at a controlled potential, followed by the reduction to form graphene nanoribbons (GNRs) having smooth edges and fewer defects, as evidenced by multiple characterization techniques, including Raman spectroscopy, atomic force microscopy, and transmission electron microscopy. This type of "unzipping" of CNTs (single-walled as well as multi-walled) in presence of an interfacial electric field provides unique advantages with respect to the orientation of CNTs, which might make possible the large scale production of GNRs with controlled widths and fewer defects. Moreover, the disappearance of radial breathing mode in Raman as well as van Hove's singularities in case of UV-Vis absorption provides confirmatory evidence for the unzipping of SWCNTs to a single layer graphene.

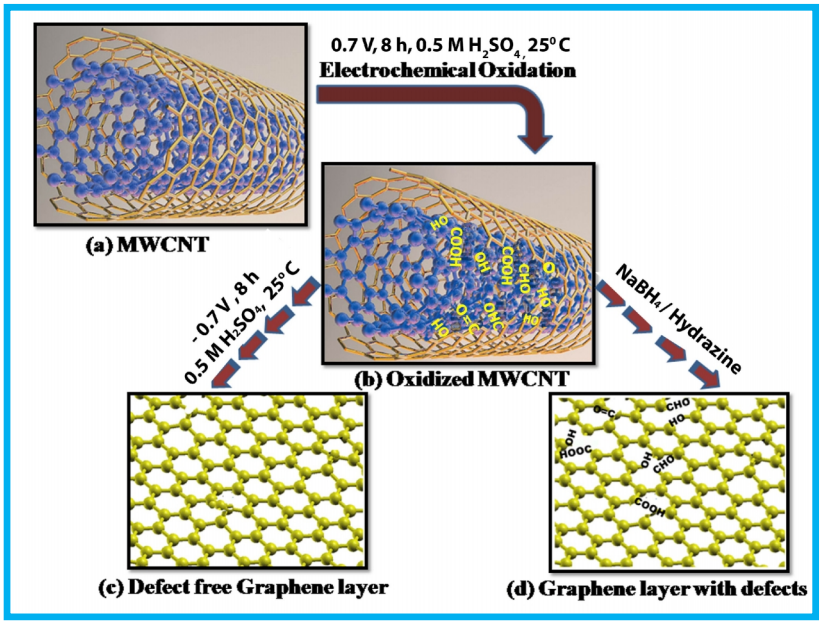

*A part of the work discussed in this chapter has been published in: *J. Am. Chem. Soc*. 2011, *133*, 4168.

2.1. Introduction:

Since the historic paper by Andrew Geim, [1] graphene has attracted tremendous attention due to its unique structural, electronic,[2] mechanical and optical properties,[3] tunable at various levels. Consequently, graphene has been considered as a promising material for a variety of applications such as field effect transistor, [4] random access memory, solar cells, fuel cells, Li ion battery, super capacitors, thin films[5] and nano-electromechanical devices [6] as explained in chapter 1. Despite most of the current research effort being focused on the synthesis of graphene and graphene nanoribbons (GNRs), there are enumerable difficulties to produce defect free and conducting GNRs especially in large yield. On the other hand, considerable progress has been made in the synthesis of multi-walled carbon nanotubes (MWCNTs), which can be viewed topologically as several graphene sheets rolled together in the form of concentric cylinders leading to a stiffer and robust carbon structure; conversely this form can also be transformed to graphene nanoribbons from a geometric perspective.

Graphene is an one-atom thick planar sheet of sp^2 bonded carbon atoms, densely packed into a honeycomb lattice. It has attracted (and still continues to attract!) tremendous attention for both fundamental research related to the exotic behavior of electrons in 2-D systems and also for potential applications like nanoelectronics, supercapacitors, solar cells and hydrogen storage.[7] For example, graphene exhibits many exciting properties, like room temperature quantum hall effect,[8] long range ballistic transport with around ten times higher electron mobility than that in Si,[9] availability of charge carriers that behave as mass-less relativistic quasi particles (Dirac fermions), quantum confinement resulting in finite band gap and coulomb blockade,[6e, 6f, 10] which could be useful to design many novel electronic devices in the near future. However, in order to fully realize the above properties and applications, development of a consistent, reliable and inexpensive method of growing high quality graphene layers in excellent yield is crucial as the existence of residual defects will heavily impact their electronic properties, despite their expected “insensitivity to impurity scattering”. Unfortunately, many of the existing methods of graphene preparation have several major limitations. For example, preparation by mechanical cleavage,[11] silicon carbide sublimation,[12] solvothermal synthesis,[13] chemical vapor deposition[14] and plasma etching[15] suffer from limitations such as a) poor quality and yield of graphene ribbons, b) formation of over oxidized and defective nanoribbons, c) substrate-dependant behavior , d) the difficulty of controlling both layer thickness and e) edge smoothness

in a predictable manner. Hence, an accurate control of the quality of graphene layers along with the preparation in good yields is a daunting task.

One of the most successful approaches to date, for converting CNTs to graphene is the recent longitudinal unzipping,[16] using a mixture of potassium permanganate and concentrated sulphuric acid, facilitating large scale preparation of GNRs. However, this method has several problems primarily involving the selection of strong oxidizing agents. First, chemical oxidation itself has serious issues like over oxidation of edges creating defect sites which hamper electronic properties of graphene. More significantly, electron mobility and conductivity diminishes with this treatment and there is also a possibility of evolution of explosive gases. [17] In addition, the use of strong reducing agents might pose difficulties in controlling the layer thickness of graphene ribbons along with disposal concerns. In comparison, electrochemical oxidation can ensure an accurate control of the degree/sites of oxidation (especially by controlled potential techniques) under ambient conditions and hence this method is capable of providing more precise unzipping of nanotubes in comparison with chemical and plasma based approaches. Since CNTs are graphene sheets seamlessly rolled into concentric tubes, from a geometrical perspective, it may be possible to have the transformation of CNTs to graphene by a longitudinal cutting of all C-C bonds along the tube axis. Many computational approaches [18] have recently been attempted to reveal the exact geometric steps as well as the energetics of the process of unzipping, which suggest that despite ardent challenges, it is possible, in principle, to open up tubes by applying appropriate electric field.

In this chapter an unprecedented method of transforming CNTs to GNRs is explained by using an electrochemical approach, which offers unique advantages of controlling the graphene layer thickness and orientation. This electrochemical approach is an effective tool to modify associated electronic states by modulating the electric field (chemical potential) to change the fermi level of the electrode materials.[19] The interfacial electric field is expected to orient the CNTs in our method and hence longitudinal unzipping with possible C-C cleavage initiated at topological defects having enough strain is more likely than random breakdown associated with chemical methods. Unfortunately, large sized graphene sheets cannot be made, since the size of graphene (i.e., width of ribbons) is limited by the diameter of the MWCNTs used in synthesis.

2.2 Experimental section:

10 mg of MWCNTs (Nanocyl, 99% pure) was added to 20 mL of ethanol (Rankem) and after sonicating for 15 minutes (or till it could disperse properly) this suspension was deposited onto a Glassy Carbon Electrode (GCE) .Typically a 5 μL of the suspension was spread on a pretreated GCE using a micro tip, followed by drying under an IR- lamp for 1 h to remove solvents, resulting into a thin uniform layer. Electrochemical oxidation of MWCNTs was carried out in a three-electrode system (Pt as counter electrode, Mercury Mercurous Sulphate (Hg/Hg_2SO4 as reference electrode) using an Autolab PGSTAT30 (Eco Chemie) at a fixed positive potential for 2, 4, 6, 8 and 12 h in 0.5 M H_2SO_4. The extent of oxidation was confirmed by various characterization techniques like X-ray diffraction (XRD), X-ray Photoelectron Spectroscopy (XPS), HR-TEM, AFM and Raman spectroscopy. In the second step of the experiment, MWCNT oxide was reduced at -0.75 V for 2, 4, 6, 8 and 12 h to get few layered graphene ribbons after the initial oxidation step. Similar experiments were also conducted with both SWCNT and DWCNT, which generated graphene in comparatively smaller yields.

2.3. Structural and morphological characterization:

2.3.1. X-ray Diffraction (XRD):

X-ray powder diffraction studies were performed using CuK_α (λ = 1.54 Å) radiation on a Philips PW1830 instrument operating at 40 kV and a current of 30 mA at room temperature in order to understand the crystallinity and diameter distribution of GNRs and also to estimate the presence of catalyst in the pristine CNTs. The diffraction patterns were collected at a step of 0.02° (2θ) using a fixed Cu-K_α radiation. The background was subtracted using the linear interpolation method. [20]

2.3.2. Field-Emission Scanning Electron Microscopy (FESEM) and Energy Dispersive X-ray Analysis (EDX):

The morphology of these structures was examined by a JEOL JSM-6700F SEM having a field emission source and exhibiting a resolution of about ~2–3 nm, with no metal deposition on the GNRs. A selected amount of GNRs sample was put in ethanol to prepare a sonicated suspension.

The surface morphology was also characterized by Kevex model EDX system (using a Lieca Stereoscan 440 model SEM). For comparative studies, the energy of the electron beam was kept constant while analyzing all samples. The micrographs of the samples were recorded with a 20 kV electrical high tension and 25 pA camera attached on the high-resolution recording unit.

2.3.3. High-resolution Transmission Electron Microscopy (HRTEM):

A selected amount of GNR sample was dispersed by sonication in ethanol to prepare a suspension. A drop of this suspension was put on lacey carbon film-coated copper micro-grids. After drying, these grids were then used for structural investigation using a transmission electron microscope (HRTEM) of Philips CM12, equipped with a high resolution objective stage, operating at 120 kV, and providing a point resolution better than 0.3 nm, the coefficient of spherical aberration being 1.35 mm. The images were digitized in the size of 256 × 256 pixels with a pixel size of 0.03994 nm and thus atomically resolved images were possible. These images were stored in the computer after digitization and the power spectra were calculated to enable detailed structural analysis in terms of inter-planar distances, angle between planes etc.

2.3.4. X-ray Photoelectron Spectroscopy (XPS):

XPS measurements were carried out on a VG MicroTech ESCA 3000 instrument at a pressure of $>1 \times 10^{-9}$ Torr (pass energy of 50 eV, electron takeoff angle 60^{o}, and overall resolution ~1 eV using monochromatic Mg Kα (source, $h\nu = 1253.6$ eV). The core level spectra of the C 1s and O 2p orbitals were recorded with an overall instrumental resolution of ~1 eV. The alignment of binding energy (BE) was carried out using Au 4f BE of 84 eV as the reference. The X-ray flux (power 70 W) was kept deliberately low to reduce the beam-induced damage. The spectra were fitted using a combined polynomial and Shirley type background function. [21]

2.3.5. Raman analysis:

Raman spectroscopy is a fundamental tool to understand the surface defects and electronic structure of nanotubes, where the tangential mode (G-band) and defect mode (D-bands) of vibrations change systematically after CNTs to graphene transformation. Accordingly, Raman spectroscopic analysis of the samples was performed on a Horiba confocal Raman spectrometer

using a 532 nm green laser in order to obtain valuable information regarding defect distribution as well as the extent of graphitization.

2.3.6. Conductivity measurements:

Electrical conductivity was measured on a 1cm^2 thin film of "as grown" sample using a KEITHLY 220 Programmable current source and a KEITHLY 181 Nanovoltmeter coupled with an OXFORD Intelligent temperature controller ITC-4. A thin film of sample was made by drop-coating on a glass slide after making a good dispersion in toluene and four point probe electrical conductivity was recorded.

2.3.7. Electrochemical measurements

All electrochemical measurements were carried out in 0.5 M H_2SO_4 using a standard three electrode cell comprising a modified glassy electrode (3 mm) as the working electrode, a Pt wire as counter electrode and Hg/Hg_2SO_4 as reference electrode. Cyclic voltammetric experiments were performed on an Autolab PGSTAT30 (ECO CHEMIE) instrument and electrochemical impedance measurements were carried out with an impedance analyzer (Autolab PGSTAT 30 with FRA software). The ac signal amplitude used was 10 mV, and the frequency range employed was 0.1 Hz–25 kHz and this data was recorded with averaging over five cycles for each frequency.

2.4 Results and Discussion:

Scheme 2.1 represents our two step process for the electrochemical transformation of MWCNTs to graphene layers. The first step comprises of applying a typical anodic potential of 0.70 V *vs* mercury mercurous sulphate (MMS) electrode to the MWCNT working electrode in 0.5 M H_2SO_4, for several hours where the applied electric field initiates the breaking of sp^2 carbon atoms, perhaps at the tip of MWCNT. This unzipping continues in the longitudinal direction as evidenced from subtle changes in the voltammogram [Fig. 2.1]. Broken MWCNT along a straight line are stretched further away by the tension in the curved surface which could result in the remarkable transformation into graphene oxide layers.[22] This speculative mechanism, however, requires more experimental evidence in order to provide a complete understanding of the intermediates formed after the speculated C-C cleavage. We have achieved

the same electrochemical unzipping process in the case of single-walled carbon nanotubes (SWCNTs) producing narrower nanoribbons, although their subsequent disentanglement appears to be more difficult.

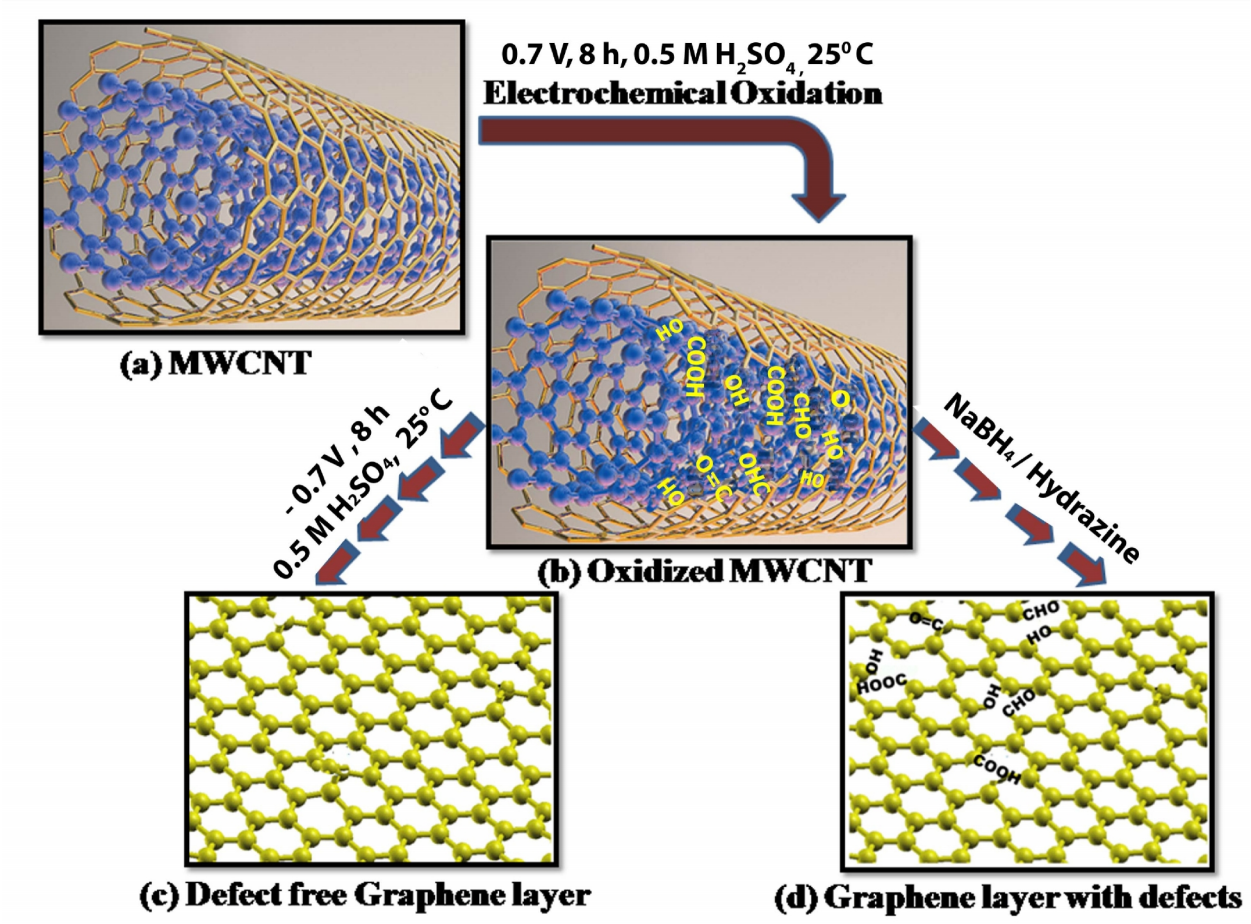

Scheme 2.1 A diagrammatic representation of the electrochemical transformation of MWCNTs into GNRs. **(a)** A Pristine MWCNT deposited on glassy carbon electrode before unzipping,**(b)** MWCNTs after oxidation under controlled potential which generates functional groups on edges so that it gets broken up, **(c)** and **(d)** indicate electrochemical and chemical reduction to graphene layers respectively.

2.4.1 Cyclic Voltammograms:

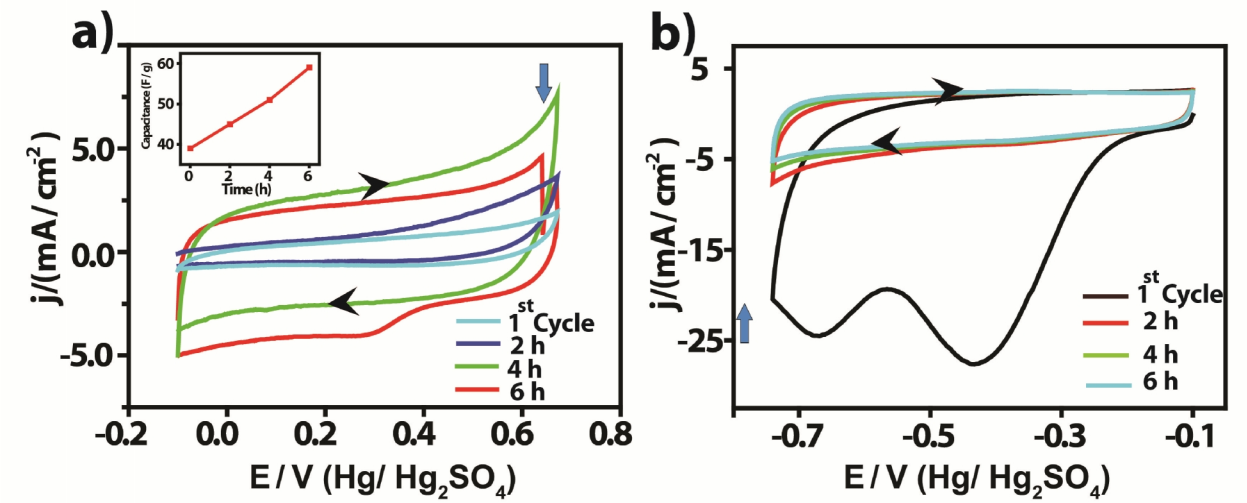

Figure 2.1 (a) Cyclic Voltammograms (oxidation) of MWCNTs in the potential window from 0.01 to 0.7 V vs Hg/Hg_2SO_4 in 0.5 M H_2SO_4 using glassy carbon electrode at 100 mV/s scan rate **(b)** Cyclic Voltammograms (reduction) of MWCNTs in the potential window of -0.01 to - 0.75 V vs. Hg/Hg_2SO_4 in 0.5 M H_2SO_4 at 100 mV/s scan rate. Arrow marked regions in CV indicate potential where CNTs have been selectively oxidized and reduced respectively. Inset shows variation of capacitance with time.

During the anodic scan from the open circuit potential of 0.01 V to 0.7 V there is no clear peak in the voltammogram. More significantly the increase in non-faradic current with cycle number (inset of Figure.1) and time suggests subtle morphological changes including that of the sample surface area. By keeping the potential at 0.7 V for 6 h, the oxidation of MWCNTs generates an enormous number of oxygen functionalities. This is indicated by the fact that the OCP increases by 60 mV at the end of oxidation. Subsequent reduction of the oxidized MWCNTs in the potential range from -0.01 to -0.75 V yields a large cathodic current at -0.43 V in the Voltammogram indicating rapid kinetics compared to that of the oxidation in the previous step. This large reduction current is ascribed to the removal of surface oxygen groups. There could also be intrinsic resistivity changes in the material as a function of cycle number. Interestingly, the double layer capacitance changes from 40 $\mu F/cm^2$ to 10 $\mu F/cm^2$ when oxidized MWCNTs get completely converted to GNRs. A significant improvement in electronic conductivity after GNR formation also supports this [Fig. 2.5 / Table 2.2].

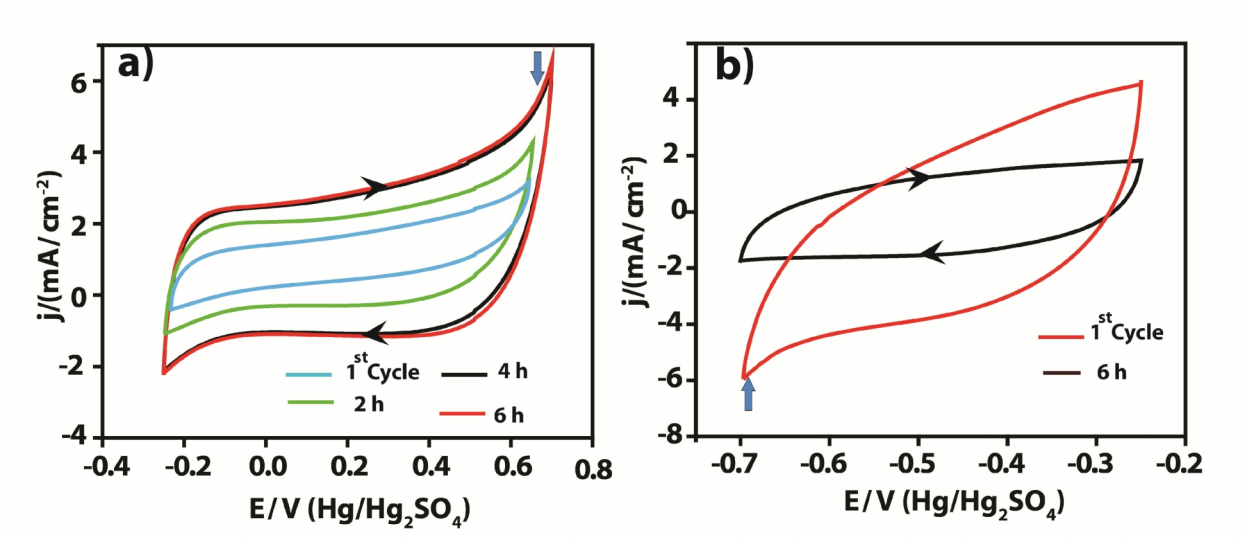

Figure 2.2 (a) Cyclic Voltammograms (oxidation) of SWCNTs in the potential window from - 0.2 to 0.7 V vs. Hg/ Hg_2SO_4 in 0.5 M H_2SO_4 using a glassy carbon electrode at a 100 mV/s scan rate **(b)** Cyclic Voltammograms (reduction) of SWCNTs in the potential window of 0.02 to - 0.7 V vs. Hg/Hg_2SO_4 in 0.5 M H_2SO_4 at a 100 mV/ s scan rate.

Similar electrochemical unzipping experiments are carried out using SWCNTs by keeping the potential at 0.7 V for 6 h, this generate enormous number of oxygen functionalities as shown in Figure 2.2, clearly revealing oxidation, confirmed by improvement in the capacitance. Subsequent reduction of SWCNT oxide modified glassy carbon electrode in -0.15 to -0.7 V range shows similar changes in the reaction kinetics compared to the MWCNTs.

2.4.2 Raman and XRD:

Raman spectroscopy is used to obtain the information of ordered and disordered bonding environment of sp^2 and sp^3 hybridized carbon. Normally in carbon nanostructures the G band is assigned to the E_{2g} phonon of sp^2 carbon atom while D band intensity corresponds to the extent of defects.[23] For example, in Figure 2.3 a, the intensity of the D band at 1329 cm^{-1} for MWCNTs increases substantially, indicating a decrease in the size of in-plane sp^2 domains due to oxidation. In pristine MWCNTs on the other hand, the intensity of the D band is much less, suggesting excellent quality of the starting materials.[24] After the electrochemical oxidation, however the intensity of the D band is considerably enhanced along with a concomitant decrease in the intensity of the G band, revealing clearly that oxidation has been completed.[24b] Interestingly, by applying a controlled cathodic potential in the second step, the oxidized broken

MWCNTs get converted to graphene as confirmed by the observation of very low intensity ratio of D/G bands. The MWCNTs used in our study after 6 h typically show a very low I_D/I_G ratio (0.11) suggesting the edges in graphene to be very sharp and defect free, this fact is also supported by Raman mapping experiments as shown in Table 2.1. Moreover, the intensity of the 2D band in graphene is found to be 60 % higher as compared to that of the G band which is also indicative the formation of a few layers of graphene. More significantly, all these observations in Raman spectra are in excellent agreement with similar changes reported recently for chemically unzipped MWCNTs. [16a]

Table 2.1: A Comparison of the intensity ratio of D and G bands for Graphene which is prepared by oxidizing and subsequently reducing MWCNT at different potentials (time) in 0.5 M H_2SO_4 using a glassy carbon electrode.

Time / h	Oxidation Potential (V)	Reduction potential(V)	I_D/I_G
4	0.6	-0.5	0.15
4	0.7	-0.6	0.14
4	0.7	-0.75	0.12
6	0.6	-0.5	0.15
6	0.7	-0.6	0.13
6	0.7	-0.75	0.11

We have carried out the Raman mapping for GNRs to get more accurate information about I_D/I_G ratio. The average I_D/I_G ratio is around 0.13 which reflects the high quality compared to the other reports available for synthesis of GNRs. [15, 16b, 18a, 25]

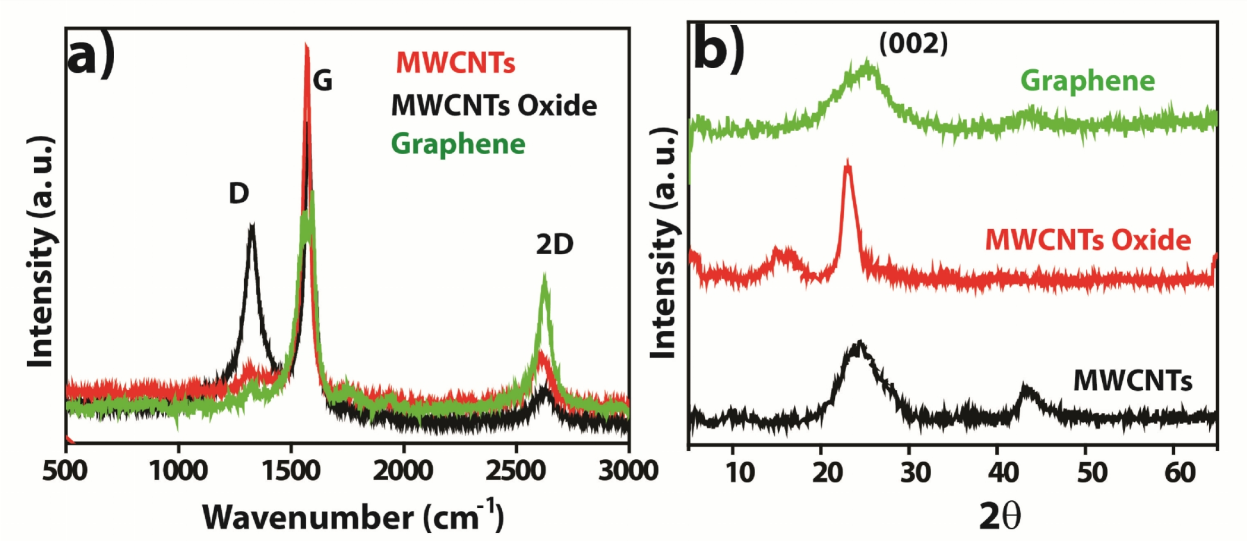

Figure 2.3 (a) A comparison of Raman Spectra of MWCNTs, Oxidized MWCNTs and graphene **(b)** A comparison of powder XRD pattern for MWCNTs, Oxidized MWCNTs and graphene.

Figure 2.3 (b) shows a comparison of the powder XRD patterns of MWCNTs, MWCNTs Oxide and graphene, which provides further valuable insights into this structural transformtion by the sensitive position of graphitic (002) peak corresponding to various degree of oxidation. Pristine MWCNTs show a strong peak at 26.2° corresponding to the d-spacing of 3.31 Å whereas partially oxidized MWCNTs show an additional small peak at 14.83° corresponding to the d spacing of 5.93 Å. A shift in the (002) peak to 22.9° suggests partial oxidation of MWCNTs achieved by holding the anodic potential at 0.7 V for 4 h.[26] This value is larger than the original d-spacing (3.31 Å) of MWNTs possibly due to the presence of intercalated water and SO_4^{2-} ions. Nevertheless, when Oxidized MWCNT is electrochemically reduced during the second step, this diffraction peak appears again at 26.6° , which is similar to the peak obtained using chemically reduced MWCNT Oxides.

2.4.3 AFM and TEM:

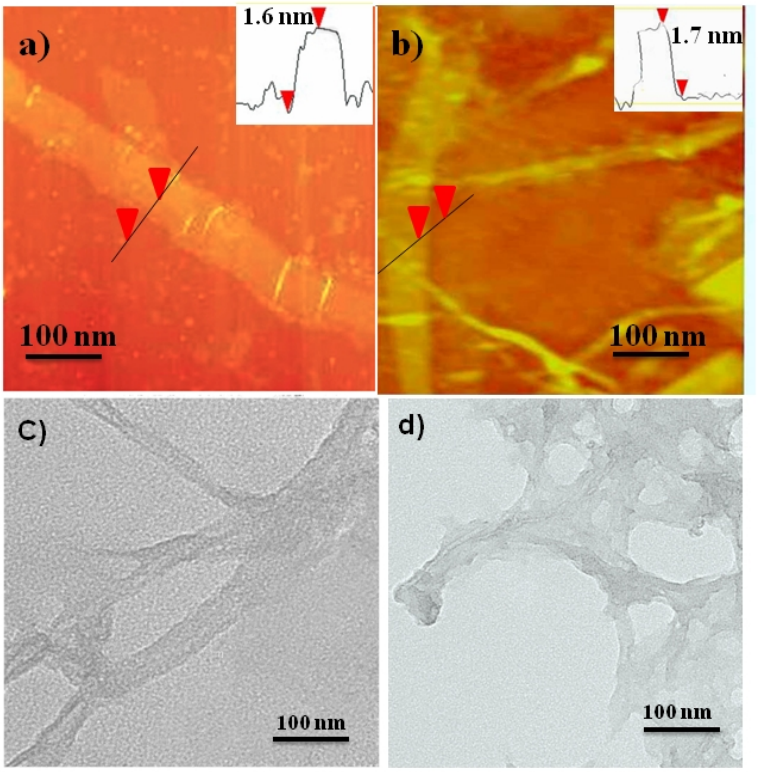

Figure 2.4. Typical AFM and TEM images of GNRs made from MWCNTs by the two step electrochemical process; Figure **(a)** is the representative AFM image of GNR synthesized at 0.7 V and **(b)** represents AFM image of GNRs synthesized at 0.5 V followed by reduction at -0.7 V for 6 h each; **(c)** and **(d)** are TEM images of MWCNTs after the two step electrochemical treatment, revealing two to three layers of graphene sheets after partial and complete transformation of MWCNT respectively.

Figure 2.4 (a and b) shows typical AFM images of GNRs prepared from MWCNTs by the two step electrochemical process where, a and b correspond to GNRs obtained using fixed anodic potential 0.7 V, followed by two different potentials of -0.75 V and -0.5 V respectively. Interestingly, Figure 2.4 a reveals long ribbons (1 μm) with straight edges and widths ranging from 70 to 110 nm indicating bi-layer GNRs of thickness ranging from 1.6 to 1.9 nm. This is also confirmed by the corresponding HR-TEM images [Fig. 2.4 (c) and (d)] which suggest a complete transformation of 40-60 nm diameter MWCNTs to few layer GNRs having more or less (70-80 nm) similar width and few micron length, which is strikingly similar to the dimensions of high quality graphene obtained using chemical methods. The graphene nano-sheets are found to be transparent and stable under the electron beam.[27] The mechanism of cutting of MWCNT along the longitudinal direction is speculated to arise because of the field

direction controlling the oxidative breaking of C–C bonds initiated at some defect sites on the sidewalls.[28] Consequently, highly aligned, narrow GNRs can be made from an array of MWCNTs using this electrochemical approach. More importantly, a combined analysis of all experimental data clearly shows that this method can convert majority of the starting material to GNRs having smooth edges by applying a two sequential potential steps (first 0.70 V anodic followed by -0.7 V cathodic each for 6 hrs respectively) facilitating high yield.

2.4.4 X-ray Photoelectron spectroscopy:

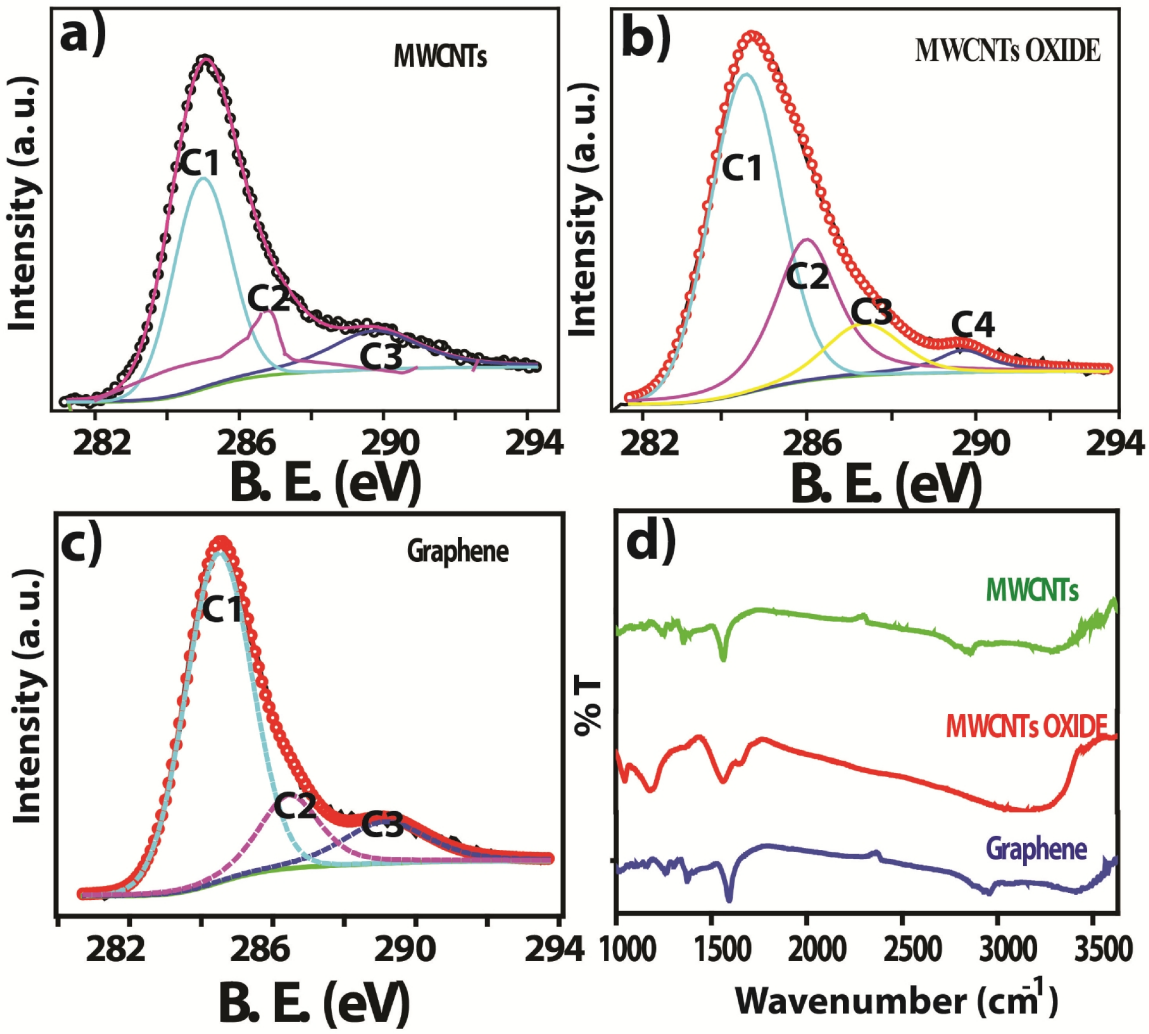

Figure 2.5. X-ray photoelectron spectra of (C 1s core level) of **(a)** MWCNT **(b)** MWCNT oxide and **(c)** Graphene; circles represent the experimental data, thick lines represent the fitted data for overall signal and the dashed lines are the de-convoluted individual peaks for different environments of carbon. **(d)** A

comparison of the FT-IR spectra of MWCNTs, MWCNTs oxide at 0.7 V for 6 h and final product graphene at -0.75 V for 6 h.

XPS data is often invaluable in distinguishing between MWCNTs, MWCNT Oxide and Graphene. In the XPS of carbon (C 1s) the C_1 peak is assigned to the C-C binding energy (sp^2 carbon) at 284.51, 283.59 and 284.49 eV for MWCNTs, MWCNTs Oxide and Graphene respectively. A decrease in intensity and binding energy (B.E.) value of C_1 in case of figure 2.5 (b) is due to the weakening of the C–C bond and the introduction of more sp^3 character in MWCNT. The C_3 peak at 285.9 eV corresponds to the C–O binding energy and the C_4 peak at 287 eV is assigned to carbonyl groups (C=O). Upon the reduction by applying a negative potential -0.75 V for 6 h, the peaks at 285.9 and 287 eV diminish to a shoulder (284.49 eV) indicating perhaps significant de-oxygenation of the nanoribbons. As reported, the most dominant peak after reduction is the C–C peak at 284.49 eV.[17, 25d, 29] MWCNTs oxide has about 23.4 at. % of oxygen which upon electrochemical reduction decreases to 4.2 at. % for graphene which is comparable to that of the XPS obtained in graphene prepared by chemical methods.

FT-IR spectrum as shown in figure (2.5 d) of MWCNT shows a strong peak at 1600 cm^{-1} corresponding to the C=C stretching frequency and another peak at 2906 cm^{-1} which represents C–C stretching. The complete oxidation of MWCNTs in 6 h is also supported by a comparison of the Fourier transform infra red (FT-IR) spectra of pristine, oxidized and subsequently reduced samples showing characteristic carbonyl stretching frequency at 1720 cm^{-1} for oxidized MWCNTs and by the decreased conductivity values of MWCNT. However, oxidized MWCNTs show a strong peak at 1720 cm^{-1} corresponding to carbonyl stretching frequency and the peak around 3340 cm^{-1} represents the presence of –OH group on MWCNT surface. After reduction, at –0.75 V the sample show an almost complete absence of C=O stretching (1720 cm^{-1}) and a significant decrease in -COOH/-O–H stretching (3600–2800 cm^{-1}). This confirms the formation of graphene nanoribbons (GNRs) having less defects. The oxidized MWCNTs however, show a number of features associated with oxygenated species which are clearly missing in the reduced GNRs.[17, 25d, 29] Graphene and RGO having different local chemical structure, moreover RGO contains small percentage of oxygen functionalities, which causes RGO unstable under significant electron beam exposure and this material having low electrical conductivity compared to graphene. [30]

2.4.5 Conductivity Measurement:

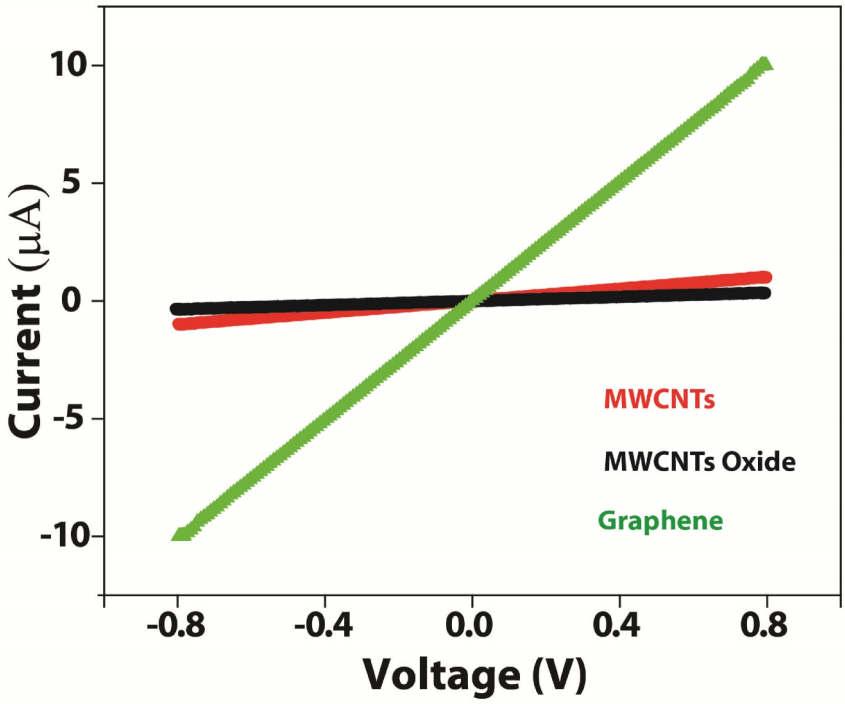

Figure 2.6 Current-Voltage characteristics of MWCNTs, MWCNT Oxide and Graphene measured using two probe system on silicon substrate by maintaining the distance between the Pt probes as 0.5 μm. The figure shows improved conductivity values for graphene.

In order to measure the electrical properties of the nanoribbons, a sample was drop casted on a Si substrate to prepare a uniform thin film (thickness of 0.5 μm) with the channel length between two Pt-electrodes being 0.5 μm.

Table 2.2: A comparison of the Conductivity determined using two probe measurements at room temperature on MWCNT, its oxide (+0.7 V for 6 h) and the subsequent reduced product (-0.7 V for 6 h)**.**

Sr. No.	Sample	Conductivity (S cm^{-1})
1.	MWCNTs	206
2.	MWCNTs Oxide	91
3.	Graphene	245

The GONR (graphene oxide nanoribbons) exhibits relatively poor conductivity as compared to that of MWCNTs. Electrochemical reduction, however, improves the conductivity dramatically which is ascribed to a major change in carrier concentration consequent to the formation of graphene[3, 24c, 31] and this is very good agreement with values from the literature for graphene[17, 29a, 31c].

2.4.6 SEM and TEM Analysis:

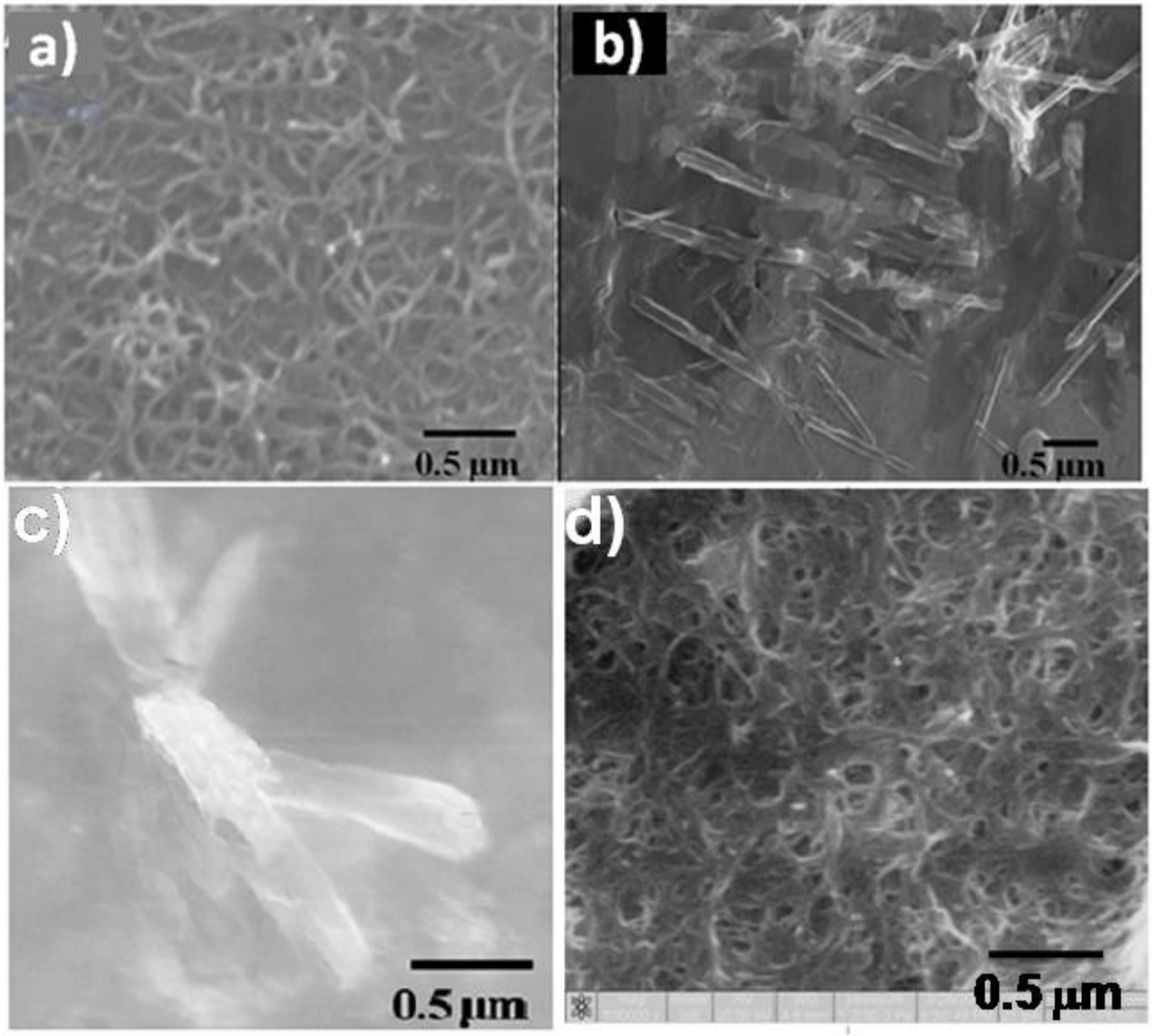

Figure 2.7. SEM images of **(a)** Pristine MWCNTs having 60 to 80 nm diameter **(b)** GNR formed upon oxidation at a controlled anodic potential (0.7 V) for 6 h and then subsequent reduction of MWCNT at –0.75 V for 6 h showing open tubes; **(c, d)** a bulk nanoribbons sample which also illustrates the high yield of the nanotube-free material.

SEM image of an ensemble of the MWCNTs, (which are dropcasted on a Si substrate using DMF as a solvent for dispersing the samples) having width 60-80 nm and length 3-4 μm is displayed in Fig. 2.7 (a) . However, images obtained after applying a controlled anodic potential 0.7 V for 6 h followed by reduction as given in Fig. 2.7 (b) clearly shows sufficiently exfoliated nanoribbons with width 100-120 nm and length comparable to that of starting material. A comparison of SEM images confirms that the exfoliated ribbons are fully open with less defects due to the controlled oxidation under the applied electric field.

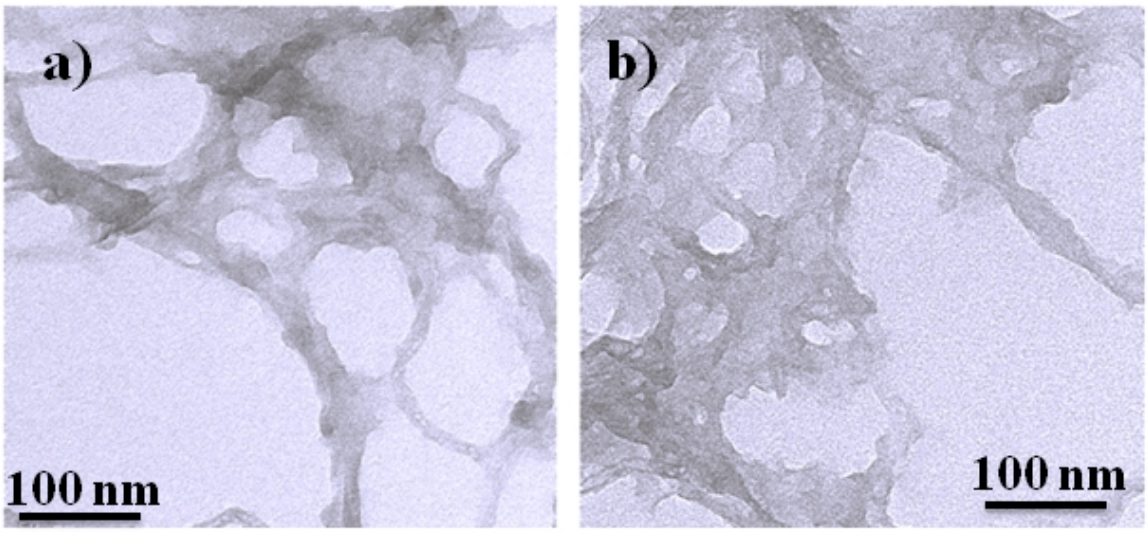

Figure 2.8. (a) TEM images of nanostructures formed upon oxidation at potential (0.6 V) for 6 h and subsequent reduction of MWCNT at −0.6 V for 4 h revealing partially unzipped tubes. **(b)** TEM images of GNR upon oxidation at potential (0.7 V) for 4 h and then subsequent reduction of MWCNT at −0.75 V for 8 h displaying fully unzipped tubes.

TEM images also show the partially and completely unzipped tubes, up on applying positive bias followed by reduction at -0.75 V for 8 h. This change in topography can successfully be considered as a final evidence for the transformation of MWCNTs to GNRs at the nanometer scale supporting the changes in Raman spectra and AFM images. For TEM images it is also easy to distinguish between pristine MWCNTs and its unzipped counterparts. The difference in the thickness and the phase contrast due to hydrophilicity difference resulting from distinct oxygen functional group in the reduction process as shown in [Fig. 2.8] besides imaging can also be considered as additional discerning parameters.[32]

2.4.7 Electrochemical Unzipping of SWCNT:

So far we have discussed various results related to the electrochemical unzipping of MWCNTs. Naturally the question of what happens to single walled carbon nanotubes will come to our mind and now we will discuss results pertaining to SWCNT in the following sections.

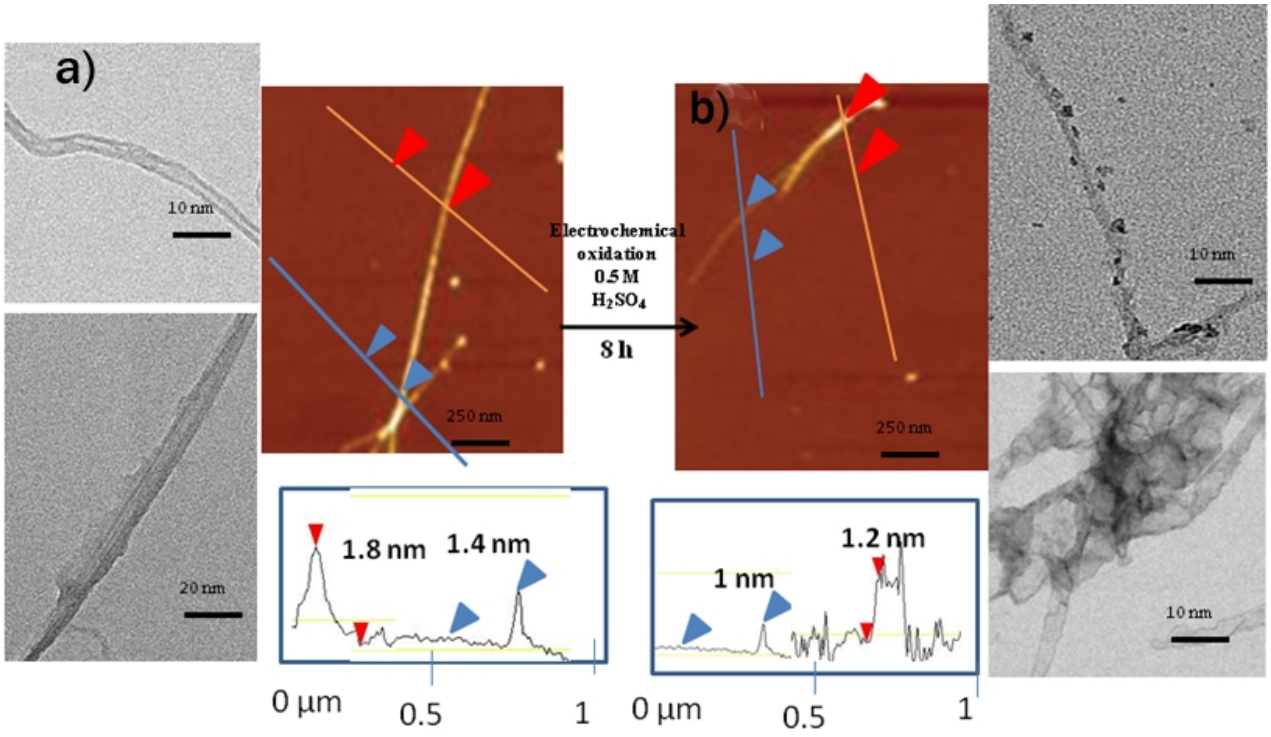

Figure 2.9 Typical TEM and AFM images of SWCNT **(a)** before and **(b)** after electrochemical oxidation showing height difference and partially unzipped tubes.

TEM and AFM images of the nanoribbons formed after a two-step electrochemical treatment of SWCNTs are shown in 2.10 to clearly indicate that a similar unzipping phenemonenon also occurs on single walled analoges. However there are crucial differences compared to SWCNT bundles, the nanostructures formed appear to be flat, less bundled, and possess larger widths with a height of 1-1.2 nm as compared to 1.4 -1.8 nm (SWCNT), which is distinct from the initial diameter. Hence, after the electrochemical oxidation, SWCNT has been assumed to be opened up longitudinally which corresponds to the height decrease to 1.1 nm, confirming the formation of a single layer of graphene. This is also supported by the

disappearance of RBM (Radial breathing mode) by in situ spectro electrochemical experiments, as shown in figure 2.10 a where a comparison of the images obtained from specific features for various electrochemical oxidizing conditions have been used to elucidate the sequential unzipping of different kinds of SWNTs to form GNRs.

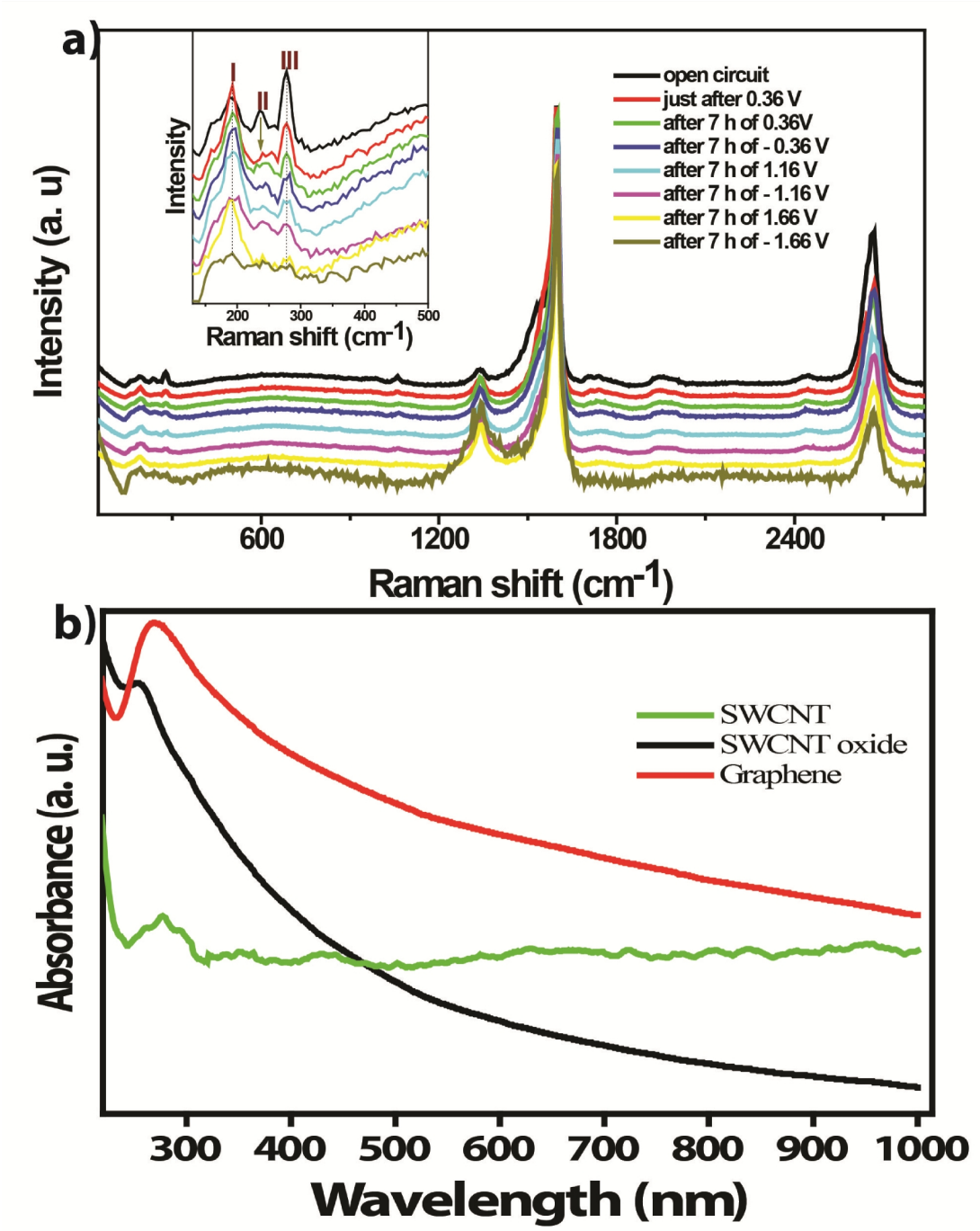

Figure 2.10. **(a)** Raman spectra of gradual unzipping of SWNTs. Inset displays the averaged RBM spectra from the sample for various conditions. The black trace is that of the parent material. The red trace (immediately after 0.36 V) does not show 2nd RBM. The 3rd RBM disappears with various conditions as one can see from the decrease in intensity of the peak around 276 cm^{-1}. Various conditions are labeled by different color. A considerable decrease in the width of G band is observed suggesting the reduction in metallicity along with an increase in D band which implies increased defects formed during the unzipping. The 2D band at 2660 cm^{-1} shows hardly any observable changes. **(b)** UV-Vis absorption spectra of pristine SWCNTs dispersed in 1 mM SDS solution in water electrochemically oxidized (0.7 V for 8 h) SWCNTs electrochemically reduced (-0.7 V for 8 h) SWCNTs.

More interestingly, electrochemically oxidized SWCNTs show a complete loss of the fine spectral features (van Hove singularities) revealing the formation of defects due to conversion of sp^2 to sp^3 carbon as indicated in Figure 2.10. which are lost upon covalent functionalization or due to defect formation. [33] In pristine SWCNT, the presence of both semiconducting and metallic SWCNTs shows individual absorption peaks that allow the monitoring of valence electrons. The disappearance of these singularities on electrochemical oxidation indicates a significant alteration in the electronic structure and properties of the nanotubes. However, a strong absorption peak at 243 nm has been observed, perhaps due to the formation of graphene.

Many electrolytes containing different cations and anions have been examined for unravelling their role during the electrochemical unzipping of MWCNTs, including anions and cations associated with KOH, HCl, HNO_3 and H_2SO_4. H_2SO_4 is the only electrolyte which exhibits excellent unzipping efficiency with minium morphological damage. In comparison, SO_4^{2-} intercalation in MWCNTs induces breakage at applied electric field resulting in to partial unzipping. More significantly, this type of unzipping is further assisted by in-situ produced H_2 in aqueous media, which supports electrochemical reduction of oxygen functionalities during the transformation of unzipped MWCNTs to GNRs. The striking similarity of experimental results in 0.5 M KOH and 0.5 M HCl to generate partially damaged MWCNTs implies that SO_4^{2-} ion plays a key role in unwrapping of MWCNTs.

2.5. Conclusions

In summary, a unique electrochemical approach for the synthesis of GNRs with controlled layer thickness is reported in this chapter using both MWCNTs and SWCNTs. Chemical unzipping often results in over-oxidation and edge defects, which can be alleviated by using this controlled potential step methodology. Although the electrochemical route for GNRs described here can have several advantages of tuning the orientation, control of edges and planes along the length upon first oxidation step, some of the electronic characteristics might get affected due to the adsorption of cations, anions and solvent molecules on the defect site or due to intercalation. However, this study opens a new pathway for the preparation of high quality graphene in good yield and there are profound implications for certain applications like fuel cells and Li battery electrodes where CNTs are continuously kept under sustained electric field.

2.6 References

[1] K. S. Novoselov, A. K. Geim, S. V. Morozov, D. Jiang, Y. Zhang, S. V. Dubonos, I. V. Grigorieva, A. A. Firsov, *Science* **2004**, *306*, 666.

[2] G. K. Ramesha, S. Sampath, *J. Phys. Chem. C* **2009**, *113*, 7985.

[3] A. H. C. Neto, N. M. R. Peres, K. S. Novoselov, A. K. Geim, *Reviews of Modern Physics* **2009**, *81*.

[4] a)T. Gokus, R. R. Nair, A. Bonetti, M. Böhmler, A. Lombardo, K. S.Novoselov, A. K. Geim, A. C. Ferrari, A. Hartschuh, *ACS Nano* **2009**, *3*, 3963; b)A. K. Geim, K. S. Novoselov, *Nat. Mater.* **2007**, *6*, 183; c)Firsov, A. K. Geim, *Phys. Rev. B* **2005**, *72*, 201401.

[5] C.-M. Gee, C.-C. Tseng, F.-Y. Wu, H.-P. Chang, L.-J. Li, Y.-P. Hsieh, C.-T. Lin, J.-C. Chen, *Displays*.

[6] a)A. C. B. Dale, K. K. Dimitrios, E. B. Craig, *Journal of Power Sources* **2011**, *196*; b)D. Sudipta, K. P. Swapan, *J. Mat. Chem.* **2010**, *20*, 8207; c)L. Vicarelli, M. Vitiello, D. Coquillat, A. Lombardo, A. Ferrari, W. Knap, M. Polini, V. Pellegrini, A. Tredicucci, *Nature materials* **2012**, *11*, 865; d)F. F. Fan, *Science* **1997**, *277*; e)F. Sols, F. Guinea, A. Neto, *Physical review letters* **2007**, *99*, 166803; f)L. Ponomarenko, F. Schedin, M. Katsnelson, R. Yang, E. Hill, K. Novoselov, A. Geim, *Science* **2008**, *320*, 356.

[7] R. Haddon, *Acc. Chem. Res.* **2013**, *46*, 1.

[8] K. S. Novoselov, Z. Jiang, Y. Zhang, S. V. Morozov, H. L. Stormer, U. Zeitler, J. C. Maan, G. S. Boebinger, P. Kim, A. K. Geim, , *Science* **2007**, *315*, 1379.

[9] a)P. Kumar, L. S. Panchakarla, C. N. R. Rao, , *Nanoscale* **2011**, *3*, 2127; b)C. N. R. Rao, A. K. Sood, R. Voggu, K. S. Subrahmanyam, , *J. Phys. Chem. Lett.* **2010**, *1*, 572.

[10] a)M. Wang, E. Song, S. Lee, J. Tang, M. Lang, C. Zeng, G. Xu, Y. Zhou, K. Wang, *ACS Nano* **2011**, *5*, 8769; b)J. Daeha, Z. Lei, I. K. Saiful, *Phys. Rev. B.* **2011**, *83*.

[11] X. Li, X. Wang, L. Zhang, S. Lee, H. Dai, *Science* **2008**, *319*, 12292.

[12] K. S. Novoselov, *Nature* **2005**, *197*, 438.

[13] M. Choucair, P. Thordarson, J. Stride, *Nat. Nanotechnoly* **2009**, *4*, 669.

[14] a)K. Kim, Y. Zhao, H. Jang, S. Lee, J. Kim, K. Kim, J.-H. Ahn, P. Kim, J.-Y. Choi, B. Hong, *Nature* **2009**, *457*, 706; b)A. Reina, X. Jia, J. Ho, D. Nezich, H. Son, V. Bulovic, M. Dresselhaus, J. Kong, *Nano Lett.* **2009**, *9*, 30.

[15] L. Jiao, L. Zhang, X. Wang, G. Diankov, H. Dai, *Nature* **2009**, *458*, 877.

[16] a)D. Kosynkin, A. Higginbotham, A. Sinitskii, J. Lomeda, A. Dimiev, B. Price, J. Tour, *Nature* **2009**, *458*, 872; b)D. V. Kosynkin, W. Lu, A. Sinitskii, G. Pera, Z. Sun, J. M. Tour, *ACS Nano*, *5*, 968.

[17] S. Park, R. Ruoff, *Nat. nanotechnol.* **2009**, *4*, 217.

[18] a)W. Jinlan, M. Liang, Y. Qinghong, Z. Liyan, D. Feng, *Angewandte Chemie* **2011**, *50*; b)H. Wang, Y. Wang, Z. Hu, X. Wang, *ACS applied materials & interfaces* **2012**, *4*, 6827; c)G. L. Luque, M. I. Rojas, E. P. M. Leiva, *Journal of Solid State Electrochemistry* **2013**, *17*, 1189; d)A. Morelos-Gómez, S. Vega-Díaz, V. González, F. Tristán-López, R. Cruz-Silva, K. Fujisawa, H. Muramatsu, T. Hayashi, X. Mi, Y. Shi, H. Sakamoto, F. Khoerunnisa, K. Kaneko, B. Sumpter, Y. Kim, V. Meunier, M. Endo, E. Muñoz-Sandoval, M. Terrones, *ACS Nano* **2012**, *6*, 2261; e)H. Santos, L. Chico, L. Brey, Phys. Rev. Lett. **2009**, *103*, 086801.

[19] H. L. Guo, X. F. Wang, Q. Y. Qian, F. B. Wang, X. H. Xia, *ACS Nano* **2009**, *3*, 2653.

[20] C. Suryanarayana, M. G. Norton, *X-Ray Diffraction: A Practical Approach*

[21] a)D. A. Shirley, *Phys. Rev. B* **1972**, *5*, 4709; b)A. Oberlin, M. Endo, T. J. Koyama, *Crystal Growth* **1976**, *32*, 335.

[22] W. S. Kim, S. Y. Moon, S. Y. Bang, B. G. Choi, H. Ham, T. Sekino, K. B. Shim, *App. Phys. Lett.* **2009,**, *95*, 0831031.

[23] F. Tuinstra, J. L. Koenig, *J. Chem. Phys.* **1970**, *53*, 1126.

[24] a)A. Ferrari, D. Basko, *Nature nanotechnology* **2013**, *8*, 235; b)M. Dresselhaus, G. Dresselhaus, M. Hofmann, *Philosophical transactions. Series A, Mathematical, physical, and engineering sciences* **2008**, *366*, 231; c)Y.-C. Lin, C.-C. Lu, C.-H. Yeh, C. Jin, K. Suenaga, P.-W. Chiu, *Nano Letters* **2012**, *12*, 414; d)A. Valota, I. Kinloch, K. Novoselov, C. Casiraghi, A. Eckmann, E. Hill, R. Dryfe, *ACS Nano* **2011**, *5*, 8809; e)H. Goto, E. Uesugi, R. Eguchi, A. Fujiwara, Y. Kubozono, *Nano Lett.* **2013**, *13*, 1126.

[25] a)M. Terrones, *ACS Nano*, *4*, 1775; b)A. L. EliÌoas, A. s. R. Botello-MeÌffndez, D. Meneses-RodriÌoguez, V. JehovaÌ GonzaÌ lez, D. RamiÌrez-GonzaÌfflez, L. Ci, E. MunÌƒoz-Sandoval, P. M. Ajayan, H. Terrones, M. Terrones, *Nano Letters* **2009**, *10*, 366; c)B. Genorio, W. Lu, A. Dimiev, Y. Zhu, A.-R. O. Raji, B. Novosel, L. Alemany, J. Tour, *ACS Nano* **2012**, *6*, 4231; d)L. Jiao, L. Zhang, L. Ding, J. Liu, H. Dai, *Nano Research* **2010**.

[26] H. K. Jeong, Y. P. Lee, R. J. W. E. Lahaye, M. H. Park, K. H. An, I. J. Kim, C. W. Yang, C. Y. Park, R. S. Ruoff, Y. H. Lee, *J. Am. Chem. Soc.* **2008**, *130*, 1362.

[27] H. K. Jeong, Y. P. Lee, R. J. Lahaye, M. H. Park, K. H. An, I. J. Kim, C. W. Yang, C. Y. Park, R. S. Ruoff, Y. H. Lee, , *J.Am.Chem.Soc.* **2008**, *130*, 1362.

[28] L. Kavan, *Chem. Rev.***1997**, *97*, 3061.

[29] a)D. Dreyer, S. Park, C. Bielawski, R. Ruoff, *Chemical Society reviews* **2010**, *39*, 228; b)H. Shen, L. Zhang, M. Liu, Z. Zhang, *Theranostics* **2012**, *2*, 283.

[30] J. Jin, J.-H. Ko, S. Yang, B.-S. Bae, *Adv. Mater.* **2010**, *22*, 4510.

[31] a)S. Virendra, J. Daeha, Z. Lei, D. Soumen, I. K. Saiful, S. Sudipta, *Progress in Materials Science* **2011**, *56*; b)T. Mauricio, R. B.-M. Andrés, C.-D. Jessica, L.-U. Florentino, I. V.-C. Yadira, J. R.-M. Fernando, E. Ana Laura, M.-S. Emilio, G. C.-M. Abraham, C. Jean-Christophe, *Nano Today* **2010**, *5*; c)Y. Zhu, S. Murali, W. Cai, X. Li, J. Suk, J. Potts, R. Ruoff, *Adv. Mater.* **2010**, *22*, 3906.

[32] a)A. L. Higginbotham, D. V. Kosynkin, A. Sinitskii, Z. Sun, J. M. Tour, *ACS Nano* **2010**, *4*, 2059; b)S. Wolfe, C. F. Ingold, R. U. Lemieux, *J. Am. Chem. Soc.* **1981**, *103*, 938; c)V. C. Tung, M. J. Allen, Y. Yang, R. B. Kaner, *Nat. Nanotechnol.* **2009**, *4*, 25; d)S. Stankovich, D. A. Dikin, R. D. Piner, K. A. Kohlhaas, A. Kleinhammes, Y. Jia, Y. Wu, S. T. Nguyen, R. S. Ruoff, *Carbon*

2007, *45*, 1558; e)S. Stankovich, D. A. Dikin, G. H. B. Dommett, K. M. Kohlhaas, E. J. Zimney, E. A. Stach, R. D. Piner, S. T. Nguyen, R. S. Ruoff, *Nature* **2006**, *442*, 282.

[33] L. Dai, *Acc. Chem. Res.* **2013**, *46*, 31.

Electrochemical Preparation of Luminescent Graphene Quantum Dots (GQDs) from Multi walled Carbon Nanotubes (MWCNTs)

Luminescent, graphene quantum dots (GQDs) with uniform sizes of 3, 5, and 8.2 (±0.3) nm diameters were prepared electrochemically from MWCNTs and N-MWCNTs in propylene carbonate and acetonitrile using $LiClO_4$ and TBAP, respectively. Both these sets of GQDs displayed a remarkable quantum efficiency of 6.3 and 5.1 %, respectively along with a size-dependent lifetime. The larger the diameter of the GQDs, shorter was the average lifetime leading to lower quantum yields (QY). This method offers a novel strategy to synthesize size-tunable GQDs as evidenced by multiple characterization techniques like transmission and scanning electron microscopy (TEM, SEM), atomic force microscopy (AFM), Raman spectroscopy and X-ray diffraction (XRD). Photoluminescence of these GQDs can be tailored by size variation regulated through a systematic change in key process parameters like diameter of carbon nanotube, additives, electric field, concentration of supporting electrolyte and temperature. GQDs are promising candidates for a variety of applications such as biomarkers, nanoelectronic devices and chemosensors due to unique features like high photo-stability, biocompatibility, non–toxicity and tunable solubility in water.

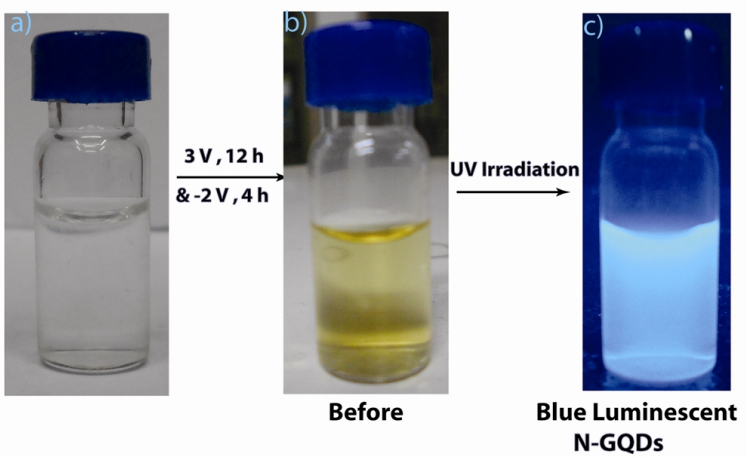

*A part of the work discussed in this chapter has been published in **"Chem. Eur. J., 2012,** 18, 12522**"**.

3.1 Introduction:

Graphene has attracted enormous recent attention because of its unique and novel electronic properties facilitating numerous promising applications.[1] However, graphene is strictly a zero band gap semiconductor, which renders its electronic and optoelectronic properties almost impossible to use for device applications.[2] Interestingly, this zero band gap material has been more recently engineered to form graphene nanoribbons[3] (GNRs) and GQDs as explained in chapter 1.[3c, 4] These materials with a finite and tunable band gap are often fluorescent producing visible light as a result of incident light of a different wavelength although this effect diminishes as soon as the source of excitement is removed. Semiconductor based quantum dots (QDs) have proven themselves as powerful inorganic fluorescent probes, especially because of its long term resistance to photo bleaching. Recent advances have led to the development of dendrimer-encapsulated quantum dots, synthesis of quantum dots in mesopores, core–shell colloidal nanostructured quantum dots, mixed semiconductor dots, and so on, although size and shape dependence is the primary interest.[5] GQDs constitute a fascinating class of recently discovered nanocarbons that comprise discrete, quasi-spherical nanoparticles with sizes below 10 nm. They possesses several favorable attributes, such as resistance to photo bleaching, size and wavelength-dependent emission, ease of production and bioconjugation, in addition to displaying several significant properties like high mobility and ballistic transport[3e, 6] due to quantum confinement[7] and edge effects.[8] Compared to conventional semiconductor quantum dots, GQDs are superior in terms of chemical inertness, low cytotoxicity and excellent biocompatibility.

The strong and tunable luminescence of GQDs is especially attractive because of its promising applications in light emitting diodes (LED),[8d] electroluminescence, organic photovoltaic devices, biological labeling and medicine.[5b, 5c, 9] Typically, GQDs contain very few carboxylic acid moieties at the edge, which is similar to that in graphene, thus imparting them with excellent water solubility and propensity for subsequent functionalization with various organic, polymeric, inorganic or biological species.[10] In addition, GQDs have many other excellent characteristics, such as high surface area, larger diameter, and better surface grafting ability using the π-π conjugated network or surface groups and other special physical properties due to the structure of graphene. As a consequence of their simple structure, as well as emerging health concerns and biological hazards, GQDs are at the center of significant research efforts and

various programs are being formulated globally to develop low-toxic, eco-friendly alternatives that have the desirable performance characteristics of QDs.[11]

Despite all these important applications, development of a simple method to produce stable and size-selective GQDs in high yield is a really daunting challenge. For example, Pan and co-workers presented a hydrothermal method for cutting pre-oxidized graphene sheets into GQDs [12] (ca. 10 nm) displaying blue luminescence due to large edge effect. Recently, Liangti Qu *et al.* recently reported the synthesis of GQDs from graphene oxide by using cyclic voltammetry (CV) within the potential window ±3 V using a phosphate buffer solution.[13] Ding *et al*. also reported the synthesis of nanocrystals from MWCNTs with a wide size distribution. Although, most of the MWCNTs became entangled together with unreacted part exhibiting swollen and curled features.[14] More recently, Klaus Mullen *et al.* reported the synthesis of GQDs of larger size by a bottom-up approach using polycyclic aromatic hydrocarbons,[10b] but with no control on edge states and consequently, there also a compromise on electronic conductivity. There are also methods based on electron beam lithography[15] and ruthenium catalyzed C_{60} transformation[16] for GQDs synthesis. Many of these methods are limited by the requirement for special equipment and the yield is also limited primarily due to the use of expensive starting materials. For example, methods which are based on graphene oxide as a starting material need toxic chemical treatments for its synthesis. Hence, it would be easier to get size controlled synthesis if starting material already has smaller domain structures of sp^2 carbon like that in MWCNTs. So an electrochemical method [17] with a potentiostatic control using selective oxidation followed by reduction would be useful to synthesize GQDs probably by a more precise control of the size and shape.

We have discussed many aspects of electrochemical unzipping of CNTs by a two step process, producing high quality GNRs having smooth edges and fewer defects in Chapter 2. Subsequent experiments to understand the effect of ionic strength and pH in aqueous media, unraveled the critical role of oxygen in opening up the CNTs. However, when similar experiments were conducted in non-aqueous media like propylene carbonate or acetonitrile we could, surprisingly, obtain GQDs, unlike that of GNRs in aqueous media. More specifically, sustained oxidation (15 h) of MWCNTs in propylene carbonate with $LiClO_4$ at 1 V followed by reduction yielded discrete spherical particles of GQDs presumably due to lateral unzipping,

although certain post-synthetic treatments were essential to have the monodispersed. These GQDs have been characterized by TEM, SEM, AFM, Raman spectroscopy and X-ray diffraction (XRD). Further, their remarkable size-dependant light-emitting behavior has been analyzed systematically to enable promising applications. This chapter also describes a unique synthetic strategy for N-GQDs using N-MWCNTs as starting materials by means of a controlled application of interfacial electric field. More importantly, this method represents a novel route for the preparation of size selective N-GQDs, with different mechanism of unzipping compared with that of pristine MWCNTs.

3.2 Experimental Section:

10 mg of MWCNTs (Nanocyl, 99% pure) was added to 20 mL of ethanol (Rankem) and sonicated for 15 minutes (or till it could disperse properly). This suspension was deposited onto a conducting substrate i.e., Glassy Carbon Electrode (GCE), after polishing with alumina powder, rinsing thoroughly in acetone and after subsequent drying. A 5 μL of the suspension was spread on a pre-treated bare GCE using a micro tip. GCE was kept under IR- lamp for 1 h to remove solvents. The electrochemical oxidation of MWCNTs was carried out in a three-electrode system (Pt flag as counter electrode, Pt wire as a quasi-reference electrode) with an Autolab PGSTAT30 (Eco Chemie) at a fixed positive potential (1V) for different time period like 7, 11 and 15 h in propylene carbonate containing 3 mM $LiClO_4$ as the supporting electrolyte. The extent of oxidation was confirmed by various characterization techniques like XRD, X-ray photoelectron spectroscopy (XPS), Raman spectroscopy. In the second step of the experiment, we reduced these oxidized MWCNTs for 2 h at a fixed negative potential (-1 V) in order to get size tunable GQDs. Samples were collected by sonication of the electrode in deionized water and washed several times before submitting for any characterization.

Nitrogen doped MWCNTs (3 wt% Nitrogen) obtained from Nanomaterials Inc. were purified according to the following protocol: the sample (50 mg) was heated for 12 h at 250 ^{0}C under argon atmosphere, further treated with 50 ml of concentrated HCl for few hours followed by thorough water washing, thereby removing the metal catalysts in the form of their chlorides. These purified N-MWCNTs were dispersed in N, N-dimethyl formamide (2 mg/ml) and drop casted (50 μL) on a GCE (diameter-3 mm) after polishing with alumina powders, followed by rinsing thoroughly in acetone and subsequent drying. Then GCE was kept under IR lamp for 1 h

to remove solvents and to form a thin uniform layer of coating of N-MWCNTs. The electrochemical oxidation of N-MWCNTs was carried out in a three-electrode system using an Pt flag as counter electrode and Pt wire as a quasi-reference electrode, with an Autolab PGSTAT30 (Eco Chemie) at a fixed positive bias like 2, 2.5 and 3 V (*vs.* QRE) in acetonitrile containing 0.1M TBAP for 12 h each followed by a subsequent reduction in the same electrolyte at -2 V for typically for duration of 4 h. The N-GQDs were purified by evaporating the acetonitrile from the solution and dissolving the remained materials in water, followed by dialyzing the aqueous solution with a cellulose ester membrane bag (MD77(8000) at 60º for two days to completely remove the supporting electrolyte. The nitrogen content within N-GQDs remains essentially the same 2.76 wt%, although the yield systematically changed as a function of the oxidation potential and time.

Steady state fluorescence emission and variable temperature measurements were performed using a Fluorolog HORIBA JOBIN YVON on fluorescence spectrophotometer. The emission as well as excitation slit width was maintained at 1 nm throughout the experiments and the data was obtained in 'Sc/R'(self coupled resonator mode) to account for the variations in lamp intensity. The fluorescence quantum yields of GQDs was determined in water using quinine sulphate in 0.1M H_2SO_4 of (Φ=0.54) as the internal standard by exciting at 350 nm. The optical density at λ 350 nm was maintained at 0.1±0.05 to avoid reabsorption artifacts. The samples were prepared by making the optical density 0.1 ± 0.05 at excitation wavelength (λ_{ex}~ 330 for GQDs in water). All experiments were performed under identical conditions. The quantum yield was calculated using the equation.[4b, 18]

$$\Phi_S = \Phi r \, [F_s \, Ar / F_r \, As] \, (\eta_s/\eta_r)^2 \quad \ldots\ldots\ldots\ldots\ldots\ldots [1]$$

Where Φ_S is the fluorescence quantum yield of the sample, F is the area of the emission peak, η_r is the refractive index of solution, and A is the absorbance of the solution at the exciting wavelength. The subscripts r and s denotes reference and sample, respectively.

3.3 Results and discussion:

Scheme 3.1 represents a simplified form of our two- step process for the electrochemical transformation of MWCNTs to GQDs. The first step comprises of applying a typical anodic potential of 1 V *vs* Pt QRE (QRE=quasi reference electrode) to the MWCNTs coated working electrode in propylene carbonate solution with $LiClO_4$, as the supporting electrolyte, where the applied electric field presumably initiates the breaking of carbon nanotubes. More interestingly, the size of GQDs is a function of oxidation time. This is attributed to the intercalation of Li+/propylene carbonate complexes resulting into exfoliation of oxidized MWCNTs, facilitating the formation of size tunable GQDs.[19]

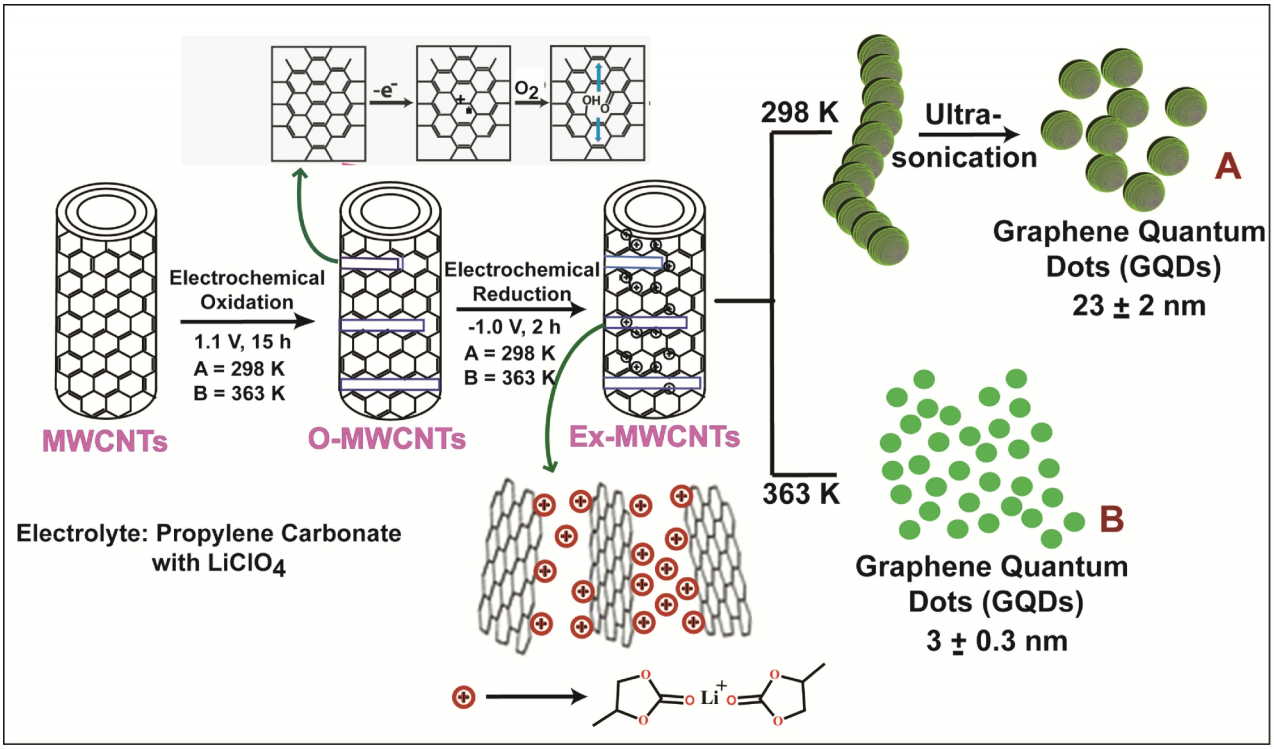

Scheme 3.1. A schematic representation of various processing stages involved in the preparation of photo luminescent GQDs from MWCNTs by this electrochemical approach.

3.3.1 Cyclic Voltammogram

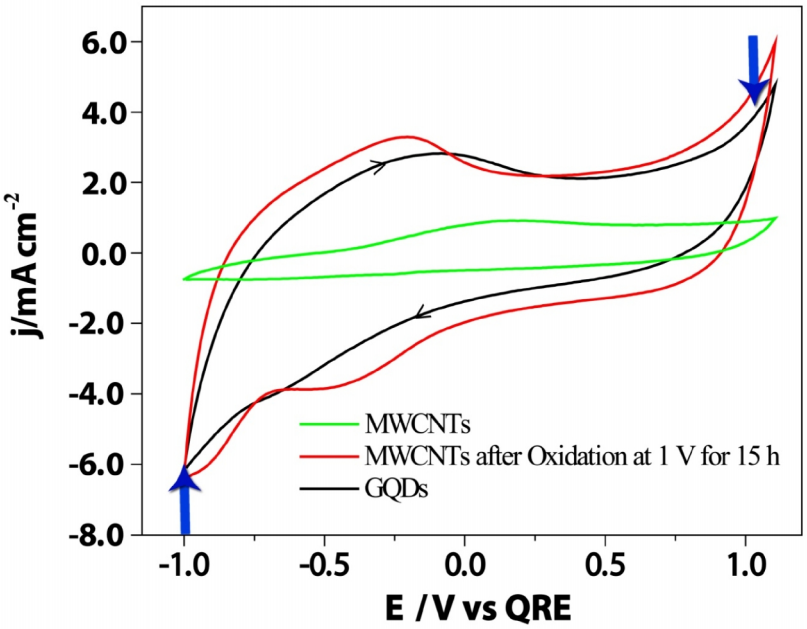

Figure 3.1. Cyclic voltammograms of MWCNTs, before and after the oxidation at 1 V (*vs* QRE) for 15 h and GQDs in a potential window of -1 to 1.1 V at 50 mV/s in propylene carbonate with 3 mM $LiClO_4$ as supporting electrolyte at room temperature. Regions marked with arrows indicate the potential, where CNTs have been selectively oxidized or reduced. Selective 5^{th} scan was recorded in each cyclic voltammograms.

Figure 3.1 shows superimposed CV of MWCNTs before and after the oxidation at 1 V for 15 h and GQDs in a potential window of -1 to 1.1 V at 50 mV/s in propylene carbonate with 3 mM $LiClO_4$ as supporting electrolyte. Voltammograms of MWCNTs are electrochemically silent, except for a small increase in non-faradaic current with cycle number, and this subtle morphological change is known. However, by keeping the potential at 1 V for 7, 11 and 15 h continually MWCNTs undergo oxidative cleavage and interestingly at the end, the open circuit potential (OCP) also increases by 54, 67 and 73 mV, respectively, clearly revealing the formation of oxidized species along with perhaps many topological defects. A similar shift in OCP has been observed in aqueous media presumably due to oxidative unzipping and IR studies indicate the presence of residual oxygen containing species. Although, 15 h oxidation could generate ultrathin, two dimensional (1-3 atomic layer thick), monodispersed, high quality GQDs.

3.3.2 Transmission Electron Microscopy (TEM)

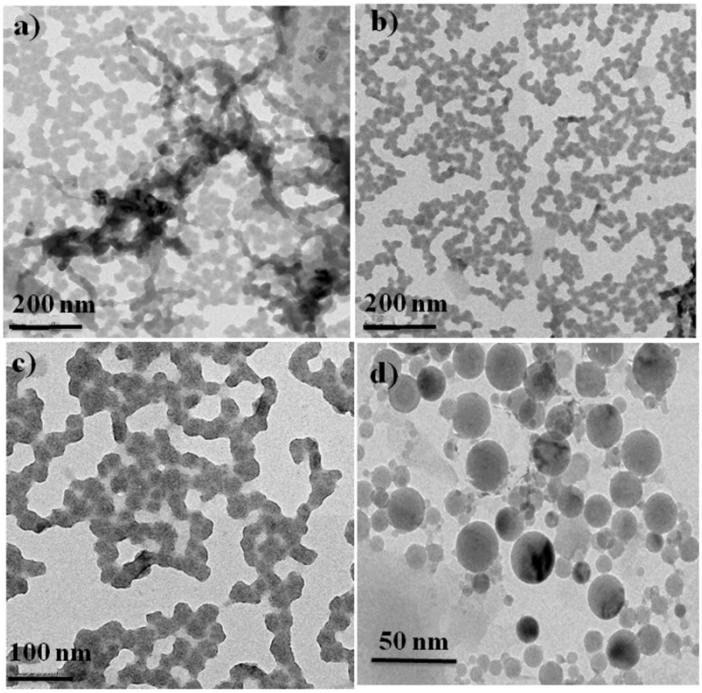

Figure 3.2. Typical TEM images of (GQDs) synthesized at 30 °C using oxidation for 1V at 7h followed by reduction at -1 V as shown in a, and b; c corresponds to GQDs prepared for 1 V at 11 h followed by reduction at -1 V with different magnifications while (d) represents GQDs with different levels of sonication prepared for 1 V at 15 h followed by reduction at -1 V.

Figure 3.2 shows typical TEM images of GQDs prepared from MWCNTs at 30 °C by the two step electrochemical process, where (3.2a) corresponds to interconnected quantum dots obtained after oxidation at 1 V for 7 h followed by subsequent reduction at -1 V for 2 h . Figure 3.2b and 3.2c correspond to swollen interconnected GQDs obtained by oxidation at 1 V for 11 h, showing two different magnifications, while (3.2d) suggests a case of complete transformation of 40-50 nm diameter MWCNTs to GQDs after oxidation at 1 V for 15 h. Also, Figure 3.3 shows TEM images of monodispersed GQDs having average size 3±0.3, 5±0.3 and 8.2±0.3 nm prepared at 90°C using oxidation at 1 V for 15 , 11 h and 7 h, respectively. This undoubtedly indicates that the time of oxidation plays an important role in controlling the size of GQDs - longer the oxidation time smaller are the resulting GQDs. Further, these GQDs have been observed to be transparent and stable under electron beam irradiation. More significantly, these

GQDs show a d-spacing of 0.33 and 0.242 nm, respectively, which corresponds to (002) and (1120) lattice planes, which is in excellent agreement with what is known for GQDs prepared using other routes [20] as shown in figure 3.3g. The structure is also confirmed from figure 3.3h, which shows a selected-area electron diffraction (SAED) pattern in complete agreement with what is known for GQDS synthesized by independent routes.[16, 21]

3.3.3 Current transient curve

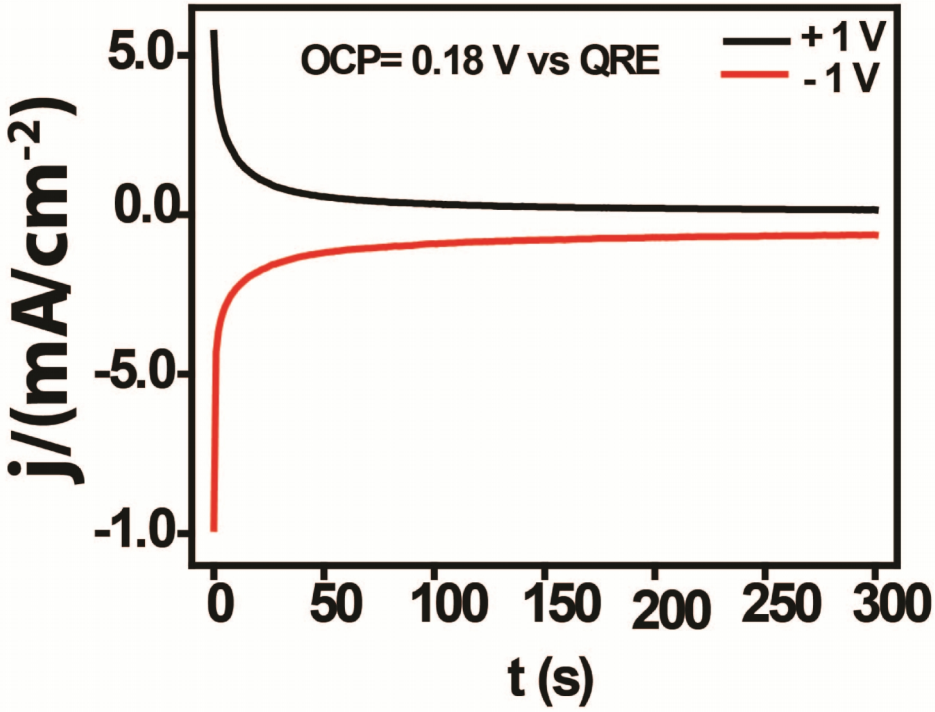

Figure 3.2.1. Typical current transient curve for GQDs (3±0.3) nm to a step voltage of +1 and -1 V.

The number of coulombs utilized has been estimated by integrating the I-t curves, and typical curves (for 5 min) are indicated in figure 3.2.1. This current transient was measured after the removal of a constant bias voltage of 1V. A anodic current is obtained, which slowly decays to zero. Similarly, a cathodic current is obtained upon the removal of a negative step voltage. This discharging current transient obtained confirms charge injection and storage in trap sites present. There are several steps in the mechanism involving oxidative C-C cleavage. However, further reduction causes a diminution in charge storage (area) although conductivity measurement (3.8 a) indicates an enhancement in carrier concentration.

3.3.4 High Resolution Transmission Electron Microscopy

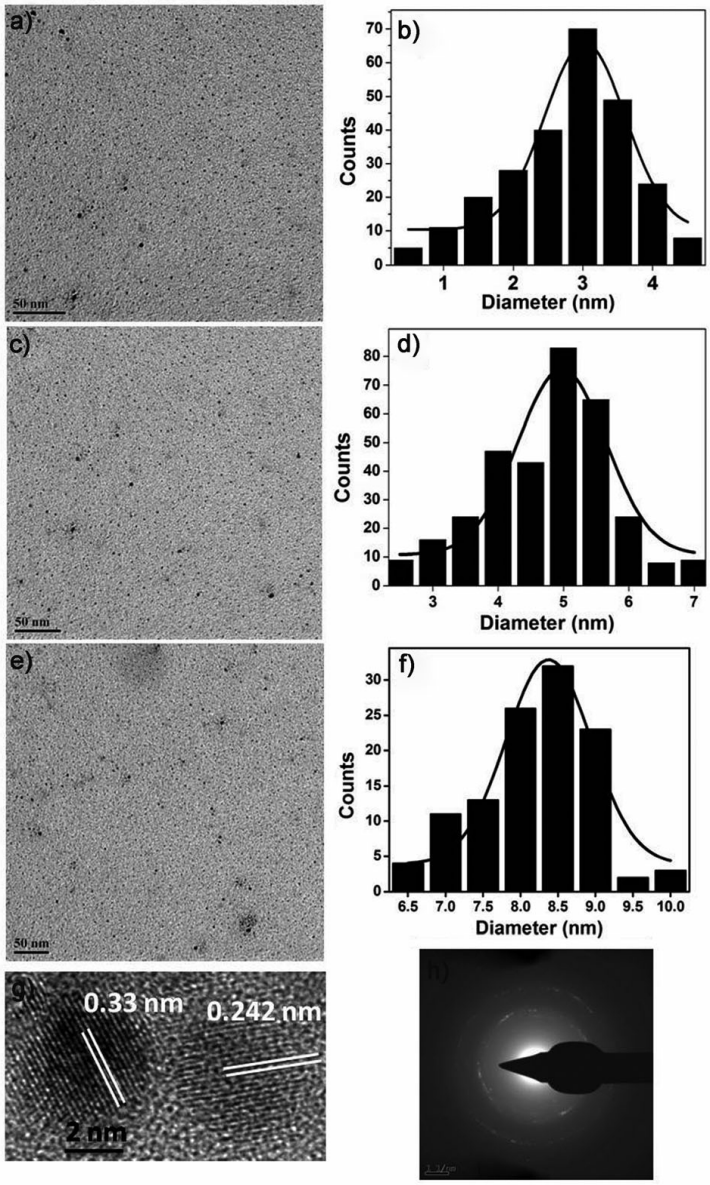

Figure 3.3. Display of TEM images correspond to the synthesis at 90 °C and oxidation at 1V for 15, 11 h and 7 h as shown in a, c and e, respectively with their size distribution histograms.; g) fringes pattern of GQDs; h) SAED pattern of GQDs (8.2±0.3 nm) displaying 002 as prominent plane.

Accurate information about the change in both height and lateral dimensions, was obtained from AFM measurements as shown in Figure 3.4a, revealing a size distribution between 3-4 nm (3.2 nm mean diameter). Interestingly, this topographic height in between 1-2 nm also

suggests the presence of 1-3 layers of graphene in each individual GQD suggesting high quality as proved from conductivity data as shown in Figure 3.8a and these GQDs are much smaller than those prepared by other methods.[5a, 18, 22] Also figure 3.4b and 3.4c displays, AFM image and their corresponding height profiles for samples prepared by using a potential of 1 V at 90°C for 11 h and 7 h, respectively, resulting in to different sized (4-5 and 6-7 nm and also height varying from 3-5 nm) monodispersed GQDs. Nevertheless, GQDs synthesized at 30°C reveal long quantum dot chains (1 μm) with straight edges and widths ranging from 30 to 40 nm and height in the range of 18-24 nm (Figure 4d) confirming a clear transformation of MWCNTs to GQDs with different yields (30-38%).

3.3.5 Atomic Force Microscopy

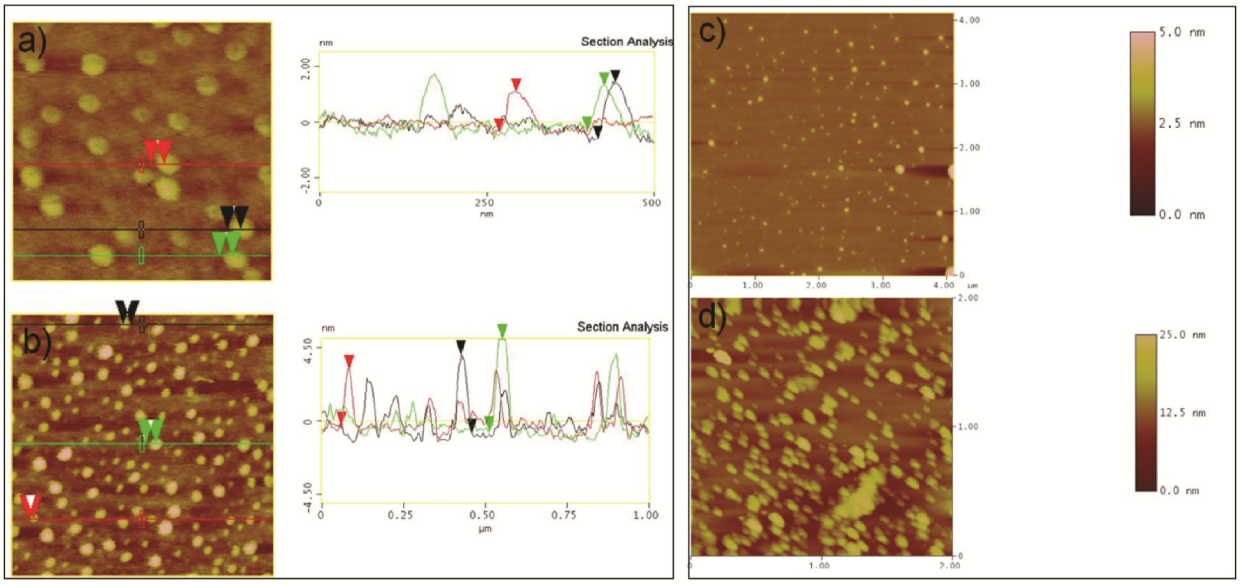

Figure 3.4. Displays AFM image of monodispersed GQDs corresponding to the synthesis at 90°C and oxidation at 1V for 15, 11 and 7 h and reduction at -1 V for 2 h each as shown in a, b and c, respectively, with their height profiles; d) corresponding to synthesis at 30°C and oxidation at 1V for 15 h showing the transformation of MWCNTs to GQDs having heights 15 -20 nm.

In order to explore the optical properties of as-synthesized GQDs, we have also carried out UV-Vis absorption and normal photoluminescence (PL) measurements. For the UV-Vis absorption, there is no clear peak, as displayed in figure 3.5a, except for an extended absorption

edge. However, the PL spectrum, interestingly shows a broad excitation-dependent peak, similar to that observed for Si nanocrystals, perhaps, due to the distribution of different emissive sites.[23] More specifically, the UV–Vis absorption spectrum of GQDs in water having solubility of 1-2 μg/ml shows an absorption band at ca. 346 nm (Figure 3.5a), while upon excitation near the absorption band, the PL spectrum shows a strong peak at 456 nm as indicated in figure 3.5b. This is in excellent agreement with the emission spectra of the GQDs synthesized hydrothermally and the origin of luminescence could be ascribed to the presence of free zigzag sites[24] with a carbene like triplet ground state. GQDs especially in the range of 3-23 nm contribute predominantly to free zigzag sites.[24] Interestingly, the carbene ground state multiplicity is related to the energy difference (δE) between σ- and π-orbitals. It has been determined earlier that for a triplet ground state, δE should be below 1.5 eV, because the triplet carbene is most common at zigzag edges.

3.3.6 Photo Luminescence Analysis

Photoluminescent excitation spectra (PLE) for 3±0.3 nm reveal two distinct electronic transitions at 268 nm (4.62 eV) and 346 nm (3.58 eV), respectively, which could be attributed to transitions from HOMO (σ- and π-orbitals) to LUMO. This δE (1.04 eV) is also interestingly, suitable for triplet carbene according to Hoffman rule.[12a] However, in sharp contrast to the blue-luminescence of GQDs synthesized hydrothermally, the electrochemically synthesized GQDs excited by 346 nm emit a green luminescence (Figure 3.5 b inset), which could presumably be attributed to the effect of bigger size and also due to different surface functional groups (Figure 3.7). Interestingly, the quantum yields are found to be 5.1-6.3 % (Table 3.1) when calibrated against quinine sulfate[25] which is indeed, better than that of GQDs prepared by independent means (3.8 %).[22] This is also comparable to that by Ding *et al* (6.4 %),[14] which signify the utility of these GQDs as promising candidates for bio-labeling and optoelectronic applications. Although luminescence mechanism of all GQDs appear to be similar, subtle changes occur since the total percentage of free zigzag edges might variably contribute as evidenced by increase in the quantum yield from 5.1 to 6.3 % and also red shift in the optimal emission wavelength (Figure 3.5c-3.5f).

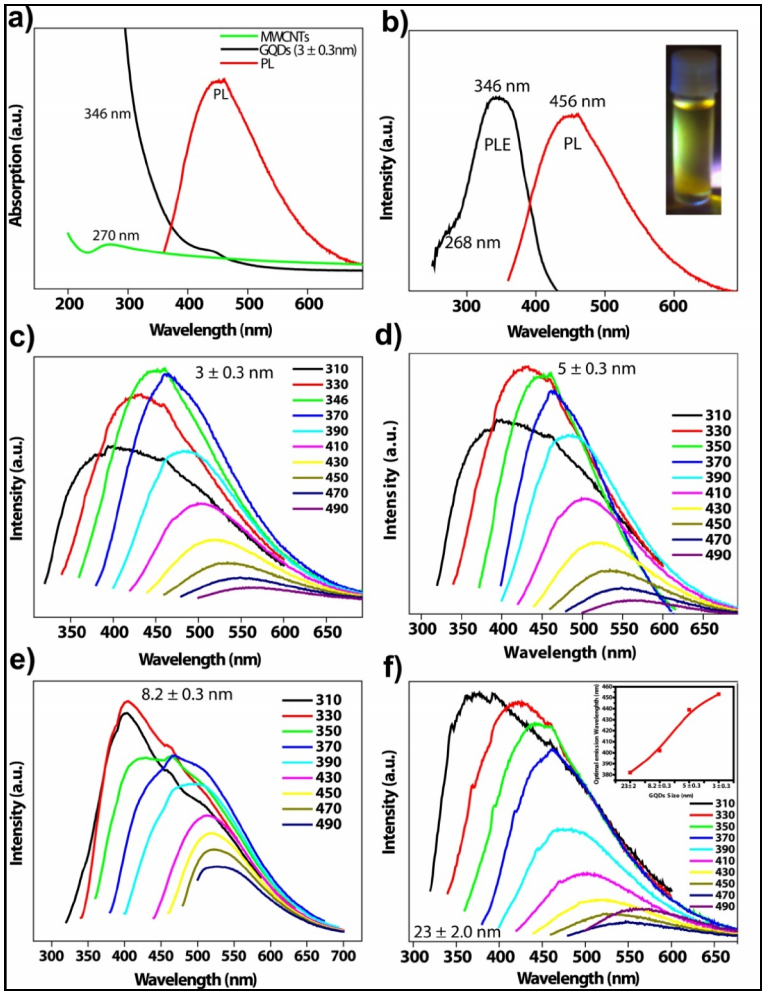

Figure 3.5. a) UV-Vis absorption and PL (at 346 nm excitation) spectra of GQDs dispersed in water b) PLE spectrum with the detection wavelength of 440 nm and PL spectrum excited at 346 nm. (c-f) PL spectra at different excitation wavelengths for 3±0.3 nm, 5±0.3, 8.2±0.3and 23±2 nm GQDs and corresponds to the size of GQDs and optimal emission wavelength.

Table 3.1: Mean GQDs Size *vs* Quantum Yield

Mean GQDs size (nm)	Quantum yield % (*vs* Quinine sulfate 54 %)
3±0.3 nm	6.3 ±0.2 %
5.2±0.3 nm	5.9±0.2 %
8.2±0.3 nm	5.4±0.2 %
23±2 nm	5.1±0.2 %

Table 3.1 displays the variation in size as a function of quantum yield. This high quantum yield for smaller size quantum dots could be understood in terms of the intrinsic electronic structure of GQDs, i.e. presence of more free zigzag sites. However, this is not straightforward as GQDs commonly contain carboxylic and epoxide groups, which can act as non-radioactive electron-hole recombination centers.[26] Thus, quantum yield is inversely proportional to the size of GQDs in a limited range and interestingly the removal of these oxygen-containing groups maybe improves the quantum yield, either by reduction or surface passivation using poly ethelene glycol (PEG), dodecyl amine, etc.[8d, 24a]

3.3.7 Life time decay of GQDs

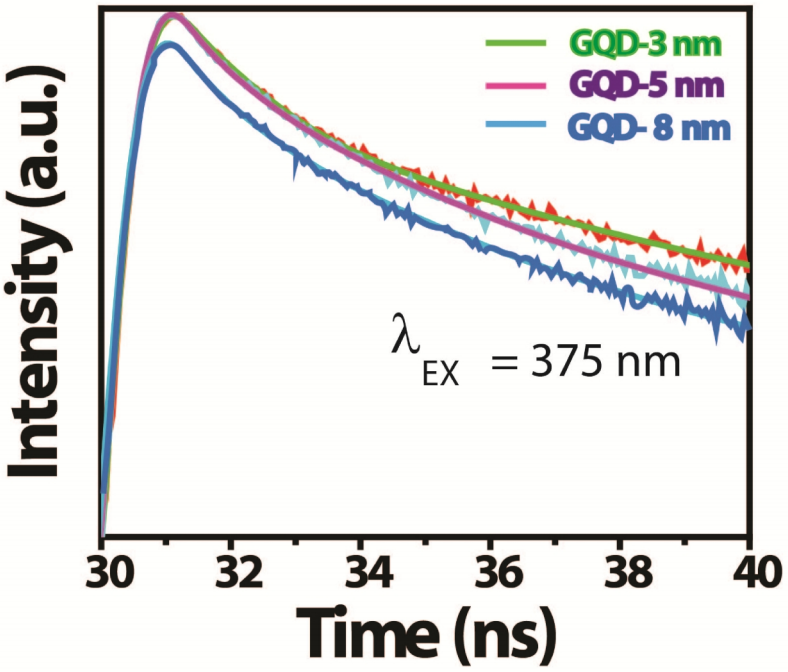

3.5.1: Average lifetime as a function of size for GQDs. $\mathbf{t}_{av}$ is the average lifetime, $\mathbf{t}_{av}$ is calculated according to $\mathbf{t}_{av} = \sum \boldsymbol{\tau}_i R_i$ [27]. Decay curves of the GQDs measured at various λ em with Φ = 2.4 nm excited by a 375 nm laser.

All the PL decay curves are well fitted by a triple-exponential function, which contains a fast decay ($\boldsymbol{\tau}_1$: 0.79–1.54 ns) and one slow decay (τ_2 : 3.16–3.88 ns,). The decay lifetimes are in good agreement with carbon based quantum dots grown by different methods, such as

chemical exfoliation.[5c] The decay curves of the GQDs with various three different diameters were excited by a wavelength of 375 nm as shown in Figure 3.5.1. Interestingly, we observed the size-dependent lifetime on the GQDs. The larger the diameter of the GQD results in a shorter average lifetime, which leads to lower quantum yield. It is well known that the non-radiative relaxation pathways, such as surface defect and vibrational relaxation may suppress radiative recombination process. Hence, lifetime decreases with decreasing nanocrystal size due to non-radiative process dominating over the radiative one.[28] However, this is exactly reverse in the case of GQDs, the experimental result reveals that the average lifetime decreases monotonically from 3.2 to 1.8 ns with increasing diameter (3to8 nm). It probably means that spatial confinement effect related to radiative relaxation, rather than nonradioactive vibrational and surface defect effects, plays an important role in the decay lifetime.

3.3.8 Raman and XRD Analysis

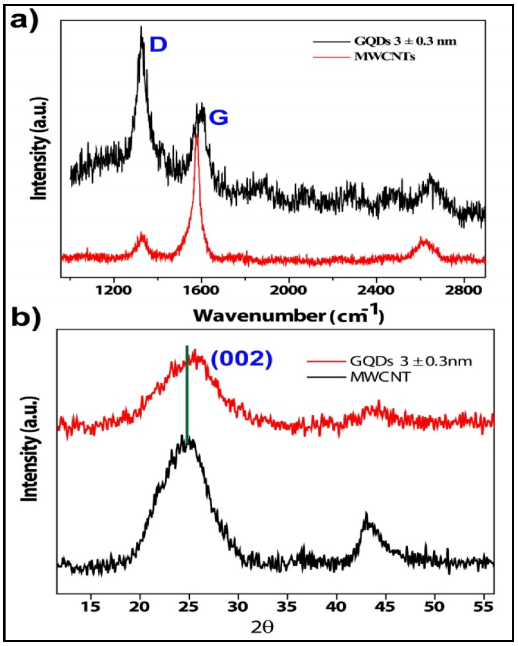

Figure 3.6. Comparison of a) Raman spectra and b) powder XRD patterns of MWCNTs and GQDs prepared by the two-step electrochemical method.

Raman spectroscopy is used to discriminate between different types of ordered and disordered bonding environment of sp^2 and sp^3 hybridized carbon.[29] Normally in carbon nanostructures, the G band is assigned to the E_{2g} phonon of sp^2 carbon atoms, while D band

corresponds to the extent of defects.[34] In Figure 3.6a, the intensity of the D band at 1329 cm^{-1} for MWCNTs increases substantially, indicating a possible decrease in the size of in-plane sp^2 domains due to oxidation. As seen in the case of pristine MWCNTs, the intensity of D band is less, suggesting excellent quality of the starting materials.[30] After the electrochemical oxidation, the intensity of D band is considerably enhanced along with a concomitant decrease in the intensity of the G band, revealing clearly that the oxidation has been completed as confirmed by the observation of a high ratio of I_D/I_G bands. For example, these types of electrochemically unzipped MWCNTs after 15 h typically show an I_D/I_G ratio of (1.23), suggesting edge effect as the central cause of fluorescence. These Raman results are in excellent agreement with the structural data from X-ray Diffraction (XRD) of our GQDs [29, 31] For example, (Figure 6b) shows a comparison of the XRD pattern of MWCNTs and GQDs. As crystalline size of 11.4 nm inferred from the full width of half maximum (FWHM) of the broader (002) peak centered at 26.8° indicates there are more number of active sites on GQDs (Figure 3.6 b) with a d-spacing 3.30 Å, revealing compactness of the structure compared to that of MWCNTs.[5b]

3.3.9 X-ray Photoelectron Spectroscopy (XPS) Analysis

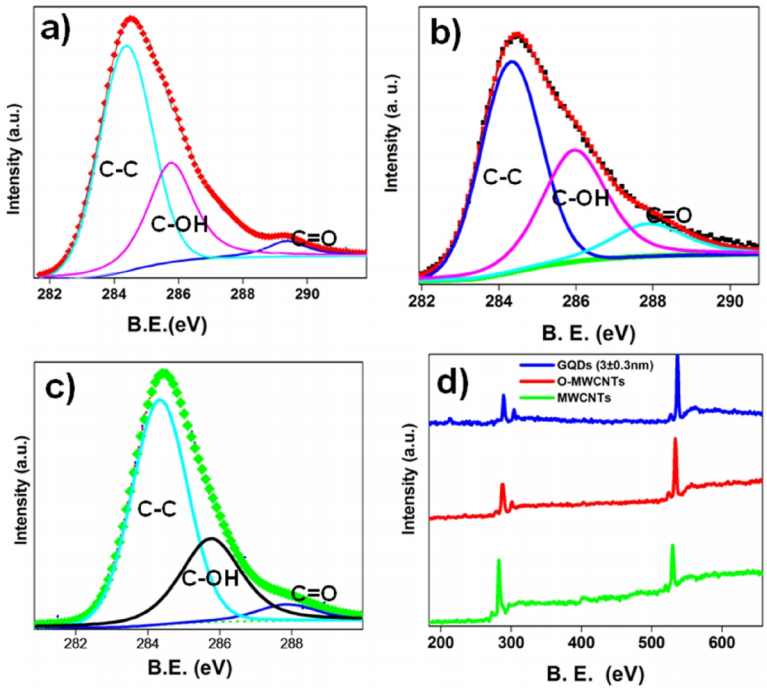

Figure 3.7. X-ray photoelectron spectra of C 1s core level a) MWCNT b) Oxidized MWCNT c) GQDs (3±0.3 nm) and d) complete XPS spectra showing percentage of carbon and oxygen; squares represent the experimental data, thick lines represent the fitting data for overall signal and the fitted lines are the de-convoluted individual peaks for different environments of carbon.

XPS data is invaluable to discriminate between MWCNTs, Oxidized MWCNTs and GQDs and also to correlate the presence of different forms of oxygen signals for calculating surface oxidation even quantitatively.[22] In the XPS of carbon (C1s) the C-C binding energy values are obtained at 284.51, 283.59 and 284.49 eV for MWCNTs, Oxidized MWCNTs and GQDs respectively. A decrease in the intensity and binding energy (B.E.) value of C-C in case of figure 3.7 (b) is assigned to the weakening of C–C bond and also perhaps to the introduction of more sp^3 character in MWCNT. The peak at 285.9 eV corresponds to C–O and peak at 287 eV is assigned to carbonyl groups (C=O). Upon the reduction by applying a negative potential -1 V for 2 h the peaks at 285.9 and 287 eV decrease by a minor extent indicating the possibility of de-oxygenation followed by exfoliation due to the intercalation of Li/ propylene carbonate resulting in to GQDs. Moreover the oxygen to carbon ratio in figure 3.7d for MWCNTs, oxidized MWCNTs and GQDs are 0.05, 0.14 and 0.10, respectively.

3.3.10 Current-Voltage Plots and PLE Analysis

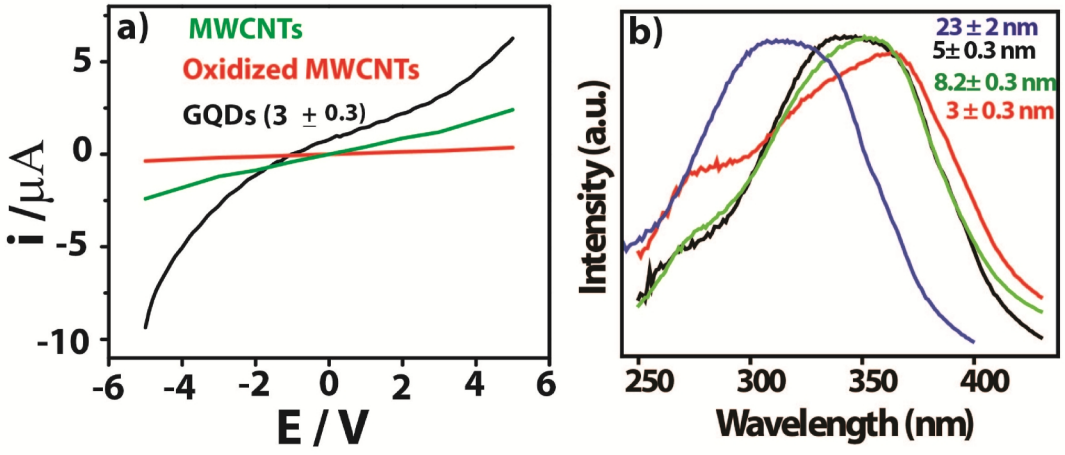

Figure 3.8: a) Current-Voltage Curves of MWCNTs, Graphene Quantum Dots showing improved conductivity values for GQDs. b) PLE (Photo luminescent excitation) spectra with the detection wavelength of 440 nm for GQDs of sizes 23±2 nm, 8.2±0.3 nm, 5±0.3 and 3±0.3 nm.

To measure the electrical properties, samples were drop casted on FTO (Fluorine doped tin oxide) substrate and I-V profiles were taken by maintaining a film thickness of 0.5 µm and also a distance between two Pt-electrodes 0.5 µm. The Oxidized MWCNTs exhibits relatively poor conductivity, compared to that of MWCNTs. The GQDs displays improved conductivity due to increase in carrier concentration.[5b] Also Figure 3.8 b displays PLE spectra of four different samples of GQDs showing size dependent red shift in the absorption wavelength, confirming the utility of such material as biomarker.

3.3.11 Nitrogen doped GQDs (N-GQDs)

In addition to the preparation of green luminescent GQDs, it is interesting to get blue luminescence by doping, which could also be used to modify the energy gap of GQDs and to tune their electronic properties via band-gap engineering. Moreover, doping leads to the disruption of the ideal sp^2 hybridization of the carbon atoms in carbon allotropes, which also additionally introduce the n-type carriers in the system, thus locally inducing significant changes in their electronic properties as well as its chemical reactivity towards many catalytic reactions.

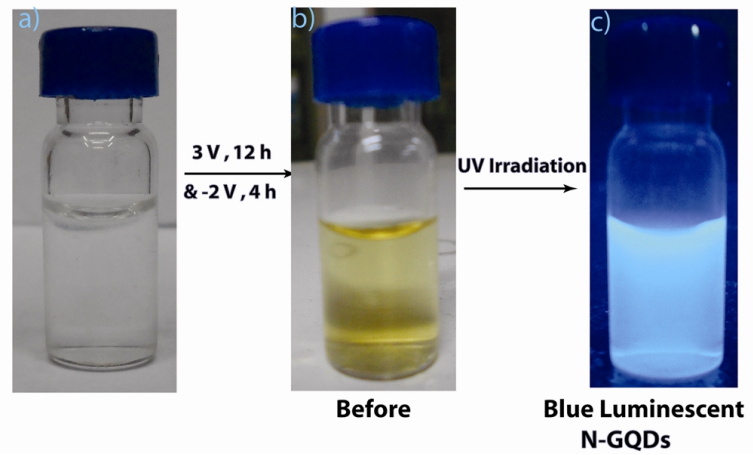

Scheme 3.2: Optical images corresponding to various stages of the synthesis of N-GQDs (size 2.5 ± 0.3 nm) from N-MWCNTs using 0.1 M TBAP in acetonitrile at 3 V for 12 h followed by their reduction at -2 V for 4 h in the same electrolyte.

3.3.12 Transmission Electron Microscopy for N-GQDs

Figure. 3.9 display a comparison of the TEM images of as prepared monodispersed N-GQDs with average sizes 2.5 ± 0.3 nm, 4.7 ± 0.3 nm and 7.2 ± 0.3 nm using a systematic control of the anodic potential at 3, 2.5 and 2 V (vs. QRE), respectively. This data demonstrates a remarkable correlation between the applied potential and the size; higher the applied potential is, smaller is the resulting N-GQDs and these smaller N-GQDs could be fractionated further by special post-synthetic treatments like dialysis and density gradient ultra centrifugation to get narrower dispersion.

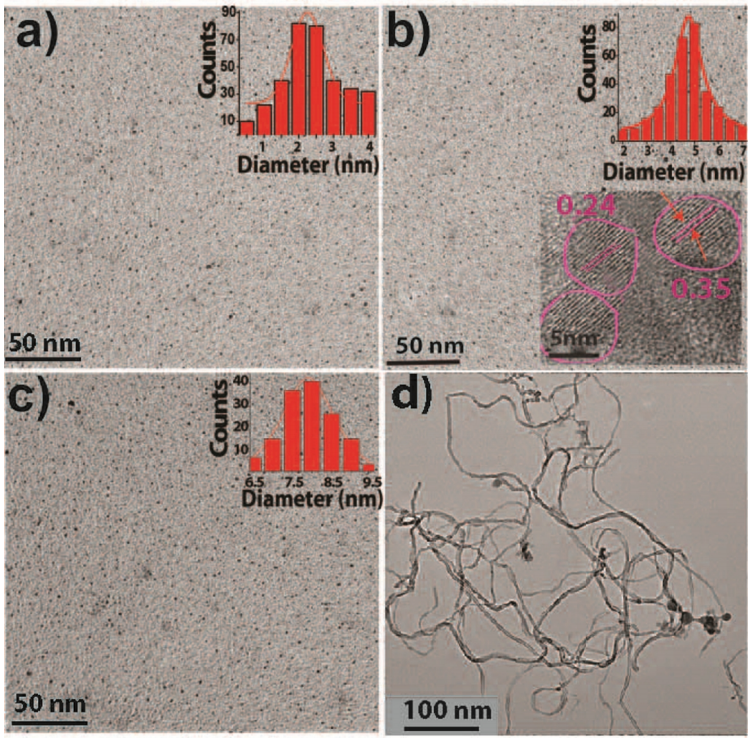

Figure. 3.9: TEM images of "as prepared" N-GQDs using anodic potential 3, 2.5 and 2 V respectively and followed by reduction at -2 V with average sizes a) 2.5 ± 0.3 nm, b) 4.7 ± 0.3 nm c) 7.2 ± 0.3 nm with their corresponding size distribution histograms and b) (Inset) Fringes pattern corresponding to size 4.7 ± 0.3 nm showing d spacing 0.35 nm and 0.24. d) TEM image of N-MWCNTs.

The constant potential used for the oxidation plays an important role in controlling the average size of N-GQDs. More significantly, these N-GQDs show a d-spacing of 0.35 and 0.24

nm corresponding to the (002) and (1120) crystal phases respectively, which is in excellent agreement with what is known for N-GQDs prepared by using independent chemical and physical routes (Figure. 3.9b Inset) and also in agreement with the XRD data(Fig 3.11b).[32] Although the exact mechanism of electric field assisted breakdown of N-MWCNTs to N-GQDs is not very clear, the critical role played by the applied potential in controlling the size of N-GQDs suggests that N-MWCNTs gets exfoliated faster due to synergetic effect of applied potential and intercalation of supporting electrolyte ions due to the presence of heteroatom and in the next step (potential -2 V for 4 h) they presumably get reduced to N-GQDs.[33]

3.3.13 X-ray Photoelectron Spectroscopy (XPS) for N-GQDs

XPS data in the form of binding energy values are invaluable for discriminating N-MWCNTs from N-GQDs and we have used this also to calculate the extent of different types of nitrogen quantitatively. The XPS of N1s spectra could be deconvoluted (Fig. 3.10) into four sub-peaks, which are due to well-known spin-orbit coupling levels. These four N sub-peaks are assigned to the pyridinic-N, pyrrolic-N, quaternary-N, and pyridine N-oxide atoms at 397.4, 399.1, 401.3, and 402.8 eV, respectively.[34] The calculated nitrogen content from the XPS data for N-MWCNTs (2.9 wt%) shows a close resemblance to that of N-GQDs (2.76 wt%) with perhaps a higher pyridinic-N content (Fig 3.10 d). The nitrogen content, however, is higher in pristine N-MWCNTs despite a minor decrease with an increase in the oxidation degree promoted by the amount of oxidation. Indeed, it is known that primary and secondary amines could be degraded by oxidation to aldehydes and ketones, thus loosing nitrogen atoms, concomitant with the generation of ammonia.[15]

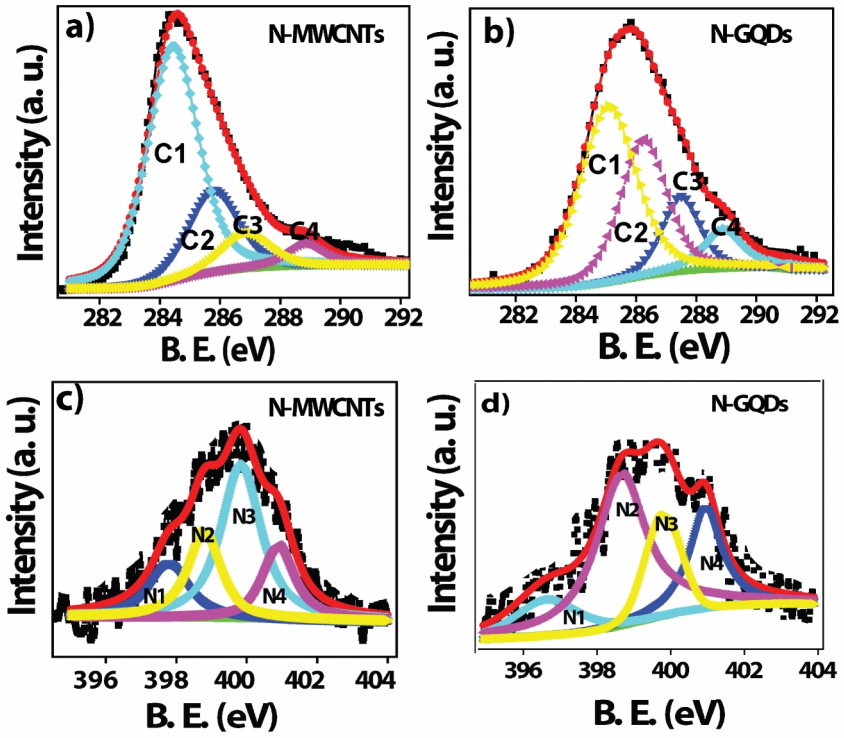

Figure. 3.10: a) Comparative XPS showing the percentage of carbon, nitrogen and oxygen in N-MWCNTs and N-GQDs respectively; b, c) deconvoluted N1s spectra of N-GQDs.

3.3.14 Raman and XRD Analysis for N-GQDs

The Raman technique is a powerful and non-destructive tool for the characterization of GQDs. The G band is assigned to the E_{2g} vibrational modes of the aromatic domains, whereas the D band arises from the defective or sp^3 carbon of the graphitic domains. Usually, the intensity ratio of "disorder" D to crystalline G (I_D/I_G) is used to compare the structural order between crystalline and amorphous graphitic systems. Furthermore, a typical Raman spectrum of these materials shows broad peaks at about 1345 and 1590 cm^{-1}, which correspond to the D and G bands, respectively (Fig. 3.11a). The relative intensity (I_D/I_G) ratios for N-MWCNTs and N-GQDs are 1.13, and 1.55, respectively. The FWHM of the D band of N-GQDs is, nevertheless, broader compared to that of pristine GQDs implying more disorder perhaps due to the presence of N atoms in the carbon framework.[29] The G-band position in pristine N-MWCNTs appears at 1585 cm^{-1}, and interestingly, after the electrochemical oxidation and followed by reduction the position of G peak is shifted to 1587 cm^{-1} for N-GQDs.

Also Fig. 3.11b shows a comparison of the XRD pattern of N-MWCNTs and N-GQDs and revealing the broadening of (002) peak at 2θ = 25.4° of N-GQDs due to smaller size.[8d] The increase in interlayer distance is attributed to the oxygen-containing groups introduced in the exfoliation and oxidation of N-MWCNTs. The interlayer spacing of N-GQDs strongly depends on their oxidation degree, that is, the attached hydroxyl, epoxy/ether, carbonyl and carboxylic acid groups which distributed on basal plane can increase the interlayer spacing of N-GQDs.

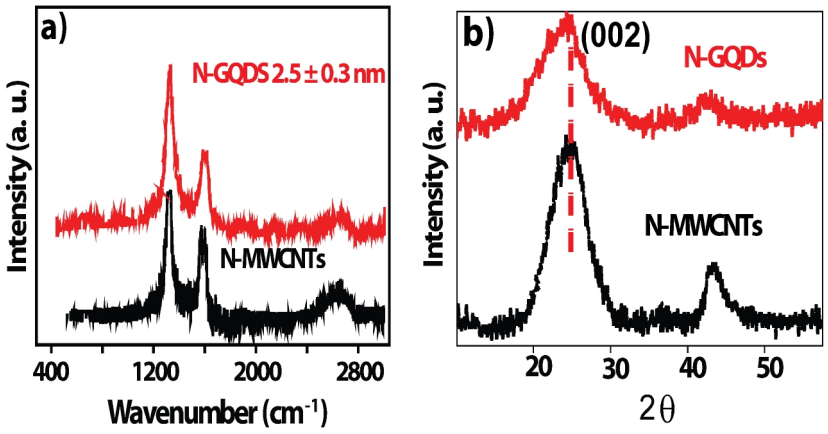

Figure. 3.11 a) comparative Raman spectra of N-MWCNTs and N-GQDs. b) comparative XRD pattern of N-MWCNTs and N-GQDs.

3.3.15 Photo Luminescence for N-GQDs

Photoluminescence spectra, show a broad excitation-dependent emission, perhaps due to the distribution of different emissive sites with a pronounced red shift in the emission at fixed excitation wavelength (320 nm) for different size N-GQDs (Fig 3.12).[10c] For example, N-GQDs show a blue luminescence (as shown in scheme 1) as compared to green luminescent pristine GQDs, perhaps due to the presence of nitrogen in the lattice. This indicates that N-GQDs possess unique topology compared to that of GQDs which could be used to replace Pt as electrocatalysts particularly for ORR.

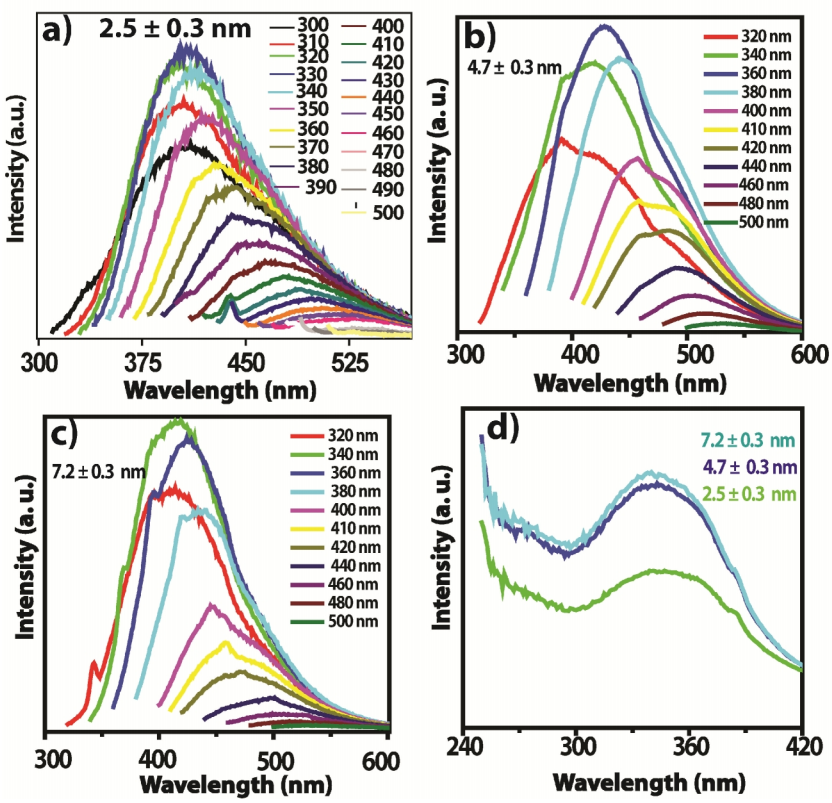

Figure 3.12. a-c) Comparative different excitation dependent emission for various sizes of N-GQDs, d) Photoluminescence excitation spectra collected at 400 nm.

One of the major problems of these GQDs for cellular and molecular imaging applications is their Li content and it is also important to understand any decisive role played by lithium cation intercalation during the mechanism of GQDs formation. Accordingly, several experiments were conducted using tetrabutyl ammonium perchlorate instead of lithium perchlorate and also to investigate the anion and solvent dependence. All these results indicate that cation/propylene carbonate complexes are primarily responsible for the high-yield exfoliation of oxidized MWCNT to produce GQDs. A possible mechanism of this transformation of MWCNT to GQDs could be formulated based on the above results (Scheme 3.1) assuming vertical unzipping in contrast to longitudinal unzipping in aqueous case. However, considering the fact that C-C cleavage can initiate at topological defects having enough strain (due to high field gradients), transverse splitting of the tube walls could be facilitated at these transient openings. According to this mechanism, the field gradient on the edges of split MWCNTs could overcome the van der Waals force between the graphene layers. The GQDs are expected to be generated by the oxidation of C–C bond, following the exfoliation of oxidized

MWCNTs – crumpled form of graphene sheets.[35] The fragmentation could be initiated by the synergetic effect of intercalation of Li and TBAP along with solvation, in the turbostratic structure under electric field, facilitated by the considerable interlayer stress created due to this.

3.4. Conclusions

This chapter discusses out focused efforts to synthesize size tunable green and blue luminescent GQDs (3±0.3, 5±0.3, 8.2±0.3 nm at 90°C, 23±2 nm at room temperature) from MWCNTs and N-MWCNTs by an electrochemical approach in non-aqueous media without using any molecular capping agent. Interestingly, we observed the size-dependent lifetime on the GQDs confirming quantum confinement effects commonly observed in all other quantum dots. The larger the diameter of the GQD is shorter is its average lifetime which in turn t leads to lower quantum yields. These quantum dots are especially useful for cellular and molecular imaging applications due to intrinsic luminescence behaviour, higher photo-stability and enhanced fluorescence quantum yield. Also the present method is unique, since an accurate control of potential (especially by potentiostatic technique) enables easy regulation and monitoring the size of graphene quantum dots and more importantly, benefits due to large scale synthesis.

3.5. References

[1] a)G. Abraham, M. Cano, J. Fernando, M. Rodríguez, C. D. Jessica, G. Claudia, G. Espinosa, T. L. Ferdinando, R. G. Daniel, D. A. Cullen, D. J. Smith, M. Terrones, Y. I. Vega-Cantu, *Nano Lett.* **2009**, *9*, 1527; b)A. K. Geim, K. S. Novoselov, *Nat. Mater.* **2007**, *6*, 183−191; c)A. A. Green, M. C. Hersam, *Nano Lett.* **2009**, *9*, 4031; d)K. S. Novoselov, A. K. Geim, S. V. Morozov, D. Jiang, Y. Zhang, S. V. Dubonos, I. V. Grigorieva, A. A. Firsov, *science* **2004**, *306*, 666.

[2] X. L. Li, X. R. Wang, L. Zhang, S. W. Lee, H. J. Dai, *Science* **2008**, *319*, 1229.

[3] a)Z. Chen, Y.-M. Lin, M. J. Rooks, P. Avouris, , *Phys. E* **2007**, *40*, 228; b)X. Yang, X. Dou, A. Rouhanipour, L. Zhi, H. J. Rader, K. Mullen, *J. Am. Chem. Soc.* **2008**, *130*, 4216; c)X. Yan, X. Cui, B. Li, L.S. Li, *Nano Lett.* **2010**, *10*, 1869; d)U. K. Parashar, S. Bhandari, R. K. Srivastava, D. Jariwala, A. Srivastava, *Nanoscale* **2011**, *3*, 3876; e)P. Kumar, L. S. Panchakarla, C. N. R. Rao, *Nanoscale* **2011**, *3*, 2127; f)M. Y. Han, B. Ozyilmaz, Y. Zhang, P. Kim, *Phys. Rev. Lett.*

2007, *98*, 206805; g)M. Sprinkle, M. Ruan, Y. Hu, J. Hankinson, M. Rubio-Roy, B. Zhang, X. Wu, C. Berger, W. A. de Heer, *Nat. Nanotechnol.* **2010**, *5*, 727.

[4] a)X. Yan, X. Cui, L.-S. Li, *J. Am. Chem. Soc.* **2010**, *132*, 5944; b)S. Zhu, J. Zhang, C. Qiao, S. Tang, Y. Li, W. Yuan, B. Li, L. Tian, F. Liu, R. Hu, H. Gao, H. Wei, H. Zhang, H. Sun, B. Yang, *Chemical communications* **2011**, *47*, 6858; c)Y. Dong, J. Shao, C. Chen, H. Li, R. Wang, Y. Chi, X. Lin, G.Chen, *Carbon* **2012**, *50*, 4738; d)Y. Dong, C. Chen, X. Zheng, L. Gao, Z. Cui, H. Yang, C. Guo, Y.Chi, C. M. Li, *J. Mater. Chem.* **2012**, *22*, 8764; e)X. Zhou, Y. Zhang, C. Wang, X. Wu, Y. Yang, B. Zheng, H. Wu, S.Guo, J. Zhang, *ACS Nano* **2012**, *6*, 6592; f)T. Gokus, R. R. Nair, A. Bonetti, M. Böhmler, A. Lombardo, K. S.Novoselov, A. K. Geim, A. C. Ferrari, A. Hartschuh, *ACS Nano* **2009**, *3*, 3963.

[5] a)S. Jianhua, Z. Yihua, Y. Xiaoling, L. Chunzhong, *Chemical Communications* **2012**, *48*; b)Z. Zhipan, Z. Jing, C. Nan, Q. Liangti, *Energy & Environmental Science* **2012**, *5*, 8869; c)J. Peng, W. Gao, B. Gupta, Z. Liu, R. Romero-Aburto, L. Ge, L. Song, L. Alemany, X. Zhan, G. Gao, S. Vithayathil, B. Kaipparettu, A. Marti, T. Hayashi, J.-J. Zhu, P. Ajayan, *Nano Letters* **2012**, *12*, 844.

[6] a)C. N. R. Rao, A. K. Sood, R. Voggu, K. S. Subrahmanyam, , *J. Phys. Chem. Lett.* **2010**, *1*, 572; b)M.S. Dresselhaus, M. Terrones, A. Jorio, M. Endo, A. Rao, Y. Kim, T. Hayashi, H. Terrones, J. Charlier, G. Dresselhaus, *Mater. Today* **2004**, *7*, 30.

[7] L. Jiao, L. Zhang, L. Ding, J. Liu, H. Dai, *Nano Research* **2010**.

[8] a)C.-S. Eduardo, J. Xiaoting, T. Humberto, G. S. Bobby, T. Mauricio, S. D. Mildred, M. Vincent, *ACS Nano* **2013**, *7*; b)G. Hidenori, U. Eri, E. Ritsuko, F. Akihiko, K. Yoshihiro, *Nano Letters* **2013**, *13*; c)H. Goto, E. Uesugi, R. Eguchi, A. Fujiwara, Y. Kubozono, *Nano Letters* **2013**, *13*, 1126; d)V. Gupta, N. Chaudhary, R. Srivastava, G. Sharma, R. Bhardwaj, S. Chand, *J. Am. Chem. Soc.* **2011**, *133*, 9960.

[9] a)H. Tetsuka, R. Asahi, A. Nagoya, K. Okamoto, I. Tajima, R. Ohta, A. Okamoto, *Advanced materials* **2012**, *24*, 5333; b)J. Lu, J.-x. Yang, J. Wang, A. Lim, S. Wang, K. Loh, *ACS Nano* **2009**, *3*, 2367.

[10] a)V. Georgakilas, M. Otyepka, A. Bourlinos, V. Chandra, N. Kim, K. Kemp, P. Hobza, R. Zboril, K. Kim, *Chemical reviews* **2012**, *112*, 6156; b)R. Liu, D. Wu, X. Feng, K. Müllen, *J. Am. Chem.*

Soc. **2011**, *133*, 15221; c)H. Shen, L. Zhang, M. Liu, Z. Zhang, *Theranostics* **2012**, *2*, 283; d)X. Xu, S. Stöttinger, G. Battagliarin, G. Hinze, E. Mugnaioli, C. Li, K. Müllen, T. Basché, *Journal of the American Chemical Society* **2011**, *133*, 18062.

[11] L. Haitao, K. Zhenhui, L. Yang, L. Shuit-Tong, *Journal of Materials Chemistry* **2012**, *22*.

[12] a)D. Pan, J. Zhang, Z. Li, M. Wu, *Advanced materials* **2010**, *22*, 734; b)D. Pan, L.Guo, J. Zhang, C. Xi, Q. Xue, H. Huang, J. Li, Z. Zhang, W.Yu, Z.Chen, Z.LiandM.Wu, *J. Mater.Chem.* **2012**, *22*, 3314.

[13] Y. Li, Y. Hu, Y. Zhao, G. Q. Shi, L. E. Deng, Y. B. Hou, L. T. Qu, *Adv. Mater.* **2011**, *23*, 776.

[14] J. Zhou, C. Booker, R. Li, X. Zhou, T.-K. Sham, X. Sun, Z. Ding, *J. Am. Chem. Soc.* **2007**, *129*, 744.

[15] L. Ponomarenko, F. Schedin, M. Katsnelson, R. Yang, E. Hill, K. Novoselov, A. Geim, *Science* **2008**, *320*, 356.

[16] J. Lu, P. S. E. Yeo, C. K. Gan, P. Wu, K. P. Loh, *Nature nanotechnology* **2011**, *45*, 247.

[17] L. Kavan, *Chem. Rev* **1997**, *97*, 3061.

[18] F. Winnik, D. Maysinger, *Accounts of chemical research* **2013**, *46*, 672.

[19] A. L. Eloas, A. R. Botello-Mendez, D. Meneses-Rodriguez, D. V. J. Gonzalez, Ramirez-Gonzalez, E. M.-S. L. Ci, P. M. Ajayan, M. H. Terrones, Terrones, *Nano Lett.* **2010**, *10*, 366.

[20] a)M. Zhang, L. Bai, W. Shang, W. Xie, H. Ma, Y. Fu, D. Fang, H. Sun, L. Fan, M. Han, C. Liu, S. Yang, *J. Mater. Chem.* **2012**, *22*, 7461; b)M. L. Mueller, X. Yan, J. A. McGuire, L.S. Li, *Nano Lett.* **2010**, *10*, 2679; c)L. Lin, S. Zhang, *Chem. Commun.* **2012**, *48*, 10177; d)L. Tang, R. Ji, X. Cao, J. Lin, H. Jiang, X. Li, K. S. Teng, C. M. Luk, S. Zeng, J. Hao, S. P. Lau, *ACS Nano* **2012**, *6*, 5102.

[21] a)J. Shen, Y. Zhu, X. Yang, J. Zong, J. Zhang, C. Li, *New J. Chem.* **2012**, *36*, 97; b)J. Shen, Y. Zhu, C. Chen, X. Yang, C. Li, *Chem. Commun.* **2011**, *47*, 2580; c)F. Yang, M. Zhao, B. Zheng, D. Xiao, L. Wu, Y. Guo, , *J. Mater.Chem.* **2012**, *22*, 25471.

[22] L. Cao, M. Meziani, S. Sahu, Y.-P. Sun, *Accounts of chemical research* **2013**, *46*, 171.

[23] S. Jin, D. H. Kim, G. Jun, S. Hong, S. Jeon, *ACS Nano* **2013**, *7*, 1239.

[24] a)S. Baker, G. Baker, *Angewandte Chemie* **2010**, *49*, 6726; b)Z. Kang, E. Wang, B. Mao, Z. Su, L. Gao, S. Lian, L. Xu, *J. Am. Chem. Soc.* **2005**, *127*, 65345.

[25] H. Li, X. He, Z. Kang, H. Huang, Y. Liu, J. Liu, S. Lian, C. Tsang, X. Yang, S.-T. Lee, *Angewandte Chemie* **2010**, *49*, 4430.

[26] S. Zhuo, M. Shao, S. T. Lee, *ACS Nano* **2012**, *6*, 1059.

[27] L. Tang, R. Ji, X. Li, K. S. Teng, S. P. Lau, *Particle & Particle Systems Characterization* **2013**, *30*, 523.

[28] M. L. Mastronardi , F. Maier-Flaig, D. Faulkner, E. J. Henderson, C. Kübel, U. Lemmer, G. A. Ozin, *Nano Lett.* **2012**, *12*, 337.

[29] M. Dresselhaus, G. Dresselhaus, M. Hofmann, *Philosophical transactions. Series A, Mathematical, physical, and engineering sciences* **2008**, *366*, 231.

[30] L. Jiao, L. Zhang, X. Wang, G. Diankov, H. Dai, *Nature* **2009**, *458*, 877.

[31] A. Ferrari, D. Basko, *Nature nanotechnology* **2013**, *8*, 235.

[32] C.-S. Rodolfo, M.-G. Aaron, V.-D. Sofia, T.-L. Ferdinando, L. E. Ana, P.-L. Nestor, M. Hiroyuki, H. Takuya, F. Kazunori, K. Yoong Ahm, E. Morinobu, T. Mauricio, *ACS Nano* **2013**, *7*.

[33] Y. Li, Y. Zhao, H. Cheng, Y. Hu, G. Shi, L. Dai, L. Qu, *Journal of the American Chemical Society* **2012**, *134*, 15.

[34] W. Haibo, M. Thandavarayan, W. Xin, *ACS Catalysis* **2012**, *2*.

[35] Y. Li, Y. Hu, Y. Zhao, G. Shi, L. Deng, Y. Hou, L. Qu, *Advanced materials* **2011**, *23*, 776.

Applications of GQDs: Single electron transfer and Electrocatalysis

A sequential, single-electron charging of Graphene Quantum Dots (GQDs) encapsulated in a dodecyl amine envelope with a high level of monodispersity, facilitating atto-farad capacitance (C_{GQDs}) is described in this chapter. Average GQDs dimensions, as ascertained from high resolution transmission electron microscopy and atomic force microscopy, ca. 3 ± 0.3, 2.6 ± 0.2, 2.2 ± 0.3 nm, indeed control this unprecedented behavior. Differential pulse voltammetry (DPV) and cyclic voltammetry (CV) for the "as prepared GQDs" interestingly, reveal evenly spaced (ΔE) peaks, manifesting subtle charge injection effects to the semiconducting core. These single-electron charging peaks, with ~90 mV width (FWHM) are quite evenly spaced at positive potential. This chapter also discusses another interesting application of the use of size dependant electrocatalytic properties of N-GQDs towards oxygen reduction reaction (ORR). The presence of N-dopants in the carbon framework not only causes faster unzipping of N-MWCNTs, but, provides more low activation energy site for enhancing the electrocatalytic activity for ORR. These results on the size dependent electrocatalytic activity of N-GQDs for ORR as illustrated by the smaller sized N-GQDs (2.5 ±0.3 nm) may be a promising alternative to Pt based electrocatalysts for fuel cell applications.

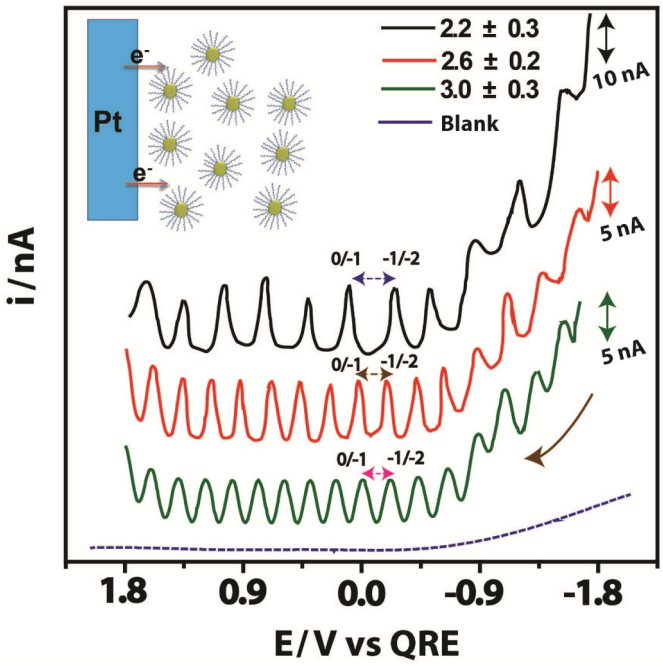

*A part of the work discussed in this chapter has been published in "*Angew. Chem.* **2013**, *52*, 2482**".**

4.1 Introduction

Metallic and semiconducting nanoclusters stabilized by a variety of organic monolayers of thiols, amines and carboxylic acids have received considerable attention in the past decade because of their size and shape-dependent electronic, chemical and electrochemical properties, especially because of the ease with which they show discrete single-electron transfer behavior.[1] This intriguing behavior is specially seen as a stair-case (sometimes known as "Coulomb staircase") in the current-voltage behavior even at room temperature, when prepared below a critical threshold size (ca. 1-3 nm), having a narrow size distribution. However, the phenomenon associated with this, also known as quantized double-layer (QDL) charging has been extensively studied for some systems, using techniques such as scanning tunneling microscopy (STM), cyclic voltammetry (CV), and differential pulse voltammetry (DPV).[2] Some earlier reports have also demonstrated QDL-charging behavior of larger-core clusters (e.g. Au_{1400}, Au_{2869}), where surface adsorption plays an important role in influencing the charge storage behavior.[3] However, most of the reports of observing the QDL charging of smaller monolayer-protected clusters (1-3 nm) have involved the use of gold, and palladium particles,[4] and there has been no reports on semiconducting quantum dots except perhaps monodispersed CdSe quantum dots prepared by special techniques.[5]

GQDs are an interesting and versatile experimental system allowing a range of operational regimes from conventional single-electron detectors to "neutrino billiards", in which size effects are exceptionally strong. Despite the fact that modern technology does not yet allow control of device's geometry on the true sub nm scale, we have demonstrated that GQDs unlike any other bulk material-remains stable, robust and highly conductive at essentially molecular scale (a few benzene rings), this finding improves prospects of graphene-based electronics if or when the nm-scale processing techniques are developed.

We have discussed an electrochemical transformation of MWCNTs to GQDs by a two step process in solution as discussed in chapter 3. In continuation, this chapter explains selected applications of these GQDs. As in the case of most nanomaterials, even smaller variations in the size (dispersity) can exhibit a mixture of properties, i.e. polydispersed samples give different potentials for the same n^{th} electron and point to the importance of post-synthetic treatments for ensuring mono-dispersed GQDs. Hence in order to obtain mono-dispersed GQDs, (3 ± 0.3 nm),

we have carried out post-synthetic size separation strategies using density gradient ultracentrifugation and dialysis. [6]

The cathode reaction in proton exchange membrane fuel cell (PEMFCs), namely oxygen reduction reaction (ORR) is more sluggish than the hydrogen oxidation,[7] and many researchers have focused on improving the ORR using low Pt or Pt-free electrocatalysts.[8] In recent studies, the carbon based materials such as carbon nanotubes (CNT), nanofibers, and graphene have received extensive attention as an alternative metal-free electrocatalyst to Pt.[8-9] Specifically, N-doped carbon materials have experimentally shown higher ORR activity mainly following the four-electron pathway. Moreover, the N-doped CNTs and graphene have been reported to display enhanced activity for ORR even in the absence of metal atoms, due to change in electronic structure of carbon atom, with respect to dopant within the framework. In general, the doping helps to modify the electronic and chemical properties of GQDs which could be contrasted with the other more common methods of surface functionalization for modulating the behavior. Nitrogen doping, is a powerful technique to modify graphitic carbonaceous materials for various applications like catalysis to nanoelectronics.[10] Increase in nitrogen content with specific bonding configuration, has resulted in many debates on what configuration is optimal and also on the mechanism of performance enhancement. Doping could also be used to modify the energy gap of GQDs and to tune their electronic properties via band-gap engineering.[7c] Moreover, doping leads to disruption of the ideal sp^2 hybridization of the carbon atoms in carbon allotropes, which also additionally introduces the n-type carriers in the system, thus locally inducing significant changes in their electronic properties as well as its chemical reactivity towards many catalytic reactions.[10] However, a clear separation of contributions of intrinsic size dependence and doping is difficult in many systems even with a strong support from computational modeling and simulation groups.[11] N-GQDs have been studied theoretically and electronic structural calculations suggest that nitrogen atoms located at their edge and near the edge might promote the electrocatalytic activity of N-GQDs towards the ORR.[12] In spite of the huge potential of N-GQDs, as an alternative to platinum, there are only very few experimental studies dealing with the synthesis and characterization of N-GQDs. For example, although Liangti Qu *et al.* reported the synthesis of N-GQDs from graphene oxide by using CV within the potential window ± 3 V in acetonitrile with tetra butyl ammonium per chlorate (TBAP) as supporting electrolyte, but the exact source of nitrogen is unclear.[10c] Similarly Li *et al.*

reported the behavior of smaller sized colloidal GQDs for ORR but the electrocatalytic activity appears to be poor compare to that of Pt.[7c] Hence, there is an urgent need to clarify the performance of N-GQDs especially with precise size control for ORR due to its enormous utility in fuel cells, electrolyzer and other electrochemical devices.

In this chapter, we have discussed the unique single electron transfer properties of GQDs along with the electrocatalytic properties of different sized N-GQDs for ORR. The smaller the N-GQDs size, greater is the activity. This could be governed by many factors, like, confinement effect, higher N-sites available for reactions on edges and higher sp^2 characters.

4.2 Experimental Section

Graphene quantum dots were synthesized according to the experimental methodology elaborately discussed in chapter 3. Briefly, MWCNTs were dispersed into N, N-dimethylforamide (DMF) by ultrasonication (4.5 mg/L). A thin coating of MWCNTs (50 μmL) were achieved by drop casting on the glassy carbon electrode (2 mm diameter) and dried under IR lamp, used as working electrode with Pt foil and Pt wire as counter and reference electrodes, respectively. After applying positive potential for different to the working electrode, followed by subsequent negative potential for corresponding time intervals, the electrodes were sonicated in water, and subsequently, the GQDs were collected and dialyzed for several days to fully remove the impurities. These purified GQDs were finally redispersed in deionized water for further characterization. On the same time, N-doped different size GQDs were synthesised by same method as above, but, instead of MWCNTs, the N-doped MWCNTs were used. The as prepared different size N-GQDs were investigated for its electrochemical activity towards ORR in alkaline media.

Moreover, GQDs (synthesized according to our previous work having carboxyl groups) were modified by covalent coupling of amine containing molecules through the creation of amide bonds (Figure 4.1). In short, in a 50 mL round bottom flask, 1 mg of GQDs was added to 10 mg of the dodecyl amine and this reaction mixture was sonicated for 30 minutes. Subsequently, the mixture was stirred for 10 minutes followed by the addition of a few drops of sulfuric acid as a catalyst. After the addition of the catalyst, the mixture was kept on a hotplate at 110° C and stirred further for 48 h. Upon completion of the reaction, the mixture was poured into

25 mL of benzene and vacuum-filtered through a filter paper (3 µm porosity). This washing operation was repeated five times with THF. The product was then washed with deionized water and acetone, and the functionalized GQDs material produced was dried in a vacuum oven at 90° C and after density gradient ultracentrifugation and dialysis, different fractions are used for further experiments having sizes and dispersity 2.2 ± 0.3, 2.6 ± 0.2, and 3 ± 0.3 nm. These amine capped GQDs were dissolved in 10 mL dichloromethane and all voltammetric experiments were carried out using Pt UME (20 µm) as working electrode, Pt foil as counter and Pt wire as a quasi-reference electrode using conventional system which is calibrated prior to all experiments against ferrocene-ferrocenium couple. DPV responses of GQDs were recorded using 0.5 mM TBAHFP as supporting electrolyte in CH_2Cl_2 for particle sizes of 2.2 ± 0.3, 2.6 ± 0.2, and 3 ± 0.3 nm, using 20 mV pulse amplitude at a typical scan rate 25 mV/s.

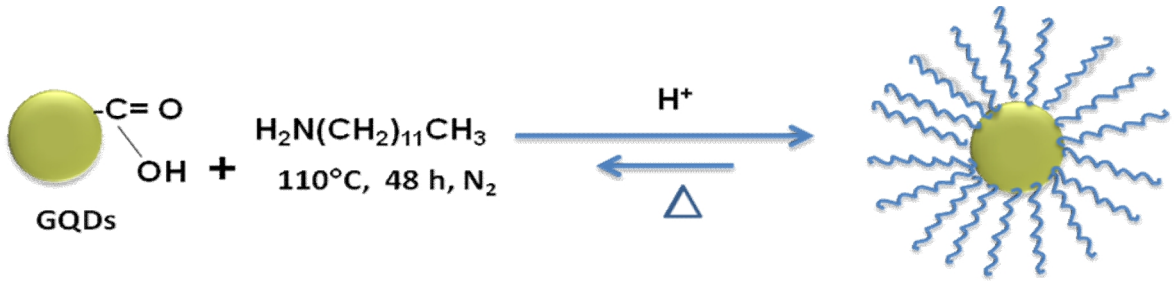

Figure 4.1. Schematic representation displaying the functionalization of GQDs with dodecyl amine.

One of the most widely used test samples for STM investigations is highly oriented pyrolytic graphite (HOPG) substrates due to its reasonable flatness in the subnanometer range and non-reacting nature. HOPG was used after cleaving off surface layers of graphite using good quality tape to create a fresh, atomically flat surface, with cleavage steps. Later, they were cleaned with acetone and ultrasonically agitated in methanol to remove impurities and adhered particles, if any. The sample for STM analysis was prepared by putting a very dilute drop of GQDs solution on HOPG substrate followed by drying for 5 min. STM studies were subsequently carried out immediately after the deposition. The STM tips were made from 0.25 mm diameter polycrystalline Pt - Rh wire by mechanically cutting them at an angle.

4.3 Results and Discussion:

4.3. 1 X-ray photoelectron spectroscopy, FT-IR, Photoluminescence and Raman to support the functionalization:

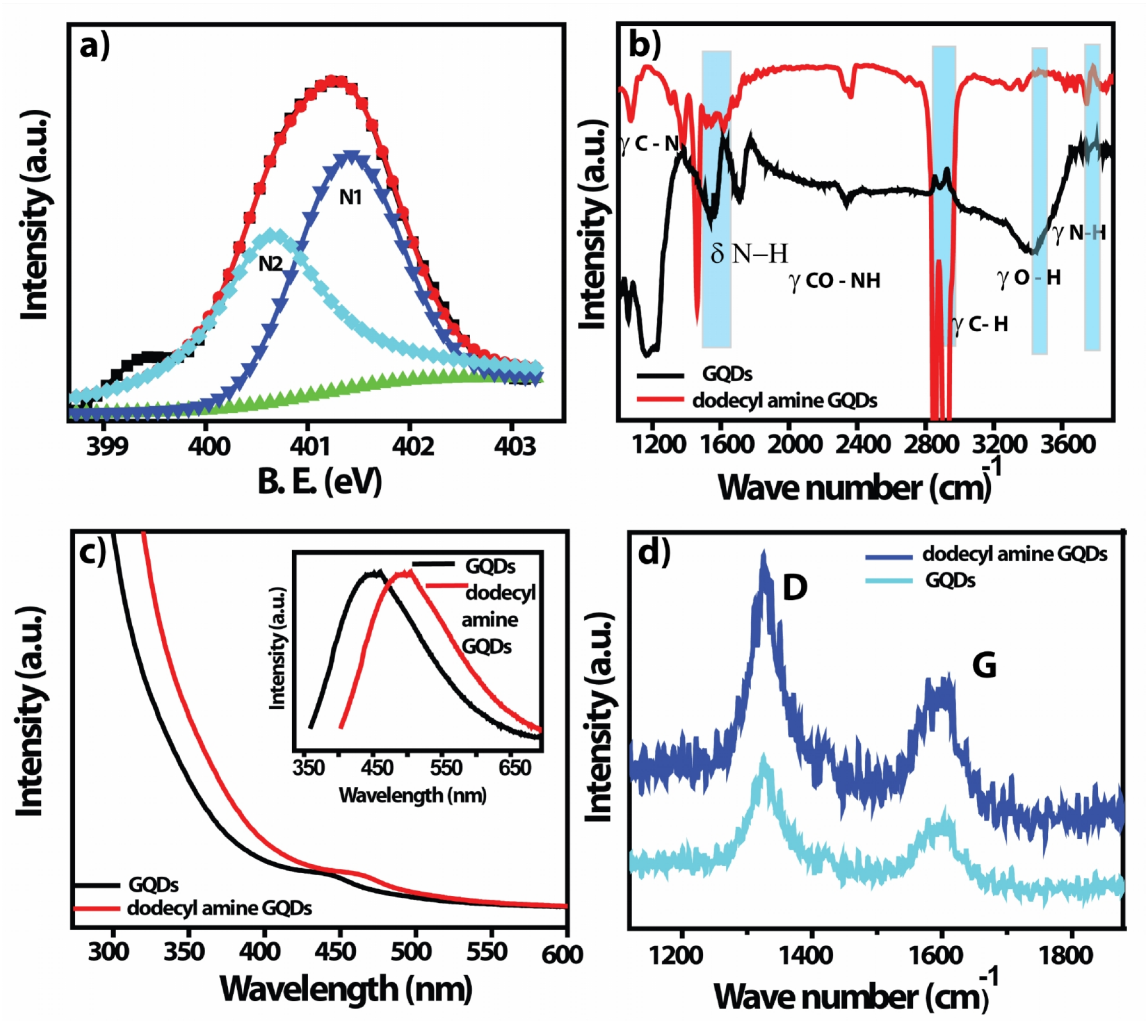

Figure 4.2. a) N 1s spectra of dodecyl amine capped GQDs displaying peak at 400.5 eV (N_2) confirming the presence of free -NH_2 and another peak at 401.9 eV (N_1) corresponding to the amide group. b) Comparative FT-IR spectra for GQDs before and after dodecyl amine functionalization. c) A comparison of the UV- Vis absorption spectra for GQDs and dodecyl amine capped GQDs showing red shift in the absorption maxima. (Inset) Photoluminescence spectra for GQDs and dodecyl amine capped GQDs showing red shift in the absorption maxima. d) Raman spectra of GQDs both before and after dodecyl amine functionalization.

As confirmed by XPS, dodecylamine functionalized GQDs revealed the presence of N 1s peak corresponding to the amide formation and also the presence of free -NH_2 at 400.5 eV. Samples for FTIR measurements were prepared by grinding GQDs with potassium bromide (~0.03 wt %.) GQDs show a broad peak at ~3450 cm^{-1}, which refers to the O-H stretch of the hydroxyl group (Figure 4.2 b). A small peak at 1708 cm^{-1} is associated with the stretching mode of carboxylic groups as observed for GQDs, carboxylic groups being formed due to the oxidation of few carbon atoms on the surface of the GQDs. New peaks appear after dodecyl amine treatment at 1123, 3500-3700 cm^{-1} respectively, and can be assigned to C-N in-plane, and N-H in-plane stretching of the amide groups.[13] Characteristic amide–carbonyl (-NH-CO) stretching vibration was observed at 1624 cm^{-1},which implies the formation of amide groups through specific interactions with -COOH.[14] The peak at 1448 cm^{-1} is attributed to the overlapping of a signal from the N-H bending mode of vibrations.

There is no clear peak in the UV-Vis absorption spectrum of GQDs but for an extended absorption edge. A clear red shift of the absorption band with the dodecyl amine functionalization was also observed in the UV-visible absorption spectra of dodecy amine-GQDs. For GQDs, the optical properties are known to be dictated by a combination of factors, i.e., size, shape, and surface functionality of GQDs. Because the dodecyl amine GQDs prepared at 110° C have almost the same shape and size, the up-converted photoluminescence could be originated only from the functionalized amine groups. Raman spectrum of dodecyl amine capped GQDs showed almost the same I_D/I_G ratio compared to that of bare GQDs. The Raman spectrum was analyzed by performing a multi-peak fit using *pseudo*-Voigt functions. Using the empirical Tuinstra–Koenig relationship[15] based on the Raman D/G peak-area ratio, the sp^2 clusters in dodecyl amine capped GQDs were estimated to have a mean size of ~3 nm.

The discreteness of the electron charge manifests itself in the conductance as a result of the Coulomb repulsion of individual electrons. If the capacitance is few attofarad (10^{-18} F) the charging energy turns out to be 100-150 meV, while thermal energy is only ~ 26 meV. Consequently, in presence of an external field, the system shows steps in the I-V characteristics due to this capacitive nature, popularly known as coulomb blockade or single electron transfer.[16] Most of the reports have discussed the synthesis of smaller metal particles and their electrochemical properties, suggesting a tiny-capacitor model for metal nano-clusters that shows multiple peaks in voltammetric experiments, corresponding to QDL charging (single-electron-

transfer phenomenon in this size regime). More accurate STM studies under high vacuum at 83 K reveal a reversible *"Coulomb blockade (CB)"* phenomenon, with multiple, equidistant charging steps with different bias.[4c] However, no report is available on single electron behavior either in solution phase or in solid-state for GQDs (Graphene Quantum Dots), despite its significance for applications like Field effect transistors. In this chapter we report a clear demonstration of discrete single-electron-transfer behavior of GQDs in the 2.2 ± 0.3, 2.6 ± 0.2 and 3 ± 0.3 nm size regime, where confinement of charge carriers creates an energy gap,[17] using independent experimental techniques like cyclic voltammetry and differential pulse voltammetry. A series of evenly spaced redox peaks has been observed at 273 K temperature which corresponds to the limiting currents controlled by the diffusion of smaller particles towards the electrode surface, thus also facilitating the adsorption of GQDs.

4.3.2 TEM and AFM Characterization:

In Figure 4.3 (a, c, e) fractionation of as-prepared GQDs after functionalization with dodecyl amine has produced a larger population of mono-disperse GQDs as is evident in the TEM images displaying average sizes (3 ± 0.3, 2.6 ± 0.2 and 2.2 ± 0.3 nm) respectively. Accurate information about the change in both height and lateral dimensions, is obtained from atomic force microscopy (AFM) measurements as shown in figure 4.3 (b, d, f) revealing a size distribution between 2.2 - 3 nm. However, the topographic height is between 1 - 2 nm indicating the presence of 2–3 layers of graphene in each individual GQD, suggesting high quality, also proved from the conductivity data. The fact that these GQDs are much smaller than those prepared by other methods along with the strong evidence for the existence of 2-3 layers presumably indicates the possible origin of this single-electron transfer behavior.[4c]

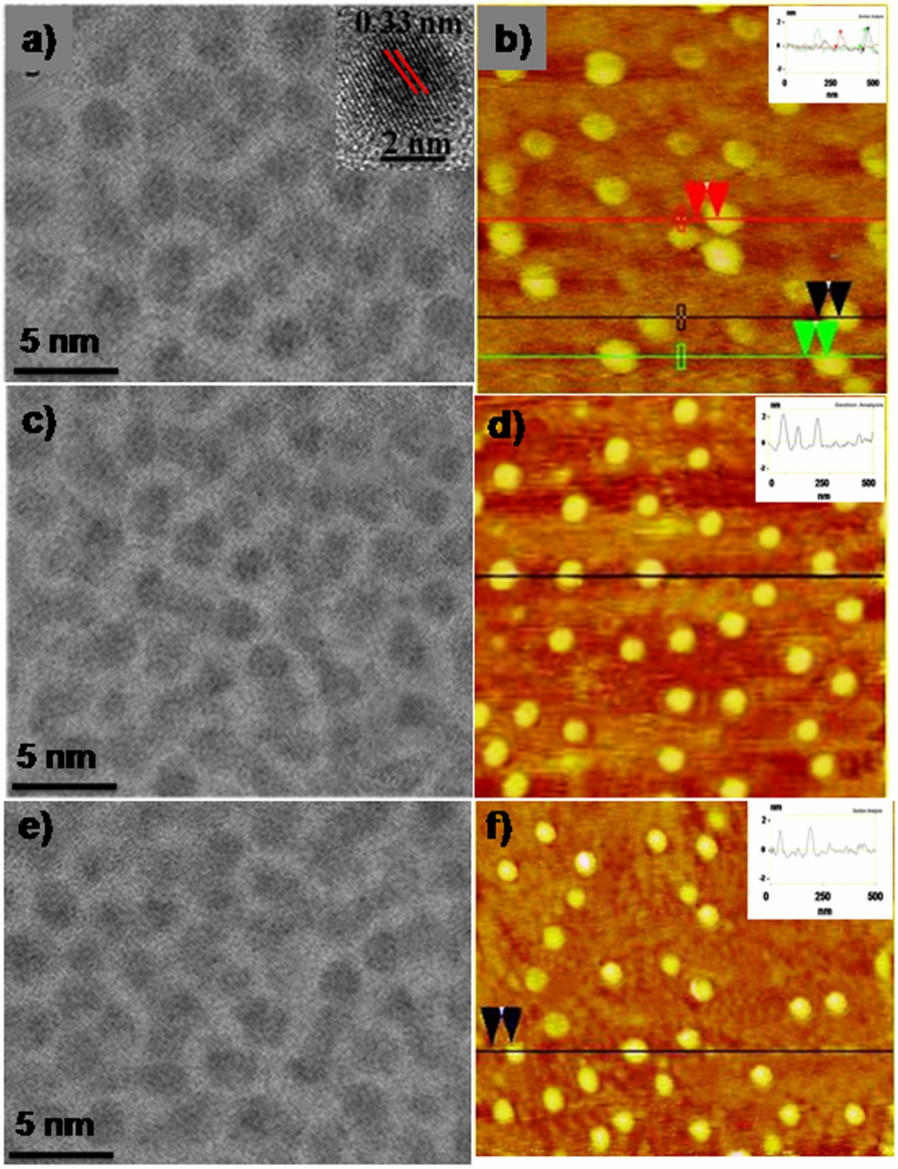

Figure 4.3. Typical TEM images of dodecyl amine capped GQDs; size and dispersion are a) 3 ± 0.3 c) 2.6 ± 0.2 (e) 2.2 ± 0.3 nm. (b, d and f) display AFM images of monodispersed dodecyl amine capped GQDs with their corresponding height profiles displaying the presence of 2-3 layers of graphene in each GQDs.

4.3.3 Differential Pulse Voltammetry:

A typical DPV response for the prepared GQDs revealing evenly spaced (ΔE) peaks, characteristic of charge injection to the core is shown in Figure 4.4. After a critical analysis of the peak spacings of DPV data it is clear that as GQDs becomes smaller, the average distance (ΔE) between peaks gradually increases, suggesting that ΔE is inversely proportional to the

'geometrical capacitance. In order to eliminate measurement artifacts, results of a blank experiment conducted without GQDs (only Pt ultra microelectrode with all other identical parameters) is also indicated in the same plot for comparison as artifacts cannot provide these single electron transfer peaks with uniform width, whereas the peak potential varies with charge number consistently as per the Nernst equation.[2a] The peak potentials can be taken as the formal redox potential E°′ for the redox couple of each GQDs with z/z±1 charge number since GQDs were presumed to be formed by the reduction at -1 V, which helps to assign a charge of z = -1. Accordingly, the first two peaks (oxidation and reduction peaks adjacent to E_{pzc}) could correspond to 0/-1 and -1/-2 redox couple, respectively. The charge steps are marked in the same graph for comparison with respect to that of a Pt quasi-reference electrode assuming the potential of zero charge as the minima of the blank electrode under similar conditions.[1, 18] Interestingly, the full width at half-maximum (FWHM) of each peak is found to be of ~90 mV, which is comparable to the values in earlier reports for the smaller-sized Au Q-dots namely, 82 mV at 273 K. This small variation in FWHM might be attributed to several complex interactions of these charged GQDs in the vicinity of electrode surface. For example, these GQDs can be viewed as an assembly of mixed valent redox centers at the electrode solution interfaces during the electrochemical process. There are also possibilities for the reorganization of charges among GQDs by electron self-exchange or disproportionation. This FWHM for various sized GQDs is identical to the expected value in case of single electron transfer in semiconductors Q-dots.[4c] These regularly spaced peaks are sharp, reversible, reproducible and comparable to similar single electron transfer behaviour of Si,[4c] CdTe Q-dots.[4e] This is perhaps the first report of such a remarkable resolution of individual redox peaks for GQDs at 273 K temperature which undoubtedly confirms that GQDs are indeed multivalent species.

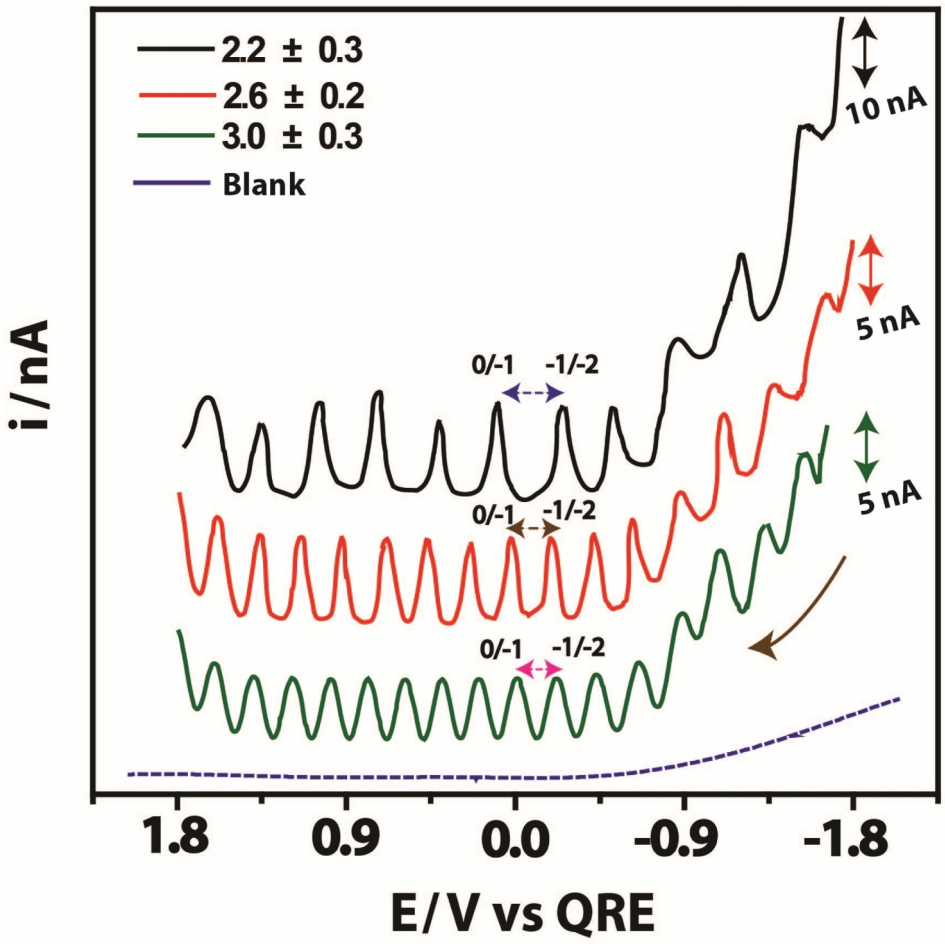

Figure 4.4. Differential pulse voltammetric (DPV) responses of GQDs in 0.5 mM TBAHFP as supporting electrolyte in CH_2Cl_2 for particle sizes of 3 ± 0.3, 2.6 ± 0.2, 2.2 ± 0.3 nm, using 20 mV pulse amplitude on a Pt ultra-microelectrode (20 μm) at a typical scan rate of 25 mV/s at 273 K, response obtained for a blank electrode (without GQDs) under similar conditions is also shown for comparison.

4.3.4 Cyclic Voltammetry and Z plots:

Figure 4.5a represents the "Z plot" for GQDs corresponding to the DPV response as shown in Figure 4.2, where a linear ($R^2 > 0.99$) behavior can be seen as expected for the ideal QDL behavior.[1, 18-19] The C_{GQDs}, and corresponding charging energy values calculated from the slope of the "Z plot" are given in **Table 4.1.** The variation of peak spacing (ΔE) with charge number z/z-1 reveals that the voltage spacing is extremely regular for GQDs at positive potential despite a minor irregularity at negative potential end; possibly due to impurities or solvent decomposition.[21] Also the gap between the onset of oxidation and reduction, i.e. HOMO-LUMO gap estimated for these GQDs as found from DPV plot inversely varies with size, which

is in good agreement with similar trends in case of GQDs and graphene nanoribbons[17, 20] notwithstanding the difference in morphology.

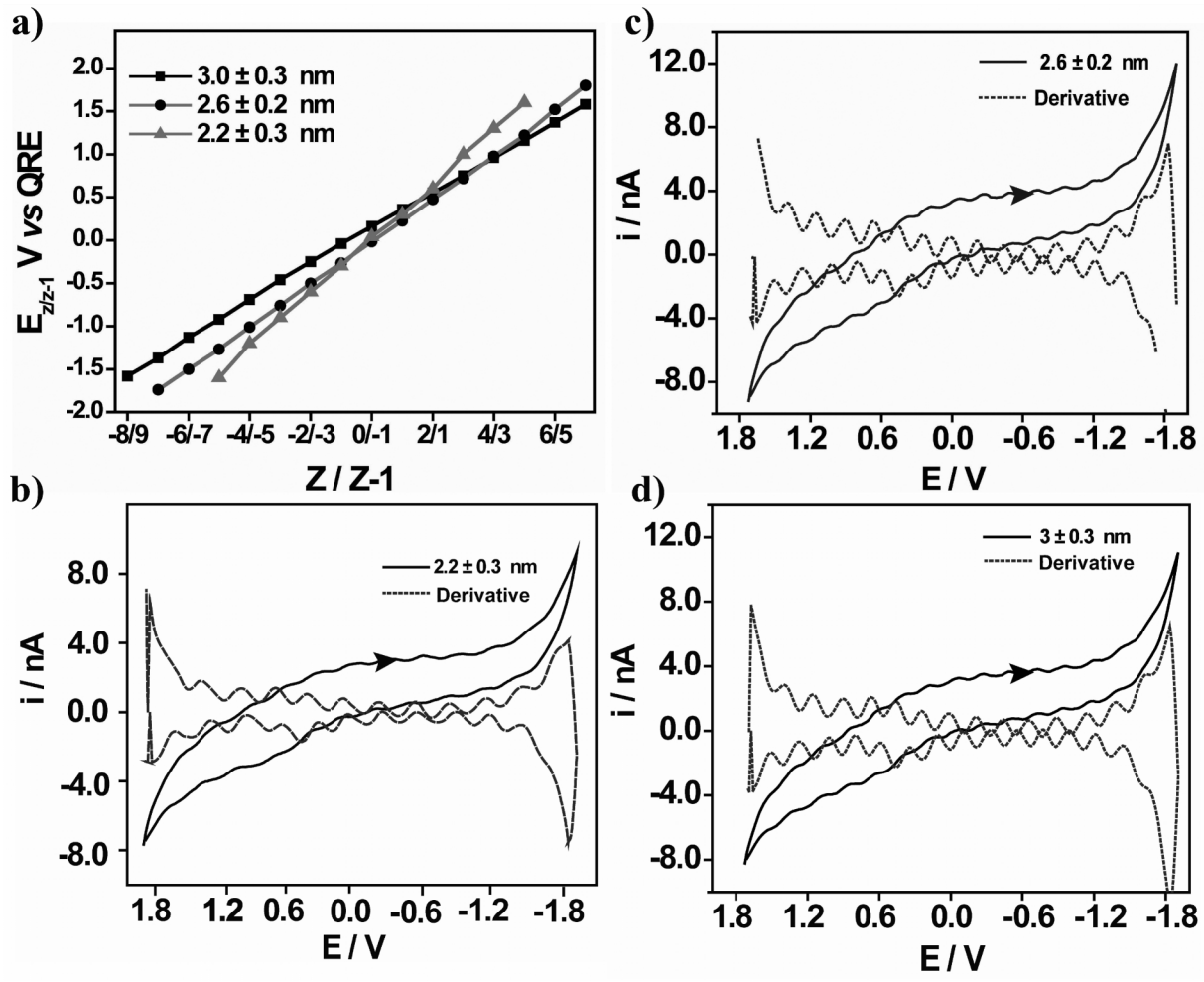

Figure 4.5: a) Z plot of E^0 vs redox couple charge (z/z±1) for GQDs of different sizes, where, linear (R^2 > 0.99) behavior can be seen as expected for the ideal QDL behavior using the Nernst equation. Superimposed cyclic voltammetric response of GQDs at (b) 2.2 ± 0.3 c) 2.6 ± 0.2 d) 3 ± 0.3 nm at 100 mV/s in DCM with 0.5 mM TBAHFP on a Pt ultra microelectrode, with its derivative response showing a series of QDL charging steps.

Table 4.1. The relative variation in the capacitance, HOMO-LUMO gap and charging energy for differently sized GQDs.

GQDs Size (nm)	Capacitance (aF)	HOMO-LUMO Gap (eV)	Charging Energy (meV)
2.2 ± 0.3	0.50	0.36	151
2.6 ± 0.2	0.63	0.25	125
3.0 ± 0.3	0.76	0.21	104

The quantized double layer (QDL) charging of GQDs core occurs because the effective capacitance (C_{GQDS}) with core diameter < 3 nm are so small (sub attofarad) that single electron change to their core charges occurs at large voltage intervals. These capacitance values are comparable to that of semiconducting QDs having sizes 4-5 nm and also charging energy E_c of the GQDs is calculated using equation 1, Which is in excellent agreement with criteria for the single-electron charging $E_c \geq kT$ (Where k is Boltzmann constant) at 273 K.[1, 18] Otherwise, thermally activated electrons will overcome the coulomb barrier and escape from the GQDs.

$$E_c = \frac{e^2}{2C_{GQDs}} \quad \text{.....} \quad 1$$

4.3.5 DPV of GQDs (2.2 ± 0.3) nm using 40 mV pulse amplitude

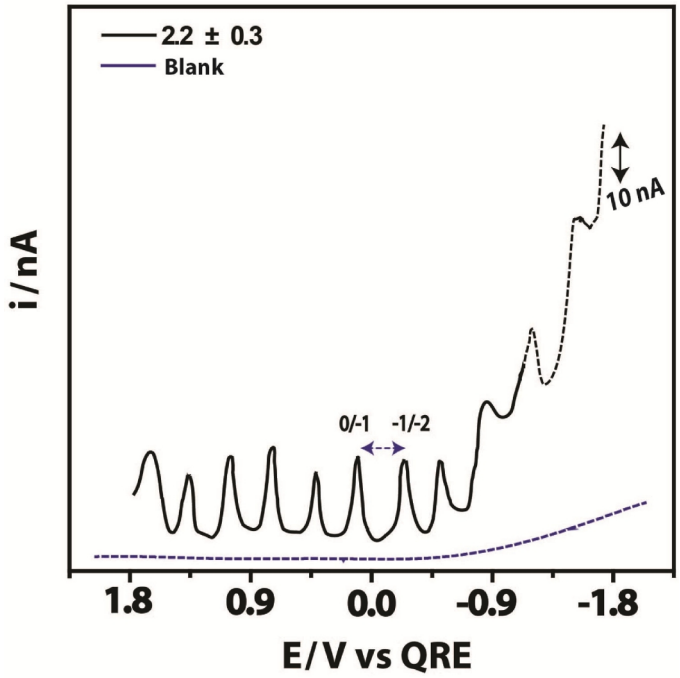

Figure 4.5: Differential pulse voltammetric (DPV) responses of GQDs in 0.5 mM TBAHFP as supporting electrolyte in CH_2Cl_2 for particle sizes of 2.2 ± 0.3 nm, using 40 mV pulse amplitude on a Pt ultra-microelectrode (20 μm) at a typical scan rate of 25 mV/s at 273 K. The response obtained for GQDs > (5 nm) in dotted curve proves that absense of QDL features.

In comparison to the DPV analysis, CV resolves this remarkably high population of charge steps, where the derivative response is particularly comparable with that of DPV results. As CV and DPV show consecutive n electrochemical reactions for GQDs, each by transfer of a new electron giving a new ionic compound. Indeed the type of doping either p-doping (extraction of electrons from the GQD) or n-doping (injection of electrons to the GQD) is implicit in both the DPV and CV results where the potential of zero charge separates these regions. Similar, processes are followed by fullerenes, carbon nanotubes or conducting polymers and estimation of HOMO-LUMO gap is based on this concept. Figure 4.4 (b, c, d) shows the cyclic voltammetric response of GQDs of different sizes at 100 mV/s scan rate superimposed with its derivative response. Since GQDs act as tiny capacitors (with charge storage capability of the order of atto-farads i.e. 10^{-18} F) the peak-to-peak spacing of the derivate of CV shows close similarity, with the corresponding peaks seen in DPV. These ΔE values are also invariant with pulse width (40 mV) as shown in figure 4.5 Similar DPV results for GQDs of larger size (>5 nm) interestingly do not show any single electron transfer behaviour at 273 K since equation 1 cannot be obeyed presumably due to higher capacitance values . Thus a combined analysis of the experimental data from DPV, CV, AFM and TEM clearly reveals that, dodecyl amine capped GQDs act as multivalent redox species, revealing evenly spaced (ΔE) peaks due to charge injection to the semiconducting core. The origin of a small irregularity in peak spacing at negative potential needs to be investigated further by considering other possible sources like solvent decomposition or impurities, etc.

4.3.6 Scanning Tunneling Microscopy (STM) images:

A typical STM image of GQDs on HOPG surface, where we can see the monodisperse GQDs located on HOPG substrate. The particle size is estimated to be ≈ 2.5 ± 0.3 c) 3 ± 0.2 d) 4.5 ± 0.3 nm from STM image as shown in Figure 4.6 shows, which are nearly comparable to the size obtained from the TEM and AFM analysis (Figure 4.3).[21]

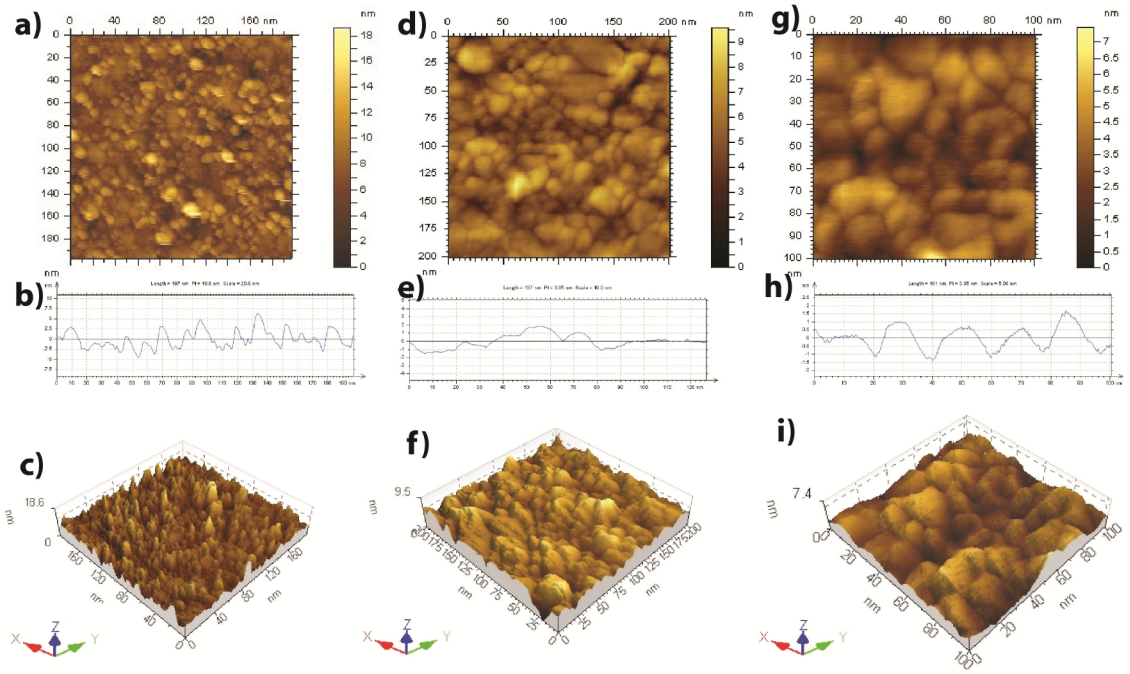

Figure 4.6 Scanning Tunneling microscopy (STM) images of monodispersed dodecyl amine capped GQDs with their 3 D view and corresponding height profiles displaying the presence of 2-3 layers of graphene in each GQDs.

4.3.7 Electrochemical study of different size N-GQDs:

A preliminary screening of the electrocatalytic activity of the N-GQDs towards ORR in alkaline media was carried out by CV and LSV study. The mass loading maintained to 20 µg on a 3 mm diameter glassy carbon working electrode. Figure 4.6 shows the CV of N-GQDs at different scan rate in nitrogen saturated 0.1 M KOH electrolyte; where Figure 4.6a is for N-GQDs-1 (size = 7.2 ± 0.3 nm), Figure 4.6b is of N-GQDs-2 (size = 4.7 ± 0.3 nm) and Figure 4.7 c is of N-GQDs-3 (size = 2.5 ± 0.3 nm). In all the cases it has been observed that, with increasing scan rate the current is increased, indicating the domination of faradaic reaction.

4.3.8 Cyclic voltammograms for different sized N-GQDs

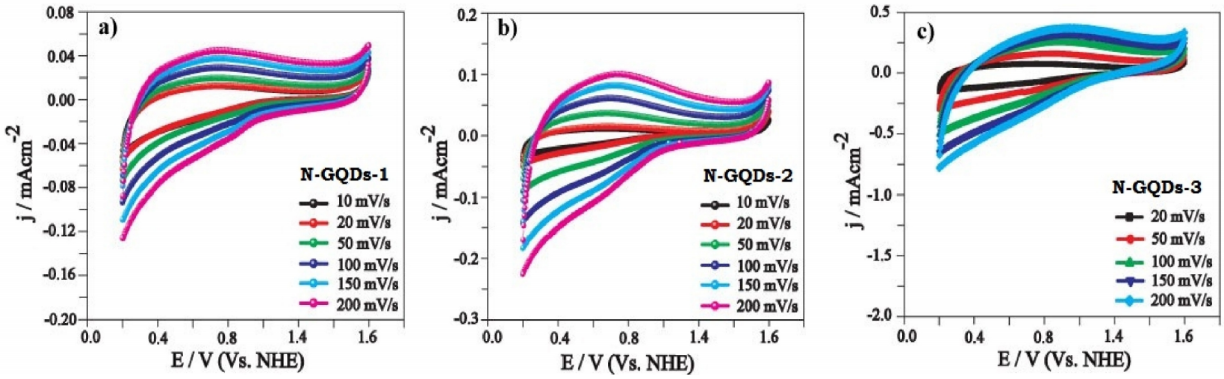

Figure 4.7: Cyclic voltammograms of electrochemically synthesized N-GQDs at different scan rate in nitrogen saturated 0.1 M KOH electrolyte; a) N-GQDs-1 (size = 7.2 ± 0.3 nm), b) N-GQDs-2 (size = 4.7 ± 0.3 nm) and c) N-GQDs-3 (size = 2.5 ± 0.3 nm) respectively.

Moreover, to investigate its activity towards ORR, we purged oxygen in a 0.1 M KOH and recorded the CV at scan rate of 50 mV/s. Accordingly, Fig. 4.8 shows superimposed CV curves of N-GQDs in an N_2 saturated aqueous 0.1 M KOH solution, exhibiting a pseudo-capacitive behavior. Moreover, a well-defined reduction peak occurs at around 0.7 V (vs. NHE) more distinctly in the O_2-saturated 0.1 M KOH aqueous solution, indicating that O_2 is more efficiently reduced on the electrode coated with N-GQDs. Furthermore, the size dependent CV shows an improved pseudo-capacitance as well as a more kinetically facile (higher cathodic peak current density) oxygen reduction behavior with decreasing the size of N-GQDs, in N_2- and O_2-saturated electrolytes, respectively (Figure 4.7). The cathodic peak current density scales in an order of diminishing size of N-GQDs-1 (-0.4 mA/cm^2) < N-GQDs-2 (-0.43 mA/cm^2) < N-GQDs-3 (-0.74 mA/cm^2) providing important evidence for size dependant electrochemical reactivity.[7a, 7b]

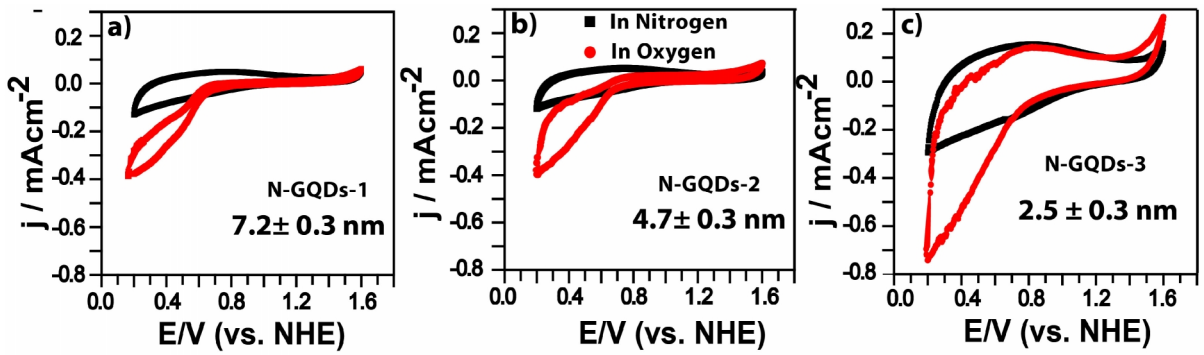

Figure 4.8: Comparative cyclic voltammograms of electrochemically synthesized N-GQDs in an nitrogen and oxygen saturated 0.1 M KOH, at a scan rate of 50 mV/s. N-GQDs show ORR activity in an O_2

saturated 0.1 M KOH solution in the potential range of 0.7 to 0.2 V (inidcated by red color). In contrast, in nitrogen saturated 0.1 M KOH electrolyte, the same features are not observed as shown in the above figures (inidcated by black color).

As mentioned above, the N-GQDs show a size dependent ORR activity and further to understand actual kinetics of N-GQDs for ORR, linear sweep voltammetry (LSV) experiments were carried out at a scan rate of 10 mV/s with O_2-saturated electrolyte. The LSV gives an idea about actual kinetic parameters of ORR in a quantitative manner by measuring current densities at various rotation speeds of 400, 900, 1200, 1600 and 2500 rpm (Figure 4.9). During the rotation of the working electrode (400 to 2500 rpm), the potential regions under kinetic and oxygen mass transport limiting control are noticeably observed and the current density increases with increasing the rotation rate, perhaps due to enhanced diffusion[13] LSV results indeed confirm that N-GQDs have size-dependent electrocatalytic activity for ORR, often comparable to that of Pt/C – a benchmark electrocatalyst used for fabricating fuel cells. Figure 4.11a; shows a comparison of the LSV curves obtained for N-GQDs 1-3 and for commercial 20 wt% Pt/C at 1600 rpm under similar conditions. As part to understand the kinetics, the Koutecky–Levich (K-L) plot has been plotted at different potential range, which is a secondary plot of LSV (Figure 4.10).

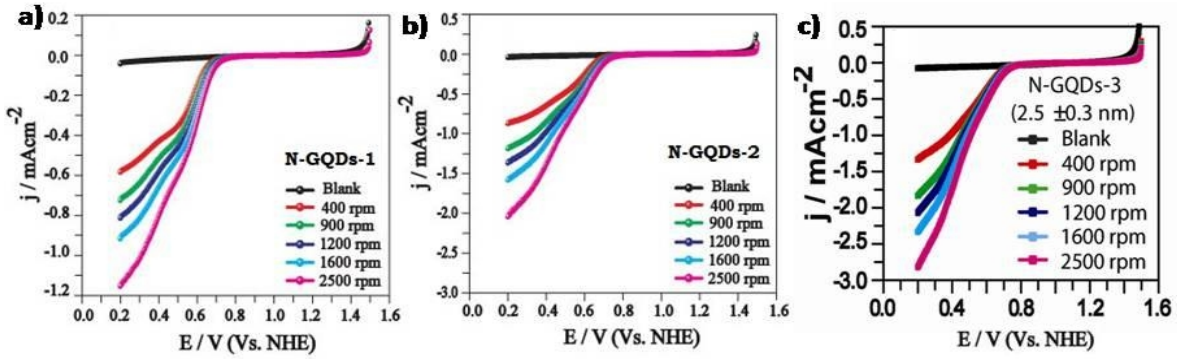

Figure 4.9: LSV study of a) N-GQDs-1 (size = 7.2 ± 0.3 nm), b) N-GQDs-2 (size = 4.7 ± 0.3 nm), and c) N-GQDs (size = 2.5 ± 0.3 nm) in an oxygen saturated 0.1 M KOH, with different rotation speed of working electrode at a scan rate of 10 mV/s.[9b, 22]

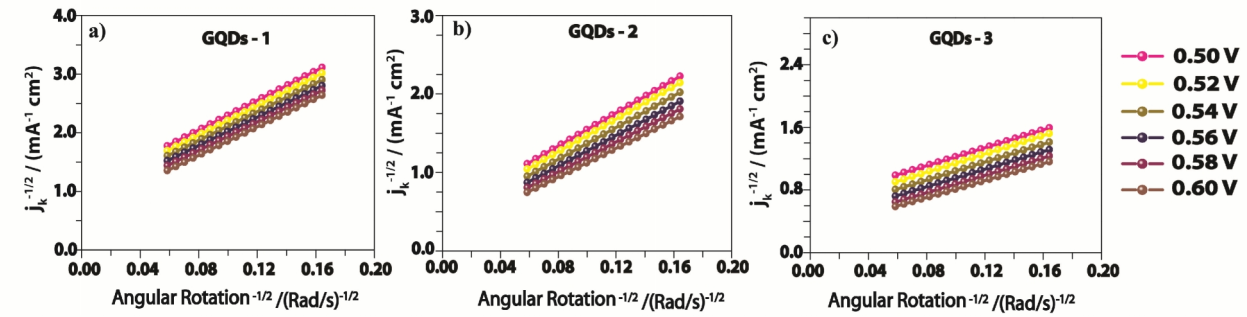

Figure 4.10: Kotechky-Levich (K-L) plots of a) N-GQDs-1 (size = 7.2 ± 0.3 nm), b) N-GQDs-2 (size = 4.7 ± 0.3 nm) and c) N-GQDs-3 (size= 2.5 ± 0.3 nm), at different potential.

The Koutecky–Levich (K-L) plot (Figure 4.9) which is plot of j_k^{-1} vs. $\omega^{-1/2}$ has been utilized to calculate the number of electron transfer and actual kinetics of ORR by using following equations:[9b, 23]

$$\frac{1}{j} = \frac{1}{j_k} + \frac{1}{j_L}$$

$$\frac{1}{j} = \frac{1}{B\omega^{\frac{1}{2}}} + \frac{1}{j_k}$$

$$B = 0.62\, nFAC_o^{*}\, D_o^{2/3}\, \nu^{-1/6}$$

$$j_k = nFAkC_o^{*}$$

Where, j is the measured current density, j_L is the diffusion-limiting current density and j_k is the kinetic current density, F is the Faraday constant (96486.4 C mol^{-1}), Do is the diffusion coefficient of oxygen (1.9 x10^{-5} cm^2 s^{-1}), ν is the kinematic viscosity (0.01 cm^2 s^{-1}), Co* is the bulk concentration of oxygen, and ω is the angular rotation ($\omega = 2\pi f$, f is rotation speed), n is number of electron transferred during ORR, and k is the electron transfer rate constant.

The best performed N-GQDs and commercial 20wt% Pt/C, comparative data has been reported in a Figure 4.11. Interestingly, N-GQDs-3 (onset potential = 0.75 V) show a 30 mV higher (more positive) onset potential shift compared to that of N-GQDs-2 (onset potential = 0.72 V) and 70 mV than that of N-GQDs-1 (onset potential = 0.68 V). These observations clearly indicate that smaller N-GQDs have higher positive onset potential compared to that of larger size of N-GQDs (Figure 4.11a), attributed to the confinement effect and more exposed N-sites due to smaller size as well as higher surface to volume ratio. However, all these N-GQDs have less positive onset

potential than that for Pt/C (onset potential = 0.92 V). The more negative onset potential and lower cathodic current density of N-GQDs as compared to that of Pt/C, at the same mass loading, indicates that N-GQDs have a greater overpotential and its electrocatalytic activities are not as good as that of commercial Pt/C.

4.3.9 Comparative LSV and K-L plots of N-GQDs

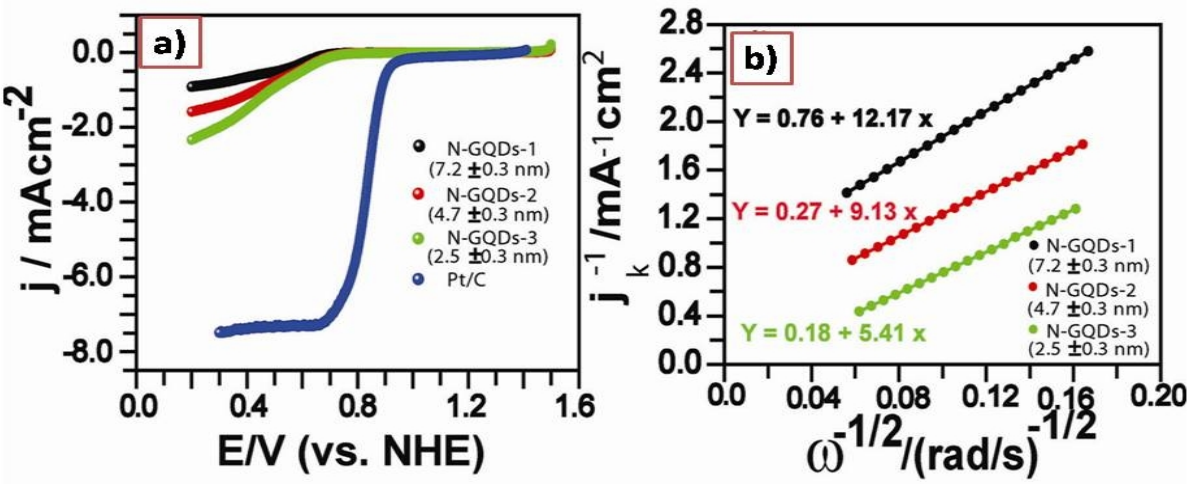

Figure 4.11: a) Comparative LSV of N-GQDs-1, -2 and -3 with that of commercially available Pt/C (20 wt%), performed at 1600 rpm at scan rate of 10 mV/s in O_2-saturated 0.1 M KOH electrolyte, b) comparative Koutecky-Levich (K-L) plot of N-GQDs-1, -2 and -3 obtained at 0.6 V from the corresponding LSV data.

Mechanistic studies show that the ORR catalysed by the N-GQDs can occur via a four-electron reduction pathway to produce water directly rather than the two-electron pathway with peroxide as an intermediate.[17] From the slope of the K-L plots (Fig. 4.11b) obtained from the LSV data, the number of electrons transferred per oxygen molecule is calculated to be about 3.7, consistent with a four-electron process. Therefore, similar catalytic mechanisms may be valid to the N-GQDs compare to other N-doped carbon system.[9b, 23] The size-dependent catalytic activity of the N-GQDs for ORR has important implications in understanding and improving the catalytic activities of N-doped carbon materials especially for fuel cell/water electrolyzer applications. However, the yield of N-GQDs is limited due to smaller surface area of working electrode and bulk production is quite possible for fuel cell application using large area working electrode.

4.4 Conclusions:

This chapter discusses two important applications of GQDs, i.e. single electron transistor, and electrocatalysis. we proved that GQDs of tunable sizes 2.2 ± 0.3, 2.6 ± 0.2 and 3 ± 0.3 nm can act as multivalent redox species using various electrochemical techniques such as CV, DPV measurements, presenting exciting opportunities for a variety of applications including single electron transistors, molecular switches, resonant tunneling diodes presumably due to atto-farad charge storage and number of electron transfer events. It is also useful for bio-mimetic applications like artificial muscles, batteries, smart membranes, and smart drug delivery devices. The capacitance values calculated from the experimental data (in the range of atto-farads) are in good agreement with single electron transfer phenomenon at 273 K temperature. While TEM images display both the tunable size and mono-dispersed nature of these GQDs, whereas AFM measurements offer indirect evidence for the presence of 2-3 graphene like layers for the smallest GQDs. The physical and electrochemical properties of these ultra small GQDs could provide interesting opportunities for the use of these size tunable narrow band gap semiconductors as future materials for nanoelectronic devices. Also N-GQDs display many unusual size dependant optoelectronic and electrocatalytic properties. The presence of nitrogen dopants in the carbon framework not only causes faster unzipping of N-MWCNTs but provides more low activation energy site for enhancing the electrocatalytic activity for oxygen reduction reaction. These results on the size dependent electrocatalytic activity of N-GQDs for ORR as illustrated by the smaller sized N-GQDs (2.5 ±0.3 nm) may be a promising alternative to Pt based electrocatalysts for fuel cell applications.

4.5 References

[1] R. W. Murray, *Chem. Rev.* **2008**, *108*, 2688.

[2] a)R. S. Ingram, M. J. Hostetler, R. W. Murray, T. G. Schaaff, J. Khoury, R. L.Whetten, T. P. Bigioni, D. K. Guthrie, P. N. First, *J. Am. Chem. Soc.* **1997**, *119*, 9279; b)S. Chen, R. S. Ingram, M. J. Hostetler, J. J Pietron, R. W Murray, T. G. Schaaff, J. T Khoury, M. M. Alvarez, R. L. Whetten, *Science* **1998**, *280*, 2098; c)A. C. Templeton, W. P. Wuelfing, R. W. Murray, *Acc. Chem. Res.* **2000**, *33*, 27; d)S. J. Chen, *Electroanal. Chem.* **2004**, *574*, 153.

[3] N. K. Chaki, P. Singh, C. V. Dharmdhikari, V. K. Pillai, *Langmuir* **2004**, *20*, 10208.

[4] a)P. Hoyer, H. Weller, , *Chem. Phys. Lett.* **1994**, *221*, 379; b)S. Chen, L. A. Truax, J. M. Sommers, *Chem. Mater.* **2000**, *12*, 3864; c)Z. Ding, B. M.Quinn, S. K. Haram, L. E. Pell, B. A. Korgel, A. J. Bard, *Science* **2002**, *296*, 1293; d)S. K. Haram, B. M. Quinn, A. J. Bard, *J. Am. Chem. Soc.* **2001**, *123*, 8860; e)Y. Bae, Y.Myung, A. J. Bard, *Nano. Lett.* **2004**, *4*, 1153.

[5] S. K. Haram, B. M. Quinn, A. J. Bard, *J. Am. Chem. Soc.* **2001**, *123*, 8860.

[6] L. M. Melanie, M. F. Florian, F. Daniel, J. H. Eric, K. Christian, L. Uli, A. O. Geoffrey, *Nano Lett.,* **2012**, *12*, 337.

[7] a)W. Haibo, M. Thandavarayan, W. Xin, *ACS Catalysis* **2012**, *2*; b)Y. Li, Y. Zhao, H. Cheng, Y. Hu, G. Shi, L. Dai, L. Qu, *Journal of the American Chemical Society* **2012**, *134*, 15; c)Y. Li, Y. Zhao, H. Cheng, Y. Hu, G. Shi, L. Dai, L. Qu, *J. Am. Chem. Soc.* **2011**, *134*, 15.

[8] a)S. Yu, W. Zheng, C. Wang, Q. Jiang, *ACS Nano* **2010**, *4*, 7619; b)C.-S. Rodolfo, M.-G. Aaron, V.-D. Sofia, T.-L. Ferdinando, L. E. Ana, P.-L. Nestor, M. Hiroyuki, H. Takuya, F. Kazunori, K. Yoong Ahm, E. Morinobu, T. Mauricio, *ACS Nano* **2013**, *7*; c)R. Cruz-Silva, A. Morelos-Gómez, S. Vega-Díaz, F. Tristán-López, A. Elias, N. Perea-López, H. Muramatsu, T. Hayashi, K. Fujisawa, Y. Kim, M. Endo, M. Terrones, *ACS Nano* **2013**, *7*, 2192.

[9] a)D. S. Yu, Q. Zhang, L. M. Dai, *J. Am. Chem. Soc.* **2010**, *132*, 15127; b)K. P. Gong, F. Du, Z. H. Xia, M. Durstock, L. M. Dai, *Science* **2009**, *323*, 760.

[10] a)S. Y. Wang, D. S. Yu, L. M. Dai, *J. Am. Chem. Soc.* **2011**, *133*, 5182; b)N. Soin, S. S. Roy, S. Roy, K. S. Hazra, D. S. Misra, T. H. Lim, C. J. Hetherington, J. A. McLaughlin, *J. Phys. Chem. C*

2011, *115*, 5366; c)Y. Li, Y. Hu, Y. Zhao, G. Q. Shi, L. E. Deng, Y. B. Hou, L. T. Qu, *Adv. Mater.* **2011**, *23*, 776; d)L. S. Li, X. Yan, *J. Phys. Chem. Lett.* **2010**, *1*, 2572.

[11] Y. F. Li, Z. Zhou, P. W. Shen, Z. F. Chen, *ACS Nano* **2009**, *3*, 1952.

[12] D. V. Kosynkin, A. L. Higginbotham, A. Sinitskii, J. R. Lomeda, A. Dimiev, B. K. Price, J. M. Tour, *Nature* **2009**, *458*, 872.

[13] Y.P. Sun, W. Huang, Y. Lin, K. Fu, A. Kitaygorodskiy, L. A. Riddle, Y. J. Yu, D. L. Carroll, *Chem. Mater.* **2001**, *13*, 2864.

[14] K. Fu, W. Huang, Y. Lin, L. A. Riddle, D. L. Carroll, Y. P. Sun, *Nano Lett.* **2001**, *1*, 439.

[15] a)L. Y. Jiao, L. Zhang, X. R. Wang, G. Diankov, H. J. Dai, *Nature* **2009** *458*, 877; b)M. A. Pimenta, G. Dresselhaus, M. S. Dresselhaus, L. G. Cancado, A. Jorio, R. Saito, *Phys. Chem. Chem. Phys.* **2007**, *9*, 1276; c)M. J. Matthews, M. A. Pimenta, G. Dresselhaus, M. S. Dresselhaus, M Endo, *Phys. Rev. B* **1999**, *59*, R6585.

[16] F. F. Fan, *Science* **1997**, *277*.

[17] a)A. K. Geim, K. S. Novoselov, , *Nat. Mater.* **2007**, *6*, 183; b)M.Y. Han, B.O. Zyilmaz, Y. Zhang, P. Kim, , *Phys. Rev. Lett.* **2007**, *98*, 206805; c)F. Sols, F. Guinea, A. H. C. Neto, *Phys. Rev. Lett.* **2007**, *99*, 166803; d)F. Miao, F. Miao, S. Wijeratne, Y. Zhang, U. C. Coskun, W. Bao, C. N. Lau, , *Science* **2007**, *317*, 1530; e)C. Stampfer, J. Guttinger, F. Molitor, D. Graf, T. Ihn, K. Ensslin, *Appl. Phys. Lett.* **2008**, *92*, 012102.

[18] D.T. Miles, R.S. Murray, *Anal. Chem.* **2003**, *75*, 1251.

[19] a)J. D. Holmes, K. J. Ziegler, R. C. Doty, L. E. Pell, K. P. Johnston, B. A. Korgel, *J. Am. Chem. Soc.* **2001**, *123*, 3743; b)S. J. Green, J. J. Stokes, M. J. Hostetler, J. Pietron, R. W. Murray, *J. Phys. Chem. B* **1997**, *101*, 2663.

[20] H. Raza, E. C. Kan, *Phys. Rev. B* **2008**, *77*, 245434.

[21] J. Lu, P. S. E. Yeo, C. K. Gan, P. Wu, K. P. Loh, *Nat. Nanotechnol.* **2011**, *6*, 247.

[22] a)Y. Wang, Y. Y. Shao, D. W. Matson, J. H. Li, Y. H. Lin, *ACS Nano* **2010**, *4*, 1790; b)X. R. Wang, X. L. Li, L. Zhang, Y. Yoon, P. K. Weber, H. L. Wang, J. Guo, H. J. Dai, *Science* **2009**, *324*, 768; c)R. L. Liu, D. Q. Wu, X. L. Feng, K. Müllen, *Angew. Chem., Int. Ed.* **2010**, *49*, 2565.

[23] L. T. Qu, Y. Liu, J. B. Baek, L. M. Dai, *ACS Nano* **2010**, *4*, 1321.

Applications of GNRs: Transparent Conducting Thin Films and Electrocatalysis

A unique hydrothermal approach for the synthesis of conductive and transparent GNRs with 80-100 % yield is discussed in this chapter using MWCNTs as starting materials. Also this chapter examines the critical role of many parameters and more specifically that of counter ions in deciding the quality and yield of GNRs in the unzipping process. More significantly, this simple, scalable and inexpensive method produces few milligrams of highly conductive and transparent (82 %), few layered GNRs in a single step. Many limitations of other exfoliation methods like partial unzipping or mixture of defective and damaged GNRs could be alleviated by using this remarkable hydrothermal method possibly with minimum contamination. Although the hydrothermal route for synthesis of GNRs described here can have several advantages like inexpensive scale-up possibility, one pot synthesis, high yield of transparent and conducting GNRs, some of the electronic characteristics might get affected due to the intercalation of cations, anions and solvent molecules. This chapter also demonstrates two important applications of GNRs; one using vacuum filtration method for preparation of flexible transparent conducting films (TCF) and other in electrocatalysis where Pt/GNRs act as promising candidates for fuel cell applications.

5.1 Introduction

Graphene is an one-atom thick two dimensional, planar sheet that offers a great promise due to its extraordinary combination of electrical, mechanical, and thermal properties, which enable them as attractive candidates for the fabrication of energy-related devices such as ultra-capacitors, Li-ion batteries and solar cells.[1] Graphene can also be manipulated to GNRs and graphene quantum dots (GQDs) which display peculiar electronic properties due to quantum confinement and edge effects, thus enabling a low energy band gap.[2] GNRs are further characterized by the presence of edges i.e. (armchair and zig-zag) and layer thickness, which play a crucial role in modulating their transport properties. Although GNRs have received an enormous amount of contemporary attention due to their tunable band gap and excellent mechanical strength facilitating many special properties still the bulk preparation of high quality GNRs with uniform layer thickness is a daunting challenge.[3]

To date, several methods have been reported with reasonable success for the synthesis of GNRs like Plasma etching, catalytic and chemical unzipping.[4] Since, CNTs can be considered as rolled-up graphene sheets from a topological perspective, it is possible to theoretically calculate the energetics of various sequential processes involved in the mechanism of the unzipping and in support of this many established procedures are available for the synthesis, placement and alignment control of nanotubes to effectively transform them into GNRs.[5] The conversion of MWCNTs to few layer GNRs of high aspect ratio has several intrinsic advantages for mechanical processing of nanocomposites especially for coating applications. For example, GNRs have been obtained through oxidative unzipping of multi-walled carbon nanotubes (MWCNTs) using potassium permanganate and sulfuric acid, but due to over oxidation of basal plane, the conductivity of resulting GNRs is poor even after annealing at higher temperature (900^0C).[6] Similarly, Cantu *et al.* reported specific intercalation of lithium into MWCNTs followed by their thermal expansion although this method fails with pristine nanotubes since a preliminary treatment of the MWCNTs with strong oxidant is an essential pre-requisite to induce defects which permit the intercalation of ammonia,solvated lithium, etc. facilitating partial unzipping.[5w]Another interesting strategy unveiled by Terrones *et al* includes longitudinal splitting of MWCNTs using transition metal clusters but gives only poor yield of GNRs consisting of 50-100 layers with significantly less conductivity.[4d] In contrast, GNRs with good

conductivity have been prepared by James *et al. via* an intercalation of potassium into MWCNTs but the resulting stacks of GNRs essentially require quenching with chlorosulfonic acid as a prerequisite for the exfoliation process.[7]Also Zhu etal reported low temprature synthesis of graphene using aromatic hydrocarbons.[8] Many other methods reported in the literature also provide poor yield and more significantly, the control of width and extent of exfoliation is not straightforward due to the involvement of high energy-intensive processes like laser, microwave, plasma, chemical vapour deposition (CVD), focussed ion beam (FIB) etc.[9] Hence, it is important to identify a scalable chemical method with high yield that can exfoliate and transform CNTs to conductive GNRs without exhibiting their notorious substrate-dependant properties.

Precious metals have been used extensively as effective cathode catalysts for oxygen reduction in proton exchange membrane fuel cells. Typically these materials are dispersed as nanosized particles on supporting substrates of high surface area to enhance accessibility and to reduce cost. In these, it has been found that the electronic interactions between the metal nanoparticles and the supporting substrates might also play a significant role in determining the electrocatalytic activity as a result of the manipulation of the electronic energy of the metal nanoparticles and hence the interactions with oxygen.[10] In both industrial and academic research, carbon-based materials are one of the most commonly used supporting substrates, such as carbon black, carbon nanotubes, and graphene sheets.[11] This is largely due to their low cost, high surface area, high conductivity, and high chemical inertness that may facilitate electron-transfer reactions at the electrode surface and hence improve catalyst stability and durability. Among these, while a relatively new addition, graphene has attracted particular research interest in fuel cell electrocatalysis.

In fact, a number of studies have been reported recently in the literature where graphene sheets are used as a support for the nanoparticle catalysts in oxygen reduction.[12] For instance, platinum nanoparticles (from 2.2 to 5.6 nm in dia.) supported on reduced graphene oxides (Pt/RGO) have been prepared by using perfluorosulfonic acid as the functionalization and anchoring reagent.[13] In these early studies, the graphene sheets are generally produced from bulk graphite by the Hummers method through chemical oxidation and exfoliation with strong acids and oxidizing reagents.[11b] The obtained graphene sheets mostly exhibit irregular shapes and a large size dispersion (ranging from nanoscale to micrometer-scale), and are prone to

folding and wrinkling because of the strong π–π interactions, thus compromising the even dispersion and ready accessibility of the metal nanoparticle catalysts.[14] To overcome such technical challenges, here we have used GNRs as support for decoration of Pt nanoparticles so that stacking might be minimized, in order to be useful for promoting oxygen diffusion through the GNRs sheets and enhancing the electrocatalytic performance of GNRs-supported Pt nanoparticles.

Transparent conducting films (TCFs) are optically transparent and electrically conductive often in the form of thin layers facilitating a multitude of applications. For example, TCFs for photovoltaic applications have been fabricated from both inorganic and organic materials. Inorganic films typically are made up of a layer of transparent conducting oxide (TCO),[15] generally in the form of indium tin oxide (ITO), fluorine doped tin oxide (FTO), and doped zinc oxide. Organic films are being developed using carbon nanotube networks and graphene, which can be fabricated to be highly transparent to infrared light, along with networks of polymers such as poly(3,4-ethylenedioxythiophene) and its derivatives. Transparent conductive oxides (TCO) are doped metal oxides used in optoelectronic devices such as flat panel displays and photovoltaics (including inorganic devices, organic devices, and dye-sensitized solar cell). On average, these applications use electrode materials that have greater than 80% transmittance of incident light as well as conductivities higher than 10^3 S/cm for efficient carrier transport. The transmittance of these films, just as in any transparent material, is limited by light scattering at defects and grain boundaries.

Transparent conductors are fragile and tend to break down due to fatigue. The most commonly used TCO are Indium-Tin-Oxide (ITO), FTO and $ZnAlO_2$ because of their good electrical properties and ease of fabrication. However, these thin films are usually fragile and such problems as lattice mismatch and stress-strain constraints and their high cost due limited abundance in nature, lead to restrictions in possible uses for TCFs. ITO has been shown to degrade with time when subject to mechanical stresses. Recent increases in cost are also forcing many to look to carbon nanotubes, graphene based flexible TCFs as a potential alternative.

In this chapter we describe a novel method of producing GNRs using a simple hydrothermal approach and specifically aimed at demonstrating their applications as electrocatalysts for oxygen reduction reaction in fuel cells and also an interesting application as

transparent conducting thin films. We have discussed about the electrocatalytic properties of different sized N-GQDs for ORR in Chapter 4, whereas this chapter in similar direction aims at the importance of GNRs as a support in enhancing the electrocatalytic performance ORR.

5.2 Experimental Section

A separate sample of pristine MWCNTs (150 mg) was dispersed in 150 ml deionized water and ultra-sonicated for 30 min after adding 0.5 moles/ l of supporting electrolyte (K_2SO_4, KNO_3, KOH and H_2SO_4) respectively in separate conical flasks. The suspension was transferred to a poly tetra fluroethylene lined autoclave (50 ml) and heated at 180 ^{0}C for 24, 36 and 48 h respectively as three different batches. After cooling to room temperature the resulting black suspension was used for further characterization after washing with dilute HCl and distilled water (till neutral pH) to remove excess potassium and other ions from GNRs.

5.2.1 Synthesis of Thin films:

The GNRs formed after (0.5 M K_2SO_4) treatment of MWCNTs was highly dispersible in DMF (1.2 mg/ml) and thin films were prepared on PTFE filter membranes (Rankem) through vacuum filtration to measure the optical transparency and sheet resistance of GNR. The PTFE membranes with GNRs films were subsequently pasted onto a PET substrate. The thickness of the film was carefully controlled by varying the volume of dispersed GNRs. For example, vacuum filtration of 5 and 10 ml of GNRs dispersion yielded ~20 and 40 nm graphene films on PET respectively. A Pressure of 0.5 Torque was applied for 20 minutes at 120 $^\circ$C using a Carver press to assure that the GNRs films firmly stuck to the PET substrate. This occurred primarily due to vander Waals interactions. The transparency of the graphene films was characterized using the UV/Vis spectroscopy (Perkin Elmer Lambda 20) and the electrical conductivity was measured using the four-point probe method. To reduce the contact resistance between the probes and the film surface, the samples were coated with Au at the positions of probe contact.

5.2.2 Synthesis of Pt/GNRs:

An aqueous solution of chloroplatinic acid was prepared by dissolving 0.1 gm in 25 ml DI water. 80 mg of GNRs was dispersed in 100 ml DI water in a 250 ml round bottom flask under constant stirring. The prepared chloroplatinic acid solution was added drop-wise to the above GNRs solution to obtain a 20 wt% of Pt in Pt/GNRs sample. Subsequently, 0.1 M (20 ml) sodium borohydride solution was added slowly to reduce chloroplatinic acid. The color of the solution turned black indicating the complete reduction of the Pt-precursor. The reaction mixture was maintained for 2 h at room temperature and then filtered through a PTFE (0.45 μm, 47 mm) membrane filter. Furthermore, it was washed several times with DI water and dried in an oven at 80 °C overnight.

All electrochemical studies were performed on an Autolab PGSTAT30 (Eco Chemie) instrument using a conventional three electrode test cell with a 5 mm diameter glassy carbon (GC) electrode coated with the sample as the working electrode (WE), Ag/AgCl as the reference electrode (RE) and Pt foil as the counter electrode (CE). The working electrode was prepared as follows. 10 ml of the slurry made by sonicating 5 mg of the catalyst in 1 ml isopropyl alcohol was drop-coated on a glassy carbon electrode. After this, 2 ml of 0.01 wt% Nafion diluted with ethanol was coated on the surface of the catalyst layer to yield a uniform thin film. This electrode was then dried in air and was used as the working electrode for all electrochemical studies. An aqueous solution of 0.5 M $HClO_4$ was used as the electrolyte for normal cyclic voltammetric (CV) and rotating disc electrode (RDE) studies. The cyclic Voltammograms were taken at a scan rate of 50, 100, 200 mV/s while Linear sweep voltammetry (LSV) experiments were carried out at a scan rate of 10 mV/s in an O_2-saturated electrolyte in order to estimate the actual kinetics of ORR in a quantitative manner by measuring currents at various rotation speeds of 400, 900, 1200, 1600 and 2500 rpm.

5.3 Results and Discussion

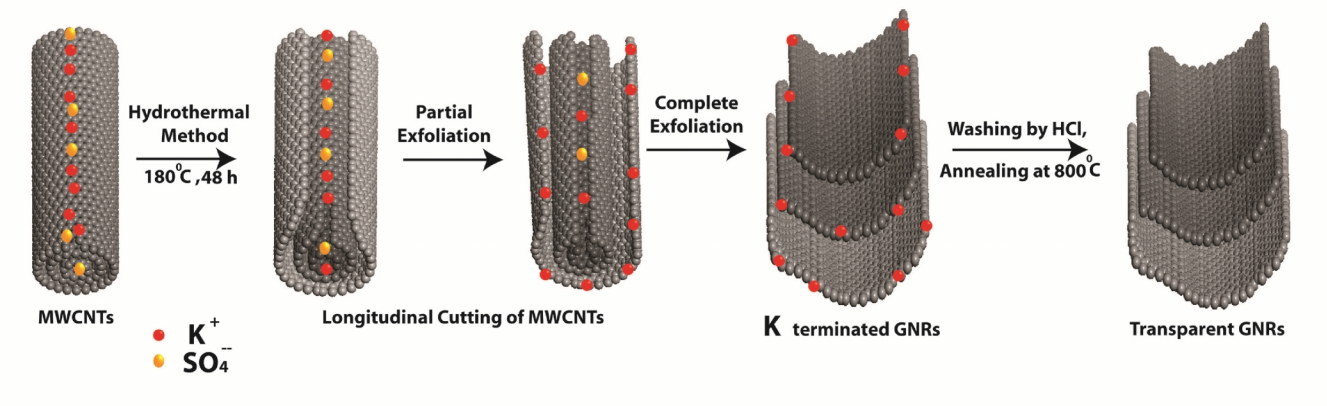

Figure 5.1. A schematic representation of the sequential, longitudinal unzipping of MWCNTs by potassium and sulfate (or nitrate) intercalation in the hydrothermal method to generate highly transparent GNRs.

Scheme 5.1 represents our hydrothermal process for the transformation of MWCNTs to GNRs. This process comprises of intercalation of potassium and creates the opening on the MWCNTs surface, perhaps at the tip of MWCNTs and this unzipping is further enhanced by the intercalation of solvated anions and results in the remarkable conversion of MWCNTs into GNRs.

5.3.1 Hydrothermal experiments using different cations, anions and temperature

Many earlier experimental reports have revealed that lithium ion alone is not capable of unzipping MWCNTs completely as only partial unzipping is possible for Li-ions in the presence of co-intercalent like ammonia [5w]. Similar ions like sodium also does not intercalate well in to graphite and also into MWCNTs.[7] In comparison, potassium intercalation in MWCNTs induces breakage at moderately elevated temperatures resulting in to partial unzipping. However, our experimental results demonstrate that sulfate and nitrate ions act as a co-intercalant along with potassium ions resulting into exfoliation of MWCNTs in an effective manner. More significantly, this type of unzipping is further assisted by in-situ produced H_2 in aqueous media,

which supports chemical reduction of oxygen functionalities during the transformation of unzipped MWCNTs to GNRs.

5.3.2 TEM Analysis

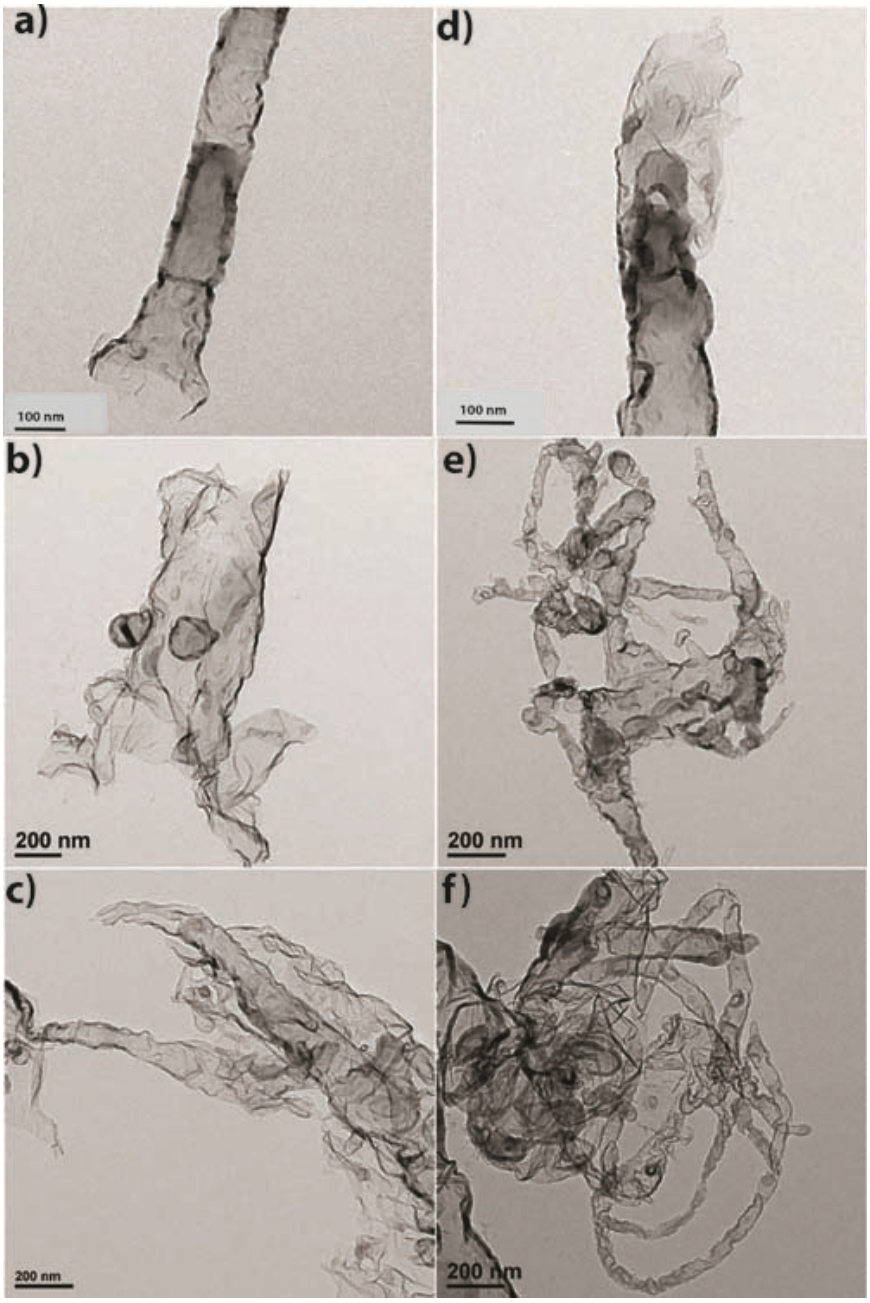

Figure 5.2. a, b and c) Typical TEM images of highly transparent GNRs prepared using the hydrothermal method in 0.5 M K_2SO_4 for 24, 36 and 48 h at 180 $^{\circ}$C respectively and d, e and f corresponds to TEM images obtained after hydrothermal treatment using 0.5 M KNO_3 for 24, 36 and 48 h at 180 $^{\circ}$C revealing few layers of high aspect ratio GNRs. The superiority of the former is clearly evident.

Transmission electron microscopy (TEM) images are used to compare the efficiency of different types of intercalation and exfoliation of MWCNTs. For example, Figure 5.2 (a, b and c) shows TEM images of highly transparent GNRs prepared by hydrothermal method using 0.5 M K_2SO_4 for 24, 36 and 48 h respectively while Fig. 5.2 (d, e and f) corresponds to a comparison of similar TEM images obtained after hydrothermal treatment using 0.5 M KNO_3 for 24, 36 and 48 h.

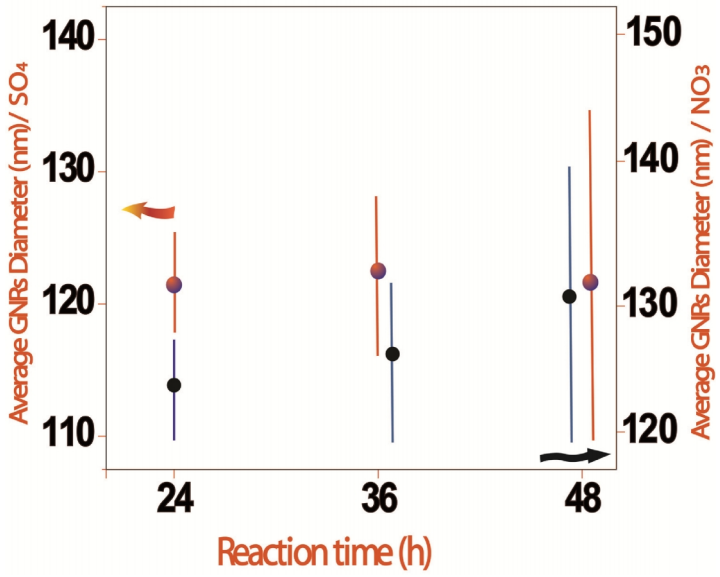

Figure 5.3. Scatter Plot displaying the hydrothermal reaction using K_2SO_4 and KNO_3 for different time (h) and corresponding average GNRs formed. (Determined using 20-25 TEM images of GNRs per reaction).

It is clear from the TEM images that the extent of unzipping of MWCNTs increases with time in case of both KNO_3, and K_2SO_4 as shown in the scatter plot (Figure 5.3). This distinctly shows that the average GNR diameter increases with the exposure time to eventually get in the range of 100-140 nm with a length of 1-3 μm. These results clearly reveal that MWCNTs are successfully transformed to GNRs using a hydrothermal method and the resultant GNRs are stable under electron beam irradiation, since there is no further dimensional change. In general chemical affinities and geometric constraints associated with intercalant size and intercalant bonding distances determine the extent of intercalation in MWCNTs and graphite. Also it is observed in the XRD data (figure 5.7) that intercalation causes crystal dilatation along the c axis:

the larger the molecular intercalates like KSO_4 > KNO_3, the larger the dilatation for MWCNTs and resulting in to proper exfoliation to GNRs.

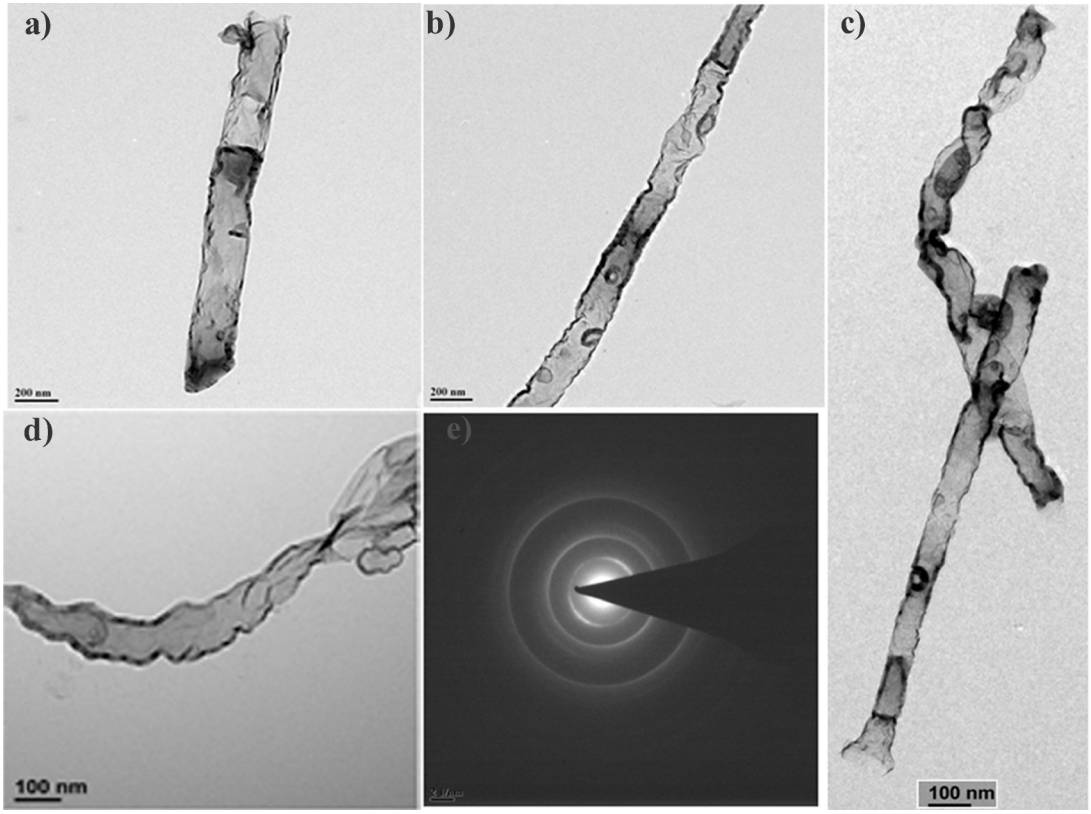

Figure 5.4. a, b) Representative TEM images of GNRs prepared by hydrothermal reaction in 0.01 and 0.1 M K_2SO_4 respectively for 48 h at 180 ^{0}C and c, d) corresponding to GNRs prepared in 0.01 and 0.1 M KNO_3 for 48 h at 180 ^{0}C. e) SAED pattern of GNRs showing high crystallinity corresponds to figure d.

The GNRs show high aspect ratio, with predominantly parallel edges and ripples on the surface although the length of GNR matches well with that of MWCNTs despite the variation in width possibly due to different extension of the exfoliation process. Thus this TEM image clearly reveals that the rate of unzipping is independent of the diameter of MWCNTs, but depends solely on the exposure time and concentration of anions and cations to create transient openings on the surface of MWCNTs for intercalation The selected area electron diffraction (SAED) pattern shows well defined crystalline spots confirming the highly crystalline nature of GNRs with a d-spacing of 0.34 nm, which is in excellent agreement with similar information derived from the XRD data Figure 5.9.

TEM and AFM analysis of at least 25 separate GNRs were monitored to estimate the efficiency of transformation during each treatment with separate anions and cations (*viz*. K_2SO_4, KNO_3, KOH, and H_2SO_4) under hydrothermal conditions. Interestingly, we found that K_2SO_4 and KNO_3 were more effective and powerful for exfoliating MWCNTs compared to KOH and H_2SO_4. This may be due to the number of defects on the MWCNTs surface playing important role for the intercalation of potassium and resulting into different extent of exfoliation of MWCNTs due to various sizes of solvated anions. It is believed that a threshold pressure (p_t) is required to exfoliate MWCNTs and to relieve lattice strain since the intercalation process changes the atomic stacking sequence and requires the motion of dislocations.[16] The intercalation threshold depends sensitively on intercalate species, and size of solvated ions, since OH^- > SO_4^{--} > NO_3^- and also polarizability varies in the order OH^- < SO_4^{--} < NO_3^- , so SO_4^{--} having moderate solvated size and polarizability, which might playing important role along with K^+ adsorption for proper exfoliation.

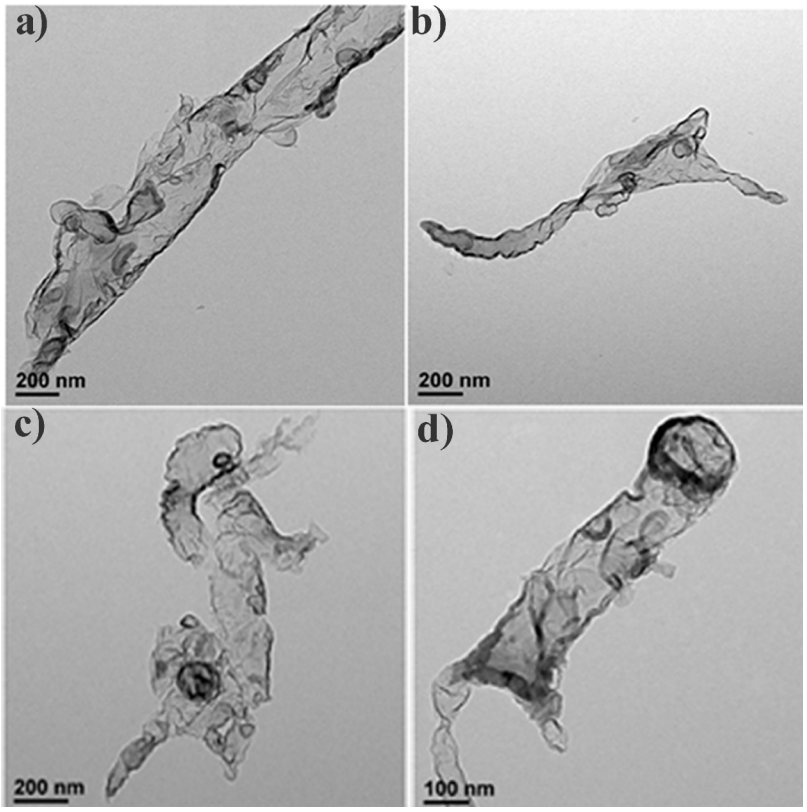

Figure 5.5. a, b) TEM images of GNRs after hydrothermal reaction using 2 M and 4 M K_2SO_4 respectively , for 48 h at 180 ^{0}C and c, d) corresponding to soft GNRs using 2 M and 4 M KNO_3 for 48 h at 180 ^{0}C.

The unzipping of -C=C bond on the outer layer of MWCNTs is triggered by sufficient number of defects created by mild oxidizer condition at edge sites and grain boundaries of the CNTs. Secondly, defective sites at the edges or grain boundaries open up due to intercalation by potassium and solvated SO_4^{2-}. This process leads to the release of gaseous H_2 causing expansion of the interlayer distance of CNTs.[17]

In order to understand the role of counter ions during the hydrothermal process, we have performed control experiments using K_2SO_4 and KNO_3 with different concentrations (2.0 and 4.0 M). The exfoliation efficiency of CNTs in 2.0 and 4.0 M K_2SO_4 is much lower than that in 0.5 M K_2SO_4, and the corresponding yield of GNRs is ~25% and ~12%, respectively. This may be due to at higher concentration of KNO_3 and K_2SO_4, since more energy is required to initiate intercalation between two graphite host layers than to sustain subsequent diffusion into the host also shown in 5.7.1. Exfoliation in 4.0 M K_2SO_4 mainly generates GNRs which get rapidly suspended after the exfoliation (Figure 5.5.)

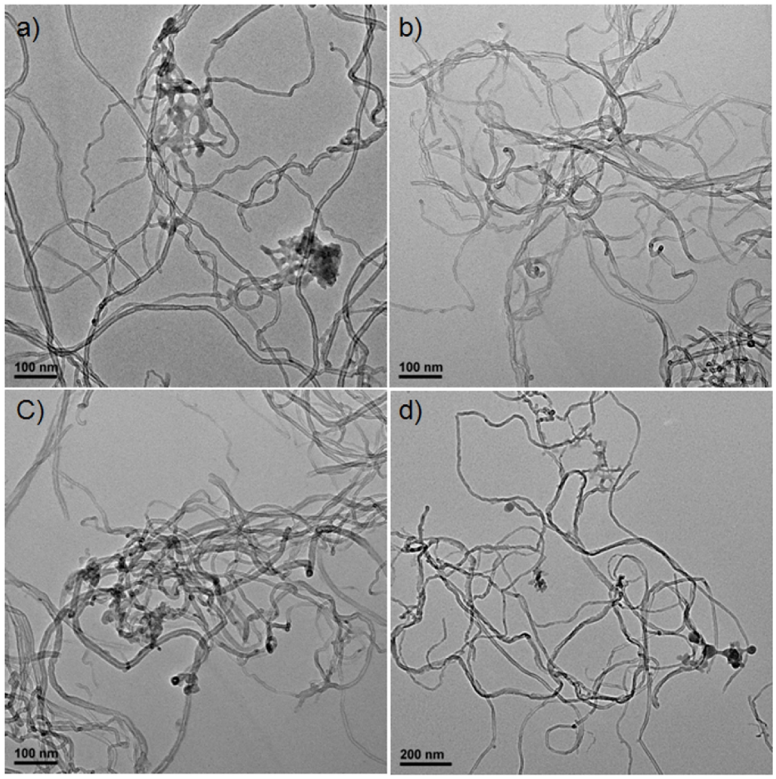

Figure 5.6. a, b)TEM images of partially unzipped MWCNTs after hydrothermal reaction using 2 and 4 M H_2SO_4 for 48 h at 180 ^{0}C respectively, and c, d) corresponding to partially unzipped MWCNTs using 2 and 4 M KOH for 48 h at 180 ^{0}C.

Also hydrothermal experiments using higher concentration 2 M, 4 M H_2SO_4 and 2M and 4 M KOH are able to generate only partially unzipped MWCNTs, thus proving the role of synergy between cation and anion (Figure 5.6.) ina given solvent as illustrated in Tables 5.1 and 5.2 and related figures.

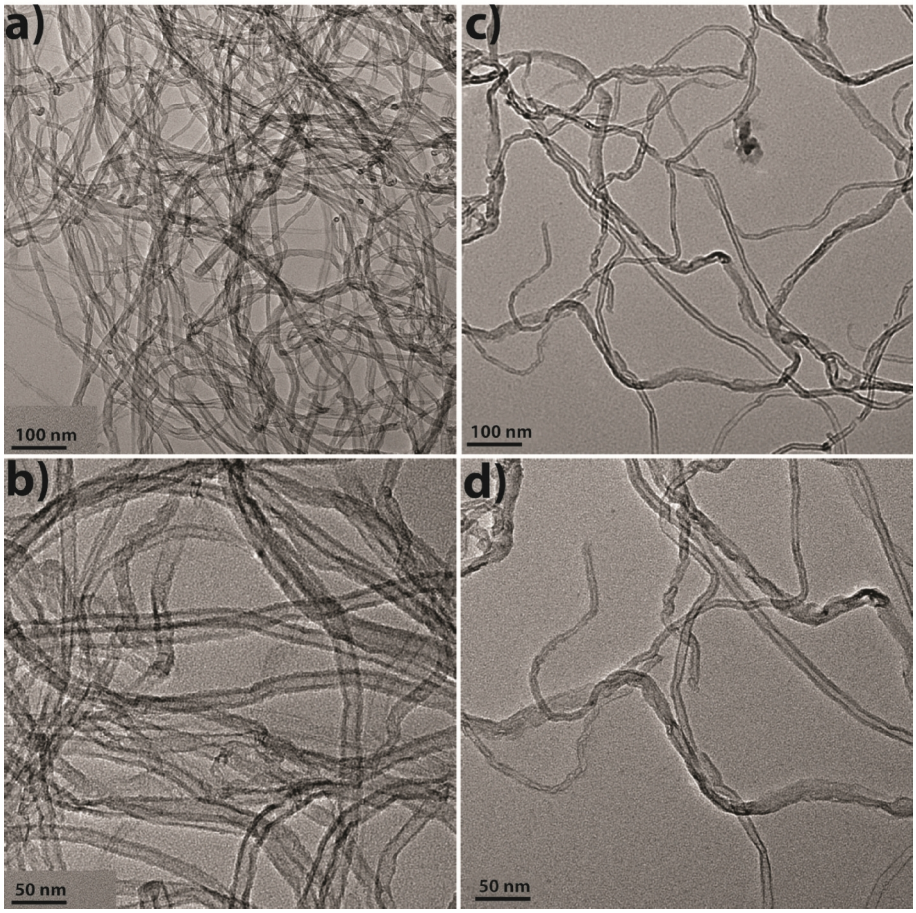

Figure 5.7. a, b)TEM images of unaffected MWCNTs after hydrothermal reaction using 0.5 M H_2SO_4 for 48 h at 180 ^{0}C and c, d) corresponding to partially unzipped MWCNTs using 0.5 M KOH for 48 h at 180 ^{0}C.

Mild sulfuric acid (0.5 M) or nitric acid causes only minimal surface oxidation (supported by XPS shown in Figure 5.11) of MWCNTs which results in to sufficient number of transient openings for potassium intercalation due to surface oxidation. As only 0.5 M H_2SO_4 and 0.5 M KOH are not able to fully unzip the MWCNTs giving almost unaffected and partially unzipped morphology respectively as shown in Figure 5.7, the importance of both co- intercalation potassium and sulphate or nitrate in the unzipping process is implicit.[18]

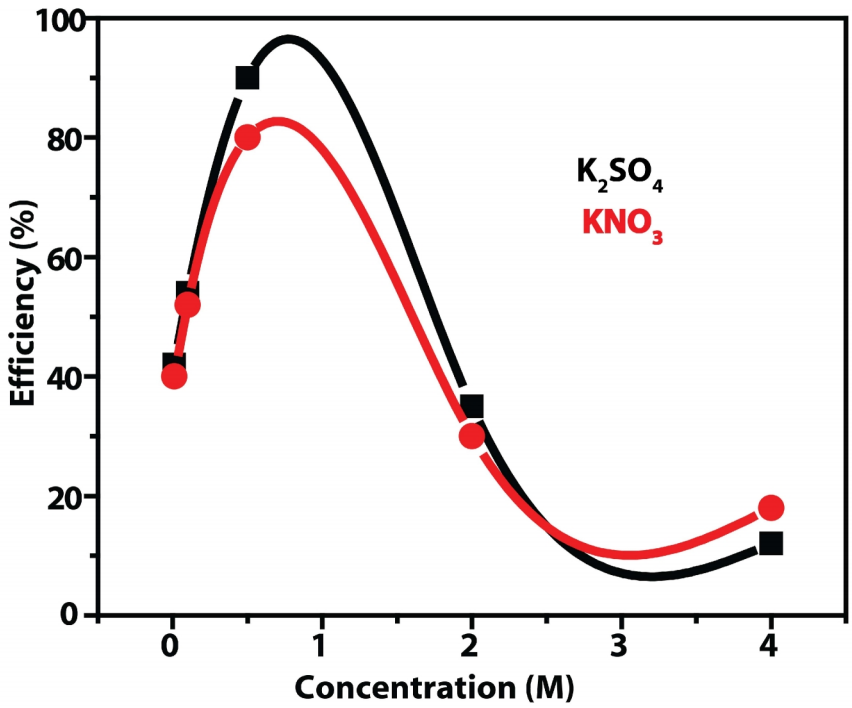

Figure 5.7.1. The plot for the exfoliation efficiency *vs* concentration of both K_2SO_4 and KNO_3 for 48 h at 180 °C h.

The figure 5.7.1 implies that the optimum concentration for the proper exfoliation using K_2SO_4 and KNO_3 for 48 h at 180 °C h is 0.5 M. For example, the presence of mild oxidizer in water is crucial for the generation of minimal number of defects that can be accessible to potassium intercalation. The striking similarity of experimental results in 0.5 M KOH and 0.5 M H_2SO_4 to generate partially damaged MWCNTs implies that no individual K^+, SO_4^{2-} or NO_3^- ion plays any critical role in unwrapping of MWCNTs, although this process is effective in the presence of both cations and anions i.e. (K^+ and SO_4^{--}) in a cooperative manner. This simple, scalable and inexpensive method produces few milligrams of highly transparent few layered GNRs in one step as confirmed from TEM, AFM and XRD data.

Table 5.1. Summary of data revealing the importance of counter-ions and their concentration dependence in the hydrothermal method of GQD preparation at 180°C for 48 h.

Salt	Concentration (M)	Results
K_2SO_4	0.01	Low exfoliation efficiency(yield 42 %)
K_2SO_4	0.1	Good exfoliation efficiency(yield 54 %)
K_2SO_4	0.5	Very good exfoliation efficiency with high aspect ratio GNRs (yield 80-100 %)
K_2SO_4	2	GNR gets soften? (yield 35 %)
K_2SO_4	4	Soft GNRs (yield 12 %)
KNO_3	0.01	GNRs are relatively thick (5-8 layers) (yield 40 %)
KNO_3	0.1	Exfoliation efficiency is moderate (yield 52 %)
KNO_3	0.5	Good exfoliation efficiency (yield 80 %)
KNO_3	2	Low yield of GNRs (30 %)
KNO_3	4	Very low yield of GNRs (18 %)

We have observed that the hydrothermal experiments containing K_2SO_4 exhibit many excellent exfoliation characteristics to follow the progress and perhaps also the kinetics. For example,SO_4^{--} ions having moderate solvated size and polarizability as compared to that of OH^- and NO_3^- ions possibly portends proper co-intercalation along with K^+ ions supporting proper exfoliation. However, the exfoliation efficiency varies with respect to the concentration as shown in Table 5.1 in an unexpected manner. Although the exact reasons are not clear due to the intricacies associated with modulating the electrostatic, solvation and van der Waals interaction by changing ionic strength, conductivity, solvation energy, viscocity etc, this indicates that an approximately constant macroscopic distribution of intercalant is required in the intergallary

space when the total intercalate uptake is only 0.5 M of its saturation value to provide sufficient mobility.

Table 5.2. Summary of data revealing the importance of the counter-ions and their concentration dependence in the hydrothermal method at 180 °C for 48 h.

Salt	Concentration (M)	Results
KOH	0.1	No obvious exfoliation
KOH	0.5	Partially unzipped MWCNTs
KOH	2	Partially unzipped MWCNTs
KOH	4	Partially unzipped MWCNTs
H_2SO_4	0.01	No obvious exfoliation
H_2SO_4	0.1	No obvious exfoliation
H_2SO_4	0.5	Partially oxidized MWCNTs
H_2SO_4	2 and 4	Partially oxidized MWCNTs

However, while using very dilute solution of K_2SO_4 (*i.e.* 0.01 M and 0.1 M), exfoliation occurs only at a much lower rate (72 h). The yield of GNRs for 0.01 M and 0.1 M K_2SO_4 are ~42% and ~53%, respectively. The low exfoliation efficiency of CNTs in diluted K_2SO_4 is most likely due to the inefficient intercalation of anions and potassium. The effect of concentration for different counter-ions is summarized in Table 5.2. As proved form TEM and XRD (figure 5.7 and 5.9 respectively) data that co-intercalent along with K^+ is an essential prerequisite for the proper exfoliation of MWCNTs, these results in to partial unzipping leaving a large number of unaffected tubes in the case of both KOH and H_2SO_4.[18]

5.3.3 AFM Analysis

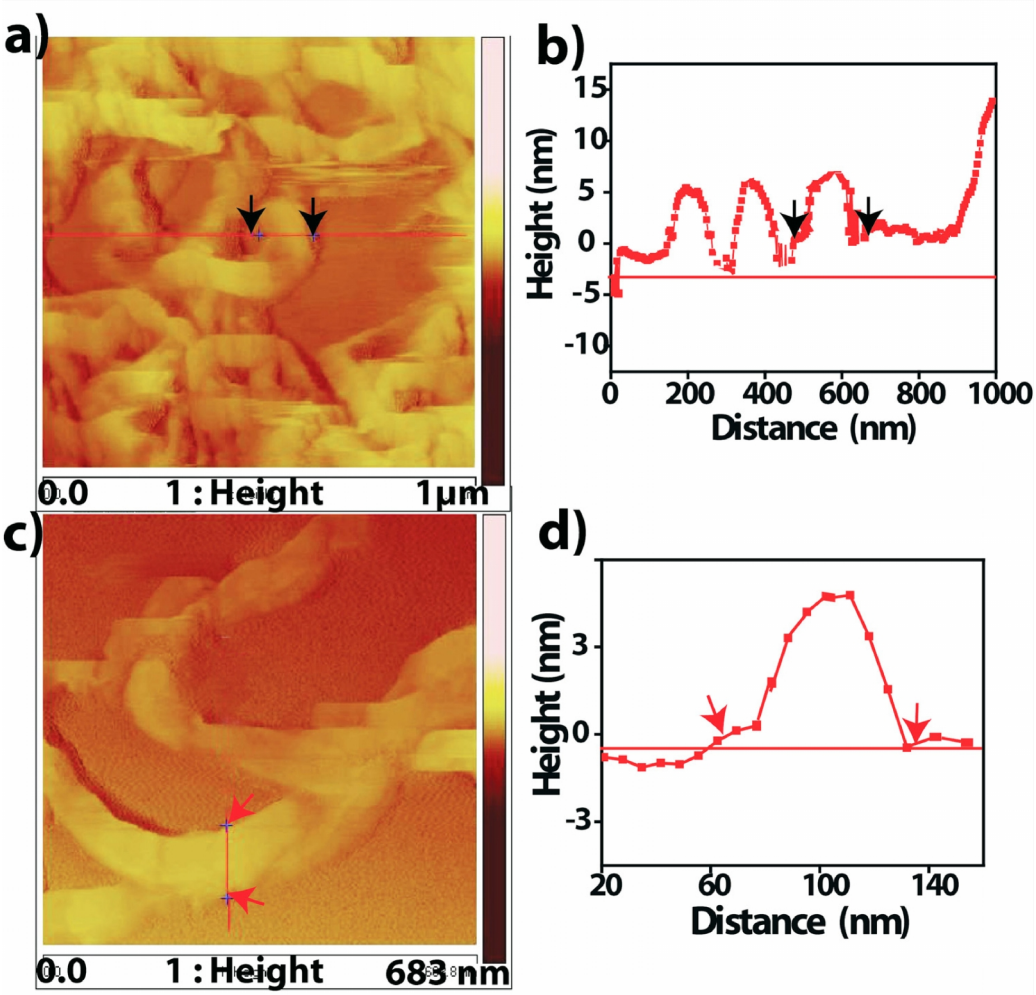

Figure 5.8. AFM images of GNRs obtained from MWCNTs using hydrothermal method in presence of a) K_2SO_4 c) KNO_3 for 48 h at 180 °C each and their corresponding height profile along one line-scan.

AFM (atomic force microscopy) is used to obtain more accurate information about the shape and topography of GNRs. For example, Figure 5.8 (a, b) reveals long ribbons (2 µm) with straight edges having widths ranging from 90 to 110 nm, illustrating the geometric correspondence between diameter of the initially used MWCNT and this experimentally obtained width. The statistical thickness analysis of GNR ensembles shows that all of GNRs have thickness ranging from 3 to 5 nm confirming the possibility of few layer GNRs. These characterizations reveal that most of the MWCNTs are unzipped along tube axis although this seems to be chirality dependent process. [6, 19] Several precautions were taken in this study to reduce tip-induced

artifacts as much as possible by increasing the scan rate and decreasing the normal force in addition to carrying out scans at multiple locations to ensure representative image. [20]

5.3.4 XRD Analysis

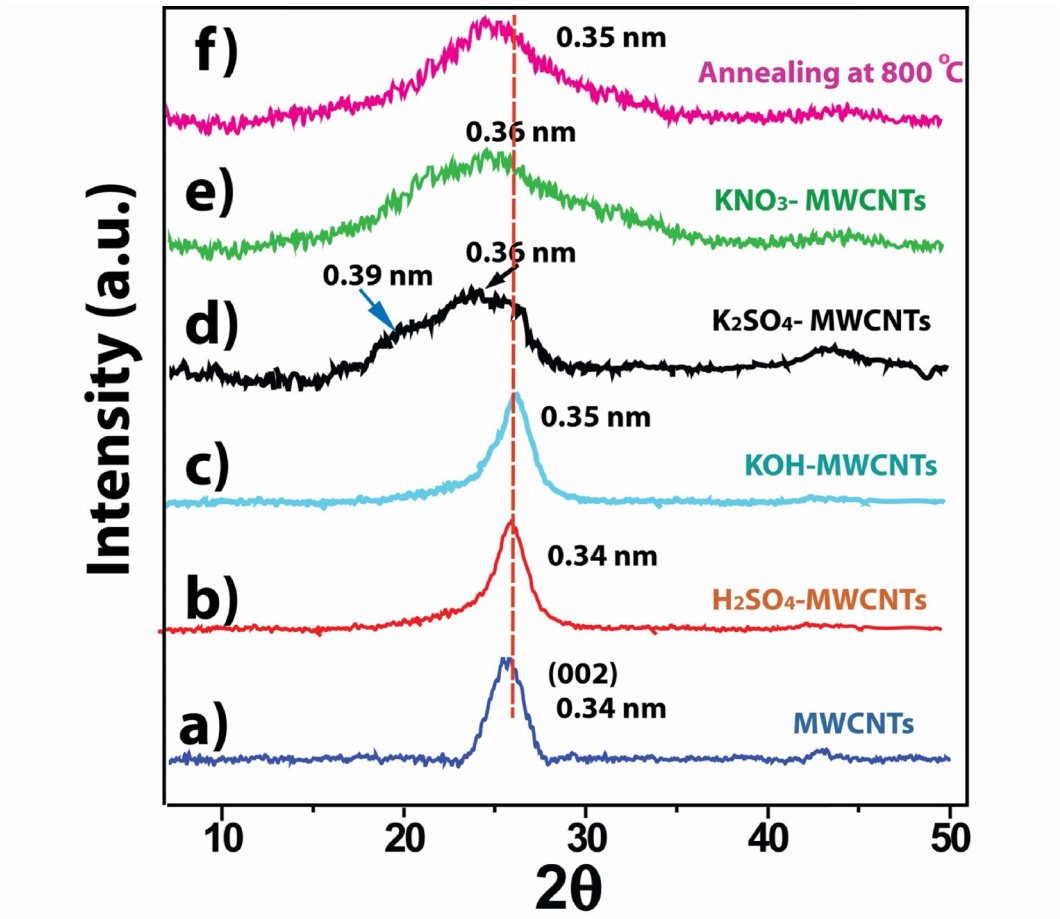

Figure 5.9: X-ray diffraction patterns for a) pristine MWCNTs and MWCNTs samples hydrothermally treated with b) 0.5 M H_2SO_4 c) 0.5 M KOH d) 0.5 M K_2SO_4 e) 0.5 M KNO_3 at 180 °C collected after subsequent washing with dil. HCl and water. f) Corresponding to K_2SO_4 treated MWCNTs samples annealed at 800 °C.

A comparison of the X-ray powder diffraction data for various samples as shown in Figure 5.9 confirms that potassium and sulfate (or nitrate) ions individually cannot effectively exfoliate MWCNTs, but, together can form disordered domains with a distinct broadening of the graphitic peak corresponding to 002 plane. This also implies that the intercalation of potassium ions

facilitates proper exfoliation of graphene layers with an average inter-planar spacing of 0.36 nm. Also, 0.5 M H_2SO_4 treated MWCNTs samples show the same graphitic peak position without broadening, compared to that of pristine MWCNTs confirming no exfoliation. However, after HCl washing and annealing at 800 ^{0}C the graphitic (002) peak reappears at 0.34 nm indicating that these GNRs undergo recrystallization. Moreover, the 0.5 M KOH treated samples show negligible shift in the 002 plane with a d spacing of 0.345 nm, suggesting that not only potassium, but anion also do play an important role for the intercalation followed by longitudinal unzipping of these MWCNTs. This data is in excellent agreement with similar reports for the Li, K ion intercalation in graphite resulting in to order- disorder transformations as a function of temperature.[18, 21]

5.3.5 Raman Analysis

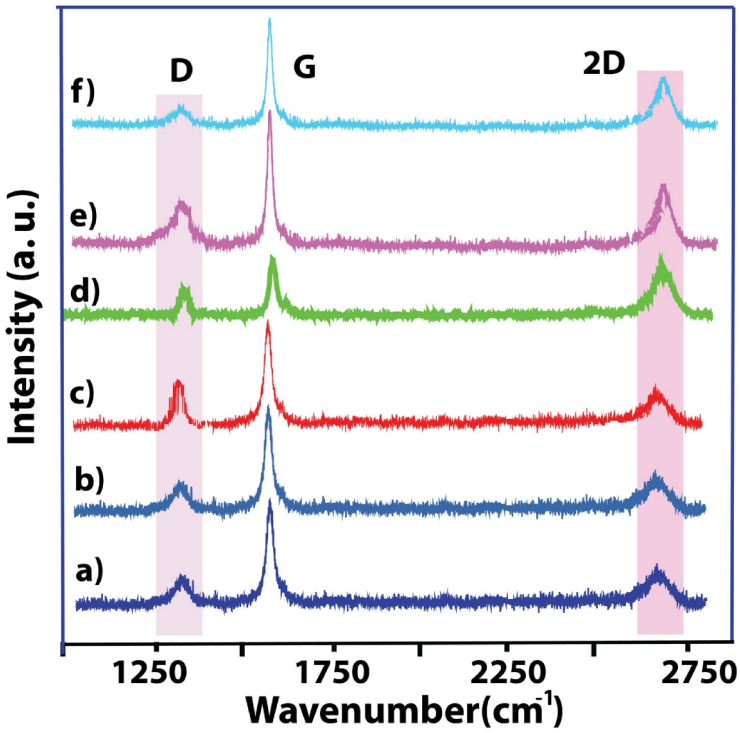

Figure 5.10. Comparative Raman spectra of a) MWCNTs and corresponding samples after hydrothermal treatment for 48 h with b) 0.5 M KOH c) 0.5 M H_2SO_4 d) 0.5 M K_2SO_4 e) 0.5 M KNO_3 collected after subsequent washing with dil HCl and water, displaying a small increase in D band as well as 2D intensity and becoming prominent in the case of K_2SO_4, and KNO_3 samples e) corresponds to K_2SO_4 treated MWCNTs samples annealed at 800 ^{0}C.

As explained in chapter 1, Raman spectroscopy is normally used to characterize the quality of graphitic structures, especially the relative population of sp^2 and sp^3 domains of the MWCNTs and GNRs. For example, an increase in the intensity of the D band over that of the G band (i.e. I_D/I_G ratio increases from 0.25 for MWCNTs to 0.29, and 0.32 and for H_2SO_4 and KOH treated MWCNTs for 48 h respectively as shown in Figure 5.10) suggests the enhancement in the sp^3 domains due to oxidation. Upon unzipping of MWCNTs, a prominent D peak is seen, which may be an indication of the disorder in the graphene structure presumably due to the high edge-content.[19, 21-22] The disordered structure also results in a slight broadening and subsequent shift in the position of the G band, perhaps due to the charge transfer effects of the potassium with GNRs. After annealing at 800 ^{0}C the I_D/I_G ratio interestingly, remains almost unaffected (i.e.0.34 to 0.32) suggesting an increase in the defects mainly from the edge contribution and not from the oxidative functional groups. Also $I_{2D}/I_{G\ ratio}$ is very π electron sensitive and gives information about layer thickness of GNRs. In the case of samples prepared using K_2SO_4 and KNO_3 this I_{2D}/I_G ratio is found to be 0.32 and 0.30 respectively implying 3-5 layer GNRs in excellent confirmation with the information obtained from an independent source like AFM image.[23]

5.3.6 X-ray photoelectron spectroscopy

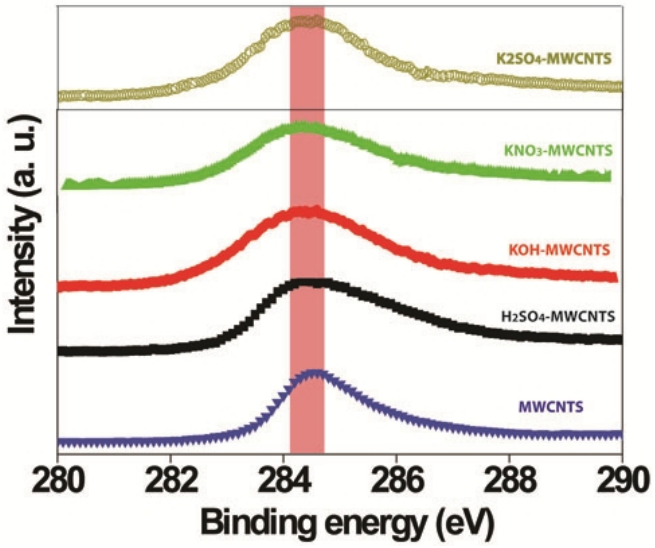

Figure 5.11. Comparative XP spectra of C1s for MWCNTs and corresponding samples after hydrothermal treatment for 48 h with 0.5 M H_2SO_4 ,0.5 M KOH showing minimal percentage of sp^3 carbon for 0.5 M K_2SO_4 and 0.5 M KNO_3 treated samples.

X-ray photoelectron spectroscopy (XPS) is used to analyse the elemental composition and carbon bonding configurations in GNRs and pristine MWCNTs. The XP spectra show the presence of carbon and negligible percentage of oxygen indicating oxidation-free GNRs. This is further confirmed by the deconvoluted XP spectrum of C1s as shown in Figure 5.11, as no peak corresponding to 286 eV (C-O) or 287 eV (C=O) is observed. The C1s spectrum of H_2SO_4 treated MWCNTs located at 284.7 eV, 285.3eV, 286.3 eV, 288.4 eV and 289.0 eV can be assigned to C=C, C–OH, C–O–C, C=O and -COOH groups, respectively, so that the small increase in the I_D/I_G ratio is solely due to edge contribution of GNRs and not due to surface oxidation. Also C1s core level spectra indicate minimal oxidation due to mild conditions of the oxidizer is used. However, this XPS data should be used with caution as carbon signals are intrinsically unreliable due to chamber contamination unlike that of oxygen or nitrogen binding energy values, which is comparable to that of the XPS obtained in graphene prepared by chemical methods.[24]

5.3.7 Current Voltage Plots for GNRs:

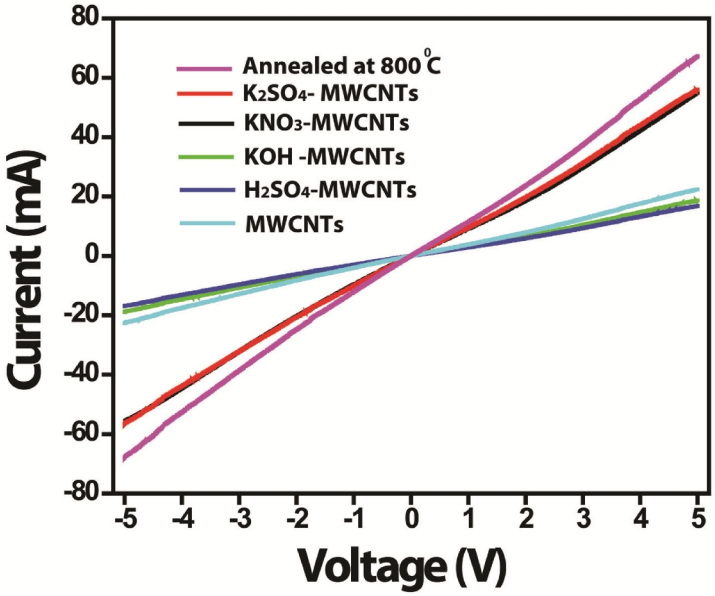

Figure 5.12. Comparative Current Voltage characteristics of pristine MWCNTs and corresponding samples after hydrothermal treatment for 48 h with 0.5 M H_2SO_4 ,0.5 M KOH and showing improved conductivity for 0.5 M K_2SO_4 and 0.5 M KNO_3 treated samples due GNRs formation; also the effect of annealing is displayed as an increase in the conductivity.

In order to measure the electrical properties of the nanoribbons, the sample was drop casted on a Si substrate to prepare a uniform thin film (thickness of 5 µm) with the channel length between two Pt-electrodes being 0.5 µm. This minimal oxygen content on the basal plane of GNRs is also supported by improved electrical conductivity values as shown from the slopes in Figure 5.12 compared to that of MWCNTs and other samples after treatments using KOH, H_2SO_4 as well as methods like chemical unzipping of MWCNTs due to the improvement in the carrier concentration.

A combined analysis of all the above experimental data clearly shows that this hydrothermal method can convert indeed 80-100 % of the starting material to high aspect ratio conductive GNRs. Also this process reveals the important role of potassium, sulfate, and nitrate ions in controlling the extent of unzipping process by intercalation. Although many mechanistic details are not clear about the role of cations and anions for unzipping process, this simple, scalable and inexpensive method produces few milligrams of transparent few layered GNRs in one step.

5.3.8 Applications as Transparent Conducting Films (TCF)

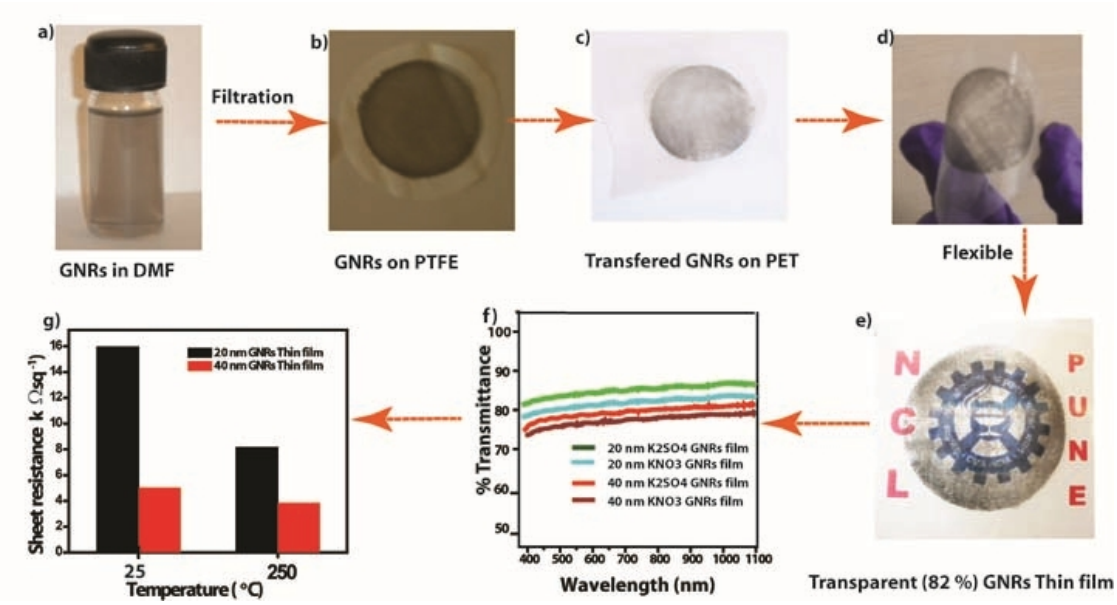

Figure 5.13. a, b, c) Schematic illustration of transfer procedure of GNRs on PET using vacuum filtration method followed by mechanical compaction; d, e) photographs of the transferred GNRs film on PET substrate displaying flexibility and transparency and, f, g) transparency and sheet resistance of GNR films with different thicknesses.

In addition to the easy and bulk synthesis of high quality GNRs, herein we used a low cost fabrication for preparing conductive, transparent and flexible thin films of GNRs on Polyethylene terephthalate (PET) substrate as discussed in experimental section 5.2. The ~20 and ~40 nm thick graphene films (diameter 5 cm) on PET have a transmittance of 82 % and 65 %, respectively (Figure 5.13 f), which is comparable to that in literature reports.[11b, 15, 24b, 25] It can be seen from the optical microscopic (OM) images (Figure 5.14) that the transferred film uniformly covers the substrates over a large area.

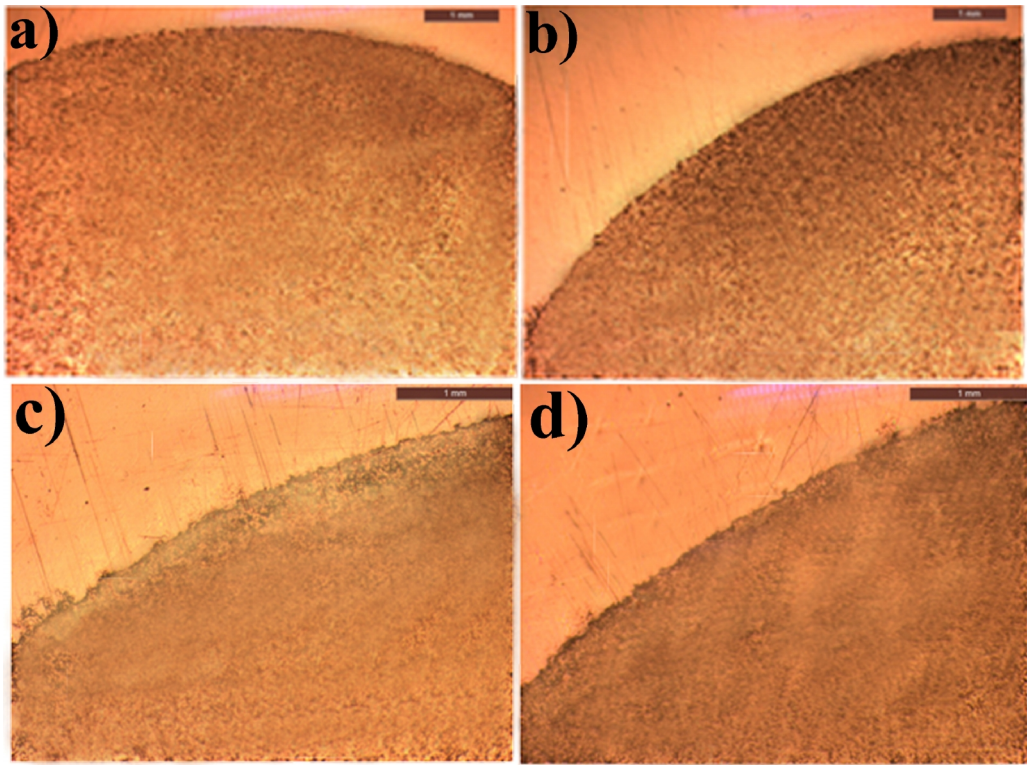

Figure 5.14: Optical images of the transferred GNRs films on PET substrate prepared using a, b) K_2SO_4 and c, d) KNO_3 where, (a) 20 nm and (b) 40 nm; (c) 20 nm (d) 40 nm thick films of GNRs with same magnification; scale bar is 1 micrometer.

The average sheet resistance of the transferred GNR films measured using the four-point probe method (Figure 5.13g) was 16.0 and 8.2 kΩ $cmsq^{-1}$ for 20 and 40 nm GNRs films, which is comparable to the values reported for CVD grown graphene.[26] After thermal annealing of the GNRs films at 200 °C for 30 min in Argon atmosphere the sheet resistance decreased dramatically to 5 and 3.8 kΩ sq^{-1}respectively. This change might be ascribed to improved film quality by the evaporation of the solvent(DMF) and also perhaps of better inter-particle

cohesion. Also the average sheet resistance was determined to be 18 and 9 kΩ sq^{-1} for 20 and 40 nm GNRs films respectively prepared using 0.5 M KNO_3 and the transparency of same films are indicated for comparison in Figure 5.13 g. This is comparable to that of the CVD based graphene and there is also further scope for the improvement in the transmittance maintaining similar conductivity.[26]

5.3.9 Applications as Electrocatalysts for Oxygen Reduction Reaction in Fuel Cells

The last part of this chapter discusses an interesting application of these GNRs as an electrocatalytic support for Pt nanoparticles for ORR in fuel cells.

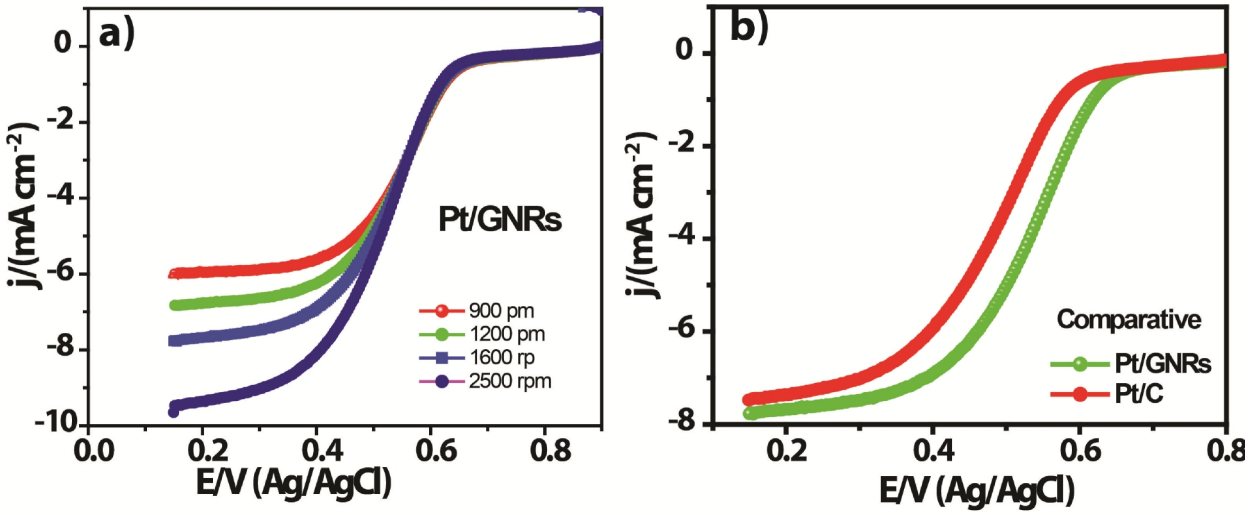

Figure 5.15. a) Linear sweep voltammogram of Pt/GNRs in an oxygen saturated 0.1 M perchloric acid with a varying rotation speed of working electrode. b) Comparative linear sweep voltammogram of Pt/GNRs and Pt/C in an oxygen saturated 0.1 M perchloric acid, showing a positive shift in onset potential for Pt/GNRs as well as higher limiting current, indicating that Pt/GNRs is thermodynamically and kinetically a more favourable electrocatalyst compared to commercial Pt/C.

LSV plot is divided in to three regions; first onset potential region ~ 0.7 V, vs. Ag/AgCl; second, 0.7 V to 0.4 V, v. Ag/AgCl, which corresponds to the diffusion region and kinetics region; finally, third, limiting region at < 0.4. From the LSV, it was observed that, rotation of working electrode will minimize the diffusion limitation effect. During rotation of the working electrode (400 to 2500 rpm), the potential regions under kinetic and oxygen mass transport

limiting control are noticeably observed and the current density increases with increasing rotation rate, perhaps due to enhanced mass transfer characteristics.[12, 27]

Moreover, the comparative LSV of Pt/GNRs and Pt/C at 1600 rpm (Fig. 5.15 b), shows that the activity of Pt/GNRs is better than that of commercially available Pt/C. The Pt/GNRs shows a positive onset potential around 70 mV as compared to that on Pt/C. The limiting current is also higher for Pt/GNRs. The improvement in the onset potential and higher limiting current is attributed to the better dispersion of Pt on GNRs and higher conductivity of GNRs as compared to carbon itself. LSV results indeed confirm that the Pt/GNRS have higher electrocatalytic activity for ORR, comparable to that of Pt/C.[28]

A preliminary screening of the electrocatalytic activity of the Pt-GNRs towards ORR in an acid media was carried out by cyclic voltammetry (CV). For comparison, we have used commercially available 20 wt% Pt/C in the same medium under similar conditions.

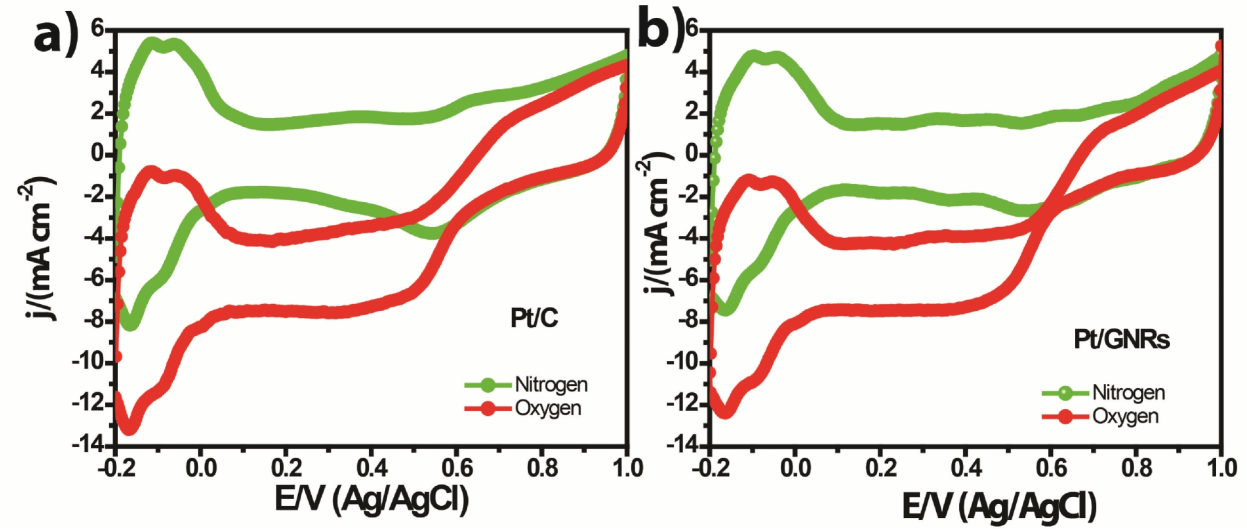

Figure 5.16. Comparative cyclic voltammograms of a) Pt/C and b) Pt/GNRs in nitrogen and oxygen saturated 0.1 M perchloric acid.

Nitrogen and oxygen saturated 0.1 M $HClO_4$ aqueous solution has been used as an electrolyte and current-voltage profiles were measured at a typical scan rate of 50 mV/s. For both systems, Pt loading was maintained to 20 µg on a glassy carbon working electrode (diameter: 3mm). Accordingly, Fig. 5.16 shows a comparative CV curve of Pt/C and Pt/GNRs in a N_2 saturated 0.1 M $HClO_4$ aqueous solution, in a potential window of -0.2 V to 1.0 V (vs. Ag/AgCl). Characteristic peaks for platinum and oxygen reduction are clearly seen. Moreover, a well-

defined reduction peak occurs at around 0.6 V (vs. Ag/AgCl) in the O_2-saturated 0.1 M $HClO_4$ aqueous solution, which indicates that O_2 is more efficiently reduced on the electrode coated with Pt-based material. The CV profile shows hydrogen adsorption-desorption occurring around an applied potential of -0.2 V to 0.2 V (Ag/AgCl). Furthermore, the Pt oxidation starts from 0.6 V and the corresponding reduction appears at 0.7 V during the cathodic scan. The Electrochemical active surface area (Apt) was calculated by using a formula.

$$Apt = Q_H / 0.21\ mC/cm^2 * [Pt]$$

Where, Q_H is the hydrogen ion desorption charge 0.21 mC/cm^2 is the charge required to desorbs the monolayer of hydrogen from the surface of Pt.

[Pt] is the concentration of Pt. The calculated electrochemical active surface area found to be 95 m^2/gm for Pt/C, which is nearly same as compare to Pt/GNRs (92 m^2/gm). These results indeed prove that GNRs are better support for Pt to improve the electrocatalytic activity in fuel cells.[12, 29]

5.4 Conclusions

In summary, a unique hydrothermal approach for the synthesis of conductive and transparent GNRs with 80-100 % yield is discussed in this chapter using MWCNTs as precursors. Also this chapter explains the importance of counter ions along with potassium intercalation in the unzipping process. This simple, scalable and inexpensive method produces few milligrams of conductive and transparent (82 %) GNRs in one step. Many limitations of other exfoliation methods like partial unzipping or mixture of defective and damaged GNRs could be alleviated by using this remarkable one-step hydrothermal method possibly with minimum contamination. Although the hydrothermal route for synthesis of GNRs described here can have several advantages like inexpensive scale-up possibility, one pot synthesis, high yield of transparent and conducting GNRs, some of the electronic characteristics might get affected due to the intercalation of cations, anions and solvent molecules. However, this study opens new pathways for the preparation of GNRs in good yield and there are also profound implications for certain applications like fuel cells, Li-battery electrodes, carbon fiber spinning, flexible transparent

electrodes and conductive polymer composites. Also this study demonstrates two important applications of GNRs; one using vacuum filtration method for preparation of flexible TCF and other in electrocatalysis where Pt/GNRs may be a promising candidate for fuel cell applications.

5.5 References:

[1] a)K. S. Novoselov, A. K.Geim, S. V. Morozov, D. Jiang, Y. Zhang, S. V. Dubonos, I. V. Grigorieva, A. A. Firsov, *Science* **2004**, 306; b)B. Luo, S. Liu, L. Zhi, *Small* **2012**, *8*, 630; c)X. Li, C. W, J. An, S. Kim, J. Nah, D. Yang, R. Piner, A. Velamakanni, I. Jung, E. Tutuc, *Science* **2009**, *324*, 1312.

[2] Q. Yu, L. A. Jauregui, W. Wu, R. Colby, J. Tian, Z. Su, H. Cao, Z. Liu, D. Pandey, D. Wei, *Nat.Mater.* **2011**, *10*, 443.

[3] a)J. Wu, W. Pisula, K. Müllen, *Chem. Rev.* **2007**, *107*, 718; b)S. Stankovich, D. A. Dikin, R. D. Piner, K. A. Kohlhaas, A. Kleinhammes, Y. Jia, Y. Wu, S. T. Nguyen, R. S. Ruoff, *Carbon* **2007**, *45*, 1558; c)H. A. Becerril, J. Mao, Z. Liu, R. M. Stoltenberg, Z. Bao, Y. Chen, *ACS Nano.* **2008**, *2*, 463.

[4] a)W. Jinlan, M. Liang, Y. Qinghong, Z. Liyan, D. Feng, *Angewandte Chemie* **2011**, *50*; b)M. Terrones, *ACS Nano*, *4*, 1775; c)L. Jiao, L. Zhang, X. Wang, G. Diankov, H. Dai, *Nature* **2009**, *458*, 877; d)A. L. EliÌoas, A. s. R. Botello-MeÌ ndez, D. Meneses-RodriÌoguez, V. JehovaÌ GonzaÌ lez, D. RamiÌrez-GonzaÌ lez, L. Ci, E. MunÌ*f*oz-Sandoval, P. M. Ajayan, H. Terrones, M. Terrones, *Nano Letters* **2009**, *10*, 366.

[5] a)Z. Chen, Y.-M. Lin, M. J. Rooks, P. Avouris, , *Phys. E* **2007**, *40*, 228; b)X. Yang, X. Dou, A. Rouhanipour, L. Zhi, H. J. Rader, K. Mullen, *J. Am. Chem. Soc.* **2008**, *130*, 4216; c)X. Yan, X. Cui, B. Li, L.S. Li, *Nano Lett.* **2010**, *10*, 1869; d)U. K. Parashar, S. Bhandari, R. K. Srivastava, D. Jariwala, A. Srivastava, *Nanoscale* **2011**, *3*, 3876; e)P. Kumar, L. S. Panchakarla, C. N. R. Rao, , *Nanoscale* **2011**, *3*, 2127; f)M. Y. Han, B. Ozyilmaz, Y. Zhang, P. Kim, *Phys. Rev. Lett.* **2007**, *98*, 206805; g)M. Sprinkle, M. Ruan, Y. Hu, J. Hankinson, M. Rubio-Roy, B. Zhang, X. Wu, C. Berger, W. A. de Heer, , *Nat. Nanotechnol.* **2010**, *5*, 727; h)M. C. Paiva, W. Xu, M. F. Proenca, R. M. Novais, E. Laegsgaard, F. Besenbacher, *Nano Lett.* **2010**, *10*, 1764; i)L. Xie, H. Wang, C. Jin, X. Wang, L. Jiao, K. Suenaga, H. Dai, , *J. Am. Chem.Soc.* **2011,**, *133,*, 10394; j)L. Tapaszto, G. Dobrik, P. Lambin, L. P. Biro, *Nat. Nanotechnol.* **2008**, *3*, 397; k)L. Jiao, X. Wang,

G. Diankov, H. Wang, H. Dai, *Nat. Nanotechnol.* **2010**, *5*, 321; l)K. Kim, A. Sussman, A. Zettl, *ACS Nano* **2010**, *4*, 1362; m)J. Shen, Y. Zhu, C. Chen, X. Yang, C. Li, *Chem. Commun.* **2011**, *47*, 2580; n)J. Campos-Delgado, J. M. Romo-Herrera, D. A. C. X. Jia, H. Muramatsu, Y. A. Kim, T. Hayashi, Z. Ren, D. J. Smith, Y. Okuno, T. Ohba, H. Kanoh, K. Kaneko, M. Endo, H. Terrones, M. S. Dresselhaus, M. Terrones, *Nano Lett.* **2008**, *8*, 2773; o)J. Cai, P. Ruffieux, R. Jaafar, M. Bieri, T. Braun, S. Blankenburg, M. Muoth, A. P. Seitsonen, M. Saleh, X. Feng, K. Mullen, R. Fasel, , *Nature* **2010**, 466; p)J. Bai, X. Duan, Y. Huang, *Nano Lett.* **2009**, *9*, 2083; q)F. Cataldo, G. Compagnini, G. Patane, O. Ursini, G. Angelini, P. R. Ribic, G.Margaritondo, A. Cricenti, G. Palleschi, F. Valentini, *carbon* **2010**, *48*, 2596; r)D. Wei, Y. Liu, H. Zhang, L. Huang, B. Wu, J. Chen, G. Yu, *J. Am. Chem. Soc.* **2009**, *131*, 11147; s)D. V. Kosynkin, W. Lu, A. Sinitskii, G. Pera, Z. Sun, J. M. Tour, *ACS Nano* **2011**, *5*, 968; t)D. Pan, L.Guo, J. Zhang, C. Xi, Q. Xue, H. Huang, J. Li, Z. Zhang, W.Yu, Z.Chen, Z.LiandM.Wu, *J. Mater.Chem.* **2012**, *22*, 3314; u)A. V. Talyzin, S. Luzan, I. V. Anoshkin, A. G. Nasibulin, H. Jiang, E. I. Kauppinen, V. M. Mikoushkin, V. V. Shnitov, D. E. Marchenko, D. Noreus, *ACS Nano* **2011**, *5*, 5132; v)A. L. Eloas, A. R. Botello-Mendez, D. Meneses-Rodriguez, D. V. J. Gonzalez, Ramirez-Gonzalez, E. M.-S. L. Ci, P. M. Ajayan, M. H. Terrones, Terrones, *Nano Lett.* **2010**, *10*, 366; w)A. G. Cano-Morquez, F. J. Rodriguez-Macias, J. Campos-Delgado, C. G. Espinosa-Gonzalez, F. Tristan-Lopez, D. Ramirez-Gonzalez, D. A. Cullen, D. J. Smith, M. Terrones, Y. I. Vega-Cantu, *Nano Lett.* **2009**, *9*, 1527.

[6] D. Kosynkin, A. Higginbotham, A. Sinitskii, J. Lomeda, A. Dimiev, B. Price, J. Tour, *Nature* **2009**, *458*, 872.

[7] D. V. Kosynkin, W. Lu, A. Sinitskii, G. Pera, Z. Sun, J. M. Tour, *ACS Nano*, *5*, 968.

[8] L. Jiang, T. Niu, X. Lu, H. Dong, W. Chen, Y. Liu, W. Hu, D. Zhu, *J. Am. Chem. Soc.* **2013**, *135*, 9050.

[9] a)A. Reina, X. Jia, J. Ho, D. Nezich, H. Son, V. Bulovic, M. Dresselhaus, J. Kong, *Nano Letters* **2009**, *9*, 30; b)L. Gomez De Arco, Y. Zhang, C. Schlenker, K. Ryu, M. Thompson, C. Zhou, *ACS Nano* **2010**, *4*, 2865.

[10] a)S. Yu, W. Zheng, C. Wang, Q. Jiang, *ACS Nano* **2010**, *4*, 7619; b)C.-S. Rodolfo, M.-G. Aaron, V.-D. Sofia, T.-L. Ferdinando, L. E. Ana, P.-L. Nestor, M. Hiroyuki, H. Takuya, F. Kazunori, K. Yoong Ahm, E. Morinobu, T. Mauricio, *ACS Nano* **2013**, *7*; c)R. Cruz-Silva, A. Morelos-Gómez, S. Vega-Díaz, F. Tristán-López, A. Elias, N. Perea-López, H. Muramatsu, T. Hayashi, K. Fujisawa, Y. Kim, M. Endo, M. Terrones, *ACS Nano* **2013**, *7*, 2192; d)A. Morelos-Gómez, S.

Vega-Díaz, V. González, F. Tristán-López, R. Cruz-Silva, K. Fujisawa, H. Muramatsu, T. Hayashi, X. Mi, Y. Shi, H. Sakamoto, F. Khoerunnisa, K. Kaneko, B. Sumpter, Y. Kim, V. Meunier, M. Endo, E. Muñoz-Sandoval, M. Terrones, *ACS Nano* **2012**, *6*, 2261.

[11] a)C. N. R. Rao, A. K. Sood, R. Voggu, K. S. Subrahmanyam, , *J. Phys. Chem. Lett.* **2010**, *1*, 572; b)S. Park, R. S. Ruoff, *Nat. Nanotechnol.* **2009**, *4*, 217; c)T. Palaniselvam, A. Irshad, B. Unni, S. Kurungot, *J. Phys. Chem. C* **2012**, *116*, 14754; d)H. Meng, N. Larouche, M. Lefèvre, F. Jaouen, B. Stansfield, J. P. Dodelet, *Electrochim. Acta* **2010**, *55*, 6450.

[12] J. Zhang, *PEM fuel cell electrocatalysts and catalyst layers: fundamentals and applications*, **2008**.

[13] D. P. He, K. Cheng, T. Peng, X. L. Sun, M. Pan, S. C. Mu, *J. Mater. Chem.* **2012**, *22*, 21298.

[14] a)X. Huang, Z. Y. Zeng, Z. X. Fan, J. Q. Liu, H. Zhang, *Adv. Mater.* **2012**, *24*, 5979; b)C. C. Huang, C. Li, G. Q. Shi, *Energy Environ. Sci.* **2012**, *5*, 8848.

[15] I. Kholmanov, M. Stoller, J. Edgeworth, W. Lee, H. Li, J. Lee, C. Barnhart, J. Potts, R. Piner, D. Akinwande, J. Barrick, R. Ruoff, *ACS Nano* **2012**, *6*, 5157.

[16] M. S. Dresselhaus, G. Dresselhaus, *Adv. Phys.* **2002**, *51*, 1.

[17] T. Enoki, M. Suzuki, M. Endo, *Graphite Intercalation Compounds and Applications*, **2003**.

[18] D. V. Kosynkin, W. Lu, A. Sinitskii, G. Pera, Z. Sun, J. M. Tour, *ACS Nano* **2011**, *5*, 968.

[19] B. Genorio, W. Lu, A. Dimiev, Y. Zhu, A.-R. O. Raji, B. Novosel, L. Alemany, J. Tour, *ACS Nano* **2012**, *6*, 4231.

[20] I. Reviakine, A. Brisson, *Langmuir* **2000**, *16*, 1806.

[21] G. Ruan, Z. Sun, Z. Peng, J. Tour, *ACS Nano* **2011**, *5*, 7601.

[22] a)M. D. Ayrat, G. Ayrat, J. W. Lon, M. T. James, *Chemical Communications* **2013**, *49*; b)A. L. Higginbotham, D. V. Kosynkin, A. Sinitskii, Z. Sun, J. M. Tour, *ACS Nano* **2010**, *4*, 2059.

[23] a)Z. Liu, K. Suenaga, P.J.F. Harris, S. Iijima, , *Phys. Rev. Lett.* **2009**, *102*, 015501; b)M.S. Dresselhaus, M. Terrones, A. Jorio, M. Endo, A. Rao, Y. Kim, T. Hayashi, H. Terrones, J.

Charlier, G. Dresselhaus, *Mater. Today* **2004**, *7*, 30; c)M. Terrones, H. Terrones, F. Banhart, J.C. Charlier, *Science* **2000**, *288*, 12269.

[24] a)L. Talirz, H. Söde, J. Cai, P. Ruffieux, S. Blankenburg, R. Jafaar, R. Berger, X. Feng, K. Müllen, D. Passerone, R. Fasel, C. Pignedoli, *Journal of the American Chemical Society* **2013**, *135*, 2060; b)K. Parvez, R. Li, S. R. Puniredd, Y. Hernandez, F. Hinkel, S. Wang, X. Feng, K. Mullen, *ACS Nano*; c)J. Cai, P. Ruffieux, R. Jaafar, M. Bieri, T. Braun, S. Blankenburg, M. Muoth, A. Seitsonen, M. Saleh, X. Feng, K. Müllen, R. Fasel, *Nature* **2010**, *466*, 470.

[25] a)S. Butler, S. Hollen, L. Cao, Y. Cui, J. Gupta, H. Gutiérrez, T. Heinz, S. Hong, J. Huang, A. Ismach, E. Johnston-Halperin, M. Kuno, V. Plashnitsa, R. Robinson, R. Ruoff, S. Salahuddin, J. Shan, L. Shi, M. Spencer, M. Terrones, W. Windl, J. Goldberger, *ACS Nano* **2013**, *7*, 2898; b)Y. Zhu, S. Murali, W. Cai, X. Li, J. Suk, J. Potts, R. Ruoff, *Advanced materials (Deerfield Beach, Fla.)* **2010**, *22*, 3906; c)S. Park, R. Ruoff, *Nature nanotechnology* **2009**, *4*, 217; d)M. Yu, O. Lourie, M.J. Dyer, K. Moloni, T.F. Kelly, R.S. Ruoff, *Science* **2000**, *287*, 637.

[26] a)K. Kim, Y. Zhao, H. Jang, S. Lee, J. Kim, K. Kim, J.-H. Ahn, P. Kim, J.-Y. Choi, B. Hong, *Nature* **2009**, *457*, 706; b)Z. Kang, E. Wang, B. Mao, Z. Su, L. Gao, S. Lian, L. Xu, *J. Am. Chem. Soc.* **2005**, *127*, 65345; c)Y. Xiong, Y. Xie, X. Li, Z. Li, *Carbon* **2004**, *42*, 14473; d)P. Mahanandia, K. Nanda, V. Prasad, S. Subramanyam, *Mater.Res. Bull.* **2008**, *43*, 32522; e)M. Motta, A. Moisala, I. Kinloch, A. Windle, *Adv. Mater.* **2007**, *19*, 37216.

[27] L. Ma, J. Wang, F. Ding, *Chemphyschem : a European journal of chemical physics and physical chemistry* **2013**, *14*, 47.

[28] B. Lim, M. Jiang, P. H. Camargo, E. C. Cho, J. Tao, X. Lu, Y. Zhu, Y. Xia, *Science* **2009**, *324*, 1302.

[29] a)G. He, Y. Song, K. Liu, A. Walter, S. Chen, S. Chen, *ACS Catalysis* **2013**, *3*, 831; b)A. C. B. Dale, K. K. Dimitrios, E. B. Craig, *Journal of Power Sources* **2011**, *196*; c)D. Sudipta, K. P. Swapan, *Journal of Materials Chemistry* **2010**, *20*, 8207.

Conclusions and Future Prospects

This last chapter deals with the significant conclusions of the present study along with some of the emerging trends of these fascinating materials. It also outlines several limitations of the present investigation of carbon based nanomaterials along with few suggestions for their improvement. Related promising developments and daunting challenges in this broad area are also discussed to extend the applications of GNRs and GQDs in view of the fundamental and technological interests ostensibly shown by a large number of interdisciplinary researchers encompassing physicists, chemists, biologists and engineers. Finally, some of the future prospects and precautions for processing GNRs and GQDs are also explained within the broad perspective of nanotechnology and its societal impact.

Graphene Nanoribbons (GNRs) and Graphene Quantum Dots (GQDs) are unique materials with remarkable electronic and mechanical properties, some stemming from their close structural relationship to graphite. GNRs are geometrically considered as elongated strips with a rectangular shape, carved out from a graphene sheet. Since they have finite width and length, in nano scale, they are again considered to be quasi-1D structures where the band gap is primarily controlled by the width. They can have different physical properties depending on their width, length and chirality, if we consider the length to be infinite, and width tending to zero they become 1D structure. However GQDs (0D) are the new type of quantum dots, which attract tremendous attention due to the possibility of creating finite gap states on an otherwise zero-band gap material like graphene by surface confinement and edge effects. The strong and tunable luminescence of GQDs is especially attractive, because of its promising applications in light emitting diodes, electroluminescence, organic photovoltaic devices, biological labeling and medicine. As many other intriguing properties have been slowly unravelled including their fascinating electronic transport, unique Raman spectra and unusual mechanical properties, the interest has grown in their potential applications also in nanoelectronics and electrocatalysts

One of the most successful approaches to date, for converting CNTs to graphene is the recent longitudinal unzipping, using a mixture of potassium permanganate and concentrated sulphuric acid, facilitating a large scale preparation of GNRs[1]. However, this method has several problems primarily involving the selection of strong oxidizing agents. First, chemical oxidation itself has serious issues like over oxidation of edges creating defect sites which hamper electronic properties of graphene. More significantly, electron mobility and conductivity get seriously diminished with this treatment and there is also a possibility of the evolution of explosive gases. Chemical unzipping often results in over-oxidation and edge defects, which can be alleviated by using this controlled potential step methodology. Nevertheless, no report exists on the preparation of GNRs using interfacial electric field, which could be helpful in understanding possible transformations in their unzipping process. As a result, we have successfully demonstrated a unique electrochemical approach for the synthesis of GNRs with controlled layer thickness in chapter 2 using both MWCNTs and SWCNTs. This electrochemical route for GNRs described here has several advantages of tuning the orientation. Moreover, the disappearance of Radial breathing mode in Raman as well as van Hove's singularities in case of

UV-Vis absorption upon the application of interfacial electric field provides confirmatory evidence for the unzipping of SWCNTs to a single layer graphene.

Although, considerable efforts have been expended recently in the synthesis of GQDs using carbon nanotubes, several important aspects related to their size selective preparation, purity, and its relation to the various applications remain unaddressed. Accordingly, we have discussed a simple and novel electrochemical approach for the size- selective synthesis of luminescent GQDs using MWCNTs in Chapter 3. This also includes the preparation of GQDs with a uniform size of 3, 5, and 8.2 (±0.3) nm diameter using MWCNT and N-MWCNTs in propylene carbonate and acetonitrile using $LiClO_4$ and TBAP, respectively. Both these sets of GQDs display a remarkable quantum efficiency of 6.3 and 5.1% respectively along with a size-dependent lifetime. The larger the diameter of the GQD the shorter was the average lifetime leading to lower quantum yields (QY).

Although the sequential, single-electron charging of Au clusters is well known[2], no report is available till date, for such a behavior of GQDs. In chapter 4, we have addressed single electron transfer property for GQDs encapsulated in a dodecyl amine envelope with a high level of monodispersity, facilitating attofarad capacitance (C_{GQDs}) of individual GQDs. Average GQDs dimensions, as ascertained from high resolution transmission electron microscopy and atomic force microscopy, ca. 3 ± 0.3, 2.6 ± 0.2, 2.2 ± 0.3 nm, indeed control this unprecedented behavior. Differential pulse voltammetry and cyclic voltammetry for the "as prepared GQDs" interestingly reveal evenly spaced (ΔE) peaks, manifesting subtle charge injection effects to the semiconducting core. This chapter also includes the size dependant electrocatalytic properties of N-GQDs. The presence of nitrogen dopants in the carbon framework not only causes faster unzipping of N-MWCNTs but provides more low activation energy site for enhancing the electrocatalytic activity for oxygen reduction reaction. These results on the size dependent electrocatalytic activity of N-GQDs for ORR as illustrated by the smaller sized N-GQDs (2.5 ±0.3 nm) may be a promising alternative to Pt based electrocatalysts for fuel cell applications.

Recently several methods have been reported with reasonable success for the synthesis of GNRs like plasma etching, catalytic synthesis and chemical unzipping. However, the bulk production of highly conductive and transparent GNRs is a daunting challenge [3]. Consequently, a synthetic procedure amenable for scale-up using hydrothermal method has been demonstrated in Chapter

5, to produce highly conductive and transparent GNRs. The use of GNRs as support in electrocatalysis and transparent conducting thin films (for applications in flexible solar cells) has garnered much attention due to their favourable characteristics such as high surface area, peculiar edge state, mechanical stability, and conductivity caused by the presence of an inert carbon network and more importantly their chemically tunable topography. If such high aspect-ratio carbon nanostructures could be coupled with metallic nanoparticles (e.g., Platinum) an improved catalytic activity for many of the important reactions like oxygen reduction reaction could be achieved.

Thus, the main results of this thesis unravel few issues in the field of GNRs and GQDs with particular emphasis on their electrochemical synthesis and functionalization for selected applications. A unique blend of electronic, mechanical, thermal and chemical properties and more importantly their tenability by size and functionalization of both GNRs and GQDs with respect to their structure, properties and applications by electrochemical preparation is expected to facilitate the prospect of this material for many more tangible applications in the foreseeable future. More specifically, since these nanostructures act as indispensable building blocks for creating designer materials, processing them into robust polymer composite thin films (after successfully overcoming barriers in dispersion) is essential for the fabrication of devices. Although, many well-established methods to synthesize and understand the properties of GNRs and GQDs have been developed recently, several daunting challenges such as the difficulty of precisely controlling their aspect ratio, lack of well defined methods for the controlled layer thickness, limitations of scale-up, impurity control, issues of cost effectiveness and environmental effects still exist, demanding breakthroughs to utilize their complete technological and social benefits in the area of electronics, energy storage, water purification and so on[4]. In addition, several existing gaps in our understanding need to be filled by urgent investigations focusing on atomically precise manufacturing of these new materials with stringent control over their structure-property correlation. For example, GNRs synthesized by CVD always contain other unwanted structures, whose removal is often troublesome[5]. All of these challenges lie before us, especially since single layer GNRs and GQDs still cost more than that of gold!

The following questions need to be discussed bolstered by more experimental data preferably from different laboratories to understand the effectiveness of the technology solutions-

- What health, safety and environmental issues arise from applications of carbon based nanomaterials, and what will be the benefits and risks?
- Is there any urgent need for new regulations especially with respect to biological applications of CNTS, GNRs and GQDs?
- What are the social and ethical issues of making new forms of carbon materials like GQD and GNR based hybrid materials, such as GQD-DNA hybrid?
- What other public perceptions would influence the development of this type of nanotechnology for cost effective innovations?

A detailed understanding of the fundamental aspects of these materials would enable several fascinating nanoelectronic devices with unprecedented capabilities, while composites would be used as materials for making smart devices. Several technologies would be expected to revolutionize applications (e.g., UN Millennium Development Goals) along with their global impact on health, environment, food, water and medicine concerning our daily life[6]. Accordingly, the cost and energy consumption for creating nanoarchitectures need also to be reduced along with ensuring their reproducibility and an understanding the essential properties of carbon-based materials is essential for achieving many of these objectives[4a, 7].

Major accomplishments of the present investigations could be summarized as follows-

- Synthesis of the high quality GNRs using CNTs using a unique electrochemical method for controlling many critical quality parameters of GNRs.
- Synthesis of GQDs from various CNTs in suitable solvents and counter ions using both chemical and electrochemical approaches.
- The effect of different sizes of GQDs and nitrogen doped GQDs (N-GQDs) on the electrocatalytic properties of oxygen reduction reaction (ORR).
- Functionalization and characterization of mono-dispersed GQDs for their unique behavior like single electron transfer and photoluminescence.

- Synthesis of conductive and transparent films of GNRs using hydrothermal method enabling applications like DSSC and FET.

In brief, our synthetic approach of GNRs and GQDs especially the ease of processing offers an unprecedented opportunity to obviate many limitations of currently employed preparation of these fascinating materials, opening new possibilities for manipulating their size dependant properties offering long term stability to evaluate their sustained superior performance. However, the limitations must be kept in mind before their commercial exploitation.

- The electrochemical approach for the synthesis of GQDS and GNRs have several advantages in terms of orientation of CNTs for unzipping but this method is limited by the poor yield compared to other chemical methods.
- The exact mechanism of unzipping is unclear although preliminary spectroscopic evidence (*in situ* Electron spin resonance ESR) points to the involvement of C-C cleavage via radical cations
- A rigorous evaluation of the influence of counter ions and solvent during hydrothermal unzipping of CNTs with possible mechanism of conversion has to be carried out in a systematic manner.

Nevertheless, the present results offer enough scope to design novel GNRs and GQDs with better efficiency, recyclability and simplified functionalization chemistry using these new generation of hybrid material in the foreseeable future.

References:

[1] D. Kosynkin, A. Higginbotham, A. Sinitskii, J. Lomeda, A. Dimiev, B. Price, J. Tour, *Nature* **2009**, *458*, 872.

[2] a)F. F. Fan, *Science* **1997**, *277*; b) N. Chaki, B. Kakade, V. K. Pillai, *Electrochemistry Communications* **2004**, *6*, 661.

[3] a)W. Jinlan, M. Liang, Y. Qinghong, Z. Liyan, D. Feng, *Angewandte Chemie* **2011**, *50*; b)C. Chen, L. Miao, K. Xu, J. Yao, C. Li, J. Jiang, *Physical chemistry chemical physics : PCCP* **2013**, *15*, 6431; c)H. Wang, Y. Wang, Z. Hu, X. Wang, *ACS applied materials & interfaces* **2012**, *4*, 6827; d)G. L. Luque, M. I. Rojas, E. P. M. Leiva, *Journal of Solid State Electrochemistry* **2013**, *17*, 1189; e)A. Morelos-Gómez, S. Vega-Díaz, V. González, F. Tristán-López, R. Cruz-Silva, K. Fujisawa, H. Muramatsu, T. Hayashi, X. Mi, Y. Shi, H. Sakamoto, F. Khoerunnisa, K. Kaneko, B. Sumpter, Y. Kim, V. Meunier, M. Endo, E. Muñoz-Sandoval, M. Terrones, *ACS Nano* **2012**, *6*, 2261; f)H. Santos, L. Chico, L. Brey, *Physical review letters* **2009**, *103*, 086801; g)J. Cai, P. Ruffieux, R. Jaafar, M. Bieri, T. Braun, S. Blankenburg, M. Muoth, A. Seitsonen, M. Saleh, X. Feng, K. Müllen, R. Fasel, *Nature* **2010**, *466*, 470.

[4] a)F. Winnik, D. Maysinger, *Accounts of chemical research* **2013**, *46*, 672; b)G. Kotchey, S. Hasan, A. Kapralov, S. Ha, K. Kim, A. Shvedova, V. Kagan, A. Star, *Accounts of chemical research* **2012**, *45*, 1770; c)R. Haddon, *Accounts of chemical research* **2013**, *46*, 1; d)L. Dai, *Accounts of chemical research* **2013**, *46*, 31.

[5] Y.-C. Lin, C.-C. Lu, C.-H. Yeh, C. Jin, K. Suenaga, P.-W. Chiu, *Nano Letters* **2012**, *12*, 414.

[6] S. Virendra, J. Daeha, Z. Lei, D. Soumen, I. K. Saiful, S. Sudipta, *Progress in Materials Science* **2011**, *56*, 1181.

[7] C. Bussy, H. Ali-Boucetta, K. Kostarelos, *Accounts of chemical research* **2012**, *46*, 692.

List of publications

[1] Preparation and characterization of rhodium nanostructures through the evolution of microgalvanic cells and their enhanced electrocatalytic activity for formaldehyde oxidation, Bhaskar R. Sathe, **Dhanraj B. Shinde**, Vijayamohanan K. Pillai. *J. Phys. Chem. C*. **2009**, *113*, 9616.

[2] Electrochemical unzipping of multi-walled carbon nanotubes for facile synthesis of high-quality graphene nanoribbons'' **Dhanraj B. Shinde**, Joyashish Debgupta, Ajay Kushwaha, Mohammed Aslam, K Vijayamohanan; *J. Am. Chem. Soc*. **2011**, *133*, 4168.

[3] Electrochemical preparation of luminescent graphene quantum dots from multiwalled carbon nanotubes'' **Dhanraj B. Shinde**, Vijayamohanan K. Pillai. *Chem. Eur. J.* **2012,** *39*, 12522.

[4] In situ electrochemical organization of CdSe nanoclusters graphene during unzipping of carbon nanotubes" Joyashish Debgupta, **Dhanraj B. Shinde**, Vijayamohanan K. Pillai; *Chem. Commun.* **2012**, *48*, 3088.

[5] Polydentate disulfides for enhanced stability of AuNPs and facile nanocavity formation" Satish C. Biradar, **Dhanraj B. Shinde**, Vijayamohanan K. Pillai, Mohan G. Kulkarni. *J. Mater. Chem.* **2012**, *22*, 10000.

[6] Morphology controlled synthesis of LiV205/Ag nanocomposite nanotubes with enhanced electrochemical performance" Rahul S. Diggikar, Vishal M. Dhavale, **Dhanraj B. Shinde**, Nihal S. Kanbargi, Bharat B. Kale; *RSC Adv*. **2012**, *2*, 3231.

[7] Electrochemical resolution of multiple redox events for graphene quantum dots" **Dhanraj B. Shinde**, Vijayamohanan K. Pillai; *Angewandte Chemie.* **2013**, *52*, 2482.

[8] Hysteresis and charge trapping in graphene quantum dots" Hemen Kalita, Harikrishnan V, **Dhanraj B. Shinde**, Vijayamohanan K. Pillai, M. Aslam; *Appl. Phys. Lett.* **2013**, *102*, 143104.

[9] Counter-ion dependent, longitudinal unzipping of multi-walled carbon nanotubes to highly conductive and transparent graphene nanoribbons **Dhanraj B. Shinde**, Vijayamohanan K. Pillai; Manuscript under review in "*Scientific reports*" **2013,** ID. **SREP-13-01836.**

[10] Stabilization of graphene quantum dots (GQDs) by encapsulation inside ZIF-8 nanocrystalsfor photoluminescence tuning Bishnu P. Biswal, **Dhanraj B. Shinde**, Vijayamohanan K. Pillai, Rahul Banerjee; Manuscript under review in "*Nanoscale*" **2013**, ID. **NR-ART-07-2013-003511.**

[11] Systematic electrochemical unzipping of SWNTs to graphene ribbons revealed by *in-situ* Raman spectroscopy and imaging" Robin John, **Dhanraj B. Shinde**, C. Vijayan, Lili Liu, Feng Ding, Zhiping Xu, Vijayamohanan K. Pillai, T. Pradeep; Manuscript under review in *ACS Nano* **2013** ID**, nn-2013-03289g**.

[12] Electrochemical preparation of nitrogen doped graphene quantum dots; Application for oxygen reduction". **Dhanraj B. Shinde**, Vishal Dhavale, Sreekumar kurungot, Vijayamohanan K. Pillai; Manuscript under review in *Journal of Physical Chemistry-C.* **2013**.

[13] Pegylated graphene quantum dots; Application for bioimaging" Anil Chandra, **Dhanraj B. Shinde**, Vijayamohanan K. Pillai, Neetu Singh; Manuscript under preparation **2013**.

Erratum